

REVISITING CHEMICAL SYSTEM SIZE USING STREUSEL (SURFACE  
TOPOLOGY RECOVERY USING SAMPLING OF THE ELECTRIC FIELD):  
THE ROLE OF SIZE IN ATOMIC, MOLECULAR, AND SOLID-STATE  
PROPERTIES

by

AUSTIN M. MROZ

A DISSERTATION

Presented to the Department of Chemistry and Biochemistry  
and the University of Oregon Division of Graduate Studies  
in partial fulfillment of the requirements  
for the degree of  
Doctorate of Philosophy

June 2022

## DISSERTATION APPROVAL PAGE

Student: Austin M. Mroz

Title: Revisiting Chemical System Size Using STREUSEL (Surface Topology REcovery Using Sampling of the ELeetric field): the role of size in atomic, molecular, and solid-state properties

This dissertation has been accepted and approved in partial fulfillment of the requirements for the Doctorate of Philosophy degree in the Department of Chemistry and Biochemistry by:

|                       |                              |
|-----------------------|------------------------------|
| James Prell           | Chair                        |
| Christopher H. Hendon | Core Member                  |
| Jeffrey Cina          | Core Member                  |
| Gregory Bothun        | Institutional Representative |

and

|                   |                                   |
|-------------------|-----------------------------------|
| Krista Chronister | Vice Provost for Graduate Studies |
|-------------------|-----------------------------------|

Original approval signatures are on file with the University of Oregon Division of Graduate Studies.

Degree awarded June 2022

© 2022 Austin M. Mroz  
All rights reserved.

## DISSERTATION ABSTRACT

Austin M. Mroz

Doctorate of Philosophy

Department of Chemistry and Biochemistry

June 2022

Title: Revisiting Chemical System Size Using STREUSEL (Surface Topology REcovery Using Sampling of the ELeetric field): the role of size in atomic, molecular, and solid-state properties

Atomic, molecular, and porous material void space shape and size play a critical role in chemistry. The most familiar method was formalized by Bondi: the van der Waal radii and volume of atoms and molecules. However, the rigid sphere approximation of atoms fails to describe highly polarized chemical systems. To overcome this challenge, numerous other approaches based on electron density have been presented, but these approaches intrinsically struggle to describe the surface area and volume of cations. Herein, we revisit the timeless problem of assessing sizes of atoms, molecules and porous material void spaces, through examination of the electric field produced by these chemical systems. In this way, we are able to recover chemical volumes and surface areas from simple DFT calculations. We perform a series of benchmarks to ensure the generality of our approach and demonstrate that electric field calculations provide unique insights into quantifying sizes of ions and polar molecules. Our method further lays the foundation for the development of analytical interaction energies based on assessment of the Coulomb potential produced by molecules systems, while providing a rigorous approach to study size dynamics as a function of chemical environment. Beyond these advancements, we demonstrate the advantageous role of electric field-derived size in determining the void space characteristics of nanoporous, crystalline materials.

## CURRICULUM VITAE

NAME OF AUTHOR: Austin M. Mroz

### GRADUATE AND UNDERGRADUATE SCHOOLS ATTENDED:

University of Oregon, Eugene, OR, USA

Rose-Hulman Institute of Technology, Terre Haute, IN, USA

### DEGREES AWARDED:

Doctor of Philosophy, Physical Chemistry, 2021, University of Oregon

Master of Science, Physical Chemistry, 2018, University of Oregon

Master of Science, Chemistry, 2017, Rose-Hulman Institute of Technology

Bachelor of Science, Mechanical Engineering, 2016, Rose-Hulman Institute of  
Technology

### AREAS OF SPECIAL INTEREST:

Electronic Structure Theory

Computer Informatics in Chemistry

Metal-Organic Frameworks

### PROFESSIONAL EXPERIENCE:

Graduate Teaching Fellow, University of Oregon, 2016-2019

Graduate Teaching Assistant, Rose-Hulman Institute of Technology, 2016

Product Engineering Intern, Alison Transmission, 2014

Design Intern, Rose-Hulman Ventures, 2013

### GRANTS, AWARDS AND HONORS:

Graduate Student Award for Excellence in Teaching of Chemistry,  
University of Oregon, 2019

Deans First Year Merit Award, University of Oregon, 2018

## PUBLICATIONS:

- Mroz, A. M.**; Hendon, C.H. "Revisiting the van der Waals radii: molecular volumes and surface areas of molecules derived from the electric field," Submitted.
- Mroz, A. M.**; Hendon, C.H. "Pore Topology Characterization using the Electric Field" In preparation.
- Mroz, A. M.**; D'Antona, N.; Sikma, E.; Cohen, S. M.; Hendon, C.H. "Engineering Conductive Pathways in Metal-Organic Frameworks via p-type Redox-Active Interstitials," In preparation.
- Mancuso, J. L.; **Mroz, A. M.**; Le, K. N., Hendon, C.H. "Electronic Structure Modeling of Metal-Organic Frameworks," *Chem. Rev.*, **2020**, 16, 8641.
- LeRoy, M. A.; **Mroz, A. M.**; Mancuso, J. L.; Miller, A.; Van Cleve, A.; Check, C.; Heinz, H.; Hendon, C. H.; Brozek, C. K. "Post-synthetic modification of ionic liquids using ligand-exchange and redox coordination chemistry," *J. Mater. Chem. A*, **2020**.
- Hamann, D. M.; Bardgett, D.; Bauers, S.R.; Kasel, T. W.; **Mroz, A. M.**; Hendon, C. H.; Medlin, D. L.; Johnson, D. C. "Influence of Nanoarchitecture on Charge Donation and Electrical Transport Properties in  $[(\text{SnSe})_1 + \delta][\text{TiSe}_2]_q$  Heterostructures," *Chem. Mater.*, **2020**, 32, 5802.
- Donor, M. T.; **Mroz, A. M.**; Prell, J. S. "Experimental and theoretical investigation of overall energy deposition in surface-induced unfolding of protein ions," *Chem. Sci.*, **2019**, 10, 1497.
- Sutton, E.C.; McDevitt, C. E.; Prochnau, J.Y.; Yglesias, M. V.; **Mroz, A. M.**; Yang, M. C.; Cunningham, R.M.; Hendon, C.H.; DeRose, V.J. "Nucleolar Stress Induction by Oxaliplatin and Derivatives," *J. Am. Chem. Soc.*, **2019**, 141, 18411.
- McDevitt, C. E.; Yglesias, M. V.; **Mroz, A. M.**; Sutton, E.C.; Yang, M. C.; Hendon, C.H.; DeRose, V.J. "Monofunctional platinum(II) compounds and nucleolar stress; is phenanthriplatin unique?," *J. Biol. Inorg. Chem.*, **2019**, 24, 899.

Kasel, T. W.; Deng, Z.; **Mroz, A. M.**, Hendon, C. H.; Butler, K. T.; Canepa, P., “Metal-free perovskites for non linear optical materials,” *Chem. Sci.*, **2019**, 10, 8187-8194.

**Mroz, A. M.**, “Pro- and Antioxidant Activity of Selenomethionine: Preventative Measures against Metal-Mediated DNA Oxidation,” M. Sc., Rose-Hulman Institute of Technology, Terre Haute, IN, **2017**.

## ACKNOWLEDGEMENTS

This work would not have been possible without the support of my advisor, Prof. Christopher H. Hendon, as well as my committee: Prof. James Prell, Prof. Jeffrey Cina, and Prof. Gregory Bothun.



## TABLE OF CONTENTS

| Chapter  | Page |
|--|------|
| I. INTRODUCTION . . . . .  | 1    |
| II. DENSITY FUNCTIONAL THEORY: AN OVERVIEW . . . . .   | 7    |
| Quantum Mechanics . . . . .  | 8    |
| Perturbation Theory . . . . .  | 10   |
| Variational Method . . . . .   | 11   |
| The Many-Body Hamiltonian and the Born-Oppenheimer Approximation   | 12   |
| Thomas, Fermi, and Dirac . . . . .   | 15   |
| Hartree, Hartree-Fock, and the Slater Determinant . . . . .  | 16   |
| The Birth of Density Functional Theory . . . . .   | 19   |
| 1. The total energy of the system is a functional of $\nu_{ext}$ , and, by extension, $n(r)$ . . . . .   | 19   |
| 2. The electron density that yields the minimized total energy is the ground state electron density, and may be solved for using the variational principle . . . . . | 21   |
| Kohn-Sham Density Functional Theory . . . . .  | 22   |
| Exchange and Correlation . . . . .   | 24   |
| The Exchange-Correlation Hole . . . . .  | 24   |
| Defining Exchange-Correlation . . . . .  | 25   |
| Pair Correlation Function . . . . .  | 28   |
| Self-Interaction Effects . . . . .   | 29   |
| Exchange-Correlation Approximations ( <i>i.e.</i> the functionals of DFT) . . . . .  | 29   |
| General Calculation Considerations . . . . .   | 33   |

| Chapter   | Page |
|---|------|
| Functional Selection . . . . .                              | 36   |
| Electronic structure modeling of extended solids . . . . .  | 41   |
| Periodic Models and <i>k</i> -Points . . . . .              | 42   |
| Electronic Band Gap . . . . .                               | 48   |
| Electronic Band Structures . . . . .                        | 51   |
| Electronic Band Dispersion . . . . .                        | 54   |
| Density of States . . . . .                                 | 55   |
| Defects . . . . .   | 56   |
| III.CHEMICAL SIZE OF ATOMS . . . . .                        | 59   |
| Introduction . . . . .                                      | 59   |
| Method Description . . . . .                                | 59   |
| Volumetric pixel resolution . . . . .                       | 60   |
| Functional Benchmarking . . . . .                           | 61   |
| Neutral and Neutral Bonded Systems . . . . .                | 69   |
| Ionic and Ionic Bonded Systems . . . . .                    | 73   |
| Ionic Liquids . . . . .                                     | 80   |
| Conclusions . . . . .                                       | 82   |
| IV.CHEMICAL SIZE OF PORES . . . . .                         | 85   |
| Abstract . . . . .  | 85   |
| Introduction . . . . .                                      | 85   |
| Results and Discussion . . . . .                            | 88   |
| Pore Volumes and Surface Areas . . . . .                    | 88   |
| Imaging Linker Vacancies using the Electric Field . . . . . | 92   |

| Chapter  | Page |
|--|------|
| V. COVALENT BRIDGE INTERSTITIALS AS A ROUTE<br>TOWARDS CONDUCTIVE FRAMEWORKS . . . . . | 97   |
| Abstract . . . . .   | 97   |
| Introduction . . . . .   | 98   |
| Results and Discussion . . . . .   | 101  |
| Infinite wire models . . . . .   | 103  |
| Calculation Details . . . . .  | 103  |
| Bulk wire formation simulations . . . . .  | 108  |
| Determining the degree of linker rotational freedom . . . . .                          | 109  |
| Generalized statistical model . . . . .  | 112  |
| Conclusions . . . . .  | 114  |
| REFERENCES CITED . . . . .   | 118  |

## LIST OF FIGURES

| Figure  | Page |
|---|------|
| <p>1. A timeline featuring the history of the atomic model (navy, top panel), experimental size quantification methods (periwinkle, middle panel), theoretical size quantification methods (teal, lower panel), and major milestones in computational chemistry (purple). . . . .</p>   | 2    |
| <p>2. Radii (y-axis) of Mg in two oxidation states (x-axis) for a series of experimental size methods (CN=coordination number). . . . .</p>   | 4    |
| <p>3. There exist several tiers of computational practices within theoretical chemistry. These range in their description of chemical system, and selection depends on system size, as well as the target properties. . . . .</p>   | 7    |
| <p>4. Jacob’s ladder of functionals where accuracy increases with computational cost. Some common functionals corresponding with each rung are listed on the right. . . . .</p>   | 38   |
| <p>5. Linear correlation between computed electronic band gap and bipyridine dicarboxylate (bipydc) incorporation in Zr-UiO-67. The HSE06 (top) and PBEsol (bottom) functionals show qualitatively the same trend, but PBEsol consistently underestimates the band gap by 1 eV. The gray star represents the extrapolated value derived from the best fit line to account for a computational limitation. Data obtained from ref<sup>(1)</sup>. Figure reprinted with permission from ref.<sup>(2)</sup>. . . . .</p> | 40   |
| <p>6. Computed electronic band gaps of HKUST-1, UiO-67, UiO-66, Zn-BTC, and linker functionalized derivatives. HSE06 systematically predicts larger band gap energies than PBE, more closely matching the experimental values. Data obtained from ref<sup>(3)</sup>. Figure reprinted with permission from ref.<sup>(2)</sup>. . . . .</p>  | 41   |

| Figure   | Page |
|--|------|
| 7. As size of a chemical system increases toward an infinite solid, the number of molecular orbitals becomes very large. For high symmetry materials, the crystallite can be described using a smaller, repeating unit, whose projection through reciprocal space generates electronic bands. Figure reprinted with permission from ref. <sup>(2)</sup> . . . . .  | 42   |
| 8. Although the smallest computational cell can save resources, an improper model may be recovered if a chemical interaction permeates beyond a single geometric cell. For example, (a) structural distortions are sometimes captured in temperature independent DFT (the ground state may feature titling of nodes); <sup>(4)</sup> and (b) magnetic ordering can be challenging if the unit cell contains an odd number of coupling metals (for example, the unit cell of Co <sub>2</sub> Cl <sub>2</sub> bis(1H-1,2,3- triazolo[4,5- <i>b</i> ],[4,5- <i>i</i> ])dibenzo[1,4]dioxin), (BTDD), contains 3 Co- (II), which do prefer to order antiferromagnetically <sup>(5)</sup> ). Figure reprinted with permission from ref. <sup>(2)</sup> . . . . .   | 44   |
| 9. General computational approach used to obtain electronic structure properties from solid-state structures. (a) Beginning with an experimentally obtained crystal structure, partial occupancies must be resolved. Then, where applicable, protons must be added to charge balance the cell, in effect establishing the oxidation state of the metals. Extrinsic solvent may be removed to simulate the activated MOF. Symmetry can then be enforced and a computational primitive cell may be available. (b) The structure can then be equilibrated, and higher level electronic structure properties can be obtained by sampling the first Brillouin zone, including electronic band structures and corresponding density of states. Figure reprinted with permission from ref. <sup>(2)</sup> . . . . . | 49   |
| 10. An illustration of the band gap in a semiconductor as a function of reciprocal space when the CBM and VBM are at the same point in reciprocal space providing a direct band gap and when they are at different points in reciprocal space creating an indirect minimum absorption energy. Figure reprinted with permissions from ref. <sup>(2)</sup> . . . . .   | 51   |

| Figure   | Page |
|--|------|
| 11. Node or linker vacancies result in charge balancing ions bound to the vacant sites (e.g., a proton or formate). Both nodes and linkers can also be redox active forming structurally bound charge carriers. Figure reprinted with permissions from ref. <sup>(2)</sup> . . . . .   | 57   |
| 12. Decreasing the volumetric pixel volume increases the time-to-solution (dashed curves) exponentially, yet minimizes the accuracy of the calculated volume (solid curves). Thus, we take the kneepoint of the time curve as the ideal volumetric pixel volume, 0.008 Å <sup>3</sup> . . . . .  | 61   |
| 13. Calculated STREUSEL volumes of H <sub>2</sub> and CH <sub>4</sub> optimized with each basis set (x-axis), normalized to the volume obtained from the aug-cc-pVTZ (y-axis). The normalized volumes represent the precision of each basis set, a metric of how close the returned electronic structure is to that obtained using aug-cc-pVTZ. aug-cc-pVTZ is considered sufficiently large – as demonstrated by the convergence of normalized volumes with larger basis sets ( <i>i.e.</i> cc-pVQZ and aug-cc-pVQZ). . . . .   | 62   |
| 14. Calculated STREUSEL volumes of a series of industrially relevant small molecules optimized with each functional (y-axis), normalized to the volumes obtained from the CCSD-full functional (x-axis). The spread of normalized volumes represents the precision of each functional, a metric of how close the returned electronic structure is to that obtained using CCSD-full, which is assumed to yield the exact geometry. The forty-nine functionals are grouped by functional type (generalized gradient approximation (GGA), generalized gradient exchange (GGE), hybrid (H), meta (M), hybrid-meta (HM), and local-density approximation (LDA). To increase resolution, Ne and F <sub>2</sub> are not included in this plot and are discussed extensively in the main text. . . . . | 63   |

| Figure  | Page |
|---|------|
| 15. Calculated STREUSEL volume of a series of industrially-relevant small molecules optimized with each functional (y-axis), normalized to the volume obtained from the CCSD-full functional (x-axis). The spread of normalized volumes represents the precision of each functional, a metric of how close the returned electronic structure is to that obtained using CCSD-full, which is assumed to yield the exact geometry. The forty-nine functionals are grouped by functional type (generalized gradient approximation (GGA), generalized gradient exchange (GGE), hybrid (H), meta (M), hybrid-meta (HM), and local-density approximation (LDA)). . . . . | 66   |
| 16. The mean absolute deviation (y-axis) of two volume methodologies (STREUSEL, van der Waals) across all of the studied functionals (x-axis). The mean absolute deviation is averaged across the mean absolute deviation for industrially relevant small molecules was calculated assuming the volume obtained from the CCSD-full optimized geometry as the chosen measure of central tendency. The mean absolute deviation is a metric of how close the returned electronic structure is to that obtained using CCSD-full, which is assumed to yield the exact geometry. The forty-nine functionals are grouped by functional type. . . . .                     | 68   |
| 17. Atomic radii for elements 1-96 of the periodic table calculated using STREUSEL are presented. Neutral atoms were modeled using functional CCSD-full with the SDDAll basis set. The radii are calculated from the STREUSEL-obtained volumes under the spherical approximation. . . . .   | 70   |
| 18. A comparison of atomic radii recovered using various conventional size metrics. <b>a)</b> Sizes computed from STREUSEL are similar to those presented by Alvarez, and Rahm and Boyd (top panel). <b>b)</b> Alternative size metrics are presented as the upper and lower limits. . . . .  | 72   |
| 19. Calculated STREUSEL ionic radii (y-axis) for relevant oxidation states of atoms 1-86 (x-axis). . . . .  | 74   |

| Figure   | Page |
|--|------|
| 20. Comparison of proton count ( $n_{protons}$ )-to-electron count ( $n_{electrons}$ ) ratio (x-axis) for the first row transition metals (y-axis) across a series of oxidation states (colors) featuring data points correlated with calculated STREUSEL ionic radii (data point size). . . . .   | 76   |
| 21. STREUSEL volumes (y-axis) for a series of six diatomic molecules were calculated for the optimized structures, and a series of models with expanded bond lengths (x-axis). Individual ion volumes ( <i>i.e.</i> Li <sup>+</sup> , F <sup>-</sup> , Cl <sup>-</sup> , and Br <sup>-</sup> ) were calculated and summed to obtain the maximum volume for each ionic compound. . . . .  | 78   |
| 22. Comparison of molecular volumes for a series of geometrically equilibrated diatomic molecules with varying dipole moments. Divergence between electronic density-based size metrics and STREUSEL depends on the system polarity and atomic electronegativity. . . . .  | 79   |
| 23. The Boyd (periwinkle), Bader (mint), and STREUSEL (charcoal) surfaces of a series of diatomic molecules. All surfaces are plotted using VESTA. The Boyd surface is depicted at an isosurface value of 0.00015 eÅ <sup>-3</sup> . The Bader surface is depicted at an isosurface value of 0.00030 eÅ <sup>-3</sup> . The STREUSEL surface is depicted at an isosurface value relative to the minimum value of the electric field surface mapped on the electrostatic potential map. . . . . | 81   |
| 24. Connolly surface area lacks information. van der Waals surface area does not account for polarized bonds. . . . .  | 88   |
| 25. There is good agreement between the pore volumes obtained using Platon and STREUSEL. Both void space calculation metrics are performed using pristine structures. The solid black line represents the values where Platon = STREUSEL. . . . .  | 89   |
| 26. Comparison of experimental pore volumes and STREUSEL pore volumes for a series of MOFs. Data points are colored according to the probe gas molecules used in the experimental measurement. there appears to be no correlation with the experimental probe gas; this is likely due to unknown differences in sample preparation and measurement conditions. The full dataset with corresponding references is presented in Appendix B. . . . .  | 90   |



| Figure   | Page |
|--|------|
| 27. Comparison of experimental surface areas calculated via BET (green) and Langmuir (blue) isotherms and STREUSEL surface areas for a series of MOFs. . . . .   | 91   |
| 28. Comparison between published Langmuir surface areas for experimental samples of MOF-5, the Connolly surface area (purple), and the STREUSEL surface area (green). . . . .  | 93   |
| 29. Three passivated models of UiO-66 are examined in this study; H <sub>2</sub> O, Cl <sup>-</sup> /H <sub>2</sub> O, F <sup>-</sup> /H <sub>2</sub> O, and formate. . . . .  | 96   |
| 30. The two examined positions for the covalent bridging motifs are labelled within the MOF-5 subunit. Five covalent bridging motifs were examined – polyaniline (PANI), polyphenylene sulfide (PPS), two thienothiophene derivatives (TT1 and TT2), and poly(p-phenylene vinylene) (PPV). Covalent bridging motif lengths are displayed. . . . .  | 102  |
| 31. The Fermi-aligned band structure of pristine MOF-5 features flat bands with a large band gap (3.50 eV). MOF-5 models featuring polyaniline (MOF-5-PANI) and polyphenylene sulfide (MOF-5-PPS) interstitials reveal increased band dispersion and smaller band gaps than their pristine counterpart. Oxidized models of MOF-5-PANI and MOF-5-PPS are also presented and feature bands that cross the Fermi level. . . . .   | 105  |
| 32. The Fermi-aligned band structure of pristine MOF-5 features flat bands with a large band gap (3.50 eV). MOF-5 models featuring two thienothiophene derivatives (MOF-5-TT1, and MOF-5-TT2) reveal increased band dispersion and smaller band gaps than their pristine counterpart. Spin-polarized electronic band structures of the oxidized models of MOF-5-TT1 and MOF-5-TT2 are also presented and feature bands that cross the Fermi level. Spins are separated by band color within the oxidized models. . . . . | 106  |
| 33. The vacuum-aligned band structure of pristine MOF-5 features flat bands with a large band gap (3.50 eV). MOF-5 models featuring polyaniline (MOF-5-PANI) and poly(p-phenylene vinylene) (MOF-5-PPV) interstitials reveal increased band dispersion and smaller band gaps than their pristine counterpart. . . . .  | 107  |

| Figure  | Page |
|---|------|
| 34. Two SH group orientations were sampled to determine the degree of linker rotational freedom; 1) toward, in which the SH groups of adjacent linkers point toward each other, and 2) away, in which the Cl groups of adjacent linkers point away from one another. . . . .  | 109  |
| 35. <b>a</b> The bulk wire length distribution totaled over 100 simulations. One run resulted in a wire length of 15 units, “model-15.” <b>b</b> The bulk wire length distribution for model-15. The MOF-5 depiction of model-15 with the longest wire highlighted in yellow. . . . .   | 111  |
| 36. <b>a</b> Net theory is used to translate the crystalline structure of MOF-5 to a tensor. <b>b</b> The tensor elements may then be iterated to represent bulk wire formation in four distinct steps; 1) the initial tensor is initialized with linker orientations, 2) paths are then identified, 3) linkers that are not in a wire are reoriented, steps 1) – 3) are repeated until no linker reorientation will result in a new wire formation, at this point, 4) the macroscopic connectivity is assessed. For visual simplicity, we do not show the layers in the third dimension – although our statistical model does take these into account. . . . . | 113  |
| 37. Unconnected linkers as a function of algorithmic step for a series of model sizes using the generalized statistical model. . . . .  | 114  |
| 38. The bulk wire length distribution for a 6-2 net topology allowing connections between 90deg linkers, totaled over 100 iterations of the general statistical model. . . . .  | 115  |
| 39. The bulk wire length distribution for a 6-2 net topology allowing connections between 180deg linkers, totaled over 100 iterations of the general statistical model. . . . .   | 116  |

## LIST OF TABLES

| Table   | Page |
|---|------|
| 1. Summary of properties embodied by five functional types: local-density approximation (LDA), generalized gradient approximation (GGA), meta-GGA (M-GGA), hybrid-GGA (H-GGA), weighted density approximation (WDA). . . . .  | 33   |
| 2. A comprehensive list of the representative functionals from each level of theory ( <i>ab initio</i> , generalized gradient exchange (GGE), local-density approximation (LDA), range separated, generalized gradient approximation (GGA), hybrid-GGA (H-GGA), hybrid-meta-GGA (HM-GGA), and meta-GGA (M-GGA)) examined in this work. . . . .  | 65   |
| 3. Molecular volumes for the relevant small molecules examined in this study calculated using the van der Waals (vdW) and the STREUSEL volume calculation methods. . . . .  | 69   |
| 4. Molecular volumes ( $\text{\AA}^3$ ) comparison between Bader, Boyd, van der Waals and STREUSEL size quantification methods. . . . .   | 71   |
| 5. Boyd, Bader, Batsanov and STREUSEL-derived molecular volume ( $\text{\AA}^3$ ) comparison for two ionic liquids possessing perchlorometallate anions. The sum of single molecule volumes for the individual constituents ( $[BMIM]^+$ , $[VCl_4]^-$ , $[CoCl_4]^{2-}$ ) are presented, as well as the fully geometry-optimized ion pair. The percent difference (%) is presented for each ionic liquid model. BMIM = 1-butyl-3-methylimidazolium . . . . . | 81   |
| 6. Comparison of electronic properties for the infinite wire models listed in order of decreasing band dispersion (meV). . . . .  | 104  |

# CHAPTER I

## INTRODUCTION

Chemical size is a fundamental property that governs a wealth of chemical interactions, including steric and non-covalent interactions,<sup>(6;7;8;9;10;11;12)</sup> enzyme docking,<sup>(13)</sup> and electrochemical properties,<sup>(14)</sup> in addition to the application performance of porous solids, such as heterogeneous gas storage,<sup>(15;16;17)</sup> separation technologies,<sup>(18;19)</sup> and catalytic activity.<sup>(20;21;22;23)</sup>

Quantifying chemical system size, however, is convoluted by the definition of the atomic “surface,” since calculated sizes depend both on the model and chemical environment.<sup>(14;24)</sup> For example, conventional size metrics predicated on the familiar van der Waals radii are not directly applicable for ions in molecular electrolyte systems because a sum of rigid ionic spheres poorly represents chemical regions of high polarization.<sup>(14)</sup> Indeed, alternative size quantification methodologies, both experimental and theoretical, are necessary.

Size quantification metrics have developed through a synergy of both experiment and theory,<sup>(24)</sup> Figure 1. Initial experimental measurements of atomic size were performed by Meyer in 1870, where he used a relationship between material density and atomic size, and obtained a periodic trend in atomic volumes.<sup>(25)</sup> These values were later refined by Bragg<sup>(26)</sup> and Pauling<sup>(27)</sup>, who developed methods for assessing atomic radii through X-ray scattering. Bond then revisited the radii presented by Pauling and Bragg, and it is Bondi’s work that underpins and is synonymous with the “van der Waals radii”.<sup>(28;29)</sup> Batsanov then expanded the van der Waals radii for elements 1-96 through examination of single crystal X-ray diffraction, molar volumes and crystal packing.<sup>(30)</sup> A more modern approach was taken by Alvarez,<sup>(31;32)</sup> and Biswas and Ghosh,<sup>(33)</sup> who extracted

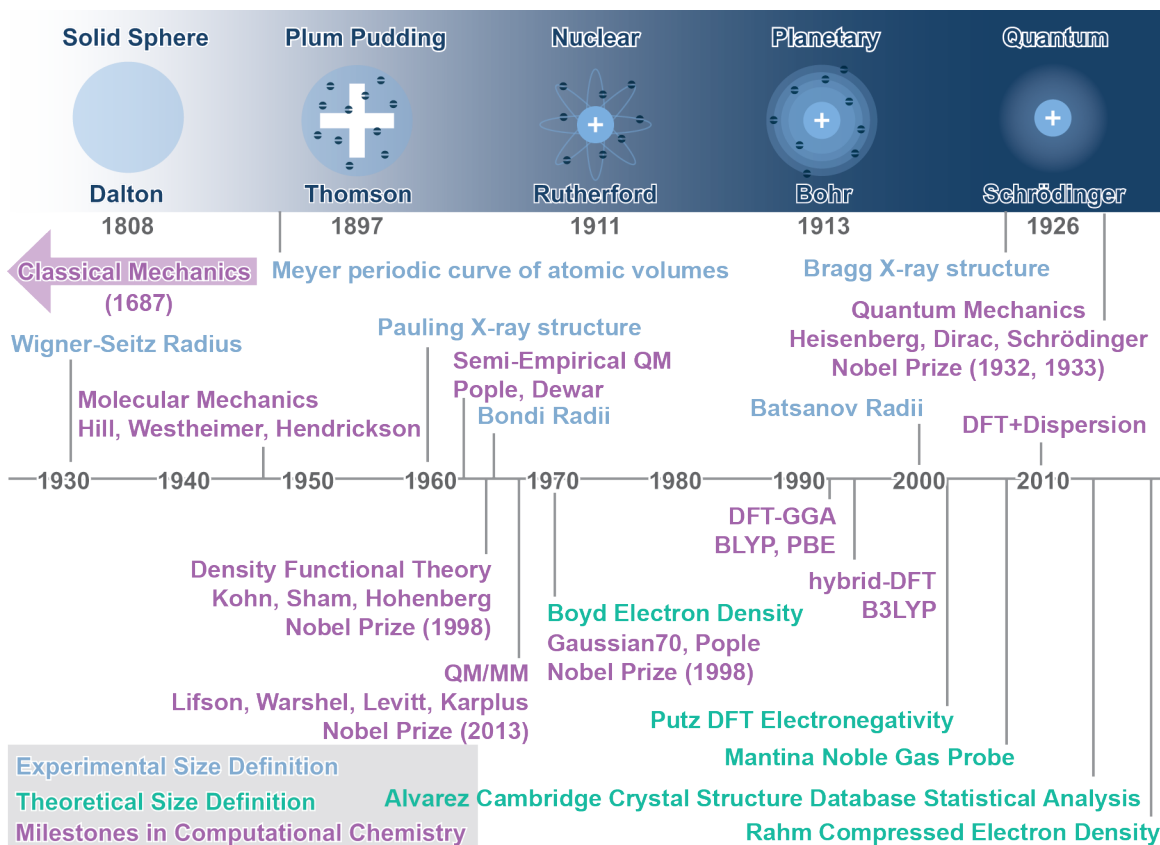


Figure 1. A timeline featuring the history of the atomic model (navy, top panel), experimental size quantification methods (periwinkle, middle panel), theoretical size quantification methods (teal, lower panel), and major milestones in computational chemistry (purple).

atomic radii using a statistical analyses of online databases. Marrying all of these approaches is atomic size derived from solid phase experiments and/or molecular spectroscopic data. This, however, limits the ability to derive accurate atomic and molecular volumes for environments not represented in empirical data,<sup>(24)</sup> posing challenges for size quantifications of molecules with high polarity<sup>(34;35;36)</sup> and unusual elongated bonds,<sup>(37;38;39)</sup> among others. These systems also pose problems for size metrics that estimate covalent interactions, *e.g.* Pyykkö radii,<sup>(40)</sup> for the same reasoning.

Independent of precise methodology, all size calculation metrics work to identify the extent to which a chemical system permeates in space. Indeed, as illustrated by the variety of methodologies presented above, there are different ways of defining the surface of a chemical system. The advent of inexpensive computational developments and hardware advancements has enabled a density functional theory (DFT)-derived size calculation methods, particularly useful for emerging exotic molecules.<sup>(41)</sup> Theory-based size metrics proved an accurate path towards assessing atomic and molecular volumes of novel chemical systems, assuming the theory is exact. Such calculations were pioneered by Slater who employed the maximum radial density of outermost single particle wavefunctions to define atomic radii.<sup>(42;43;44)</sup> Further theoretical size quantifications explored deriving size from potential minima,<sup>(45;46;47)</sup> gradients of Tomas-Fermi kinetic energy functional and exchange-correlation energy,<sup>(48)</sup> electronegativity derived using DFT,<sup>(49)</sup> and electronic moment calculations.<sup>(50)</sup>

Bader<sup>(51)</sup> first identified the utility of quantum chemical simulation and computed size at the Hartree-Fock level of theory, in defining the surface of a chemical system and ultimately calculating the size by defining an electron density cutoff of  $0.002 e \text{ bohr}^{-3}$ . This cutoff was further refined by Boyd<sup>(52)</sup> to be  $0.001 e \text{ bohr}^{-3}$  with the justification that any smaller value of electron density would result in a negligible change in calculated radii.<sup>(52)</sup> Recently, Rahm and Hoffmann applied the Boyd cutoff to anions and cations using electron densities obtained from DFT<sup>(24)</sup> with a hybrid GGA functional, PBE0<sup>(53;54;55)</sup>, and a sufficiently large basis set, ANO-RCC. There, the authors highlight that since DFT is founded on the Hohenberg-Kohn theorems, which state that the ground state energy of a many electron system is defined by the distribution of the electron density,<sup>(56;57)</sup>

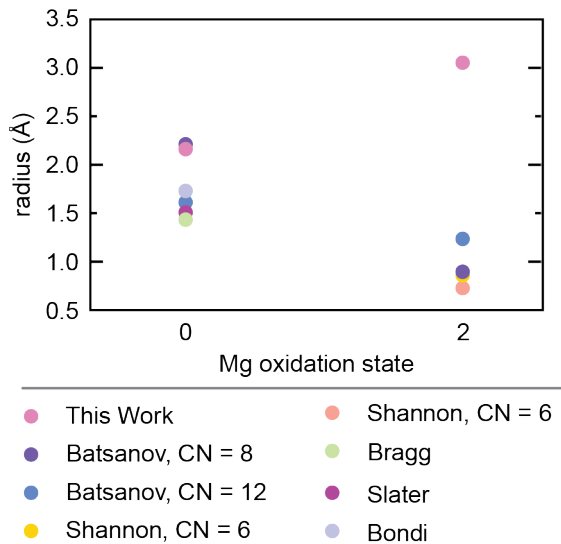


Figure 2. Radii (y-axis) of Mg in two oxidation states (x-axis) for a series of experimental size methods (CN=coordination number).

DFT itself is an approximation of an exact exchange-correlation functional. Thus, simply using DFT to compute size presents its own challenges as there are many available functional types, which differ in their treatment of electron density, and yield differing resultant properties.<sup>(58;59;60)</sup> Yet, the key benefit of theory-based methods makes them attractive, as they are inherently general and may be applied to both molecules and materials that are not presented in online repositories.

Further, the use of electron density poses problems for modeling cations, who certainly interact with their surroundings far beyond their electron cloud via strong Coulombic interactions.<sup>(61)</sup> Thus, instead of examining the density of electrons, this work revisits the size quantification problem through examination of the electrostatic potential, and associated electric field. This method is, in principle, robust even for polarized and ionic systems, in addition to enabling quantification of atomic, molecular, and porous scaffold void size, and possibly even analytical interaction energies.

While previous metrics are concerned with the space that a chemical system resides in – *occupied space* – this work focuses on the volume that a chemical system affects – *affected space*. This is best demonstrated by examining Mg and  $\text{Mg}^{2+}$ , Figure 2. Owing to the increased oxidation relative to the neutral counterpart, cations are expected to possess a smaller occupied space; this is reflected in published ionic size metrics,<sup>(26;62;63;64;65;66;67)</sup> which are compiled for Mg, Figure 2. These metrics are inherently dependent on coordination number, resulting in several accepted values for Mg, and reveals how close other chemical species may bond with Mg. Yet, this does not reveal how close chemical species need to be to be attracted to Mg. Perhaps counter-intuitively, electric field-based sizes increase with increasing oxidation.

Within neutral atoms, the number of protons is equivalent to the number of electrons; therefore, the net electric field produced is 0. Ions, however, possess an inequivalent number of electrons and protons, thus, there exists a net field that extends beyond the neutral atom – ultimately resulting in a larger *affected size*. Thus, the electric field-based size metric presented in this work reveals that  $\text{Mg}^{2+}$  is larger than Mg, Figure 2. In this way, we assess the known long-range interactions associated with cations.<sup>(68;69)</sup>

The utility of this methodology is facilitated by the culmination of this thesis – a post-DFT software termed STREUSEL (Structure Topology REcovery Using Sampling of the ELeetric field).<sup>(70)</sup> The validity of the approach facilitated by this software is assessed via several atomic, molecular, and solid-state experiments detailed in the following chapters.

Chapter 2 presents the background and subsequent derivations leading to the eventual development of DFT. Chapter 3 outlines the atomic studies used



to validate this approach, as well as several molecular experiments depicting the utility of the electric field-based size approach. Chapter 5 outlines the necessity of electric field-based size in calculating the void space properties of porous scaffold, namely metal-organic frameworks (MOFs). Chapter 6 expands on the application of the presented size metric to MOFs, in which the presented size metric is used to assess the likelihood certain MOF scaffolds will accommodate a variety of redox-active interstitials. Chapter 7 outlines future applications, developments and directions for the STREUSEL software package.

## CHAPTER II

### DENSITY FUNCTIONAL THEORY: AN OVERVIEW

The history of chemical modeling finds its foundation in the evolution of the atomic model, Figure 1. While theories concerning the connectivity and shapes of atoms date back to the 17<sup>th</sup> century,<sup>(71)</sup> we begin our discussion with the emergence of the solid sphere atomic model postulated by John Dalton in 1808<sup>(72)</sup> and the eventual development of quantum mechanics in 1926. Within this time frame, the scientific foundation of modeling was refined, eventually leading to the vast computational toolbox available today. The simplified schematic presented in Figure 3 features the models primarily applied within chemistry, which range in level of theory.

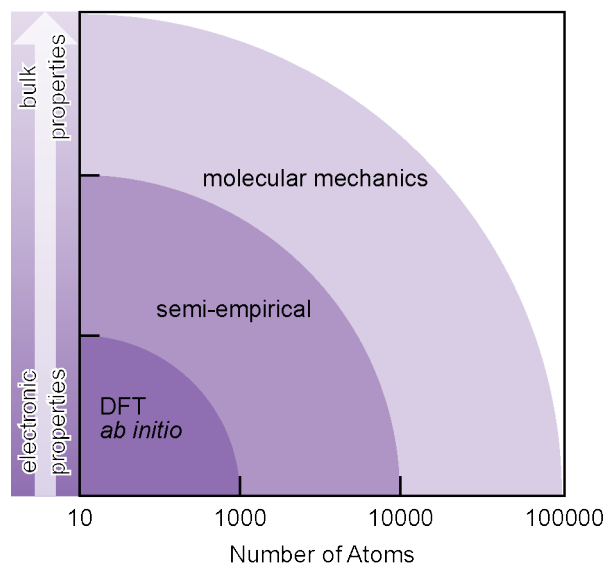


*Figure 3.* There exist several tiers of computational practices within theoretical chemistry. These range in their description of chemical system, and selection depends on system size, as well as the target properties.

The highest level of theory, *ab initio*, is derived from quantum mechanics and rely on varying methods of determining a solution to the Schrödinger Equation

and provide electronic insights into chemical phenomena. While the most accurate, quantum mechanics-based methods are largely limited by system size.

Within the context of this thesis, all chemical modeling was performed using density functional theory (DFT), as implemented in the Vienna *Ab Initio* Software Package (VASP),<sup>(73;74;75;76)</sup> and Gaussian09.<sup>(77)</sup>

The chapter is organized as follows: We start with the six tenets of quantum mechanics, followed by a discussion of the many-body Hamiltonian and the pivotal role of the Born-Oppenheimer Approximation. We then move into a discussion of the contributions of Tomas, Fermi, and Dirac; followed by the developments presented by Hartree and Fock, and the role of the Slater Determinant. The derivation of theory is culminated in a discussion of Kohn-Sham density functional theory (DFT), which includes a practical discussion of exchange and correlation. We conclude this chapter with a practical discussion of general calculation considerations when using electronic structure theory, as well as a discussion of electronic structure theory applied to the solid-state.

## **Quantum Mechanics**

Several experiments performed in the late 19<sup>th</sup> and early 20<sup>th</sup> centuries revealed the wave-particle duality of matter, leading scientists to eventually develop the more general theory of quantum mechanics to describe these newly observed phenomena. The birth of quantum mechanics was spurred by the discovery of the photon credited to Planck,<sup>(78)</sup> notion of quantized light from Einstein,<sup>(79)</sup> and the subsequent presentation of the atomic model presented by Bohr.<sup>(80)</sup> The field was furthered by the introduction of the spin quantum number,<sup>(81)</sup> and the development of the de Broglie wavelength,<sup>(82)</sup> which ultimately supported the wave-particle duality hypothesis that is critical to modern quantum mechanics.

These developments enabled Heisenberg<sup>(83)</sup> and Born<sup>(84;85)</sup> to present a non-relativistic theory of quantum mechanics. This was followed by the presentation of the wave-mechanical description of the atom by Schrödinger,<sup>(86)</sup> and the development of the Heisenberg uncertainty principle.<sup>(87)</sup> These developments ultimately led to the tenets of quantum mechanics,<sup>(88)</sup> with which we will begin our discussion of *ab initio* computational methods. We will follow the description presented by McQuarrie:<sup>(89)</sup>

1. The exact state of any quantum mechanical system is described by its wavefunction,  $\Psi(r, t)$ , which is dependent on the positions ( $r$ ) of the particles in the system at a specific time ( $t$ ). While  $\Psi(r, t)$  often contains imaginary components,  $\Psi^*(r, t)\Psi(r, t)$  is real and represents the probability a particle resides in  $r$  at  $t$ . Thus, by extension, the likelihood of a particle occupying *any* region of space is

$$\int_{-\infty}^{\infty} \Psi^*(r, t)\Psi(r, t)dr = 1 \quad (2.1)$$

2. There exists a quantum mechanical Hermitian operator whose expectation value is real that describes every experimental observable.
3. Any measurement of an observable described by operator  $\hat{A}$  will only be eigenvalues ( $a$ ) that satisfy

$$\hat{A}\Psi = a\Psi \quad (2.2)$$

Thus, a measurement of a system in eigenstate  $\hat{A}$  will yields its eigenvalue,  $a$ . The state of a system is not required to be an eigenstate of  $\hat{A}$ , and can be expanded to a complete set of eigenvectors of  $\hat{A}$ ,

$$\hat{A}\Psi_i = a_i\Psi_i \quad (2.3)$$

as

$$\Psi = \sum_i^n c_i \Psi_i \quad (2.4)$$

However, if the observable is measured, only one of the eigenvalues ( $a_i$ ) is observed, the identity of which is described as a probability. Upon measurement of  $\Psi$  that returns an eigenvalue,  $a_i$ ,  $\Psi$  collapses to the corresponding eigenstate ( $\Psi_i$ ) associated with  $a_i$ .

4. The average value of an observable can be calculated using

$$\langle A \rangle = \int_{-\infty}^{\infty} \Psi^* \hat{A} \Psi d\tau = \langle \Psi | \hat{A} | \Psi \rangle \quad (2.5)$$

if the system is in a state that can be described by a normalized wavefunction.

5. The time-dependent Schrödinger equation

$$\hat{H}\Psi(r, t) = i\hbar \frac{\partial \Psi}{\partial t} \quad (2.6)$$

describes the evolution of the wavefunction of a system in time.

6. With respect to all coordinates, the total wavefunction ( $\Psi(r, t)$ ) must be antisymmetric. Lastly, electron spin is a required coordinate.

There does not exist an exact solution to the Schrödinger equation for systems larger than the Hydrogen atom. Approximate methods must be used to obtain solutions; these include perturbation theory and the variational method.

**Perturbation Theory.** The major assertion of Perturbation Theory is that the Hamiltonian ( $\hat{H}$ , operator describing the total energy of a system) may be split into two components, i) the “unperturbed” Hamiltonian, which can be solved, and ii) the “perturbed” Hamiltonian, which cannot be solved. Contingent on a small perturbation, this theory is used to continually refine the “unperturbed”

Hamiltonian such that the contributions of the “perturbed” Hamiltonian are realized.

**Variational Method.** The Variational Method is an analytical procedure whereby “trial” wavefunctions are continually guessed for the system. These wavefunctions include a series of variable (“variational”) parameters, which are iterated until the energy of the trial wavefunction is minimized. This method is based on the Variational Principle, which states that any energy obtained using the Variational Method is greater than the true total energy of the system. The Variational Principle is derived as follows.

Let  $\phi$  represent the trial wavefunction described by a linear combination of exact eigenfunctions  $\Psi_i$

$$\phi = \sum_i c_i \Psi_i \quad (2.7)$$

Thus, the approximated energy ( $E$ ) of  $\phi$  is

$$E[\phi] = \frac{\int \phi^* \hat{H} \phi}{\int \phi^* \phi} \quad (2.8)$$

Substituting (2.7) into (2.8) yields

$$E[\phi] = \frac{\sum_{ij} c_i^* c_j \int \Psi_i^* \hat{H} \Psi_j}{\sum_{ij} c_i^* c_j \int \Psi_i^* \Psi_j} \quad (2.9)$$

Recall,  $\Psi_j$  are exact eigenfunctions of  $\hat{H}$ , thus

$$\hat{H} \Psi_j = \varepsilon_j \Psi_j \quad (2.10)$$

Using(2.10), and the considering that eigenfunctions of  $\hat{H}$  form an orthonormal set, we find

$$E[\phi] = \frac{\sum_i c_i^* c_i \varepsilon_i}{\sum_i c_i^* c_i} \quad (2.11)$$

Subtracting the exact ground state energy,  $\varepsilon_0$  from (2.11)

$$E[\phi] - \varepsilon_0 = \frac{\sum_i c_i^* c_i (\varepsilon_i - \varepsilon_0)}{\sum_i c_i^* c_i} \quad (2.12)$$

Since

$$\frac{\sum_i c_i^* c_i (\varepsilon_i - \varepsilon_0)}{\sum_i c_i^* c_i} \geq 0 \quad (2.13)$$

then

$$E[\phi] - \varepsilon_0 \geq 0 \quad (2.14)$$

$$E[\phi] \geq \varepsilon_0 \quad (2.15)$$

Thus any calculated energy of a trial wavefunction is *always* greater than or equal to the exact ground state energy.

### The Many-Body Hamiltonian and the Born-Oppenheimer Approximation

We examine the formulation of the many-body Hamiltonian using the organization presented by Szabo and Ostlund.<sup>(90)</sup> The many-body Hamiltonian,  $\hat{H}$ , accounts for the kinetic energy of the electrons ( $\hat{T}_e$ ) and the nuclei ( $\hat{T}_n$ ), as well as the potential energy of electron-electron repulsion ( $\hat{U}_{ee}$ ), nuclei-nuclei repulsion ( $\hat{U}_{nn}$ ), and electron-nuclei Coulombic attraction ( $\hat{U}_{en}$ )

$$\hat{H} = \hat{T}_e + \hat{T}_n + \hat{U}_e + \hat{U}_n + \hat{U}_{en} \quad (2.16)$$

The kinetic energy terms take the form

$$\begin{aligned} \hat{T}_n &= - \sum_i \frac{\hbar^2}{2M_i} \nabla_{R_i}^2 \\ \hat{T}_e &= - \sum_i \frac{\hbar^2}{2m_e} \nabla_{r_i}^2 \end{aligned} \quad (2.17)$$

where  $M_i$  is the mass of nucleus  $i$ ,  $m_e$  is the mass of an electron,  $R$  represent the nuclear coordinates, and  $r$  represents electronic coordinates. The potential energy

terms take the form

$$\begin{aligned}
\hat{U}_{nn} &= \frac{1}{2} \sum_i \sum_{j \neq i} \frac{Z_i Z_j e^2}{4\pi\epsilon_0 |R_i - R_j|} \\
\hat{U}_{ee} &= \frac{1}{2} \sum_i \sum_{j \neq i} \frac{e^2}{4\pi\epsilon_0 |r_i - r_j|} \\
\hat{U}_{en} &= - \sum_i \sum_j \frac{Z_i e^2}{4\pi\epsilon_0 |R_i - r_j|}
\end{aligned} \tag{2.18}$$

where  $Z_x$  is the nuclear charge of nuclei  $x$ , and  $e$  is the elementary charge.

Consider a Hamiltonian that is a function of only two coordinate terms,  $q_1$  and  $q_2$ ; then

$$\hat{H} = \hat{H}_1(q_1) + \hat{H}_2(q_2) \tag{2.19}$$

By extension, the Schrodinger equation becomes

$$\hat{H}\Psi(q_1, q_2) = E\Psi(q_1, q_2) \tag{2.20}$$

Assuming that  $\Psi(q_1, q_2)$  is separable such that  $\Psi(q_1, q_2) = \psi_1(q_1)\psi_2(q_2)$ , and  $\psi_a(q_a)$  is an eigenfunction of  $\hat{H}_a$  possessing eigenvalue  $E_a$ , then

$$\begin{aligned}
\hat{H}\Psi(q_1, q_2) &= (\hat{H}_1 + \hat{H}_2)\psi_1(q_1)\psi_2(q_2) \\
&= \hat{H}_1\psi_1(q_1)\psi_2(q_2) + \hat{H}_2\psi_1(q_1)\psi_2(q_2) \\
&= E_1\psi_1(q_1)\psi_2(q_2) + E_2\psi_1(q_1)\psi_2(q_2) \\
&= (E_1 + E_2)\psi_1(q_1)\psi_2(q_2) \\
&= E\Psi(q_1, q_2)
\end{aligned} \tag{2.21}$$

Therefore, the product of the individual eigenfunctions yields the total eigenfunction, and the individual eigenvalues are additive.

The many-body Hamiltonian, (2.16), is also a function of two coordinates, nuclear ( $R$ ), and coordinates of the electrons ( $r$ )

$$\hat{H}(R, r) = \hat{T}_e(r) + \hat{U}_e(r) + \hat{T}_n(R) + \hat{U}_n(R) + \hat{U}_{en}(R, r) \tag{2.22}$$



Problematically,  $\hat{U}_{en}(R, r)$  prevents the separation of the nuclear and electronic components of the Hamiltonian and subsequently the separation of the wavefunction.

Thus, we use the Born-Oppenheimer Approximation, which posits that nuclei are stationary with respect to the reference frame of an electron, due to the large difference in masses between these two particles. In this way, we examine a fixed nuclear configuration, which leads to the electronic Schrodinger equation

$$\hat{H}_e \psi_e(R, r) = E_e \psi_e(R, r) \quad (2.23)$$

where  $\hat{H}_e = \hat{T}_e(r) + \hat{U}_{ee}(r) + \hat{U}_{en}(R, r)$  excludes the nuclear components. The total energy ( $E_{tot}$ ) is, thus, described using the original Hamiltonian presented in (2.16),

$$\hat{H} \psi_e(R, r) \psi_N(R) = E_{tot} \psi_e(R, r) \psi_N(R) \quad (2.24)$$

Equation 2.24 is afforded only after invoking the Born-Oppenheimer approximation, which allows us to separate the electronic ( $\psi_e(r)$ ) and nuclear ( $\psi_N(R)$ ) components of the wavefunction ( $\Psi$ ). The electronic wavefunction is solved using

$$\begin{aligned} \hat{H}_e \psi_e(R, r) &= \left\{ -\frac{1}{2} \sum_i \nabla_i^2 - \sum_{n,i} \frac{Z_n}{r_{ni}} + \sum_{i>j} \frac{1}{r_{ij}} \right\} \psi_e(R, r) \\ &= E_e(R) \psi_e(R, r) \end{aligned} \quad (2.25)$$

where the summation terms are iterated over electrons ( $i, j$ ) and nuclei ( $n, m$ ). The resulting electronic energy ( $E_e$ ) is then employed in the nuclear Hamiltonian to solve for the total system energy ( $E_{tot}$ )

$$\begin{aligned} \hat{H}_N \psi_N(R) &= \left\{ -\sum_n \frac{1}{2M_n} \nabla_n^2 + E_e(R) + \sum_{n>m} \frac{Z_n Z_m}{R_{nm}} \right\} \psi_N(R) \\ &= E_{tot} \psi_N(R) \end{aligned} \quad (2.26)$$

Often commercial electronic structure theory software packages, such as Gaussian90 and VASP, solving the many-electron wavefunction return the total energy at a

fixed geometry, *i.e.*  $E_e$ , solving only the electronic Schrödinger equation. We turn now to the varying approximations made so that the many-electron wavefunction may be solved.

### Thomas, Fermi, and Dirac

The culmination of contributions from Thomas, Fermi, and Dirac, termed Thomas-Fermi-Dirac theory, yielded a theory that only depends on the total electron density ( $\rho(r)$ ). This simplifies the problem because the density is only a function of three variables, the (x, y, z,) coordinates. The total energy of a system ( $E^{TF}$ ) is written as

$$E^{TF}[\rho(r)] = A_k \int \rho(r)^{5/3} dr + \int \rho(r)v_{ext}(r)dr + \frac{1}{2} \int \int \frac{\rho(r)\rho(r')}{|r - r'|} drdr' \quad (2.27)$$

where the first term is the electronic kinetic energy associated with a system of non-interacting electrons in a homogeneous gas, the second term is the classic electrostatic energy of attraction between nuclei and electrons, and the third term is the electronic Coulombic repulsion term. Thus, to assess the ground state energy of a system within Thomas-Fermi theory (2.27) is minimized, while keeping the number of electrons constant.

Defining the energy in terms of the electron density is powerful, yet there are several disadvantages to the Thomas-Fermi theory; i) this theory does not predict the bonding of atoms, thus solids and molecules cannot form, ii) the kinetic energy is a gross approximation, in which small errors have a large impact on the final computed value, and iii) the description of the Coulombic repulsion is classical, neglecting the exchange-correlation interaction term. Moreover, owing to its inability to self-consistently reproduce atomic shell structure, this theory fails.

To mediate the last disadvantage of the Thomas-Fermi approximation, Dirac proposed an approximation for the exchange-correlation term based on the

homogeneous electron gas

$$E_{xc}[\rho(r)] = -\frac{3}{4} \left(\frac{3}{\pi}\right)^{1/3} \int \rho(r)^{3/4} dr \quad (2.28)$$

The exchange correlation term may then be written in terms of the exchange-correlation energy ( $\varepsilon_{xc}[\rho(r)]$ ), which is dependent on the Seitz radius ( $r_s$ ) and is defined as

$$\varepsilon_x[\rho(r)] = -\frac{3}{4} \left(\frac{9}{4\pi^2}\right)^{1/3} \frac{1}{r_s} \approx -\frac{0.4582}{r_s} \quad (2.29)$$

and the total energy is

$$E_{xc}^{LDA}[\rho(r)] = \int \rho(r) \varepsilon_{xc}[\rho(r)] dr \quad (2.30)$$

The Dirac exchange-correlation term, (2.30), was added to the Thomas-Fermi theory, (2.27), yet this did not improve the Thomas-Fermi theory. The subsequent improvement to this theory was the Hartree Approximation, which replaces the many-electron wavefunction with a product of single-electron wavefunctions.

### Hartree, Hartree-Fock, and the Slater Determinant

We turn our attention to solving the electronic wavefunction ( $\psi_e(r)$ ), where we exclude the nuclear coordinates ( $R$ ) for the remaining discussion. Thus far we have neglected the spin component of the electrons; to account for the spin ( $\omega$ ), we introduce an additional term,  $x = \{r, \omega\}$ . The electronic wavefunction is a function of  $x_N$ ,  $\psi_e(x_1, x_2, \dots, x_N)$ , where  $N$  is the number of electrons in the system. Including electronic spin accounts for the sixth postulate of quantum mechanics (the precursor to the Pauli exclusion principle), which posits that a wavefunction must be interchangeable across coordinates between fermions. This is represented mathematically

$$\psi_e(x_1, \dots, x_x, \dots, x_y, \dots, x_N) = -\psi_e(x_1, \dots, x_y, \dots, x_x, \dots, x_N) \quad (2.31)$$

The Hartree Approximation is the simplest approximation of electron-electron interactions. Within this approximation, the true  $N$ -electron wavefunction is replaced by a product of single particle orbitals

$$\Psi(r_1s_1, r_2s_2, \dots, r_ns_n) = \frac{1}{\sqrt{N}} \psi_1(r_1, s_1) \psi_2(r_2s_2) \dots \psi_n(r_ns_n) \quad (2.32)$$

where the single particle orbitals are comprised by a spatial function ( $\phi_i(r_i)$ ) and an electron spin function ( $\sigma_i(s_i)$ )

$$\psi_i(r_is_i) = \phi_i(r_i) \sigma_i(s_i) \quad (2.33)$$

The electron spin function takes values of  $\alpha, \beta$ , or  $\uparrow, \downarrow$ . Yet (2.33) does not satisfy (2.31), thus the Hartree Approximation does not consider exchange interactions, which is otherwise required by the Pauli exclusion principle.

Exchange interactions are accounted for in the Hartree-Fock theory, which defines the wavefunction as an asymmetrised product of orbitals. Thus, the Hartree-Fock wavefunction is reminiscent of a linear combination of terms in (2.33).

$$\Psi_{HF} = \frac{1}{\sqrt{N!}} [\psi_1(r_1s_1) \psi_2(r_2s_2) \dots \psi_N(r_Ns_N) - \psi_1(r_2s_2) \psi_2(r_1s_1) \dots \psi_N(r_ns_n) + \dots] \quad (2.34)$$

$\Psi_{HF}$  can easily be represented using the Slater determinant

$$\Psi_{HF} = \frac{1}{\sqrt{N!}} \begin{vmatrix} \psi_1(r_1s_1) & \psi_1(r_2s_2) & \cdots & \psi_1(r_Ns_N) \\ \psi_2(r_1s_1) & \psi_2(r_2s_2) & \cdots & \psi_2(r_Ns_N) \\ \vdots & \vdots & \ddots & \vdots \\ \psi_N(r_1s_1) & \psi_N(r_2s_2) & \cdots & \psi_N(r_Ns_N) \end{vmatrix}$$

The orbitals within  $\Psi_{HF}$  follow

$$\int \psi_i^*(r) \psi_j(r) dr = \langle \psi_i | \psi_j \rangle = \delta_{ij} \quad (2.35)$$

which is otherwise known as the orthonormal constraint.

The Hartree-Fock total energy ( $E_{HF}$ ) is obtained by taking the expectation value of the Hamiltonian ( $\hat{H}$ ),

$$\begin{aligned}
E_{HF} &= \langle \Psi_{HF} | \hat{H} | \Psi_{HF} \rangle \\
&= \sum_i^N \int \psi_i^*(r) \left( -\frac{1}{2} \nabla^2 + \nu_{ext}(r) \right) \psi_i(r) dr \\
&\quad + \frac{1}{2} \sum_i^N \sum_j^N \int \int \frac{|\psi_i(r)|^2 |\psi_j(r)|^2}{|r-r'|} dr dr' \\
&\quad - \frac{1}{2} \sum_i^N \sum_j^N \int \int \frac{\psi_i^*(r) \psi_i(r) \psi_j^*(r) \psi_j(r)}{|r-r'|} \delta_{s_j s_i} dr dr'
\end{aligned} \tag{2.36}$$

The final term of (2.36) is the exchange energy, and is a product of the Pauli exclusion principle. To complete (2.36), an ionic repulsion term must also be included.

Minimizing (2.36) subject to (2.35) yields the Hartree-Fock ground state energy ( $E_0^{HF}$ ) and is accomplished by taking advantage of the Euler Lagrange method. The stationary equation given by

$$\delta \left( E_0^{HF} - \sum_i^N \sum_j^N \varepsilon_{ij} (\langle \psi_i | \psi_j \rangle - 1) \right) \tag{2.37}$$

Importantly,  $\varepsilon_{ij}$  represents a Hermitian matrix, and the Hartree-Fock equations are subsequently represented

$$\left( -\frac{1}{2} \nabla^2 + \nu_{ext}(r) + \sum_j^N \int \frac{|\psi_j(r')|^2}{|r-r'|} \right) \psi_i(r) - \sum_j^N \int \frac{\psi_i(r') \psi_j^*(r') \psi_j(r)}{|r-r'|} \delta_{s_i s_j} dr' = \varepsilon_i \psi_i(r) \tag{2.38}$$

Generally (2.38) are solved using the self-consistent field procedure.  $\psi_i(r)$  of (2.38) are the ground state orbitals, also known as the self-consistent orbitals. Within the self-consistent procedure, the set of orbitals is iterated until the energy is minimized.

Yet, HF theory involves only one determinant of the electronic wavefunction, neglecting a large number of alternative, possible wavefunctions. It is statistically unlikely that the true wavefunction for the chemical system is contained within the set of iterative wavefunctions. Beyond this, single determinant is only truly accurate for a non-interacting set of electrons; thus, an additional interaction energy term is necessary and is achieved by including the correlation energy ( $E_c$ ), where

$$E_c = E_0 - E_{HF} \quad (2.39)$$

and  $E_{HF} \geq E_0$ , according to the variational principle. HF includes correlation energy by using a linear combination of Slater determinants to account for excited state configurations. This requires a lot of computing resources, which is feasible for only small systems.

### The Birth of Density Functional Theory

DFT addresses the the disadvantages of HF theory and is founded on the Hohenberg-Kohn (HK) theorems,<sup>(91)</sup> which ultimately builds on the Tomas-Fermi use of electron density ( $n(r)$ ) to solve the quantum many-body problem. Consider a system composed of electrons moving under the influence of an external potential ( $\nu_{ext}(r)$ ). HK-DFT posits that

**1. The total energy of the system is a functional of  $\nu_{ext}$ , and, by extension,  $n(r)$ .** The total energy functional ( $E[n(r)]$ ) can thus be presented in terms of  $\nu_{ext}$

$$\begin{aligned} E[n(r)] &= \int n(r)\nu_{ext}(r)dr + F[n(r)] \\ &= \langle \Psi | \hat{H} | \Psi \rangle \end{aligned} \quad (2.40)$$

where  $F[n(r)]$  is an unknown, universal functional describing electron density, and  $\hat{H}$  is a function of the electronic  $\hat{H}(\hat{F})$  and the external potential ( $\hat{V}_{ext}$ )

$$\hat{H} = \hat{F} + \hat{V}_{ext} \quad (2.41)$$

and  $\hat{F}$  relies on the kinetic energy operator ( $\hat{T}$ ) and the interaction operator ( $\hat{V}_{ee}$ )

$$\hat{F} = \hat{T} + \hat{V}_{ee} \quad (2.42)$$

Since  $\hat{F}$  is consistent across all N-electron systems,  $\hat{H}$  depends solely on the number of electrons and  $\hat{V}_{ext}$ .

We can prove this theorem by reductio ad absurdum.

Consider the case where there are two external potentials ( $\nu_1$ , and  $\nu_2$ ) that yield the same electron density ( $n_0(r)$ ). Thus the Hamiltonian describing each system ( $\hat{H}_1$  and  $\hat{H}_2$ ) each possessing a ground state wavefunction ( $\Psi_1$  and  $\Psi_2$ ).

By the variational principle and (2.40), we can generate an inequality relating the ground state energies of each system ( $E_1^0$  and  $E_2^0$ )

$$\begin{aligned} E_1^0 &< \langle \Psi_2 | \hat{H}_1 | \Psi_2 \rangle = \langle \Psi_2 | \hat{H}_2 | \Psi_2 \rangle + \langle \Psi_2 | \hat{H}_1 - \hat{H}_2 | \Psi_2 \rangle \\ &= E_2^0 + \int n_0(r) [\nu_{ext_1}(r) - \nu_{ext_2}(r)] dr \end{aligned} \quad (2.43)$$

Notably, upon exchanging the subscripts, (2.43) still holds. Let  $\int n_0(r) [\nu_{ext_x}(r) - \nu_{ext_y}(r)] dr = c$ . Then

$$E_1^0 < E_2^0 + c \quad (2.44)$$

$$E_2^0 < E_1^0 + c \quad (2.45)$$

Summing (2.44) and (2.45) yields

$$E_1^0 + E_2^0 < E_2^0 + E_1^0 \quad (2.46)$$

a direct contradiction. Therefore, the ground state electron density determines the position of the nuclei within a chemical system, and give rise to the electronic properties.

**2. The electron density that yields the minimized total energy is the ground state electron density, and may be solved for using the variational principle.** Considering that the electron density gives rise to the external potential, and the Hamiltonian depends on the external potential and the number of electrons, then the wavefunction is a functional of the electron density ( $\Psi[n(r)]$ ). Subsequently,

$$\hat{F}[n(r)] = \langle \Psi | \hat{F} | \Psi \rangle \quad (2.47)$$

We can then write the total energy functional in a  $\nu$ -representable form ( $E_\nu[n(r)]$ ) in terms of another electron density ( $n'(r)$ )

$$E_\nu[n(r)] = \int n'(r) \nu_{ext}(r) dr + \hat{F}[n'(r)] \quad (2.48)$$

By the variational principle

$$\langle \psi' | \hat{F} | \psi' \rangle + \langle \psi' | \hat{V}_{ext} | \psi' \rangle > \langle \psi | \hat{F} | \psi \rangle + \langle \psi | \hat{V}_{ext} | \psi \rangle \quad (2.49)$$

From (2.47) and (2.48), we arrive at the final representation of the second Hohenberg-Kohn theorem

$$\int n'(r) \nu_{ext}(r) dr + F[n'(r)] > \int n(r) \nu_{ext}(r) dr + F[n(r)] E_\nu[n'(r)] > E_\nu[n(r)] \quad (2.50)$$

The Hohenberg-Kohn theorems, however, do not provide a method of solving the electron density of a ground state system. Instead, they provide the foundation to the conventional DFT that is employed today – Kohn-Sham DFT.



## Kohn-Sham Density Functional Theory

The Kohn-Sham (KS) formulation maps the system containing the interacting electrons onto a fictitious system of non-interacting electrons whose movement is described by a series of KS single particle potentials ( $\nu_{KS}(r)$ ). From the Hohenberg-Kohn theorems, we may achieve the ground state energy of a system by minimizing the energy functional, (2.40), while keeping the total number of electrons constant,

$$\delta \left[ F[n(r)] + \int \nu_{ext}(r)n(r)dr - \mu \left( \int n(r)dr - N \right) \right] = 0 \quad (2.51)$$

where  $\mu$  is

$$\mu = \frac{\delta F[n(r)]}{\delta n(r)} + \nu_{ext}(r) \quad (2.52)$$

By considering a non-interacting system of electrons, the exact kinetic energy can be calculated directly using the KS formalism.

Similar to HF theory, the KS ground state wavefunction ( $\Psi_{KS}$ ) is a combination of single-particle orbitals ( $\psi_i(r_i)$ )

$$\Psi_{KS} = \frac{1}{\sqrt{N!}} \det [\psi_1(r_1)\psi_2(r_2) \cdots \psi_N(r_N)] \quad (2.53)$$

The unknown, universal functional describing the electron density,  $F[n(r)]$ , is composed of three terms

$$F[n(r)] = T_s[n(r)] + E_H[n(r)] + E_{xc}[n(r)] \quad (2.54)$$

Here,  $T_s[n(r)]$  is the kinetic energy of the non-interacting electron gas,  $E_H$  is the classical electrostatic energy of the electrons where  $E_H[n(r)] = \frac{1}{2} \int \int \frac{n(r)n(r')}{|r-r'|} dr dr'$ , and  $E_{xc}$  is the exchange-correlation energy that speaks to the difference between the non-interacting kinetic energy and the exact kinetic energy, as well as the non-classical contribution of the electron-electron interactions.

Expanding (2.52) leads to

$$\mu = \frac{\delta T_s[n(r)]}{\delta n(r)} + \nu_{KS}(r) \quad (2.55)$$

The KS potential,  $\nu_{KS}(r)$ , is a function of the external potential ( $\nu_{ext}(r)$ ), Hartree potential ( $\nu_H(r)$ ), and the exchange-correlation potential ( $\nu_{xc}(r)$ )

$$\nu_{KS}(r) = \nu_{ext}(r) + \nu_H(r) + \nu_{xc}(r) \quad (2.56)$$

where

$$\begin{aligned} \nu_H(r) &= \frac{\delta E_H[n(r)]}{\delta n(r)} = \int \frac{n(r')}{|r - r'|} dr' \\ \nu_{xc}(r) &= \frac{\delta E_{xc}[n(r)]}{\delta n(r)} \end{aligned} \quad (2.57)$$

Similar to HF theory, we obtain the ground state electron density and total energy by solving for the N 1-electron Schrödinger equations

$$\left[ -\frac{1}{2}\nabla^2 + \nu_{KS}(r) \right] \psi_i(r) = \varepsilon_i \psi_i(r) \quad (2.58)$$

where  $\varepsilon_i$  is the Lagrange multiplier associated with the orthonormality of the single particle states,  $\psi_i$ . The electron density ( $n(r)$ ) is then

$$n(r) = \sum_{i=1}^N |\psi_i(r)|^2 \quad (2.59)$$

and the non-interacting kinetic energy ( $T_s[n(r)]$ ) is

$$T_s[n(r)] = -\frac{1}{2} \sum_{i=1}^N \int \psi_i^*(r) \nabla^2 \psi_i(r) dr \quad (2.60)$$

Similar to the HF scheme, the Kohn-Sham equations, (2.56) - (2.60), are solved self-consistently. As opposed to solving one equation for the electron density directly (as is done in Tomas-Fermi theory), the N one-electron equations must be solved. This is quite advantageous; when system complexity increases (*i.e.* size increases), only the number of equations that must be solved changes. Yet, KS-DFT is still an approximate method – the exact exchange correlation energy

$(E_{xc}[n(r)])$  is not known. The implicit form,

$$E_{xc}[n(r)] = T[n(r)] + T_s[n(r)] + E_{ee}[n(r)] - E_H[n(r)] \quad (2.61)$$

depends on the exact kinetic energy ( $T[n(r)]$ ), the KS kinetic energy ( $T_s[n(r)]$ ), the exact electron-electron interaction energy ( $E_{ee}[n(r)]$ ), and the Hartree energy ( $E_H[n(r)]$ ). Subsequent developments to DFT focus on developing an increasingly accurate description of this exchange-correlation energy term.

## Exchange and Correlation

**The Exchange-Correlation Hole.** Consider the non-relativistic many-body electronic Hamiltonian,

$$\begin{aligned} \hat{H} &= \hat{T} + \hat{V}_{ext} + \hat{V}_{ee} \\ &= -\frac{1}{2} \sum_{i=1}^N \nabla_i^2 + \sum_{i=1}^N \nu_{ext}(r) + \sum_{i=1}^N \sum_{j>i}^N \frac{1}{|r - r'|} \end{aligned} \quad (2.62)$$

which depends on the kinetic energy ( $\hat{T}$ ), the external potential ( $\hat{V}_{ext}$ ), and the electron-electron interaction energy ( $\hat{V}_{ee}$ ). The expectation value of  $\hat{V}_{ee}$  takes the form

$$\langle \Psi | \hat{V}_{ee} | \Psi \rangle = \frac{1}{2} \int \int \frac{P(r, r')}{|r - r'|} dr' dr \quad (2.63)$$

where  $\Psi$  is the normalised antisymmetric ground state wavefunction of the system, and  $P(r, r')$  is the pair density function,

$$P(r, r') = N(N-1) \int \cdots \int |\psi(rs, r's', r_3s_3, \cdots, r_Ns_N)|^2 dr_3s_3 \cdots dr_Ns_N \quad (2.64)$$

The pair density function describes the probability that a pair of electrons reside at points  $r$  and  $r'$ , respectively. Perhaps more useful, we can write the electron density as a function of the pair density function,

$$n(r) = \frac{1}{N-1} \int P(r, r') dr' \quad (2.65)$$

Since  $\int n(r)dr = N$ ,

$$\int \int P(r, r')dr'dr = N(N - 1) \quad (2.66)$$

Within the classical description, electrons are not correlated. Thus, the pair density function takes the form

$$P_{classical}(r, r') = n(r)n(r') \quad (2.67)$$

Using (2.67) would be incorrect, however, because electrons are subject to Fermi statistics. We must account for quantum mechanical forces, such as non-Coulombic interactions and the Pauli exclusion principle. The exchange-correlation interactions ultimately reduces the electron density at  $r$  due to its pair at  $r'$ ; in this way, each electron is associated with a volume of decreased electron density (*e.g.* hole) surrounding itself. This can be accounted for by including another term in the pair density function, which becomes

$$P(r, r') = n(r)n(r') + n(r)n_{xc}(r, r') \quad (2.68)$$

where  $n_{xc}(r, r')$  is the exchange-correlation hole density, containing the quantum mechanical effects surrounding each electron. Importantly,  $n_{xc}(r, r')$  must follow the normalisation condition

$$\int n_{xc}(r, r')dr' = -1 \quad (2.69)$$

which asserts that the hole corresponds with a decrease in electron density and cancels out the charge of one electron.

**Defining Exchange-Correlation.** The exact definition of  $E_{xc}[n(r)]$  can be obtained using coupling constant integration. Within this method, a coupling constant ( $\lambda$ ) that describes the relationship between the non-interacting system and the interacting system is defined. At its core, this term describes the strength of the electron-electron interactions within the system. The exchange-correlation

energy is thus

$$E_{xc}[n(r)] = \frac{1}{2} \int n(r) dr \int \frac{n_{xc}(r, r')}{|r - r'|} dr' \quad (2.70)$$

where  $n_{xc}(r, r')$  is the exchange-correlation hole, which is averaged over the coupling constant-dependent hold ( $n_{xc}^\lambda(r, r')$ )

$$n_{xc}(r, r') = \int_0^1 n_{xc}^\lambda(r, r') d\lambda \quad (2.71)$$

from which the exchange-correlation energy density ( $\varepsilon_{xc}[n(r)]$ ) can be defined

$$\varepsilon_{xc}[n(r)] = \frac{1}{2} \int \frac{n_{xc}(r, r')}{|r - r'|} dr' \quad (2.72)$$

While this definition holds, we do not know the exact form of  $n_{xc}(r, r')$ , and, thus, cannot solve the many-body Schrödinger problem. Yet, this method provides the relationship between the interacting and non-interacting kinetic energies, as well as the connection between the electron density pivotal to DFT and the many-body wavefunction with the definition of the exchange-correlation hole.

Importantly, we can show that the magnitude of the exchange-correlation hole density will always be smaller than the electron density, from (2.69) with the pair density at zero, leading to

$$n_{xc}(r, r') \geq -n(r') \quad (2.73)$$

An important characteristic of the pair density is that it is symmetric under coordinate exchange,

$$P(r, r') = P(r', r) \quad (2.74)$$

In combination with (2.68), we can define

$$\begin{aligned} P(r, r') &= n(r)n(r') + n(r)n_{xc}(r, r') \\ P(r', r) &= n(r')n(r) + n(r')n_{xc}(r', r) \end{aligned} \quad (2.75)$$

using (2.74), it follows that the equations of (2.75) are equivalent

$$n(r)n(r') + n(r)n_{xc}(r, r') = n(r')n(r) + n(r')n_{xc}(r', r) \quad (2.76)$$

solving for  $n_{xc}(r, r')$  yields

$$\begin{aligned} n(r)n_{xc}(r, r') &= n(r')n(r) + n(r')n_{xc}(r', r) - n(r)n(r') \\ &= n_{xc}(r', r')n(r') \end{aligned} \quad (2.77)$$

leading to

$$n_{xc}(r, r') = n_{xc}(r', r) \frac{n(r')}{n(r)} \quad (2.78)$$

The exchange and correlation components of the exchange-correlation hole density are independent,

$$n_{xc}(r, r') = n_x(r, r') + n_c(r, r') \quad (2.79)$$

where the exchange (Fermi) hole ( $n_x(r, r')$ ) is

$$n_x(r, r') = n_{xc, \lambda=0}(r, r') \quad (2.80)$$

and the correlation (Coulomb) hole ( $n_c(r, r')$ ) is

$$n_c(r, r') = n_{xc, \lambda=0}(r, r') - n_x(r, r') \quad (2.81)$$

Fortunately, the exchange hole may be known exactly using the Hartree-Fock definition of the exchange correlation energy ( $E_x$ ),

$$E_x = \frac{1}{2} \int n(r) dr \int \frac{n_x(r, r')}{|r - r'|} dr' \quad (2.82)$$

where  $n_x(r, r')$  is a function of the spin orbitals ( $\psi_j(r, s)$ ),

$$n_x(r, r') = -\frac{1}{n(r)} \sum_s \left[ \sum_j^N |\psi_j^*(rs)\psi_j(r's)| \right]^2 \quad (2.83)$$

Ultimately resulting in,

$$\int n_x(r, r') dr' = -1 \quad (2.84)$$

From (2.69) and (2.79) we can assert

$$\int n_c(r, r') dr' = 0 \quad (2.85)$$

**Pair Correlation Function.** For simplicity, we can redefine  $n_{xc}(r, r')$  in terms of a pair-correlation function ( $g_{xc}(r, r')$ ),

$$n_{xc}(r, r') = n(r')[g_{xc}(r, r') - 1] \quad (2.86)$$

and

$$g_{xc}(r, r') = \int_0^1 g_{xc}^\lambda(r, r') d\lambda \quad (2.87)$$

Thus, far away from electrons, the pair correlation function tends towards unity and we know that  $n_{xc}(r, r')$  decreases with increasing  $r'$ . For continuity, we can also show that the pair-correlation function is, in fact, a probability. Let  $P(r, r') = 0$  of (2.68), which leads to

$$0 = n(r)n(r') + n(r)n_{xc}(r, r') \quad (2.88)$$

Solving for  $n_{xc}(r, r')$ ,

$$\begin{aligned} n_{xc}(r, r') &= -\frac{n(r)n(r')}{n(r)} \\ &= -n(r') \end{aligned} \quad (2.89)$$

Expanding (2.86) leads to

$$n_{xc}(r, r') = n(r')g_{xc}(r, r') - n(r') \quad (2.90)$$

Thus, from (2.89) we know that when  $P(r, r') = 0$ , then  $g_{xc} = 0$ . This essentially tells us that the probability of an electron at  $r'$  given an electron is located at  $r$  is dictated by  $g_{xc}(r, r')$ .

While a universal model for  $g_{xc}(r, r')$  is non-existent, we may calculate the exact pair-correlation function for specific cases. This method is routinely employed for quantum Monte Carlo techniques.

**Self-Interaction Effects.** Another important attribution of the exchange-correlation hole is that it cancels the self-interacting effects that are installed by the Hartree term. We can demonstrate this effectively by observing a 1-electron system, which we can model by setting one of the spin densities to 0 ( $n_\beta = 0$ ), which leads to

$$\int n_\alpha(r)dr = \int n(r)dr = 1 \quad (2.91)$$

Thus, we obtain the exact kinetic and potential energies of the system and  $P(r, r') = 0$  due to the lack of electron-electron interactions. Further,  $g_{xc}(r, r') = 0$  because there is only one electron in the system; (2.86) thus becomes

$$\begin{aligned} n_{xc}(r, r') &= n(r')[g_{xc}(r, r') - 1] \\ &= -n(r') \end{aligned} \quad (2.92)$$

In this way, the exchange-correlation energy cancels the Hartree Energy of the system, thereby eliminating the self-interaction effects.

We can also define the exchange ( $\nu_{x,\alpha}$ ) and correlation ( $\nu_{c,\alpha}$ ) potentials,

$$\begin{aligned} \nu_{x,\alpha}([n_\alpha(r)]) &= -\nu_H([n(r)]) + C_1 \\ \nu_{c,\alpha}([n_\alpha(r)]) &= 0 + C_2 \end{aligned} \quad (2.93)$$

where  $\nu_H$  is the Hartree potential, and  $\nu_{x,\alpha}$  and  $\nu_{c,\alpha}$  are only definable up to a constant,  $C_1, C_2$ , respectively. Most functions are not sufficient, resulting in a self-interaction error ( $E^{SIE}$ ) in the total energy,

$$E^{SIE} = E_H[n(r)] + E_{xc}[n_\alpha(r), 0] \quad (2.94)$$

In this way, the self-interaction error allows us to assess the degree of self-interaction still present with a given exchange-correlation approximation.

**Exchange-Correlation Approximations (*i.e.* the functionals of DFT).** Functionals are employed that model the exchange-correlation hole to



varying degrees of accuracy. The general form of an exchange-correlation functional ( $E_{xc}[n(r)]$ ) is

$$E_{xc}[n(r)] = \int n(r)\varepsilon_{xc}(r)dr \quad (2.95)$$

where  $\varepsilon_{xc}$  is the energy density. Essentially, functionals differ in the way that they determine  $\varepsilon_{xc}(r)$  surrounding each electron. We will discuss five functional types:

1. *Local Density Approximation (LDA)* – Within this framework, the true exchange-correlation energy is approximated locally as the exchange-correlation energy of a homogeneous electron gas of the same density. This is because the exchange-correlation energy is known exactly for a homogeneous electron gas. Thus, LDA only depends on the local density, leading to

$$E_{xc}^{LDA}[n(r)] = \int n(r)\varepsilon_{xc}^{homo}[n(r)]dr \quad (2.96)$$

where  $\varepsilon_{xc}^{homo}$  is the energy density of the homogeneous electron gas.

$E_{xc}^{LDA}[n(r)]$  may be separated into exchange  $E_x^{LDA}[n(r)]$  and correlation  $E_c^{LDA}[n(r)]$  contributions.  $E_x^{LDA}[n(r)]$  is known, whereas  $E_c^{LDA}[n(r)]$  is solved for in an iterative manner. LDA is known to perform better for solids than for molecules.

2. *Generalized Gradient Approximation (GGA)* – GGA is built from the gradient expansion approximation (GEA), which was originally suggested by Hohenberg and Kohn as an extension to LDA. Within this approximation, additional higher order density gradient terms are included in the definition of the exchange-correlation energy. Yet, first-order GEA does not follow the non-positivity constraint, where the exact on-top condition for a pair of opposite spin electrons  $n_x(r, r') = -n(r)$ , nor does GEA follow the sum rule of

(2.85). GGA is an expansion of GEA – ultimately solving the aforementioned challenges with GEA.

Perdew presented a procedure that cuts off the GEA exchange hole in real space.<sup>(92)</sup> This remedies the original challenges faced with GEA. The GGA exchange-correlation energy ( $E_{xc}^{GGA}[n(r)]$ ) is commonly written in terms of the enhancement factor ( $F_{xc}[n(r), \nabla n(r)]$ ), which describes the differences between the present system and a homogeneous electron gas,

$$E_{xc}^{GGA}[n(r)] = \int n(r) \varepsilon_{xc}^{homo}[n(r)] F_{xc}[n(r), \nabla n(r)] dr \quad (2.97)$$

where  $F_{xc}$  is commonly written as a function of the seitz radius ( $r_s$ ) and the dimensionless reduced density gradient ( $s(r)$ ),

$$s(r) = \frac{|\nabla n(r)|}{2k_F(r)n(r)} \quad (2.98)$$

$k_F$  is the Fermi wavevector,

$$k_F = [3\pi^2 n(r)]^{1/3} \quad (2.99)$$

$F_{xc}(r_s, s)$  takes different forms for each GGA functional. Often GGA functionals are compared by plotting the enhancement factors for a series of  $r_s$  values.

3. *meta-GGA (M-GGA)* – M-GGA functionals differ from conventional GGA functionals in that they are composed of additional semi-local terms, such as additional higher order density gradients and kinetic energy density terms ( $\tau(r)$ ),

$$\tau(r) = \frac{1}{2} \sum_i^{occ.} |\nabla \psi_i(r)|^2 \quad (2.100)$$

Integrated  $\tau(r)$  yields the non-interacting kinetic energy ( $T_s[n(r)]$ )

$$T_s[n(r)] = \int \tau(r) dr \quad (2.101)$$

The general form of the M-GGA exchange-correlation energy is

$$E_{xc}^{MGGA}[n(r)] = \int f[n(r), \nabla n(r), \nabla^2 n(r), \tau(r), \mu(r), \dots, \gamma(r)] dr \quad (2.102)$$

where  $\mu(r) \dots \gamma(r)$  represent additional semi-local quantities. M-GGA functionals are typically constructed using empirical molecular data, which introduces an inherent bias.

4. *hybrid-GGA (H-GGA)* – As their name suggests, H-GGA functionals are a hybrid of exact Hartree-Fock exchange and conventional GGA. H-GGA functionals commonly take the general form,

$$E_{xc}^{HGGA} = \alpha(E_x^{HF} - E_x^{GGA}) + E_{xc}^{GGA} \quad (2.103)$$

where  $E_x^{HF}$  is the Hartree-Fock exchange using Kohn-Sham orbitals, and  $\alpha$  is the exchange mixing coefficient, which is typically fitted semi-empirically. This was further supported by Becke, **CITE THIS** who approximated the adiabatic connection integral for the exact exchange-correlation as

$$E_{xc} = \int_0^1 U^\lambda d\lambda = \frac{1}{2}U^0 + \frac{1}{2}U^1 \quad (2.104)$$

$\lambda = 0$  is the exchange-only limit, thus,  $\lambda = 1$  is the most local part of the electron interactions.

5. *Non-Local* – Fully non-local approximations employ the exact density functional expression for  $E_{xc}[n(r)]$ , in addition to describing the exact exchange-correlation hole using analytical functions. Two examples of fully non-local approximations are the Average Density Approximation (ADA), and the Weighted Density Approximation (WDA). The general expression takes the form

$$E_{xc}^{NL}[n(r)] = \frac{1}{2} \int n(r) dr \int \frac{n_{xc}^{model}(r, r')}{|r - r'|} dr \quad (2.105)$$

There are both advantages and disadvantages to using fully non-local approximations. Notably, these functional types do not involve as many assumptions as their counterparts; in this way they achieve forms that are closer to the exact functional. While this is powerful, these functionals are highly computationally intensive, and intractable for many systems.

Table 1 summarizes properties of the discussed exchange-correlation functional types.

Table 1. Summary of properties embodied by five functional types: local-density approximation (LDA), generalized gradient approximation (GGA), meta-GGA (M-GGA), hybrid-GGA (H-GGA), weighted density approximation (WDA).

| Property  | LDA              | GGA              | M-GGA            | H-GGA           | WDA             | Exact           |
|---|------------------|------------------|------------------|-----------------|-----------------|-----------------|
| non-empirical                                     | ■                | ■ <sup>†</sup>   |                  |                 | ■               | --              |
| Locality <sup>α</sup>                             | L                | SL               | SL               | NL/SL           | NL              | NL              |
| explicit local exchange hole                      | ■                |                  |                  |                 | ■               | ■               |
| explicit $\varepsilon_{xc}(r)$                    | ■                |                  |                  |                 | ■               | ■               |
| $\lim_{r \rightarrow \infty} \varepsilon_{xc}(r)$ | $-e^{-\alpha r}$ | $-e^{-\alpha r}$ | $-e^{-\alpha r}$ | $-\frac{1}{2r}$ | $-\frac{1}{2r}$ | $-\frac{1}{2r}$ |
| $\lim_{r \rightarrow \infty} \nu_{xc}(r)$         | $-e^{-\beta r}$  | $-e^{-\beta r}$  | $-e^{-\beta r}$  | --              | $-\frac{1}{2r}$ | $-\frac{1}{r}$  |
| HEG limit <sup>β</sup>                            | ■                | ■                | ■                |                 | ■               | ■               |
| self-interaction correction                       |                  |                  |                  |                 | ■ <sup>‡</sup>  | ■               |

† - GGAs may also be defined semi-empirically

α - Local (L), Semi-Local (SL), Non-Local (NL)

‡ - typically only valid in principle

β - Homogeneous Electron Gas (HEG)

## General Calculation Considerations

This section borrows heavily from my published work,<sup>(2)</sup> in which we discuss the application of electronic structure theory to metal-organic frameworks (MOFs).

Electronic structure calculations provide insight into chemical systems at a fidelity that may be evasive with experimentation alone. The reliability and robustness of the calculations depend not only on the structure and identity of the

chemical system but also on the functional and basis set. To judge the accuracy of a model, calculated results are compared with experimental or higher level computational data<sup>(93)</sup> (e.g., band gap for electronic properties, bond length/angles and lattice parameters for structure, or vibrations and formation enthalpies to investigate stability).<sup>(94;95)</sup> The interdependence of functional and structure poses a multifaceted challenge of functional selection to obtain both realistic physical parameters and electronic wave functions.

By far the most important factor in obtaining reliable computational data is using reliable atomic coordinates. As such, it is good practice to perform electronic calculations on structures equilibrated at that level of theory; small deviations in atomic positions can result in large electronic disparities.<sup>(96)</sup> Yet, it is routine to report high-level electronic structure calculations on geometries obtained using structures equilibrated at lower levels of theory;<sup>(97;98)</sup> we will later discuss the implications of doing so, and why it has been so successful. Still, there are reports of practitioners using experimental crystallographic positions in density functional theory (DFT) models for large and complex systems when computational equilibration exceeds the abilities of the computational resources available; this has proven useful in rationalizing experimental phenomena.<sup>(99;100)</sup> While none of these approaches provide the true ground state electronic density associated with the terminal functional used for the reported the electronic properties,<sup>(101)</sup> the models themselves are reproducible and consistently provide useful insights into the chemistry of both molecules and MOFs alike.<sup>(1;97;102)</sup>

Although one may become disenchanted with computational approaches because, at face value, it would appear one could “turn knobs” to recover essentially any desired result, responsible benchmarking and control studies curtail

problematic model reductions and parametrizations. In reality, no DFT approach is perfect because the nature of the functional that recovers the exact density and energy is unknown and a vast array of functionals and corrective terms exist simply to account for deficiencies in the mathematical description of electron exchange and correlation. But it is worth remembering what modelers are trying to achieve; fundamentally, the primary objectives of an electronic structure model are 2-fold: (i) be reproducible, such that future studies invoking a published methodology may build from past results, and (ii) effectively describe the realistic chemical system in light of the various approximations and additions that were chosen during model construction. The many knobs thus exist because of the breadth of physics present in MOFs. For example, it may be necessary to add additional dispersion terms to recover computational lattice parameters in highly conjugated frameworks that more closely match experiment and spin-orbit coupling (SOC) may not be important for tetrahedral Zn(II), but will certainly be needed for tetrahedral Co(II).<sup>(103)</sup>

Of course, the basis set also plays a role in the accuracy of computed properties. Here we will only make a few general remarks but refer the interested reader to an excellent series of previous works.<sup>(104;105;106;107;108)</sup> For polar compounds, and MOFs in particular, it is important to describe the localization of electrons and their polarization and diffusivity. To do so requires a basis set of “sufficient size”, which refers to the minimum number of functions necessary to accurately describe the shape of the electron density. Basis functions themselves come in many forms, the most intuitive being “atom-centered”,<sup>(104;109;110;111)</sup> which construct molecular orbitals or bands from some linear combination of atomic orbitals. In addition to inclusion of valence orbitals, other functions

can be added to describe diffuse electron density far from the nuclei (useful for noncovalent interactions and anions) and electronic polarization (arising from chemical interactions between atoms with different electronegativities). The most common basis in solid-state calculations is a series of plane-waves,<sup>(73;112)</sup> which simultaneously enable the description of the bonding interactions within the unit cell while also enabling sampling of long-range interactions beyond the periodic boundary condition. The basic assumption for the remainder of this Review is that a sufficiently large basis set has been used to properly account for diffuse and polarized electron density.<sup>(113)</sup>

One further assumption for charge analysis and other postprocessing techniques is a preconverged wave function generated from a self-consistent field (SCF) routine,<sup>(114)</sup> i.e., for a given geometry, the electronic component of the Hamiltonian has reached the minimum value within a certain tolerance. The following subsection will serve to detail functional and basis set selection when applying electronic structure theory to MOFs.

**Functional Selection.** As discussed previously, DFT is founded on the theorems of Hohenberg and Kohn, which purport that the energy of a chemical system is a direct function of the ground-state electron density.<sup>(91)</sup> In practice, the Kohn-Sham<sup>(56)</sup> formalism is used to construct the ground-state electron density of interacting electrons in a static external potential from density functions describing individual, noninteracting electrons. The main shortcoming of DFT, however, is that there is no known functional that satisfies the Hohenberg and Kohn theorem, and hence we are unable to compute the exact energy or ground-state density of a system. Instead, a range of available functionals exist that vary in their approximate treatment of the exchange-correlation term of the Hamiltonian

(where exchange and correlation are purely quantum mechanical effects that can be thought of as a repulsive and attractive term, respectively); the challenge lies in identifying which functional provides the best electron density or energy for a particular chemical system based on the parameters considered during functional construction and the dominant physics present in the MOF. There is ongoing dialogue about the relative advantages of employing a functional parametrized to better approximate the “real” electron density, or “real” energy; however, there is room in electronic structure modeling for both philosophies.<sup>(115)</sup>

Within the DFT construct, functionals are divided into broad classes based on their treatment of the electron density gradient; this hierarchy of electronic structure approaches is sometimes referred to as Jacob’s ladder, Figure 4.<sup>(116;117)</sup> The bottom rung of the ladder begins with the local (spin) density approximation (LDA, LSDA), which assumes a homogeneous distribution of electrons throughout the material. LDA functionals therefore are readily applied to metals, i.e., materials with nonzero density of states (DOS) at the Fermi level ( $E_F$ ), such as bulk platinum. Some common LDA functionals include VWN<sup>(118)</sup> and PZ81.<sup>(119)</sup> However, it would be misguided to apply any variation of LDA to the subset of metallic MOFs<sup>(120;121;122;123)</sup> (e.g.,  $\text{Ni}_3(\text{HITP})_2$ ),<sup>(124;125)</sup> despite their nonzero DOS at  $E_F$ . The electron density is not homogeneously distributed throughout the scaffold; the electron density on the Ni and N are vastly different and the bond will be improperly described.

Instead, the generalized gradient approximation (GGA)<sup>(126;127)</sup> and related methods are applied to systems with varying electron density (e.g., molecules, MOFs, inorganic clusters, etc.). GGA considers both the electron density and the gradient of the electron density when recovering energetic values and hence



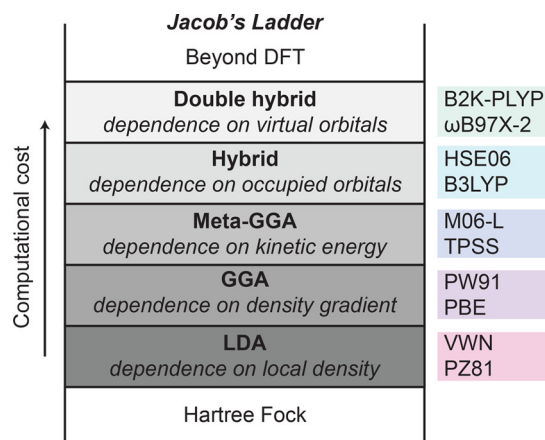


Figure 4. Jacob’s ladder of functionals where accuracy increases with computational cost. Some common functionals corresponding with each rung are listed on the right.

enables better descriptions of systems with inhomogeneous charge density, such as metal-organic hybrids. Familiar “pure” GGA functionals include PBE<sup>(54)</sup> and PW91,<sup>(127)</sup> and these have been widely invoked in both the molecular and solid-state communities for both structure and derivative electronic property analysis.<sup>(128;129)</sup>

Still, the core shortcoming of all standard GGA approaches (and DFT approaches in general) is their inability to correctly describe both electron exchange and correlation;<sup>(130)</sup> a variety of more extravagant GGA methods combining progressively more complicated mathematics have been implemented in order to better describe these two key components of electronic structure theory. So-called meta-GGA functionals (such as M06-L<sup>(131)</sup> and TPSS<sup>(132)</sup>) historically invoke both the first and second derivative of the electron density to describe the system, while hybrid GGA functionals include some amount of exact electron exchange as computed with the Hartree-Fock exchange functional (HF). The GGA functional PBE, for example, becomes the hybrid functional PBE0<sup>(133)</sup> upon addition of 25% exact exchange. Some functionals can have a screened potential added, becoming

HSE06.<sup>(134)</sup> Conversely, the most ubiquitous hybrid GGA functional, B3LYP,<sup>(135)</sup> has components of exchange computed with HF, LDA / VWN, and GGA / B,<sup>(136)</sup> in addition to the exchange and correlation computed at the GGA / LYP<sup>(53)</sup> level.

Given the diverse library of functionals to choose from, it is unsurprising that both experimentalists and theorists can feel overwhelmed in the early stages of model construction. Indeed, the most common practice is to invoke a well-documented functional known to recover the appropriate electron density or energy for similar chemical systems. With this in mind, hybrid- GGA methods are widely viewed as the minimum level of theory necessary to describe the electronic structure of systems where exchange and correlation play a major role in the electronic structure. This is particularly pertinent in MOFs containing spin-polarized transition metals,<sup>(137)</sup> where exchange interactions not only play a leading role in the energy of the material, but also define the nature of the frontier orbitals/bands, as well as the band gap of semiconducting materials. In light of these considerations, by far the most common hybrid functionals used in MOF modeling are PBE0, HSE06, B3LYP, M06, and variations thereof,<sup>(138)</sup> despite their significant increase in computational demand.<sup>(139)</sup>

Rather than boldly sticking with one functional, systematic functional analyses may be performed to identify the optimal exchange-correlation treatment for each material or study. DFT results can be benchmarked to quantities derived from experiment or higher level ab initio calculations such as band gap energy,<sup>(140)</sup> ionization potential,<sup>(98)</sup> lattice parameters,<sup>(93)</sup> and formation enthalpies.<sup>(3)</sup> One study monitored the incorporation of bipyridine dicarboxylate (bipydc) linkers into UiO-67 (a MOF formally made from biphenyldicarboxylate, bpdc) by comparison of computed band gap and experimental lattice parameter contraction. There,

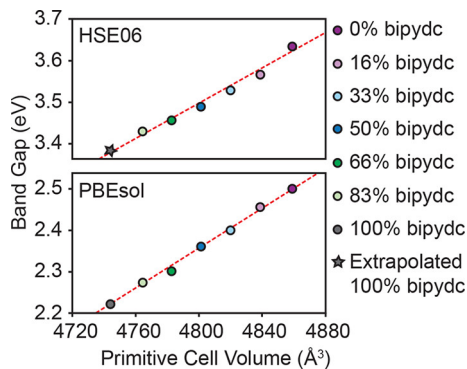


*Figure 5.* Linear correlation between computed electronic band gap and bipyridine dicarboxylate (bipydc) incorporation in Zr-UiO-67. The HSE06 (top) and PBEsol (bottom) functionals show qualitatively the same trend, but PBEsol consistently underestimates the band gap by 1 eV. The gray star represents the extrapolated value derived from the best fit line to account for a computational limitation. Data obtained from ref.<sup>(1)</sup>. Figure reprinted with permission from ref.<sup>(2)</sup>.

they found excellent agreement between experimental lattice parameters and unit cells optimized with the PBE functional corrected for solids (PBEsol), Figure 5.<sup>(1)</sup> In the same study, the PBEsol<sup>(141)</sup> yielded consistently smaller band gaps than HSE06 (HSE06 was routinely greater by 1 eV), but qualitatively comparable trends in electronic differences as a function of substitution are observed. A similar conclusion was reached in another study examining a larger selection of MOFs with an analogous metal and ligand chemistry, Figure 6.<sup>(3)</sup> The data in Figures 5 and 6 also highlight a common theme in the literature: GGA functionals tend to underestimate both the experimental and hybrid-computed band gap, and the addition of exact (HF) exchange is necessary to recover more realistic electronic band gaps.<sup>(142;143;144)</sup> In sum, assuming a sufficiently high-fidelity basis set, pure GGA functionals are the lowest level of theory required to provide a reasonable electronic description of most MOFs. However, the recovery of experimental semiconducting properties requires the incorporation of some exact exchange.

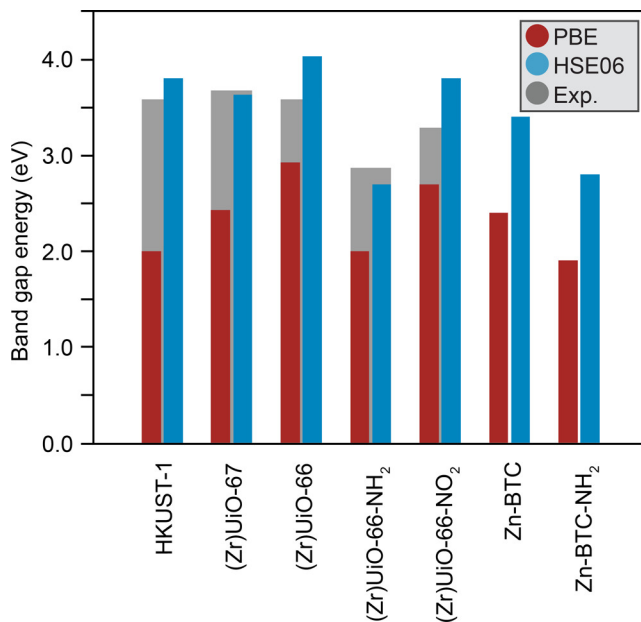


*Figure 6.* Computed electronic band gaps of HKUST-1, UiO-67, UiO-66, Zn-BTC, and linker functionalized derivatives. HSE06 systematically predicts larger band gap energies than PBE, more closely matching the experimental values. Data obtained from ref<sup>(3)</sup>. Figure reprinted with permission from ref. <sup>(2)</sup>.

Sometimes, however, the disagreement between experiment and theory is more subtly hidden in poorly described interactions such as long-range dispersion; the addition of correctional terms can also help empirically tune a DFT output to match an experimental data set or simply add additional physics that may better describe the system. These additional Hamiltonian terms were not necessary in the models presented in this thesis, and, thus, are outside the scope of this discussion.

### **Electronic structure modeling of extended solids**

With the exception of rare amorphous variants,<sup>(145;146;147;148;149;150;151)</sup> MOFs are ordered solids. Thus, conventional solid-state modeling techniques can be applied where MOF crystals possess symmetry operations that enable the description of the extended material using a repeating unit. This section is intended to provide a background and some general calculation considerations when

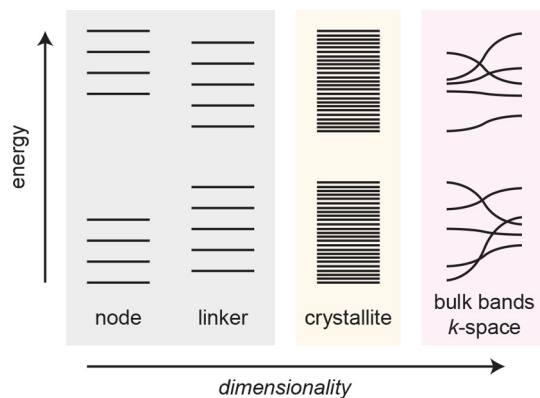


*Figure 7.* As size of a chemical system increases toward an infinite solid, the number of molecular orbitals becomes very large. For high symmetry materials, the crystallite can be described using a smaller, repeating unit, whose projection through reciprocal space generates electronic bands. Figure reprinted with permission from ref.<sup>(2)</sup>.

modeling periodic MOF properties, including their electronic band gaps, electronic band structures, and DOS, as well as their lattice vibrations. Finally, we discuss MOFs with imperfections, those that host vacancies and interstitials.

**Periodic Models and  $k$ -Points.** Viewing MOFs as an extended array of molecules, each component (i.e., the linker and the pre-nucleated node) contains a family of molecular orbitals. Upon self-assembly of the MOF these electrons mix to form new molecular orbitals that expand over larger and larger regions of space. In principle, one could model a complete MOF crystallite (i.e., a very large chemical system as a molecule) and obtain the exact electron energetics and spatial distributions for all possible molecular orbitals in the material. Owing to symmetry, however, several of the molecular orbitals in the crystallite will be very similar in energy and centered on the same atoms. These geometric degeneracies enable a reduction in computational cost by modeling the associated electrons as interacting periodically in bands, Figure 7.

Electronic bands can be thought of as delocalized molecular orbitals whose energy depends on the extent of electronic interaction in crystallographic directions within the crystal. Indeed, Bloch's Theorem purports that for a nondefective material, the periodicity of the lattice describes the periodicity of the overall wave function.<sup>(152)</sup> Information on both the structural and electronic properties of a bulk sample can therefore be gleaned from a single unit cell (although the approach does not provide information about the surface chemistry at the grain boundaries of a crystallite). One way of thinking about the construction of bands in solids is to first create molecular orbitals for all atoms contained within the computational cell, then, using harmonics, the electronic interactions with neighboring cells are computed.<sup>(153)</sup> By doing so, both the electronic properties of the discrete unit cell are recovered, as well as the influence of longer ranged (de)localization and electrostatics, which can only be observed by sampling beyond one computational cell.<sup>(154)</sup>

While it is convenient to visualize bands as large delocalized molecular orbitals in real space, they are often computed in reciprocal space (i.e.  $k$ -space) using Bloch's theorem paired with a basis set constructed from interfering planewaves to determine the combinations and populations of electronics bands.  $k$ -space vectors can be loosely thought to sample long-range interactions in the crystallographic directions defined by the  $k$ -vector.

From experimental convention, a crystallographic unit cell (or conventional cell) contains the smallest chemical representation of a system that exhibits the same overall symmetry as the pristine lattice. Calculations using this geometry, composition, and associated lattice parameters will certainly be suitable for direct calculation of electronic properties, however, some space groups offer symmetry

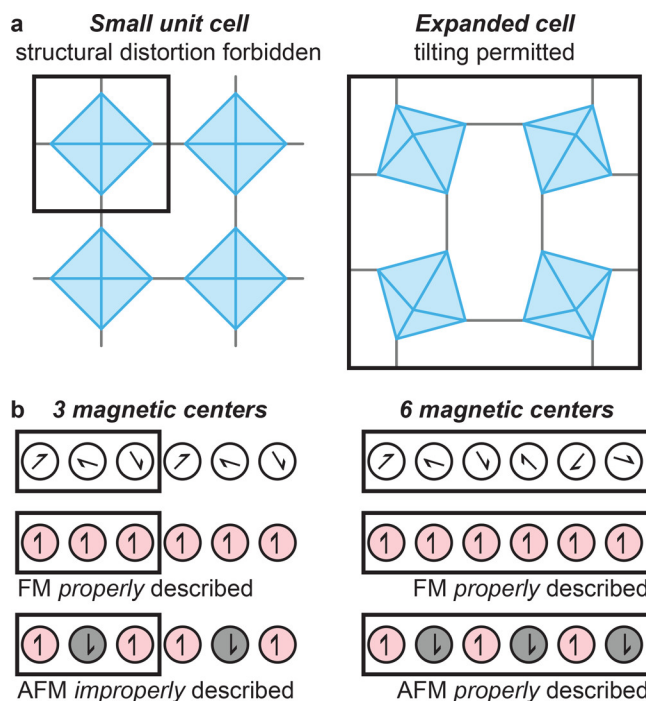


Figure 8. Although the smallest computational cell can save resources, an improper model may be recovered if a chemical interaction permeates beyond a single geometric cell. For example, (a) structural distortions are sometimes captured in temperature independent DFT (the ground state may feature tilting of nodes);<sup>(4)</sup> and (b) magnetic ordering can be challenging if the unit cell contains an odd number of coupling metals (for example, the unit cell of  $\text{Co}_2\text{Cl}_2\text{bis}(1\text{H}-1,2,3\text{-triazolo}[4,5-b],[4,5-i]\text{dibenzo}[1,4]\text{dioxin})$ , (BTDD), contains 3 Co- (II), which do prefer to order antiferromagnetically<sup>(5)</sup>). Figure reprinted with permission from ref.<sup>(2)</sup>.

related primitive cells that contain a smaller repeating crystalline unit of lower symmetry.<sup>(155)</sup> Typically, calculations are run on the primitive cell unless the unit cell is required to capture magnetic ordering or structural deformations that cannot be described using the smallest repeating unit, some examples of which are shown in Figure 8.

Every ordered MOF crystallizes into one of 230 unique space groups,<sup>(156)</sup> each containing a series of high symmetry k-points.<sup>(157)</sup> The lowest crystal symmetry, P1, features no internal symmetry operations, all atoms in the cell

are unique and must be explicitly computed, and hence there is only one high symmetry  $k$ -point in the first Brillouin zone,  $\Gamma$ .<sup>(157)</sup> Chemically, the  $\Gamma$ -point is the equivalent of projecting the molecular orbitals contained within the unit cell in three dimensions: the electronics of the material are governed by the interactions captured explicitly within the computational cell rather than their interactions with neighboring cells. MOFs typically crystallize in high symmetry space groups,<sup>(152)</sup> and often feature more than one symmetrically unique  $k$ -point that will contribute to the total energy of the system, and hence should be sampled during the SCF.

Within crystals that feature anisotropic bonding (for example, graphene, 2D MOFs, etc.) certain crystallographic directions contribute more significantly to the bonding and stabilization of the system than others. In the 2D examples, the in-plane and out-of-plane interactions will contribute differently and sometimes seemingly unpredictably to the total energy of the system. It is hence good practice to sample as many  $k$ -points as possible to ensure a more tightly converged total electronic energy.

The selection of  $k$ -points depends on the crystal symmetry, and these  $k$ -points traverse the first Brillouin zone.<sup>(158)</sup> In practice, the contribution of each sampled  $k$ -point is taken as a weighted average (determined by symmetry) to recover the total system energy. The position of sampled  $k$ -points through the first Brillouin zone is computed with one of two philosophically dissimilar approaches: a  $\Gamma$ -centered Monkhorst-Pack, or a non- $\Gamma$ -centered Monkhorst-Pack  $k$ -grid. The main difference is that the former forces sampling of the  $\Gamma$ , while the latter does not guarantee that any high symmetry points are sampled.<sup>(159)</sup> Crystal symmetry thus helps inform two key computational considerations: (i) the feasibility of using a computational primitive cell, and (ii) the  $k$ -path to explicitly examine how



electron energies changed in the extended solid. Almost all of these considerations are enabled in freely available software, and high symmetry points of the first Brillouin zone can be found in online databases like the Bilbao Crystallographic Server.<sup>(157)</sup>

In principle, one would compute the total energy of a system by integrating over the entire first Brillouin zone or approximating the integration with the summation of a very large number of  $k$ -points. In practice, the total energy is asymptotically related to the number of  $k$ -points and a convergence test is required to elucidate when a sufficiently dense grid has been invoked. We can distill the key considerations for  $k$ -grid generation and their impact on the material properties down to the following:

- In Bloch’s theorem, planewave cutoff (i.e., the basis set) and the  $k$ -points are independent. Yet both affect the total energy of the system. Hence, to obtain converged results, it is good practice to benchmark the  $k$ -grid and basis set separately.
- Generally, sampling additional  $k$ -points provides better descriptions of long-range orbital interactions within a crystal system. Increasing  $k$ -grid density does not always reduce the total energy of the system that depends on the nature of the bonding and antibonding orbitals.<sup>(160)</sup> It is therefore difficult to predict the impact on total energy without first running the calculation.
- Empirically, a  $k$ -grid with a density of  $25 \times (\text{lattice parameter})^{-1}$  provides an estimate of the  $k$ -point density required for a reasonable sampling of electronic interactions within the crystal.<sup>(155)</sup> Computational feasibility of the resultant grids relies on large lattice parameters, which typically infer large

numbers of explicitly defined chemical interactions within the unit cell, the extent of electronic interactions rapidly diminishes in real space, hence why large crystals often show little dependence on increased k-point density. There is a trade-off between modeling large systems with many explicit electrons, versus small systems with many explicit k-points. Moreover, while a reduction to the primitive cell vastly reduces the Slater determinant's size, it comes at the penalty of requiring several additional  $k$ -points (which contribute significantly to the computational time).

- In MOF chemistry, it is common to perform geometric optimizations with a sufficient  $k$ -grid at a lower level of theory, then refine the electronic structure with a singlepoint energy calculation at a higher level of theory; the size of the  $k$ -grid in either case is determined by MOF symmetry and resource availability.
- Importantly, there is no formal relationship between lattice parameter and k-point density; rather, large unit cells often contain sufficient descriptions of strong interactions, and hence long-range sampling does not overly alter the energetics of the system. Regardless of whether this is true for all MOFs, this procedure produces a highly reproducible systematic error in the total energy of the system that is acceptable in many cases.
- Most MOFs crystallize in high symmetry space groups, and it is good practice to include all high symmetry kpoints in the computation of the total energy of the system, and ideally during the optimization routine.

Regardless of how many  $k$ -points are selected for the optimization routine, the material must be geometrically equilibrated (and the SCF must be converged)

to ensure that the energetics are computed without spurious numerical fluctuation. A schematic of the general computational approach for solid-state materials is shown in Figure 9. Assuming that a structure has been optimized, the following sections discuss the computable properties and utility of using a solid-state model for MOF systems.

**Electronic Band Gap.** The ionic lattices of most MOFs feature a discrete electronic band gap, while some can be described as metallic (classified as having nonzero DOS at the Fermi level).<sup>(161)</sup> Within the subgroup of materials that feature electronic band gaps, their conductive properties depend on numerous other properties (e.g., the material’s defect chemistry, the mobility of the charges, the electronic band gap, etc.). Because standard solid-state computations omit temperature, and without an exhaustive defect analysis, we are unable to assign the position of the Fermi level. In light of this, MOFs are largely insulating materials, but we note that they are interchangeably referred to as semiconductors in the literature.<sup>(162;163;164;165)</sup>

The fundamental energy gap,  $E_g$ , is defined by the lowest energy occupied-to-unoccupied transition in a system (independent of whether it is symmetry allowed);<sup>(166)</sup> its magnitude is the difference in energy between the VBM and CBM. Because of a derivative discontinuity and other localization errors associated with the exchange potential in semiconducting systems, GGA functionals systematically underestimate MOF band gaps.<sup>(167;168;169)</sup> Empirically, this systematic underestimation can be improved by incorporating a component of exact HF exchange into the Hamiltonian.<sup>(170;171)</sup> However, the computational expense associated with hybrid functionals<sup>(172)</sup> prompts the recovery of semiconducting

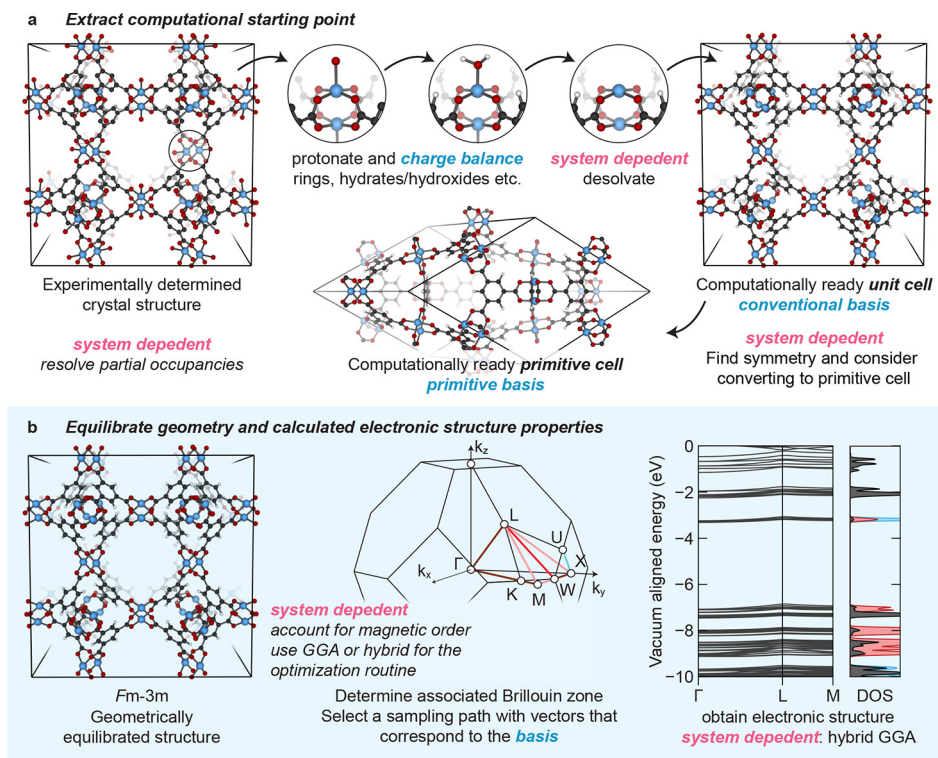


*Figure 9.* General computational approach used to obtain electronic structure properties from solid-state structures. (a) Beginning with an experimentally obtained crystal structure, partial occupancies must be resolved. Then, where applicable, protons must be added to charge balance the cell, in effect establishing the oxidation state of the metals. Extrinsic solvent may be removed to simulate the activated MOF. Symmetry can then be enforced and a computational primitive cell may be available. (b) The structure can then be equilibrated, and higher level electronic structure properties can be obtained by sampling the first Brillouin zone, including electronic band structures and corresponding density of states. Figure reprinted with permission from ref. (2).

properties from single-point calculations at this level of theory on a structure obtained using GGA.<sup>(173)</sup>

MOFs with bands that exhibit different energies as a function of  $k$ -space (*i.e.*, band dispersion) may exhibit an indirect band gap, schematically presented in Figure 10, where the VBM and CBM occur at different points in reciprocal space. In such cases,  $\Gamma$ -point sampling is insufficient to capture the dominant electronic influences. The lowest energy transition in an indirect band gap material requires the coupling of photon absorption/ emission to a phonon mode in order to conserve energy and momentum because the wave vector at the top of the valence band does not match the wave vector at the bottom of the conduction band.<sup>(174)</sup> Indirect band gaps thus diminish the intensity but extend the lifetime of formed excitons by preventing recombination; indirect band gaps are desirable in photoactive solids for the enhancement of quantum efficiency.<sup>(175)</sup> Although there are almost no reported indirectband MOFs,<sup>(176;177)</sup> the changing band gap energy in reciprocal space is a phenomenon ripe for exploration.

Certainly, most MOFs feature wide band gaps and highly localized electronic structures that give rise to flat bands with well-defined orbital contributions to the frontier states and direct gaps. The localization of electrons makes MOFs intriguing for photocatalytic applications,<sup>(178;179;180;181;182;183)</sup> as it affords one route toward accessing dense populations of high energy electrons localized on transiently reduced motifs.<sup>(184;185)</sup> Moreover, electronic structure may be tuned to desirable bulk properties, facilitated by the inherent modularity of MOFs.

Although the nature of band edges is material/composition dependent, the electronic band gap of a MOF can be modified by metathesis and functionalization

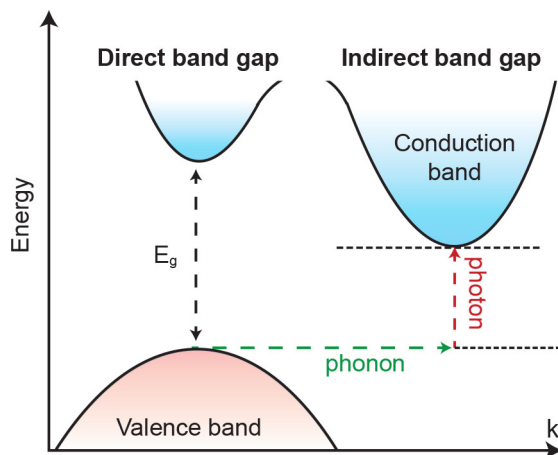


*Figure 10.* An illustration of the band gap in a semiconductor as a function of reciprocal space when the CBM and VBM are at the same point in reciprocal space providing a direct band gap and when they are at different points in reciprocal space creating an indirect minimum absorption energy. Figure reprinted with permissions from ref. <sup>(2)</sup>.

of the linker and/or inorganic node. There are four possible frontier orbital orientations in MOFs, wherein the band edges are defined by (i) ligand-to-ligand, (ii) ligand-to-metal, (iii) metal-to-ligand, or (iv) metal-to-metal excitations, ultimately dictated by the material composition. Countless examples of DFT screenings are reported for band gap modulation via metal<sup>(97;186;187;188;189;190;191)</sup> and linker exchange<sup>(102;192;193;194;195;196;197;198;199;200)</sup> across the gamut of MOFs. MOF-5, which is a pivotal part of Chapter 5 for example, has been subject to numerous theoretical studies systematically exchanging components of the inorganic node<sup>(188;191;201;202;203;204)</sup> or the linker.<sup>(205;206;207;208)</sup>

**Electronic Band Structures.** Electronic band structures are a plot of electronic energy as a function of  $k$ -space (*i.e.*, electron momentum). The shape of the bands provides tremendous amounts of information about material properties, including the potential to transport charges, overall material stability and, to the trained eye, even the composition. Given MOFs are made from discrete molecules,

it is somewhat unsurprising most feature localized (*i.e.*, flat) electronic bands that facilitate the use of cluster models. However, through development with a complement of experiment and theory, there are increasing examples of MOFs featuring curved (*i.e.*, dispersive) bands and interesting MOF applications that rely on the description of bulk electronic structure. Thus, this section will discuss the calculation and implications of MOF electronic band structures.

The electronic band structure is simply constructed by sampling the energy of electrons at various  $k$ -points. The difference in energy between the bottom and top of the band at two dissimilar  $k$ -points is referred to as the bandwidth, or band dispersion, and is essentially a measure of the “curviness” of the bands. Higher band dispersion means more mobile charge carriers and also indicates something about the extent of orbital overlap and long-range interactions in that crystallographic vector. Because these plots ultimately depict electron momentum, the second derivative of a band near a high symmetry  $k$ -point (sometimes called special points) yields the effective mass of a charge carrier in that band.

Perhaps it is somewhat intuitive that a highly symmetric crystal would feature a large degree of electronic degeneracy within the unit cell; it is less intuitive to imagine how crystal symmetry affects the bulk electronic properties, *i.e.*, those that extend beyond a single computational cell. As mentioned in the previous section, the material should be properly equilibrated using all of the high symmetry  $k$ -points in addition to a dense grid between them. Practically, however, this is often impossible, but also unnecessary; generally flat-banded materials (like MOFs) can be described with  $\Gamma$ -only sampling because the insulating interface between the metal and ligand is sufficiently accounted for by explicit orbital interactions within the computational unit cell.<sup>(209;210;211)</sup> It is, however, typically

good practice to sample all labeled high symmetry k-points for the given space group,<sup>(156;212;213)</sup> as presented in the *Bilbao Crystallographic Server*,<sup>(157)</sup> ensuring that the total energy has included all important long-range interactions.<sup>(214)</sup>

Although the chemical connectivity in MOFs is usually highly symmetric, MOFs themselves have highly anisotropic electron density through the crystallographic unit cell: there are pores! Thus, it is expected that the electronic band structures should contain some interesting information, albeit subtle, arising from the periodic absences of electron density. Indeed, one paradigm in the conductive MOF literature is whether the charge carriers are more delocalized through-space or through-bonds.<sup>(215;216)</sup> The band structure sheds light on this. Consider two similar scaffolds made from  $\pi$ -stacked triphenylene-based linkers: in the case of Ln(hexahydroxytriphenylene), the inorganic nodes form continuous ionic bonds throughout the material,<sup>(217)</sup> whereas in Ni<sub>3</sub>(HITP)<sub>2</sub> the sheets are nonbonded. In both cases, the greatest band curvature is found to be centered on the linker, but associated with the out-of-plane direction. In other words, the conductivity mode is “through space”.<sup>(215;216)</sup> The delineation of “through-bond” or “through space” should not be confused with that between band or hopping conduction, which are separate mechanisms that can be distinguished by the presence of an activation energy associated with the conduction.<sup>(215;218;219)</sup>

Electronic band structure calculations primarily serve to graphically identify crystallographic directions in which electrons are highly delocalized and strongly interacting. Such plots contain a significant amount of information when paired with the crystal structure and a map of the high symmetry kpoints for the MOFs parent space group. The analysis can be further complimented by quantitative



analysis of the electronic band dispersion (a concept we have already introduced), and most importantly, the density of states.

**Electronic Band Dispersion.** Band dispersion is the difference in energy of a band between two high symmetry points in reciprocal space. Greater dispersion is thought to indicate the material may be a better electrical conductor in that direction.<sup>(220)</sup> Perhaps a more apt description is to think of dispersion (or curvature) as an indicator of electron and hole delocalization. In this mindset, the “effective mass” of a charge carrier can be computed to quantify the extent of delocalization associated with a band. In doing so, the mass of a free charge carrier in vacuum,  $m_0$ , is renormalized to describe its behavior in the periodic potential of the MOF. The second derivative of a band near a special point or crossing the Fermi-level yields the effective mass,  $m^*$ , of the electron or hole that would populate that band via

$$\frac{1}{m^*} = \frac{1}{\hbar} \frac{\partial^2 E(k)}{\partial k^2} \quad (2.106)$$

where  $\hbar$  is Planck’s constant.<sup>(221)</sup> In practice, this is readily solved by fitting a parabola to a series of k-points very near the point of interest. Often, practitioners will present both “heavy” and “light” effective masses, corresponding to the bands with the least and most curvature, respectively.

A final consideration in the computation of the electronic band structure is that while the computed band dispersion is recovered from temperature-independent DFT, the experimental observation of the band dispersion itself does depend on temperature. Thus, dispersion energies less than  $kT$  (*i.e.*, the Boltzmann distribution at the operating temperature) are lost by the thermal smearing of states and can be considered essentially flat; the precision enabled by DFT may cause the appearance of subtle electronic phenomena, such as an

indirect band gap, that are inconsequential under realistic thermal conditions. This particular issue was highlighted in a recent publication, where the authors predict band dispersion on the order of  $kT$  ( $<30$  meV) and attributed the observable bulk properties of Zn- SURMOF-2<sup>(222)</sup> to this dispersion and its indirect band gap. While it is difficult to imagine a dispersion of this magnitude being a factor at room temperature, it does highlight that periodic DFT is precise and does enable high fidelity studies of dissimilar electronic states in materials with subtly changing energetics.

**Density of States.** DOS plots are critical to assessing electronic band parentage, providing information about the type of charge transport that may exist, be it ligand-to-ligand, metal-to-ligand, ligand-to-metal, or metal-to-metal fundamental gap. Hence, together with the electronic band structure and analysis of band dispersion, the DOS paints a comprehensive picture of the MOF's anticipated function. The integral of the DOS indicates how many electrons occupy that energy level, and its parentage informs which atoms/ orbitals are contributing to that energy level. Often, DOS plots are partitioned into atomic specific contributions (atom-projected DOS, pDOS) or orbital specific contributions (orbital-projected DOS), providing tremendous amount of insight into the nature of the bands in a material, as well as a lens through which the effects of linker functionalization, compositional substitutions, and interstitial influences may be assessed.<sup>(194) (192;223;224)</sup> The DOS is computed for all sampled  $k$ -points, enabling practitioners to examine the DOS at a single  $k$ -point, or the sum of them. The former can be helpful when MOF bands cross one another in  $k$ -space and has been used fruitfully in MOF calculations for systems with large unit cells.<sup>(225)</sup> In spin polarized materials, the DOS representation may be further partitioned by spin.

This knowledge is valuable because the spin bias afforded by the high degree of spinsplitting is advantageous for spintronic devices that require precise control over electron dipole orientation.<sup>(226)</sup>

DOS plots have also been helpful in determining the directionality of charge transport in conductive MOFs. Charge hopping is likely the mechanism of electron transport in most MOFs, commonly promoted accessing mixed valency through either partial redox of the metal/linker or via photoexcitation.<sup>(227;228;229;230;231)</sup>

In sum, the electronic DOS provides a detailed view of the atomistic contributions to energy levels, which can be quite complex for large chemical systems. Information gleaned from these analyses gives modelers the ability to predict the locality and direction of electron transfer, which are important in catalytic applications. The DOS also helps classify a material as a metal or semiconductor/insulator based on the absence or presence of density at the Fermi level. However, this section only focused on the utility and application of electronic DOS, which can be identified at a single  $k$ -point or summed over the entire kgrid. A similar sampling and DOS analysis can be performed on vibrational band structures (*i.e.*, phonon bands), where the DOS then describes the population of oscillators, a dynamic phenomenon.

**Defects.** MOFs are largely been treated as pristine, defect-free extended solids. Indeed, periodic boundary conditions demand crystallinity. This approximation is deeply rooted in the characterization of MOFs, as evidenced by the procedures for obtaining the crystal structure, pore volume, and gas uptake properties, which typically assume a pristine architecture.<sup>(232)</sup> However, defect formation is entropically favorable,<sup>(233)</sup> thus all materials contain defects. Indeed, significant effort has been invested in minimizing experimental defect

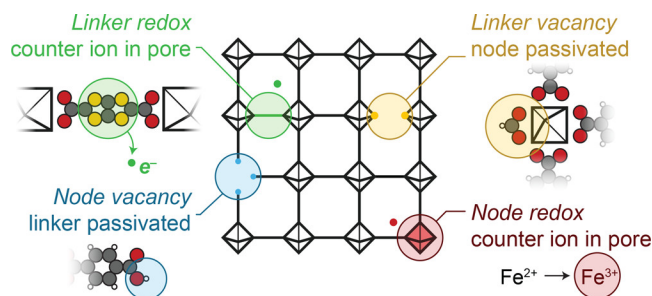


*Figure 11.* Node or linker vacancies result in charge balancing ions bound to the vacant sites (e.g., a proton or formate). Both nodes and linkers can also be redox active forming structurally bound charge carriers. Figure reprinted with permissions from ref. <sup>(2)</sup>.

concentrations,<sup>(234)</sup> but defects can also give rise to highly desirable properties (including the formation of charge carriers via doping pathways, open metal sites for catalysis, creating chromophores,<sup>(235)</sup> etc.),<sup>(236)</sup> and as such are an emerging area of interest to the MOF field.<sup>(237)</sup>

In conventional crystalline materials (*e.g.*, Si) there are three general types of defects: (i) vacancies, where an atom is missing from the lattice, (ii) substitutions, where a lattice atom is exchanged for one that does not normally occupy that lattice site, and (iii) interstitials, where an additional atom is in a typically unfilled lattice site.<sup>(234;238)</sup> MOFs regularly exhibit vacancies in the form of missing nodes or linkers,<sup>(239)</sup> and substitutions through isorecticular chemistry or postsynthetic metathesis, Figure 11.<sup>(240)</sup> Further, MOFs can play host to a variety of species within their pores, which can be considered interstitials. Each of these defect types may spawn additional functionality and modularity to the parent framework, the most catalogued of which is the liberation of active sites for catalysis via linker vacancies.<sup>(241)</sup>

Pairs or groups of these lattice point defects yield further terminology: Frenkel and Schottky defects. A Frenkel defect is essentially a vacancy and

compensatory interstitial that yield a charge neutral material, while Schottky defects are defined by multiple vacancies that sum to zero charge. Because MOFs are ionic, both Frenkel and Schottky defects are common. For example, a combined node and linker vacancy may be considered a Schottky defect and a linker omission passivated by an additional formate may be considered a Frenkel defect. Moreover, exotic Frenkel defects may be installed by including a charge balancing ion within the pore after the redox of a MOF component (Figure 11); this is uniquely enabled in MOFs considering they contain large amounts of vacuous space to support the ions.<sup>(242;243;244;245;246)</sup>

Because defects are often enthalpically disfavored, and installation is driven by entropy, there is a concentration limit at which the free energy of the formation of additional defects becomes positive. The defect concentration limit depends on the host material, but conventional semiconductors are limited to only a few percent.<sup>(247)</sup> Because of their low lattice density and limited electronic delocalization, MOFs can uniquely exceed these concentrations by at least an order of magnitude, sustaining very high vacancy populations.<sup>(248)</sup> For example, MUF-32, can reversibly reach linker vacancy defect concentrations of 80%.<sup>(249)</sup> These high defect concentrations come as a mixed blessing because on one hand we are able to model them in a crystallographic unit cell and not have to worry about their effective concentration, but we must worry about the impact of artificial defect periodicity. Hence, one challenge with pristine models is that they neglect the electronic impact of defects present in real systems.

Defects are discussed in further detail in the following chapters. Specifically, vacancies are explored in Chapter 4, and interstitials are discussed in Chapter 5.

## CHAPTER III

### CHEMICAL SIZE OF ATOMS

#### **Introduction**

Atomic and molecular shape and size play a critical role in chemistry. The most familiar method was formalized by Bondi: the van der Waal radii and volume of atoms and molecules. However, the rigid sphere approximation of atoms fails to describe highly polarized chemical systems. To overcome this challenge, numerous other approaches based on electron density have been presented, but these approaches intrinsically struggle to describe the surface area and volume of cations. Herein, we revisit the timeless problem of assessing sizes of atoms and molecules, through examination of the electric field produced by atoms and molecules. In this way, we are able to recover chemical volumes and surface areas of simple density functional theory (DFT) calculations. We perform a series of benchmarks to ensure the generality of our approach and demonstrate the electric field calculations provide unique insights into quantifying sizes of ions and polar molecules. Our method further lays the foundation for the development of analytical interaction energies based on assessment of the Coulomb potential provided by molecular systems, while providing a rigorous approach to study size dynamics as a function of chemical environment.

#### **Method Description**

To begin, we have developed a post-processing DFT software, STREUSEL (Surface Topology REcovery Using Sampling of the ELectric field), to recover volumes and surface areas of atoms, molecules, and materials, from their electric field. Since electric field is defined as the negative gradient of the electrostatic potential, the electric field embodies the direction of greatest increase in

electrostatic potential. This is significant because the increased slope of the electric field enables us to more clearly define the edge of a chemical system in space, while additionally accounting for the long-range interactions observed with cations.

We define the edge of a chemical system as the point in space where there is “near-zero” variance in the electric field magnitude. Due to computation efficiency, DFT calculations return the electrostatic potential values on the order of  $10^{-6}$  eV ( $2.306 \times 10^{-5}$  kcal mol $^{-1}$ ), thus we consider a change of less than  $10^{-5}$  eV ( $2.306 \times 10^{-5}$  kcal mol $^{-1}$ ) to be the most precise we can obtain. This definition is justifiable thermodynamically – a typical van der Waals interaction is on the order of 0.9560-1.912 kcal mol $^{-1}$ .<sup>(250;251)</sup> Our cutoff is significantly smaller and thus able to assess these weak interactions. Indeed, the utility of “cutoffs” within chemical size quantification methodologies is not unheard of.<sup>(24;51;52)</sup>

**Volumetric pixel resolution.** In order to employ this definition of size and identify the chemical surface we use the electrostatic potential provided by DFT at a discrete number of volumetric pixels (voxels). The result of this sampling procedure is thus dependent on the size of the voxels (*i.e.* resolution of the electrostatic potential calculation), at the tradeoff of an exponential relationship between time-to-volume/surface area solution and voxel resolution.

The electrostatic potential tensors are extracted from the Gaussian optimization calculations. The dimension of the tensor (number of elements per side) and the length (in Euclidean space) of each side is variable; the resolution is best represented as the real space volume that each element in the tensor represents (holding the total length of the computational box constant). At large ( $> 0.02$  Å $^3$ ) voxel volume is on the order of the volume of the chemical species, resulting in artificially large calculated volumes.

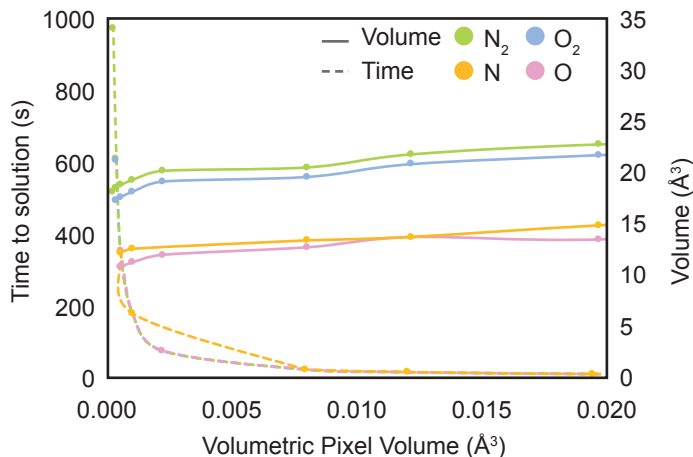


Figure 12. Decreasing the volumetric pixel volume increases the time-to-solution (dashed curves) exponentially, yet minimizes the accuracy of the calculated volume (solid curves). Thus, we take the kneepoint of the time curve as the ideal volumetric pixel volume,  $0.008 \text{ \AA}^3$ .

To identify the optimal resolution (maximizing the voxel volume, while minimizing the time-to-solution) the time-to-solution and calculated volumes were calculated for four representative models ( $\text{N}_2$ ,  $\text{O}_2$ ,  $\text{N}$ , and  $\text{O}$ ), Figure 12.

From these data, we find a voxel volume of  $\text{\AA}^3$  to yield a desirable trade-off between computation time and volumetric property resolution. This voxel volume is reasonable, given a typical chemical system is on the order of  $\text{\AA}$ .

### Functional Benchmarking

As with all electronic structure methods, the size and shape of molecules depends on both the functional and basis set used in the model development. Recently, a systematic assessment of 128 DFT functionals canvassed their performance for the recovery of total energy, and, separately, electron density.<sup>(115)</sup> While that paper revealed a significant energetic and structure dependence on functional, it did not directly emphasize the functional also changes the shape of the molecules. Since atomic position is determined by electron density, and electron



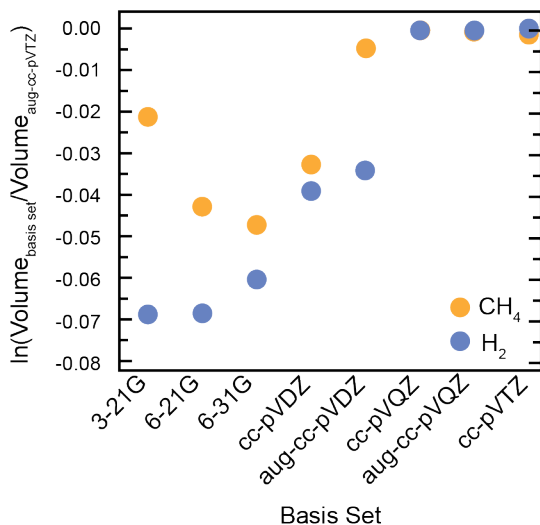


Figure 13. Calculated STREUSEL volumes of H<sub>2</sub> and CH<sub>4</sub> optimized with each basis set (x-axis), normalized to the volume obtained from the aug-cc-pVTZ (y-axis). The normalized volumes represent the precision of each basis set, a metric of how close the returned electronic structure is to that obtained using aug-cc-pVTZ. aug-cc-pVTZ is considered sufficiently large – as demonstrated by the convergence of normalized volumes with larger basis sets (*i.e.* cc-pVQZ and aug-cc-pVQZ).

density is determined by atomic position (*i.e.* the self-consistent field and geometry optimization routine), there is therefore an inherent dependence on functional selection in our size quantification approach.<sup>(252)</sup>

To elucidate these dependencies, and arrive at an ideal method to recover size using STREUSEL, we examine fifteen small, neutral molecules (Br<sub>2</sub>, C<sub>2</sub>H<sub>2</sub>, CH<sub>4</sub>, Cl<sub>2</sub>, CNCl, CO<sub>2</sub>, F<sub>2</sub>, H<sub>2</sub>, H<sub>2</sub>S, N<sub>2</sub>, NH<sub>3</sub>, O<sub>2</sub>, SO<sub>2</sub>, CO, and H<sub>2</sub>O) using forty-nine functionals and a large basis set, aug-cc-pVTZ.<sup>(253)</sup> We benchmarked the basis set to ensure that it was sufficient to describe polarized and diffuse electronic systems, Figure 13. Each molecules’ size is computed using the geometry obtained from equilibration using the stated functional. These values are compared to the geometry, volume, and surface area computed with CCSD-full<sup>(254;255;256;257)</sup> – which we use as our reference for the exact solution.<sup>(115)</sup> We also examined the use of

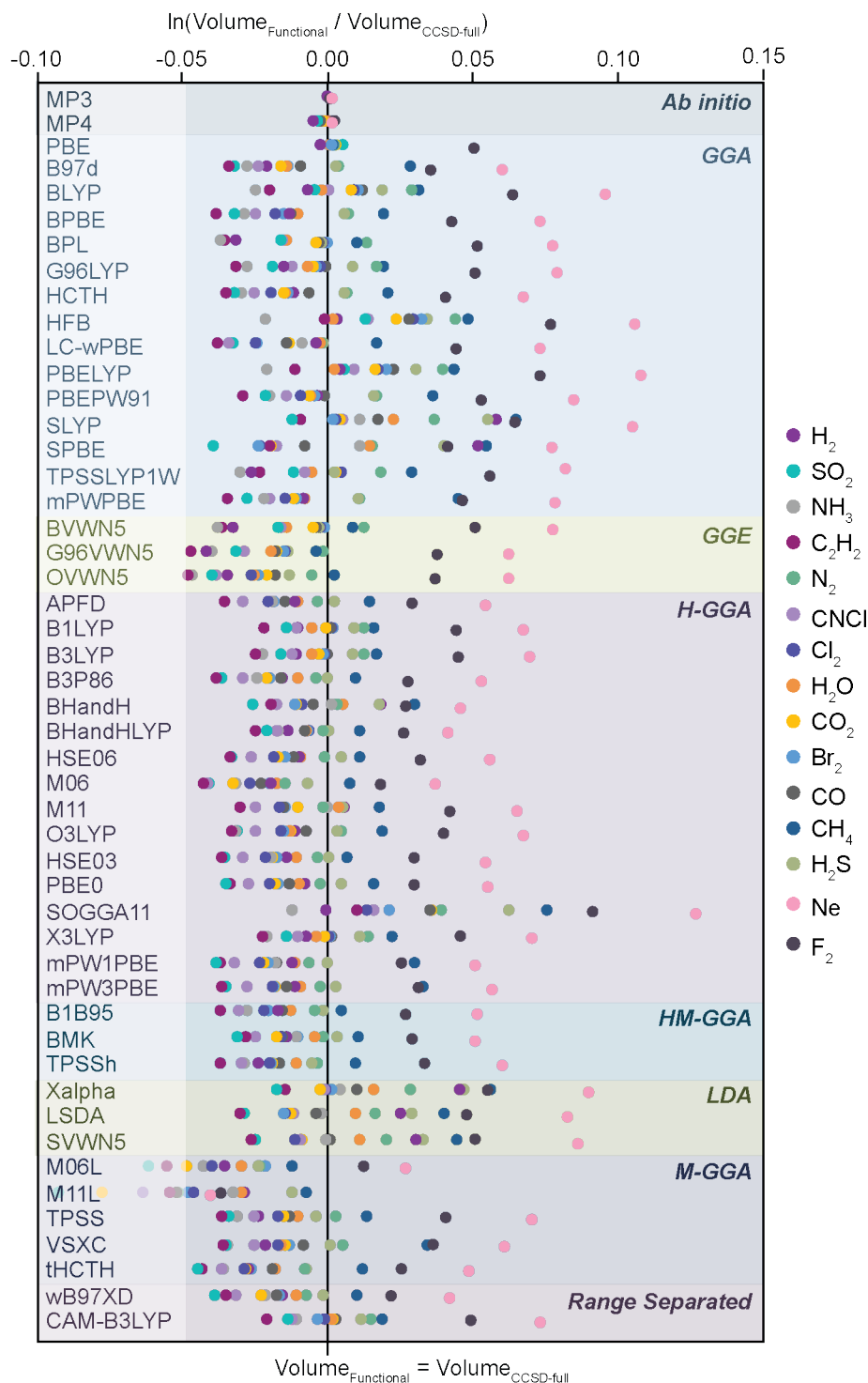


Figure 14. Calculated STREUSEL volumes of a series of industrially relevant small molecules optimized with each functional (y-axis), normalized to the volumes obtained from the CCSD-full functional (x-axis). The spread of normalized volumes represents the precision of each functional, a metric of how close the returned electronic structure is to that obtained using CCSD-full, which is assumed to yield the exact geometry. The forty-nine functionals are grouped by functional type (generalized gradient approximation (GGA), generalized gradient exchange (GGE), hybrid (H), meta (M), hybrid-meta (HM), and local-density approximation (LDA)). To increase resolution, Ne and  $\text{F}_2$  are not included in this plot and are discussed extensively in the main text.

each functional applied to the structure obtained from the CCSD-full calculation in order to isolate the impact of structure on functional performance (since it is becoming increasingly routine to perform geometry optimizations using a low level functional, and higher fidelity electronic structure single point calculations on these geometries). Individual molecular volumes are presented, Figure 14

While our approach is limited to the upper rungs of Jacob’s ladder,<sup>(2;117)</sup> we canvas eight electronic structure classes (*ab initio*, generalized gradient approximation (GGA), generalized gradient exchange (GGE), hybrid-GGA (H-GGA), hybrid-meta-GGA (HM-GGA), local-density approximation (LDA), meta-GGA (M-GGA), and range separated functionals. A comprehensive list of studied functionals is presented, Table 2

Perhaps surprisingly, there appears to be no clear trend in prediction of electric field-based molecular size as we ascend Jacob’s Ladder, Figure 34, *i.e.* higher-level DFT functionals do not necessarily outperform lower level ones, excluding *ab initio* methods, which are highly accurate. Yet, GGE, HM-GGA, and M-GGA functionals appear to systematically underestimate molecular volumes, while the commonly invoked PBE (GGA) functional performs similarly to other functionals, such as B97-D, X3LYP, BLYP, B3LYP, and TPSSLYP1W.. With reference to Ref.<sup>(115)</sup>, our approach offers no opinion on whether the theoretical method should be selected to provide accurate density, or energy, but rather prefer functionals that correctly recover *geometry* closest to that obtained from CCSD-full.

We compare the ability of two size methodologies (Batsanov expanded set of atomic van der Waals radii and electric field) to recover small molecule volumes similar to those obtained using CCSD-full, Figure 33. Here, we plot the mean

Table 2. A comprehensive list of the representative functionals from each level of theory (*ab initio*, generalized gradient exchange (GGE), local-density approximation (LDA), range separated, generalized gradient approximation (GGA), hybrid-GGA (H-GGA), hybrid-meta-GGA (HM-GGA), and meta-GGA (M-GGA)) examined in this work.

| <b>ab initio</b>                       | <b>GGE</b>                              | <b>LDA</b>                       |
|--|---|----------------------------------|
| CCSD-full <sup>(254;255;256;257)</sup> | BVWN5 <sup>(118;258)</sup>              | Xalpha <sup>(56;91;259)</sup>    |
| MP3 <sup>(260;261)</sup>               | G96VWN5 <sup>(118;262)</sup>            | LSDA <sup>(56;91;118;259)</sup>  |
| MP4 <sup>(263;264)</sup>               | OVWN5 <sup>(118;265;266)</sup>          | SVWN5 <sup>(56;91;118;259)</sup> |
| <b>Range Separated</b>                 | <b>GGA</b>                              | <b>H-GGA</b>                     |
| wB97XD <sup>(267)</sup>                | PBE <sup>(92;268)</sup>                 | APFD <sup>(269)</sup>            |
| CAM-B3LYP <sup>(270)</sup>             | B97d <sup>(271)</sup>                   | B1LYP <sup>(53;258;272)</sup>    |
|  | BLYP <sup>(53;258;272)</sup>            | B3LYP <sup>(53;258;272)</sup>    |
|  | BPBE <sup>(54;258;268)</sup>            | B3P86 <sup>(258)</sup>           |
|  | BPL <sup>(258)</sup>                    | BHandH <sup>(273)</sup>          |
|  | G96LYP <sup>(53;264;272)</sup>          | BHandHLYP <sup>(273)</sup>       |
|  | HCTH <sup>(274;275;276)</sup>           | HSE06                            |
|  | HFB <sup>(258)</sup>                    | M06 <sup>(138)</sup>             |
|  | LC-wPBE <sup>(277;278;279)</sup>        | M11 <sup>(280)</sup>             |
|  | PBELYP <sup>(53;54;268;272)</sup>       | O3LYP <sup>(265;266)</sup>       |
|  | PBEPW91 <sup>(54;127;268;281;282)</sup> | HSE03 <sup>(134;139)</sup>       |
|  | SLYP <sup>(56;91;259)</sup>             | PBE0 <sup>(133;283)</sup>        |
|  | SPBE <sup>(56;91;259)</sup>             | SOGGA11 <sup>(284)</sup>         |
|  | TPSSLYP1W <sup>(53;132;272)</sup>       | X3LYP <sup>(53;272;285)</sup>    |
|  | mPWPBE <sup>(54;268;286)</sup>          | mPW1PBE <sup>(286)</sup>         |
|  |   | mPW3PBE <sup>(286)</sup>         |
| <b>HM-GGA</b>                          | <b>M-GGA</b>                            |                                  |
| B1B95 <sup>(258)</sup>                 | M06L <sup>(131)</sup>                   |                                  |
| BMK <sup>(287)</sup>                   | M11L <sup>(288)</sup>                   |                                  |
| TPSSh <sup>(132;289;290)</sup>         | TPSS <sup>(132)</sup>                   |                                  |
|  | VSXC <sup>(291)</sup>                   |                                  |
|  | tHCTH <sup>(292)</sup>                  |                                  |

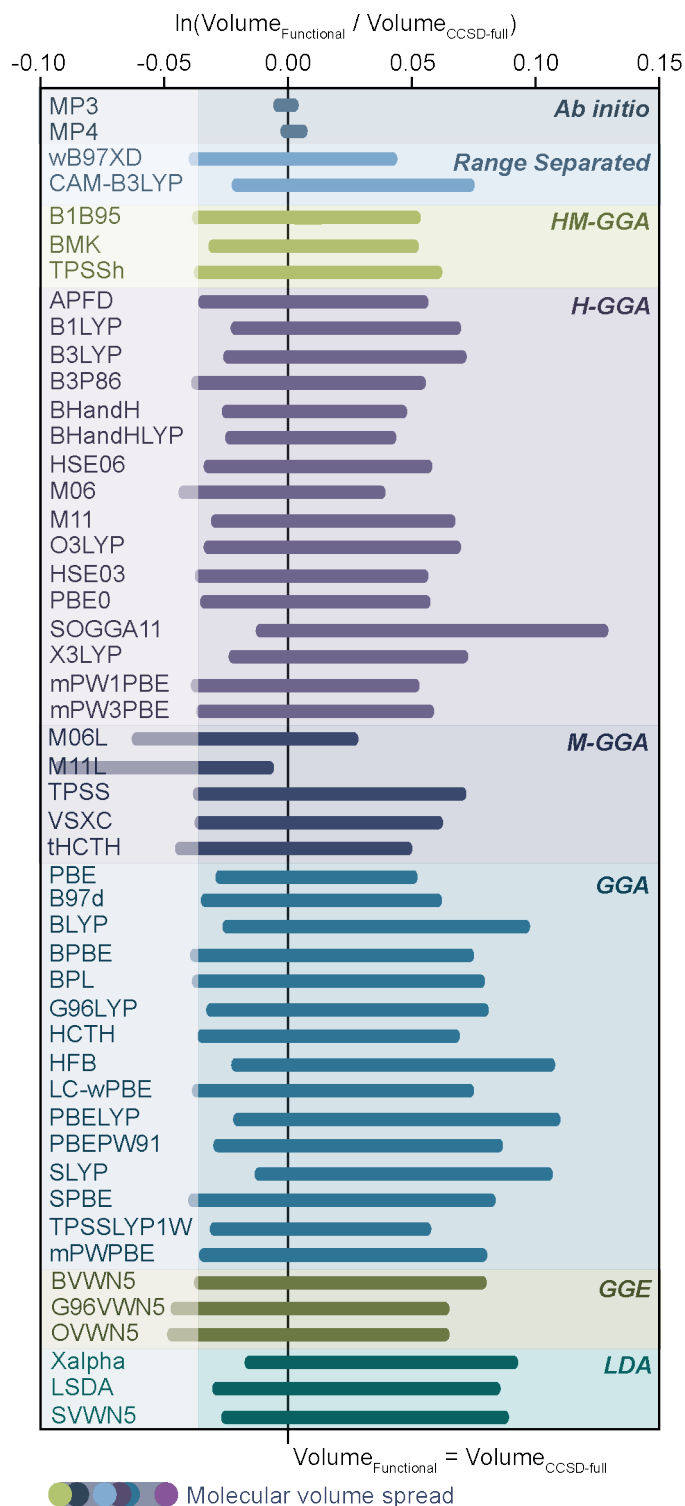


Figure 15. Calculated STREUSEL volume of a series of industrially-relevant small molecules optimized with each functional (y-axis), normalized to the volume obtained from the CCSD-full functional (x-axis). The spread of normalized volumes represents the precision of each functional, a metric of how close the returned electronic structure is to that obtained using CCSD-full, which is assumed to yield the exact geometry. The forty-nine functionals are grouped by functional type (generalized gradient approximation (GGA), generalized gradient exchange (GGE), hybrid (H), meta (M), hybrid-meta (HM), and local-density approximation (LDA)).

absolute deviation across the small molecule volumes for each functional, where the volume obtained using the CCSD-full optimized geometry is treated as the chosen measure of central tendency. This provides a statistical metric of similarity between the volumes recovered using each functional and CCSD-full for two size metrics. Owing to the rigid sphere approximation and negligible changes in bond lengths between functionals, we observe van der Waals volumes are least affected by the functional geometry. The mean absolute deviation of the electric field-based sizes is larger than those returned by van der Waals; this ultimately indicates that the electric field is more sensitive to small changes in geometry.

Indeed, deviations in van der Waals volumes for different functionals, Table 3, arises solely from variations in the resulting geometries (*i.e.* bond lengths), as opposed to the varying treatments of the electronics. Therefore, it would be misleading to present an average difference between STREUSEL and van der Waals derived volumes; the variability of STREUSEL and van der Waals volumes arises from differences in atomic radii, which are exacerbated in polyatomic systems. Unsurprisingly, differences between van der Waals and STREUSEL computed volumes or the fifteen industrially relevant molecules are not predictable, Table 3.

With respect to Figure 33, we are guided to favor functionals and *ab initio* methods displaying the lowest mean absolute deviation from each functional class, including: MP3 and MP4 (*ab initio*); CAM-B3LYP (range separated); BMK (HM-GGA); BHandH, BHandHLYP, and X3LYP (H-GGA); TPSS and VSXC (M-GGA); BPL and G96LYP (GGA); BVWN5 (GGE); Xalpha (LDA). Generally, however, higher level functionals return volumes closer to those obtained from CCSD-full across the three examined size quantification methodologies.

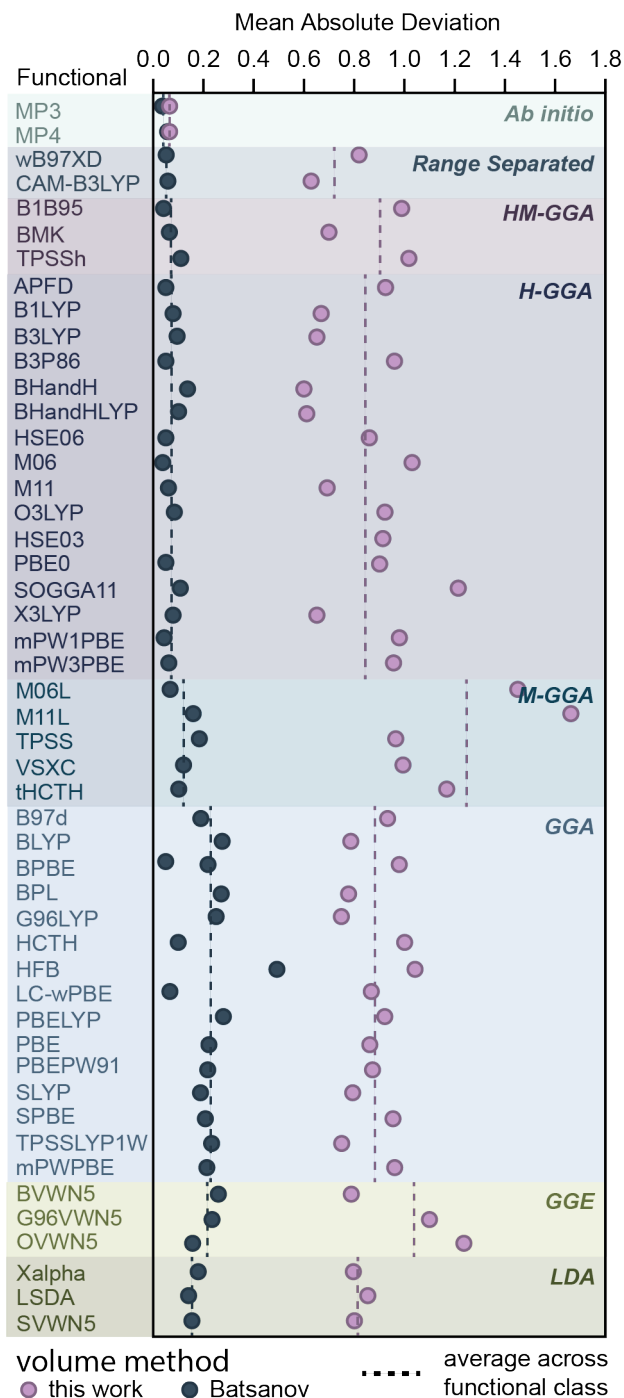


Figure 16. The mean absolute deviation (y-axis) of two volume methodologies (STREUSEL, van der Waals) across all of the studied functionals (x-axis). The mean absolute deviation is averaged across the mean absolute deviation for industrially relevant small molecules was calculated assuming the volume obtained from the CCSD-full optimized geometry as the chosen measure of central tendency. The mean absolute deviation is a metric of how close the returned electronic structure is to that obtained using CCSD<sub>full</sub>, which is assumed to yield the exact geometry. The forty-nine functionals are grouped by functional type.

Table 3. Molecular volumes for the relevant small molecules examined in this study calculated using the van der Waals (vdW) and the STREUSEL volume calculation methods.

| Molecule                      | vdW volume ( $\text{\AA}^3$ ) | STREUSEL volume ( $\text{\AA}^3$ ) | Difference (%) |
|-------------------------------|-------------------------------|------------------------------------|----------------|
| Ne                            | 11.25                         | 8.260                              | 26.58          |
| F <sub>2</sub>                | 22.03                         | 17.25                              | 21.70          |
| O <sub>2</sub>                | 22.97                         | 18.77                              | 18.28          |
| H <sub>2</sub> O              | 19.28                         | 23.43                              | -21.52         |
| N <sub>2</sub>                | 23.49                         | 19.69                              | 16.18          |
| CO                            | 26.68                         | 22.81                              | 14.51          |
| NH <sub>3</sub>               | 22.68                         | 26.16                              | -15.34         |
| CH <sub>4</sub>               | 28.15                         | 25.08                              | 10.91          |
| Kr                            | 26.52                         | 24.26                              | 8.522          |
| H <sub>2</sub>                | 10.49                         | 9.690                              | 7.626          |
| C <sub>2</sub> H <sub>2</sub> | 34.56                         | 32.30                              | 6.539          |
| CO <sub>2</sub>               | 33.21                         | 31.49                              | 5.179          |
| Cl <sub>2</sub>               | 39.54                         | 37.50                              | 5.159          |
| SO <sub>2</sub>               | 39.02                         | 39.94                              | -2.358         |
| Br <sub>2</sub>               | 47.87                         | 46.99                              | 1.838          |
| H <sub>2</sub> S              | 29.43                         | 29.49                              | -0.2039        |

**Neutral and Neutral Bonded Systems.** For illustrative purposes, we use our general approach to predict the radii for the periodic table of non-interacting atoms, Figure 35. The atomic radii recovered by STREUSEL are comparable with those presented by Alvarez,<sup>(31;32)</sup> Boyd,<sup>(52)</sup> and Rahm,<sup>(24)</sup> Figure 36. The related Rahm and Boyd radii from electron density cutoff values show excellent agreement in relative size trends. The largest disagreement occurs at high atomic numbers where the diffusivity of electrons is often poorly described due to partial occupancy of higher energy orbitals, and basis set error.<sup>(293)</sup> Yet, close similarity of STREUSEL radii with both Rahm and Boyd radii is unsurprising, considering the shared dependence on a cutoff value derived from DFT.



|           |           |  |  |  |  |  |  |  |  |  |  |         |
|-----------|-----------|--|--|--|--|--|--|--|--|--|--|---------|
| 1         | 2         |  |  |  |  |  |  |  |  |  |  | 18      |
| 1         | 2         |  |  |  |  |  |  |  |  |  |  | 2       |
| H         | He        |  |  |  |  |  |  |  |  |  |  | He      |
| 1.24      | 1.05      |  |  |  |  |  |  |  |  |  |  | 1.05    |
| hydrogen  | helium    |  |  |  |  |  |  |  |  |  |  | helium  |
| 3         | 4         |  |  |  |  |  |  |  |  |  |  | 10      |
| Li        | Be        |  |  |  |  |  |  |  |  |  |  | Ne      |
| 2.06      | 1.92      |  |  |  |  |  |  |  |  |  |  | 1.26    |
| lithium   | beryllium |  |  |  |  |  |  |  |  |  |  | neon    |
| 11        | 12        |  |  |  |  |  |  |  |  |  |  | 18      |
| Na        | Mg        |  |  |  |  |  |  |  |  |  |  | Ar      |
| 2.13      | 2.15      |  |  |  |  |  |  |  |  |  |  | 1.69    |
| sodium    | magnesium |  |  |  |  |  |  |  |  |  |  | argon   |
| 19        | 20        |  |  |  |  |  |  |  |  |  |  | 36      |
| K         | Ca        |  |  |  |  |  |  |  |  |  |  | Kr      |
| 2.35      | 2.49      |  |  |  |  |  |  |  |  |  |  | 1.84    |
| potassium | calcium   |  |  |  |  |  |  |  |  |  |  | krypton |
| 37        | 38        |  |  |  |  |  |  |  |  |  |  | 54      |
| Rb        | Sr        |  |  |  |  |  |  |  |  |  |  | Xe      |
| 2.42      | 2.59      |  |  |  |  |  |  |  |  |  |  | 2.03    |
| rubidium  | strontium |  |  |  |  |  |  |  |  |  |  | xenon   |
| 55        | 56        |  |  |  |  |  |  |  |  |  |  | 86      |
| Cs        | Ba        |  |  |  |  |  |  |  |  |  |  | Rn      |
| 2.54      | 2.75      |  |  |  |  |  |  |  |  |  |  | 2.11    |
| caesium   | barium    |  |  |  |  |  |  |  |  |  |  | radon   |
| 87        | 88        |  |  |  |  |  |  |  |  |  |  |         |
| Fr        | Ra        |  |  |  |  |  |  |  |  |  |  |         |
| 2.55      | 2.74      |  |  |  |  |  |  |  |  |  |  |         |
| francium  | radium    |  |  |  |  |  |  |  |  |  |  |         |
| 1         |           |  |  |  |  |  |  |  |  |  |  |         |
| 2         |           |  |  |  |  |  |  |  |  |  |  |         |
| 3         |           |  |  |  |  |  |  |  |  |  |  |         |
| 4         |           |  |  |  |  |  |  |  |  |  |  |         |
| 5         |           |  |  |  |  |  |  |  |  |  |  |         |
| 6         |           |  |  |  |  |  |  |  |  |  |  |         |
| 7         |           |  |  |  |  |  |  |  |  |  |  |         |
| 8         |           |  |  |  |  |  |  |  |  |  |  |         |
| 9         |           |  |  |  |  |  |  |  |  |  |  |         |
| 10        |           |  |  |  |  |  |  |  |  |  |  |         |
| 11        |           |  |  |  |  |  |  |  |  |  |  |         |
| 12        |           |  |  |  |  |  |  |  |  |  |  |         |
| 13        |           |  |  |  |  |  |  |  |  |  |  |         |
| 14        |           |  |  |  |  |  |  |  |  |  |  |         |
| 15        |           |  |  |  |  |  |  |  |  |  |  |         |
| 16        |           |  |  |  |  |  |  |  |  |  |  |         |
| 17        |           |  |  |  |  |  |  |  |  |  |  |         |
| 18        |           |  |  |  |  |  |  |  |  |  |  |         |
| 19        |           |  |  |  |  |  |  |  |  |  |  |         |
| 20        |           |  |  |  |  |  |  |  |  |  |  |         |
| 21        |           |  |  |  |  |  |  |  |  |  |  |         |
| 22        |           |  |  |  |  |  |  |  |  |  |  |         |
| 23        |           |  |  |  |  |  |  |  |  |  |  |         |
| 24        |           |  |  |  |  |  |  |  |  |  |  |         |
| 25        |           |  |  |  |  |  |  |  |  |  |  |         |
| 26        |           |  |  |  |  |  |  |  |  |  |  |         |
| 27        |           |  |  |  |  |  |  |  |  |  |  |         |
| 28        |           |  |  |  |  |  |  |  |  |  |  |         |
| 29        |           |  |  |  |  |  |  |  |  |  |  |         |
| 30        |           |  |  |  |  |  |  |  |  |  |  |         |
| 31        |           |  |  |  |  |  |  |  |  |  |  |         |
| 32        |           |  |  |  |  |  |  |  |  |  |  |         |
| 33        |           |  |  |  |  |  |  |  |  |  |  |         |
| 34        |           |  |  |  |  |  |  |  |  |  |  |         |
| 35        |           |  |  |  |  |  |  |  |  |  |  |         |
| 36        |           |  |  |  |  |  |  |  |  |  |  |         |
| 37        |           |  |  |  |  |  |  |  |  |  |  |         |
| 38        |           |  |  |  |  |  |  |  |  |  |  |         |
| 39        |           |  |  |  |  |  |  |  |  |  |  |         |
| 40        |           |  |  |  |  |  |  |  |  |  |  |         |
| 41        |           |  |  |  |  |  |  |  |  |  |  |         |
| 42        |           |  |  |  |  |  |  |  |  |  |  |         |
| 43        |           |  |  |  |  |  |  |  |  |  |  |         |
| 44        |           |  |  |  |  |  |  |  |  |  |  |         |
| 45        |           |  |  |  |  |  |  |  |  |  |  |         |
| 46        |           |  |  |  |  |  |  |  |  |  |  |         |
| 47        |           |  |  |  |  |  |  |  |  |  |  |         |
| 48        |           |  |  |  |  |  |  |  |  |  |  |         |
| 49        |           |  |  |  |  |  |  |  |  |  |  |         |
| 50        |           |  |  |  |  |  |  |  |  |  |  |         |
| 51        |           |  |  |  |  |  |  |  |  |  |  |         |
| 52        |           |  |  |  |  |  |  |  |  |  |  |         |
| 53        |           |  |  |  |  |  |  |  |  |  |  |         |
| 54        |           |  |  |  |  |  |  |  |  |  |  |         |
| 55        |           |  |  |  |  |  |  |  |  |  |  |         |
| 56        |           |  |  |  |  |  |  |  |  |  |  |         |
| 57        |           |  |  |  |  |  |  |  |  |  |  |         |
| 58        |           |  |  |  |  |  |  |  |  |  |  |         |
| 59        |           |  |  |  |  |  |  |  |  |  |  |         |
| 60        |           |  |  |  |  |  |  |  |  |  |  |         |
| 61        |           |  |  |  |  |  |  |  |  |  |  |         |
| 62        |           |  |  |  |  |  |  |  |  |  |  |         |
| 63        |           |  |  |  |  |  |  |  |  |  |  |         |
| 64        |           |  |  |  |  |  |  |  |  |  |  |         |
| 65        |           |  |  |  |  |  |  |  |  |  |  |         |
| 66        |           |  |  |  |  |  |  |  |  |  |  |         |
| 67        |           |  |  |  |  |  |  |  |  |  |  |         |
| 68        |           |  |  |  |  |  |  |  |  |  |  |         |
| 69        |           |  |  |  |  |  |  |  |  |  |  |         |
| 70        |           |  |  |  |  |  |  |  |  |  |  |         |
| 71        |           |  |  |  |  |  |  |  |  |  |  |         |
| 72        |           |  |  |  |  |  |  |  |  |  |  |         |
| 73        |           |  |  |  |  |  |  |  |  |  |  |         |
| 74        |           |  |  |  |  |  |  |  |  |  |  |         |
| 75        |           |  |  |  |  |  |  |  |  |  |  |         |
| 76        |           |  |  |  |  |  |  |  |  |  |  |         |
| 77        |           |  |  |  |  |  |  |  |  |  |  |         |
| 78        |           |  |  |  |  |  |  |  |  |  |  |         |
| 79        |           |  |  |  |  |  |  |  |  |  |  |         |
| 80        |           |  |  |  |  |  |  |  |  |  |  |         |
| 81        |           |  |  |  |  |  |  |  |  |  |  |         |
| 82        |           |  |  |  |  |  |  |  |  |  |  |         |
| 83        |           |  |  |  |  |  |  |  |  |  |  |         |
| 84        |           |  |  |  |  |  |  |  |  |  |  |         |
| 85        |           |  |  |  |  |  |  |  |  |  |  |         |
| 86        |           |  |  |  |  |  |  |  |  |  |  |         |
| 87        |           |  |  |  |  |  |  |  |  |  |  |         |
| 88        |           |  |  |  |  |  |  |  |  |  |  |         |
| 89        |           |  |  |  |  |  |  |  |  |  |  |         |
| 90        |           |  |  |  |  |  |  |  |  |  |  |         |
| 91        |           |  |  |  |  |  |  |  |  |  |  |         |
| 92        |           |  |  |  |  |  |  |  |  |  |  |         |
| 93        |           |  |  |  |  |  |  |  |  |  |  |         |
| 94        |           |  |  |  |  |  |  |  |  |  |  |         |
| 95        |           |  |  |  |  |  |  |  |  |  |  |         |
| 96        |           |  |  |  |  |  |  |  |  |  |  |         |
| 97        |           |  |  |  |  |  |  |  |  |  |  |         |
| 98        |           |  |  |  |  |  |  |  |  |  |  |         |
| 99        |           |  |  |  |  |  |  |  |  |  |  |         |
| 100       |           |  |  |  |  |  |  |  |  |  |  |         |
| 101       |           |  |  |  |  |  |  |  |  |  |  |         |
| 102       |           |  |  |  |  |  |  |  |  |  |  |         |
| 103       |           |  |  |  |  |  |  |  |  |  |  |         |
| 104       |           |  |  |  |  |  |  |  |  |  |  |         |
| 105       |           |  |  |  |  |  |  |  |  |  |  |         |
| 106       |           |  |  |  |  |  |  |  |  |  |  |         |
| 107       |           |  |  |  |  |  |  |  |  |  |  |         |
| 108       |           |  |  |  |  |  |  |  |  |  |  |         |
| 109       |           |  |  |  |  |  |  |  |  |  |  |         |
| 110       |           |  |  |  |  |  |  |  |  |  |  |         |
| 111       |           |  |  |  |  |  |  |  |  |  |  |         |
| 112       |           |  |  |  |  |  |  |  |  |  |  |         |
| 113       |           |  |  |  |  |  |  |  |  |  |  |         |
| 114       |           |  |  |  |  |  |  |  |  |  |  |         |
| 115       |           |  |  |  |  |  |  |  |  |  |  |         |
| 116       |           |  |  |  |  |  |  |  |  |  |  |         |
| 117       |           |  |  |  |  |  |  |  |  |  |  |         |
| 118       |           |  |  |  |  |  |  |  |  |  |  |         |
| 119       |           |  |  |  |  |  |  |  |  |  |  |         |
| 120       |           |  |  |  |  |  |  |  |  |  |  |         |
| 121       |           |  |  |  |  |  |  |  |  |  |  |         |
| 122       |           |  |  |  |  |  |  |  |  |  |  |         |
| 123       |           |  |  |  |  |  |  |  |  |  |  |         |
| 124       |           |  |  |  |  |  |  |  |  |  |  |         |
| 125       |           |  |  |  |  |  |  |  |  |  |  |         |
| 126       |           |  |  |  |  |  |  |  |  |  |  |         |
| 127       |           |  |  |  |  |  |  |  |  |  |  |         |
| 128       |           |  |  |  |  |  |  |  |  |  |  |         |
| 129       |           |  |  |  |  |  |  |  |  |  |  |         |
| 130       |           |  |  |  |  |  |  |  |  |  |  |         |
| 131       |           |  |  |  |  |  |  |  |  |  |  |         |
| 132       |           |  |  |  |  |  |  |  |  |  |  |         |
| 133       |           |  |  |  |  |  |  |  |  |  |  |         |
| 134       |           |  |  |  |  |  |  |  |  |  |  |         |
| 135       |           |  |  |  |  |  |  |  |  |  |  |         |
| 136       |           |  |  |  |  |  |  |  |  |  |  |         |
| 137       |           |  |  |  |  |  |  |  |  |  |  |         |
| 138       |           |  |  |  |  |  |  |  |  |  |  |         |
| 139       |           |  |  |  |  |  |  |  |  |  |  |         |
| 140       |           |  |  |  |  |  |  |  |  |  |  |         |
| 141       |           |  |  |  |  |  |  |  |  |  |  |         |
| 142       |           |  |  |  |  |  |  |  |  |  |  |         |
| 143       |           |  |  |  |  |  |  |  |  |  |  |         |
| 144       |           |  |  |  |  |  |  |  |  |  |  |         |
| 145       |           |  |  |  |  |  |  |  |  |  |  |         |
| 146       |           |  |  |  |  |  |  |  |  |  |  |         |
| 147       |           |  |  |  |  |  |  |  |  |  |  |         |
| 148       |           |  |  |  |  |  |  |  |  |  |  |         |
| 149       |           |  |  |  |  |  |  |  |  |  |  |         |
| 150       |           |  |  |  |  |  |  |  |  |  |  |         |
| 151       |           |  |  |  |  |  |  |  |  |  |  |         |
| 152       |           |  |  |  |  |  |  |  |  |  |  |         |
| 153       |           |  |  |  |  |  |  |  |  |  |  |         |
| 154       |           |  |  |  |  |  |  |  |  |  |  |         |
| 155       |           |  |  |  |  |  |  |  |  |  |  |         |
| 156       |           |  |  |  |  |  |  |  |  |  |  |         |
| 157       |           |  |  |  |  |  |  |  |  |  |  |         |
| 158       |           |  |  |  |  |  |  |  |  |  |  |         |
| 159       |           |  |  |  |  |  |  |  |  |  |  |         |
| 160       |           |  |  |  |  |  |  |  |  |  |  |         |
| 161       |           |  |  |  |  |  |  |  |  |  |  |         |
| 162       |           |  |  |  |  |  |  |  |  |  |  |         |
| 163       |           |  |  |  |  |  |  |  |  |  |  |         |
| 164       |           |  |  |  |  |  |  |  |  |  |  |         |
| 165       |           |  |  |  |  |  |  |  |  |  |  |         |
| 166       |           |  |  |  |  |  |  |  |  |  |  |         |
| 167       |           |  |  |  |  |  |  |  |  |  |  |         |
| 168       |           |  |  |  |  |  |  |  |  |  |  |         |
| 169       |           |  |  |  |  |  |  |  |  |  |  |         |
| 170       |           |  |  |  |  |  |  |  |  |  |  |         |
| 171       |           |  |  |  |  |  |  |  |  |  |  |         |
| 172       |           |  |  |  |  |  |  |  |  |  |  |         |
| 173       |           |  |  |  |  |  |  |  |  |  |  |         |
| 174       |           |  |  |  |  |  |  |  |  |  |  |         |
| 175       |           |  |  |  |  |  |  |  |  |  |  |         |
| 176       |           |  |  |  |  |  |  |  |  |  |  |         |
| 177       |           |  |  |  |  |  |  |  |  |  |  |         |
| 178       |           |  |  |  |  |  |  |  |  |  |  |         |
| 179       |           |  |  |  |  |  |  |  |  |  |  |         |
| 180       |           |  |  |  |  |  |  |  |  |  |  |         |
| 181       |           |  |  |  |  |  |  |  |  |  |  |         |
| 182       |           |  |  |  |  |  |  |  |  |  |  |         |
| 183       |           |  |  |  |  |  |  |  |  |  |  |         |
| 184       |           |  |  |  |  |  |  |  |  |  |  |         |
| 185       |           |  |  |  |  |  |  |  |  |  |  |         |
| 186       |           |  |  |  |  |  |  |  |  |  |  |         |
| 187       |           |  |  |  |  |  |  |  |  |  |  |         |
| 188       |           |  |  |  |  |  |  |  |  |  |  |         |
| 189       |           |  |  |  |  |  |  |  |  |  |  |         |
| 190       |           |  |  |  |  |  |  |  |  |  |  |         |
| 191       |           |  |  |  |  |  |  |  |  |  |  |         |
| 192       |           |  |  |  |  |  |  |  |  |  |  |         |
| 193       |           |  |  |  |  |  |  |  |  |  |  |         |
| 194       |           |  |  |  |  |  |  |  |  |  |  |         |
| 195       |           |  |  |  |  |  |  |  |  |  |  |         |
| 196       |           |  |  |  |  |  |  |  |  |  |  |         |
| 197       |           |  |  |  |  |  |  |  |  |  |  |         |
| 198       |           |  |  |  |  |  |  |  |  |  |  |         |
| 199       |           |  |  |  |  |  |  |  |  |  |  |         |
| 200       |           |  |  |  |  |  |  |  |  |  |  |         |
| 201       |           |  |  |  |  |  |  |  |  |  |  |         |
| 202       |           |  |  |  |  |  |  |  |  |  |  |         |
| 203       |           |  |  |  |  |  |  |  |  |  |  |         |
| 204       |           |  |  |  |  |  |  |  |  |  |  |         |
| 205       |           |  |  |  |  |  |  |  |  |  |  |         |
| 206       |           |  |  |  |  |  |  |  |  |  |  |         |
| 207       |           |  |  |  |  |  |  |  |  |  |  |         |
| 208       |           |  |  |  |  |  |  |  |  |  |  |         |
| 209       |           |  |  |  |  |  |  |  |  |  |  |         |
| 210       |           |  |  |  |  |  |  |  |  |  |  |         |
| 211       |           |  |  |  |  |  |  |  |  |  |  |         |
| 212       |           |  |  |  |  |  |  |  |  |  |  |         |
| 213       |           |  |  |  |  |  |  |  |  |  |  |         |
| 214       |           |  |  |  |  |  |  |  |  |  |  |         |
| 215       |           |  |  |  |  |  |  |  |  |  |  |         |
| 216       |           |  |  |  |  |  |  |  |  |  |  |         |
| 217       |           |  |  |  |  |  |  |  |  |  |  |         |
| 218       |           |  |  |  |  |  |  |  |  |  |  |         |
| 219       |           |  |  |  |  |  |  |  |  |  |  |         |
| 220       |           |  |  |  |  |  |  |  |  |  |  |         |
| 221       |           |  |  |  |  |  |  |  |  |  |  |         |
| 222       |           |  |  |  |  |  |  |  |  |  |  |         |
| 223       |           |  |  |  |  |  |  |  |  |  |  |         |
| 224       |           |  |  |  |  |  |  |  |  |  |  |         |
| 225       |           |  |  |  |  |  |  |  |  |  |  |         |
| 226       |           |  |  |  |  |  |  |  |  |  |  |         |
| 227       |           |  |  |  |  |  |  |  |  |  |  |         |
| 228       |           |  |  |  |  |  |  |  |  |  |  |         |
| 229       |           |  |  |  |  |  |  |  |  |  |  |         |
| 230       |           |  |  |  |  |  |  |  |  |  |  |         |
| 231       |           |  |  |  |  |  |  |  |  |  |  |         |
| 232       |           |  |  |  |  |  |  |  |  |  |  |         |
| 233       |           |  |  |  |  |  |  |  |  |  |  |         |
| 234       |           |  |  |  |  |  |  |  |  |  |  |         |
| 235       |           |  |  |  |  |  |  |  |  |  |  |         |
| 236       |           |  |  |  |  |  |  |  |  |  |  |         |
| 237       |           |  |  |  |  |  |  |  |  |  |  |         |
| 238       |           |  |  |  |  |  |  |  |  |  |  |         |
| 239       |           |  |  |  |  |  |  |  |  |  |  |         |
| 240       |           |  |  |  |  |  |  |  |  |  |  |         |
| 241       |           |  |  |  |  |  |  |  |  |  |  |         |
| 242       |           |  |  |  |  |  |  |  |  |  |  |         |
| 243       |           |  |  |  |  |  |  |  |  |  |  |         |
| 244       |           |  |  |  |  |  |  |  |  |  |  |         |
| 245       |           |  |  |  |  |  |  |  |  |  |  |         |
| 246       |           |  |  |  |  |  |  |  |  |  |  |         |
| 247       |           |  |  |  |  |  |  |  |  |  |  |         |
| 248       |           |  |  |  |  |  |  |  |  |  |  |         |
| 249       |           |  |  |  |  |  |  |  |  |  |  |         |
| 250       |           |  |  |  |  |  |  |  |  |  |  |         |
| 251       |           |  |  |  |  |  |  |  |  |  |  |         |
| 252       |           |  |  |  |  |  |  |  |  |  |  |         |
| 253       |           |  |  |  |  |  |  |  |  |  |  |         |
| 254       |           |  |  |  |  |  |  |  |  |  |  |         |
| 255       |           |  |  |  |  |  |  |  |  |  |  |         |
| 256       |           |  |  |  |  |  |  |  |  |  |  |         |
| 257       |           |  |  |  |  |  |  |  |  |  |  |         |
| 258       |           |  |  |  |  |  |  |  |  |  |  |         |
| 259       |           |  |  |  |  |  |  |  |  |  |  |         |
| 260       |           |  |  |  |  |  |  |  |  |  |  |         |
| 261       |           |  |  |  |  |  |  |  |  |  |  |         |
| 262       |           |  |  |  |  |  |  |  |  |  |  |         |
| 263       |           |  |  |  |  |  |  |  |  |  |  |         |
| 264       |           |  |  |  |  |  |  |  |  |  |  |         |
| 265       |           |  |  |  |  |  |  |  |  |  |  |         |
| 266       |           |  |  |  |  |  |  |  |  |  |  |         |
| 267       |           |  |  |  |  |  |  |  |  |  |  |         |
| 268       |           |  |  |  |  |  |  |  |  |  |  |         |
| 269       |           |  |  |  |  |  |  |  |  |  |  |         |
| 270       |           |  |  |  |  |  |  |  |  |  |  |         |
| 271       |           |  |  |  |  |  |  |  |  |  |  |         |
| 272       |           |  |  |  |  |  |  |  |  |  |  |         |
| 273       |           |  |  |  |  |  |  |  |  |  |  |         |
| 274       |           |  |  |  |  |  |  |  |  |  |  |         |
| 275       |           |  |  |  |  |  |  |  |  |  |  |         |
| 276       |           |  |  |  |  |  |  |  |  |  |  |         |
| 277       |           |  |  |  |  |  |  |  |  |  |  |         |
| 278       |           |  |  |  |  |  |  |  |  |  |  |         |
| 279       |           |  |  |  |  |  |  |  |  |  |  |         |
| 280       |           |  |  |  |  |  |  |  |  |  |  |         |
| 281       |           |  |  |  |  |  |  |  |  |  |  |         |
| 282       |           |  |  |  |  |  |  |  |  |  |  |         |
| 283       |           |  |  |  |  |  |  |  |  |  |  |         |
| 284       |           |  |  |  |  |  |  |  |  |  |  |         |
| 285       |           |  |  |  |  |  |  |  |  |  |  |         |
| 286       |           |  |  |  |  |  |  |  |  |  |  |         |
| 287       |           |  |  |  |  |  |  |  |  |  |  |         |
| 288       |           |  |  |  |  |  |  |  |  |  |  |         |
| 289       |           |  |  |  |  |  |  |  |  |  |  |         |
| 290       |           |  |  |  |  |  |  |  |  |  |  |         |
| 291       |           |  |  |  |  |  |  |  |  |  |  |         |
| 292       |           |  |  |  |  |  |  |  |  |  |  |         |
| 293       |           |  |  |  |  |  |  |  |  |  |  |         |
| 294       |           |  |  |  |  |  |  |  |  |  |  |         |
| 295       |           |  |  |  |  |  |  |  |  |  |  |         |
| 296       |           |  |  |  |  |  |  |  |  |  |  |         |
| 297       |           |  |  |  |  |  |  |  |  |  |  |         |
| 298       |           |  |  |  |  |  |  |  |  |  |  |         |
| 299       |           |  |  |  |  |  |  |  |  |  |  |         |
| 300       |           |  |  |  |  |  |  |  |  |  |  |         |
| 301       |           |  |  |  |  |  |  |  |  |  |  |         |
| 302       |           |  |  |  |  |  |  |  |  |  |  |         |
| 303       |           |  |  |  |  |  |  |  |  |  |  |         |
| 304       |           |  |  |  |  |  |  |  |  |  |  |         |
| 305       |           |  |  |  |  |  |  |  |  |  |  |         |
| 306       |           |  |  |  |  |  |  |  |  |  |  |         |
| 307       |           |  |  |  |  |  |  |  |  |  |  |         |
| 308       |           |  |  |  |  |  |  |  |  |  |  |         |
| 309       |           |  |  |  |  |  |  |  |  |  |  |         |
| 310       |           |  |  |  |  |  |  |  |  |  |  |         |
| 311       |           |  |  |  |  |  |  |  |  |  |  |         |
| 312       |           |  |  |  |  |  |  |  |  |  |  |         |
| 313       |           |  |  |  |  |  |  |  |  |  |  |         |
| 314       |           |  |  |  |  |  |  |  |  |  |  |         |
| 315       |           |  |  |  |  |  |  |  |  |  |  |         |
| 316       |           |  |  |  |  |  |  |  |  |  |  |         |
| 317       |           |  |  |  |  |  |  |  |  |  |  |         |
| 318       |           |  |  |  |  |  |  |  |  |  |  |         |
| 319       |           |  |  |  |  |  |  |  |  |  |  |         |
| 320       |           |  |  |  |  |  |  |  |  |  |  |         |
| 321       |           |  |  |  |  |  |  |  |  |  |  |         |
| 322       |           |  |  |  |  |  |  |  |  |  |  |         |
| 323       |           |  |  |  |  |  |  |  |  |  |  |         |
| 324       |           |  |  |  |  |  |  |  |  |  |  |         |
| 325       |           |  |  |  |  |  |  |  |  |  |  |         |
| 326       |           |  |  |  |  |  |  |  |  |  |  |         |
| 327       |           |  |  |  |  |  |  |  |  |  |  |         |
| 328       |           |  |  |  |  |  |  |  |  |  |  |         |
| 329       |           |  |  |  |  |  |  |  |  |  |  |         |
| 330       |           |  |  |  |  |  |  |  |  |  |  |         |
| 331       |           |  |  |  |  |  |  |  |  |  |  |         |
| 332       |           |  |  |  |  |  |  |  |  |  |  |         |
| 333       |           |  |  |  |  |  |  |  |  |  |  |         |
| 334       |           |  |  |  |  |  |  |  |  |  |  |         |
| 335       |           |  |  |  |  |  |  |  |  |  |  |         |
| 336       |           |  |  |  |  |  |  |  |  |  |  |         |
| 337       |           |  |  |  |  |  |  |  |  |  |  |         |
| 338       |           |  |  |  |  |  |  |  |  |  |  |         |
| 339       |           |  |  |  |  |  |  |  |  |  |  |         |
| 340       |           |  |  |  |  |  |  |  |  |  |  |         |
| 341       |           |  |  |  |  |  |  |  |  |  |  |         |
| 342       |           |  |  |  |  |  |  |  |  |  |  |         |
| 343       |           |  |  |  |  |  |  |  |  |  |  |         |
| 344       |           |  |  |  |  |  |  |  |  |  |  |         |
| 345       |           |  |  |  |  |  |  |  |  |  |  |         |
| 346       |           |  |  |  |  |  |  |  |  |  |  |         |
| 347       |           |  |  |  |  |  |  |  |  |  |  |         |
| 348       |           |  |  |  |  |  |  |  |  |  |  |         |
| 349       |           |  |  |  |  |  |  |  |  |  |  |         |
| 350       |           |  |  |  |  |  |  |  |  |  |  |         |
| 351       |           |  |  |  |  |  |  |  |  |  |  |         |
| 352       |           |  |  |  |  |  |  |  |  |  |  |         |
| 353       |           |  |  |  |  |  |  |  |  |  |  |         |
| 354       |           |  |  |  |  |  |  |  |  |  |  |         |
| 355       |           |  |  |  |  |  |  |  |  |  |  |         |
| 356       |           |  |  |  |  |  |  |  |  |  |  |         |
| 357       |           |  |  |  |  |  |  |  |  |  |  |         |
| 358       |           |  |  |  |  |  |  |  |  |  |  |         |
| 359       |           |  |  |  |  |  |  |  |  |  |  |         |
| 360       |           |  |  |  |  |  |  |  |  |  |  |         |
| 361       |           |  |  |  |  |  |  |  |  |  |  |         |
| 362       |           |  |  |  |  |  |  |  |  |  |  |         |
| 363       |           |  |  |  |  |  |  |  |  |  |  |         |
| 364       |           |  |  |  |  |  |  |  |  |  |  |         |
| 365       |           |  |  |  |  |  |  |  |  |  |  |         |
| 366       |           |  |  |  |  |  |  |  |  |  |  |         |
| 367       |           |  |  |  |  |  |  |  |  |  |  |         |
| 368       |           |  |  |  |  |  |  |  |  |  |  |         |
| 369       |           |  |  |  |  |  |  |  |  |  |  |         |
| 370       |           |  |  |  |  |  |  |  |  |  |  |         |
| 371       |           |  |  |  |  |  |  |  |  |  |  |         |
| 372       |           |  |  |  |  |  |  |  |  |  |  |         |
| 373       |           |  |  |  |  |  |  |  |  |  |  |         |
| 374       |           |  |  |  |  |  |  |  |  |  |  |         |
| 375       |           |  |  |  |  |  |  |  |  |  |  |         |
| 376       |           |  |  |  |  |  |  |  |  |  |  |         |
| 377       |           |  |  |  |  |  |  |  |  |  |  |         |
| 378       |           |  |  |  |  |  |  |  |  |  |  |         |
| 379       |           |  |  |  |  |  |  |  |  |  |  |         |
| 380       |           |  |  |  |  |  |  |  |  |  |  |         |
| 381       |           |  |  |  |  |  |  |  |  |  |  |         |
| 382       |           |  |  |  |  |  |  |  |  |  |  |         |
| 383       |           |  |  |  |  |  |  |  |  |  |  |         |
| 384       |           |  |  |  |  |  |  |  |  |  |  |         |
| 385       |           |  |  |  |  |  |  |  |  |  |  |         |
| 386       |           |  |  |  |  |  |  |  |  |  |  |         |
| 387       |           |  |  |  |  |  |  |  |  |  |  |         |
| 388       |           |  |  |  |  |  |  |  |  |  |  |         |
| 389       |           |  |  |  |  |  |  |  |  |  |  |         |
| 390       |           |  |  |  |  |  |  |  |  |  |  |         |
| 391       |           |  |  |  |  |  |  |  |  |  |  |         |
| 392       |           |  |  |  |  |  |  |  |  |  |  |         |
| 393       |           |  |  |  |  |  |  |  |  |  |  |         |
| 394       |           |  |  |  |  |  |  |  |  |  |  |         |
| 395       |           |  |  |  |  |  |  |  |  |  |  |         |
| 396       |           |  |  |  |  |  |  |  |  |  |  |         |
| 397       |           |  |  |  |  |  |  |  |  |  |  |         |
| 398       |           |  |  |  |  |  |  |  |  |  |  |         |
| 399       |           |  |  |  |  |  |  |  |  |  |  |         |
| 400       |           |  |  |  |  |  |  |  |  |  |  |         |
| 401       |           |  |  |  |  |  |  |  |  |  |  |         |
| 402       |           |  |  |  |  |  |  |  |  |  |  |         |
| 403       |           |  |  |  |  |  |  |  |  |  |  |         |
| 404       |           |  |  |  |  |  |  |  |  |  |  |         |
| 405       |           |  |  |  |  |  |  |  |  |  |  |         |
| 406       |           |  |  |  |  |  |  |  |  |  |  |         |
| 407       |           |  |  |  |  |  |  |  |  |  |  |         |
| 408       |           |  |  |  |  |  |  |  |  |  |  |         |
| 409       |           |  |  |  |  |  |  |  |  |  |  |         |
| 410       |           |  |  |  |  |  |  |  |  |  |  |         |
| 411       |           |  |  |  |  |  |  |  |  |  |  |         |
| 412       |           |  |  |  |  |  |  |  |  |  |  |         |
| 413       |           |  |  |  |  |  |  |  |  |  |  |         |
| 414       |           |  |  |  |  |  |  |  |  |  |  |         |
| 415       |           |  |  |  |  |  |  |  |  |  |  |         |
| 416       |           |  |  |  |  |  |  |  |  |  |  |         |
| 417       |           |  |  |  |  |  |  |  |  |  |  |         |
| 418       |           |  |  |  |  |  |  |  |  |  |  |         |
| 419       |           |  |  |  |  |  |  |  |  |  |  |         |
| 420       |           |  |  |  |  |  |  |  |  |  |  |         |
| 421       |           |  |  |  |  |  |  |  |  |  |  |         |
| 422       |           |  |  |  |  |  |  |  |  |  |  |         |
| 423       |           |  |  |  |  |  |  |  |  |  |  |         |
| 424       |           |  |  |  |  |  |  |  |  |  |  |         |
| 425       |           |  |  |  |  |  |  |  |  |  |  |         |
| 426       |           |  |  |  |  |  |  |  |  |  |  |         |
| 427       |           |  |  |  |  |  |  |  |  |  |  |         |
| 428       |           |  |  |  |  |  |  |  |  |  |  |         |
| 429       |           |  |  |  |  |  |  |  |  |  |  |         |
| 430       |           |  |  |  |  |  |  |  |  |  |  |         |
| 431       |           |  |  |  |  |  |  |  |  |  |  |         |
| 432       |           |  |  |  |  |  |  |  |  |  |  |         |
| 433       |           |  |  |  |  |  |  |  |  |  |  |         |
| 434       |           |  |  |  |  |  |  |  |  |  |  |         |
| 435       |           |  |  |  |  |  |  |  |  |  |  |         |
| 436       |           |  |  |  |  |  |  |  |  |  |  |         |
| 437       |           |  |  |  |  |  |  |  |  |  |  |         |
| 438       |           |  |  |  |  |  |  |  |  |  |  |         |
| 439       |           |  |  |  |  |  |  |  |  |  |  |         |
| 440       |           |  |  |  |  |  |  |  |  |  |  |         |
| 441       |           |  |  |  |  |  |  |  |  |  |  |         |
| 442       |           |  |  |  |  |  |  |  |  |  |  |         |
| 443       |           |  |  |  |  |  |  |  |  |  |  |         |
| 444       |           |  |  |  |  |  |  |  |  |  |  |         |
| 445       |           |  |  |  |  |  |  |  |  |  |  |         |
| 446       |           |  |  |  |  |  |  |  |  |  |  |         |
| 447       |           |  |  |  |  |  |  |  |  |  |  |         |
| 448       |           |  |  |  |  |  |  |  |  |  |  |         |
| 449       |           |  |  |  |  |  |  |  |  |  |  |         |
| 450       |           |  |  |  |  |  |  |  |  |  |  |         |
| 451       |           |  |  |  |  |  |  |  |  |  |  |         |
| 452       |           |  |  |  |  |  |  |  |  |  |  |         |
| 453       |           |  |  |  |  |  |  |  |  |  |  |         |
| 454       |           |  |  |  |  |  |  |  |  |  |  |         |
| 455       |           |  |  |  |  |  |  |  |  |  |  |         |
| 456       |           |  |  |  |  |  |  |  |  |  |  |         |
| 457       |           |  |  |  |  |  |  |  |  |  |  |         |
| 458       |           |  |  |  |  |  |  |  |  |  |  |         |
| 459       |           |  |  |  |  |  |  |  |  |  |  |         |
| 460       |           |  |  |  |  |  |  |  |  |  |  |         |
| 461       |           |  |  |  |  |  |  |  |  |  |  |         |
| 462       |           |  |  |  |  |  |  |  |  |  |  |         |
| 463       |           |  |  |  |  |  |  |  |  |  |  |         |
| 464       |           |  |  |  |  |  |  |  |  |  |  |         |
| 465       |           |  |  |  |  |  |  |  |  |  |  |         |
| 466       |           |  |  |  |  |  |  |  |  |  |  |         |
| 467       |           |  |  |  |  |  |  |  |  |  |  |         |
| 468       |           |  |  |  |  |  |  |  |  |  |  |         |
| 469       |           |  |  |  |  |  |  |  |  |  |  |         |
| 470       |           |  |  |  |  |  |  |  |  |  |  |         |
| 471       |           |  |  |  |  |  |  |  |  |  |  |         |
| 472       |           |  |  |  |  |  |  |  |  |  |  |         |
| 473       |           |  |  |  |  |  |  |  |  |  |  |         |
| 474       |           |  |  |  |  |  |  |  |  |  |  |         |
| 475       |           |  |  |  |  |  |  |  |  |  |  |         |
| 476       |           |  |  |  |  |  |  |  |  |  |  |         |
| 477       |           |  |  |  |  |  |  |  |  |  |  |         |
| 478       |           |  |  |  |  |  |  |  |  |  |  |         |
| 479       |           |  |  |  |  |  |  |  |  |  |  |         |
| 480       |           |  |  |  |  |  |  |  |  |  |  |         |
| 481       |           |  |  |  |  |  |  |  |  |  |  |         |
| 482       |           |  |  |  |  |  |  |  |  |  |  |         |
| 483       |           |  |  |  |  |  |  |  |  |  |  |         |
| 484       |           |  |  |  |  |  |  |  |  |  |  |         |
| 485       |           |  |  |  |  |  |  |  |  |  |  |         |
| 486       |           |  |  |  |  |  |  |  |  |  |  |         |
| 487       |           |  |  |  |  |  |  |  |  |  |  |         |
| 488       |           |  |  |  |  |  |  |  |  |  |  |         |
| 489       |           |  |  |  |  |  |  |  |  |  |  |         |
| 490       |           |  |  |  |  |  |  |  |  |  |  |         |
| 491       |           |  |  |  |  |  |  |  |  |  |  |         |
| 492       |           |  |  |  |  |  |  |  |  |  |  |         |
| 493       |           |  |  |  |  |  |  |  |  |  |  |         |
| 494       |           |  |  |  |  |  |  |  |  |  |  |         |
| 495       |           |  |  |  |  |  |  |  |  |  |  |         |
| 496       |           |  |  |  |  |  |  |  |  |  |  |         |
| 497       |           |  |  |  |  |  |  |  |  |  |  |         |
| 498       |           |  |  |  |  |  |  |  |  |  |  |         |
| 499       |           |  |  |  |  |  |  |  |  |  |  |         |
| 500       |           |  |  |  |  |  |  |  |  |  |  |         |
| 501       |           |  |  |  |  |  |  |  |  |  |  |         |
| 502       |           |  |  |  |  |  |  |  |  |  |  |         |
| 503       |           |  |  |  |  |  |  |  |  |  |  |         |
| 504       |           |  |  |  |  |  |  |  |  |  |  |         |
| 505       |           |  |  |  |  |  |  |  |  |  |  |         |
| 506       |           |  |  |  |  |  |  |  |  |  |  |         |
| 507       |           |  |  |  |  |  |  |  |  |  |  |         |
| 508       |           |  |  |  |  |  |  |  |  |  |  |         |
| 509       |           |  |  |  |  |  |  |  |  |  |  |         |
| 510       |           |  |  |  |  |  |  |  |  |  |  |         |
| 511       |           |  |  |  |  |  |  |  |  |  |  |         |
| 512       |           |  |  |  |  |  |  |  |  |  |  |         |
| 513       |           |  |  |  |  |  |  |  |  |  |  |         |
| 514       |           |  |  |  |  |  |  |  |  |  |  |         |
| 515       |           |  |  |  |  |  |  |  |  |  |  |         |
| 516       |           |  |  |  |  |  |  |  |  |  |  |         |
| 517       |           |  |  |  |  |  |  |  |  |  |  |         |
| 518       |           |  |  |  |  |  |  |  |  |  |  |         |
| 519       |           |  |  |  |  |  |  |  |  |  |  |         |
| 520       |           |  |  |  |  |  |  |  |  |  |  |         |
| 521       |           |  |  |  |  |  |  |  |  |  |  |         |
| 522       |           |  |  |  |  |  |  |  |  |  |  |         |
| 523       |           |  |  |  |  |  |  |  |  |  |  |         |
| 524       |           |  |  |  |  |  |  |  |  |  |  |         |
| 525       |           |  |  |  |  |  |  |  |  |  |  |         |
| 526       |           |  |  |  |  |  |  |  |  |  |  |         |
| 527       |           |  |  |  |  |  |  |  |  |  |  |         |
| 528       |           |  |  |  |  |  |  |  |  |  |  |         |
| 529       |           |  |  |  |  |  |  |  |  |  |  |         |
| 530       |           |  |  |  |  |  |  |  |  |  |  |         |
| 531       |           |  |  |  |  |  |  |  |  |  |  |         |
| 532       |           |  |  |  |  |  |  |  |  |  |  |         |
| 533       |           |  |  |  |  |  |  |  |  |  |  |         |
| 534       |           |  |  |  |  |  |  |  |  |  |  |         |
| 535       |           |  |  |  |  |  |  |  |  |  |  |         |
| 536       |           |  |  |  |  |  |  |  |  |  |  |         |
| 537       |           |  |  |  |  |  |  |  |  |  |  |         |
| 538       |           |  |  |  |  |  |  |  |  |  |  |         |
| 539       |           |  |  |  |  |  |  |  |  |  |  |         |
| 540       |           |  |  |  |  |  |  |  |  |  |  |         |
| 541       |           |  |  |  |  |  |  |  |  |  |  |         |
| 542       |           |  |  |  |  |  |  |  |  |  |  |         |
| 543       |           |  |  |  |  |  |  |  |  |  |  |         |
| 544       |           |  |  |  |  |  |  |  |  |  |  |         |
| 545       |           |  |  |  |  |  |  |  |  |  |  |         |
| 546       |           |  |  |  |  |  |  |  |  |  |  |         |
| 547       |           |  |  |  |  |  |  |  |  |  |  |         |
| 548       |           |  |  |  |  |  |  |  |  |  |  |         |
| 549       |           |  |  |  |  |  |  |  |  |  |  |         |
| 550       |           |  |  |  |  |  |  |  |  |  |  |         |
| 551       |           |  |  |  |  |  |  |  |  |  |  |         |
| 552       |           |  |  |  |  |  |  |  |  |  |  |         |
| 553       |           |  |  |  |  |  |  |  |  |  |  |         |
| 554       |           |  |  |  |  |  |  |  |  |  |  |         |
| 555       |           |  |  |  |  |  |  |  |  |  |  |         |
| 556       |           |  |  |  |  |  |  |  |  |  |  |         |
| 557       |           |  |  |  |  |  |  |  |  |  |  |         |
| 558       |           |  |  |  |  |  |  |  |  |  |  |         |
| 559       |           |  |  |  |  |  |  |  |  |  |  |         |
| 560       |           |  |  |  |  |  |  |  |  |  |  |         |
| 561       |           |  |  |  |  |  |  |  |  |  |  |         |
| 562       |           |  |  |  |  |  |  |  |  |  |  |         |
| 563       |           |  |  |  |  |  |  |  |  |  |  |         |
| 564       |           |  |  |  |  |  |  |  |  |  |  |         |
| 565       |           |  |  |  |  |  |  |  |  |  |  |         |

Table 4. Molecular volumes ( $\text{\AA}^3$ ) comparison between Bader, Boyd, van der Waals and STREUSEL size quantification methods.

|                | <b>Bader</b> | <b>Boyd</b> | <b>STREUSEL</b> | <b>van der Waals</b> |
|----------------|--------------|-------------|-----------------|----------------------|
| O <sub>2</sub> | 14.93        | 17.18       | 18.81           | 22.91                |
| N <sub>2</sub> | 17.09        | 19.66       | 19.69           | 23.49                |

Separately, the empirical dependence of both the Alvarez and Pykkö radii, which are self-consistently derived by using empirical and calculated data of atoms in molecules, <sup>(40)</sup> It is, thus, unsurprising that STREUSEL radii are considered larger than Pykkö radii, which considers atoms in bonded environments. Further, unscaled Boyd radii represent the upper bound in accepted atomic radii, deriving radii from vacuum, neutral atomic calculations. <sup>(52)</sup> The STREUSEL radii yield neither the upper, nor lower bounds of accepted atomic radii values, indicating that our approach is not too farfetched.

The reported van der Waals and Pykkö radii are consistently lower than those obtained using STREUSEL, Boyd, Rahm or Alvarez. On average, the resultant volumes computed with STREUSEL are 5% larger than those obtained from the conventional van der Waals approach. This may be due, in part, to the crystallographic basis for the atomic radii, which inherently considers atoms in bonded environments. van der Waals radii are obtained from crystallographic data under two assumptions: i) contact distances obtained from X-ray diffraction data are temperature dependent, and ii) atoms are approximated as spheres. <sup>(32)</sup>

The difference between van der Waals volumes, the electron density cutoffs presented by Bader and Boyd, and the electric field cutoff recovered using STREUSEL is illustrated via a volumetric comparison of O<sub>2</sub> and N<sub>2</sub>, Table 4. We use the example in part to demonstrate that STREUSEL is yielding comparable size results to other approaches, but also to emphasize that the approach is

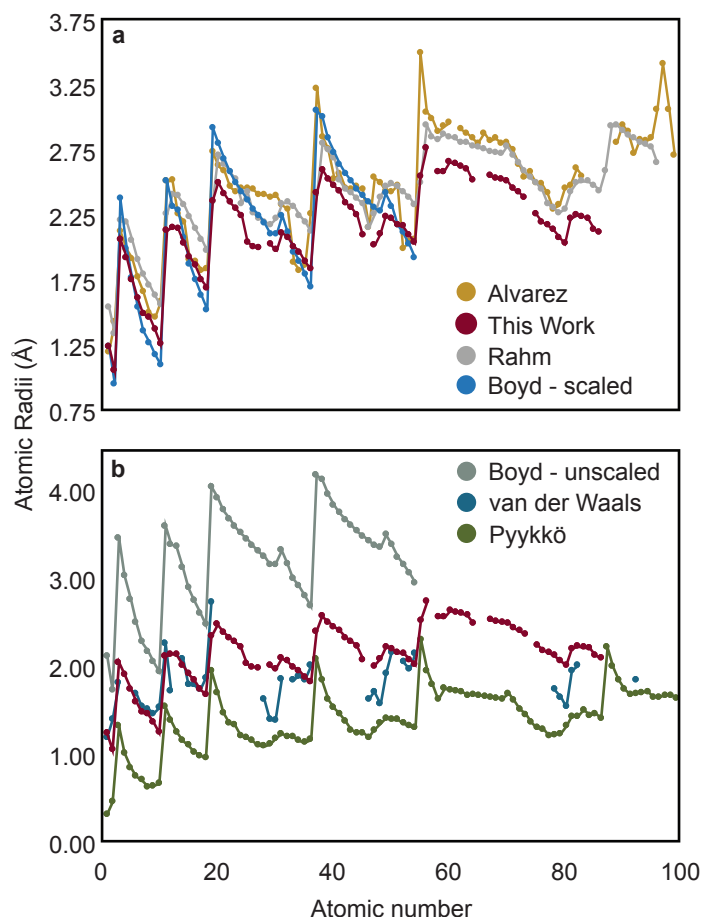


*Figure 18.* A comparison of atomic radii recovered using various conventional size metrics. **a)** Sizes computed from STREUSEL are similar to those presented by Alvarez, and Rahm and Boyd (top panel). **b)** Alternative size metrics are presented as the upper and lower limits.

sensitive to composition, geometry, and electronic structure. In this case, the diatomic molecule geometries were obtained from CCSD-full<sup>(254;255;256;257)</sup> paired with the aug-cc-pVTZ<sup>(253)</sup> basis set, as implemented by Gaussian09.<sup>(77)</sup> Often O<sub>2</sub> and N<sub>2</sub> are considered to be near-equivalent in size,<sup>(294;295)</sup> posing historical challenges with size-based separations.<sup>(296)</sup> While greater difference in volume between O<sub>2</sub> and N<sub>2</sub> recovered by electron density-based size metrics is expected considering the dissimilar bonding and electronic configurations of these two gases, the STREUSEL and Batsanov approaches obtain values aligning with experimental trends – they are difficult to separate.

**Ionic and Ionic Bonded Systems.** The primary shortcoming of the van der Waals size method is the inability to accurately recover sizes of polar chemical systems. Indeed, polar molecules are instrumental in essentially all chemistry, but particularly operative in both electrochemistry and condensed matter systems, such as ionic liquids, where size plays an important role in determining many physically relevant properties.<sup>(297;298)</sup> Beyond molecular examples, size has also been reported to contribute to charge mobility in transparent oxides,<sup>(299)</sup> as well as ion mobility in batteries. For example, INSERT. Indeed, there are several examples of ionic size metrics in literature,<sup>(24;26;27;62;63;64;65;67)</sup> each reporting ionic radii of similar magnitude.

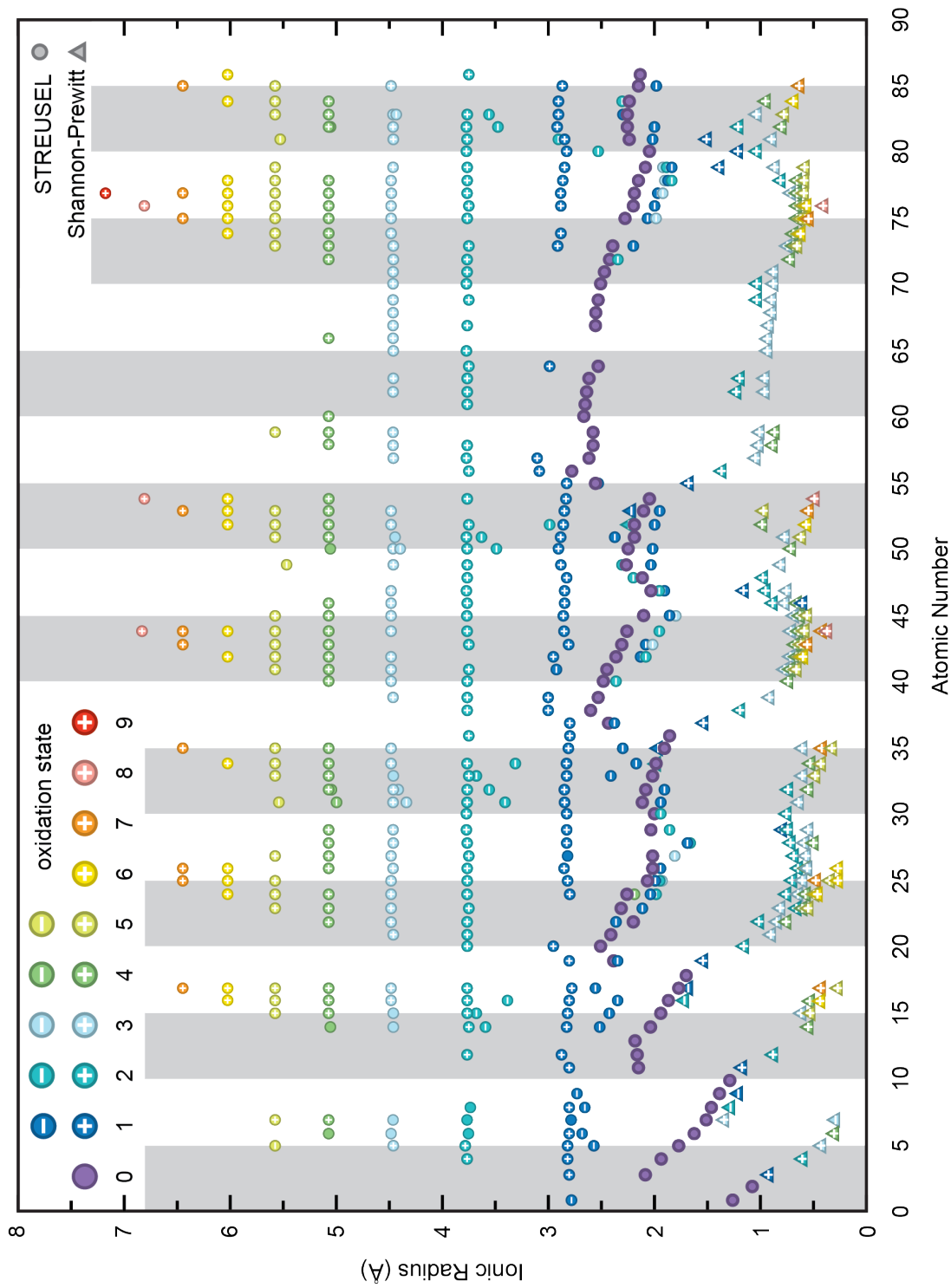


Figure 19. Calculated STREUSEL ionic radii (y-axis) for relevant oxidation states of atoms 1-86 (x-axis).

We present the electric field-derived radii or relevant ions, Figure 23. Unsurprisingly, the STREUSEL ionic radii are larger than the Shannon-Prewitt radii – since STREUSEL radii consider free ions (*i.e.* not associated with a coordination number). As such, divergence between the Shannon-Prewitt size metric and STREUSEL relates to the type of size that is addressed by each metric – Shannon-Prewitt focuses on the space that each ion *occupies*, while STREUSEL accesses the space that each ion *affects*.

Interestingly, the electric field-derived ionic radii are highly dependent on oxidation state. First row transition metals are presented, Figure 38, for a more detailed examination of competing factors. From general physics we know that electric fields are generated by charged particles – in the case of ions, there are two oppositely charged, interacting particles (protons and electrons), which produce a net field. As oxidation state is changed, the ratio of protons to electrons changes (since oxidation state is correlated with this charge ratio) and the field propagates further/closer to the ion center. Thus, ionic radius increases with increasing number of protons relative to electrons, demonstrated by STREUSEL in Figure 38.

Yet, the STREUSEL ionic radii are independent of coordination. Indeed, the size of atoms change depending on the field that they are subjected to; this is evident from the coordination number specifications on many empirically-derived ionic radii.<sup>(32;62;63;64;67)</sup> One of the key aspects of our electric field-derived approach is the ability to theoretically assess a change in size based on proximity to other electric fields. For example, the field produced by a  $\text{Li}^+$  should be larger than  $\text{Li}^+$  in an ion pair,  $\text{LiCl}$ , simply because the field is proportional to the charge – they passicate one another. We can demonstrate that the size of ions depends on atomic

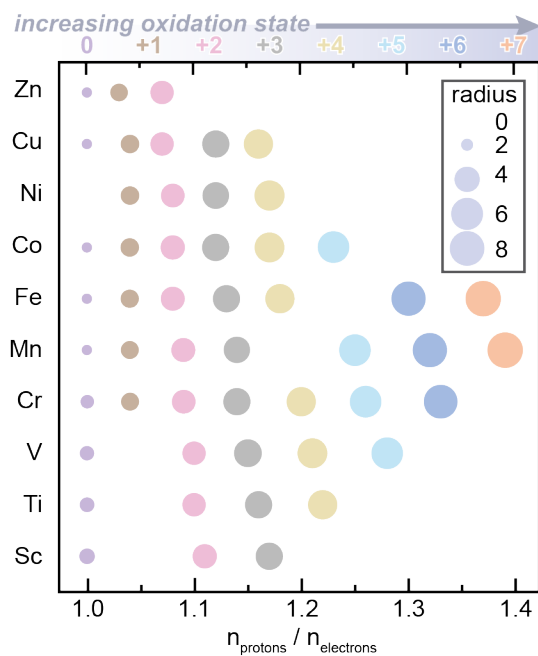


Figure 20. Comparison of proton count ( $n_{\text{protons}}$ )-to-electron count ( $n_{\text{electrons}}$ ) ratio (x-axis) for the first row transition metals (y-axis) across a series of oxidation states (colors) featuring data points correlated with calculated STREUSEL ionic radii (data point size).

proximity, through progressive increase in bond length in a series of diatomic molecules (HF, HCl, HBr, LiF, LiCl, LiBr), Figure 21. Here, the volumes of LiF, LiCl, and LiBr increase with increasing bond length. Interestingly, the volumetric trend of the dissociated diatomics ( $\text{Li}^+ + \text{F}^- > \text{Li}^+ \text{Cl}^- > \text{Li}^+ + \text{Br}^-$ ) presents a size trend in opposition with the periodic table atomic size trends. We find  $\text{F}^-$  is larger than  $\text{Cl}^-$ , which is larger than  $\text{Br}^-$ , due to the effective core charge relationship. This is at odds with the generally accepted metric that  $\text{Br}^-$  is the largest of the three, which is certainly true from an electron density and bonding perspective, but orthogonal to the inherent reactivity and *affected size* of the free ions themselves. From this perspective, the larger of the three anions is expected to be the most electronegative,  $\text{F}^-$ . We also present the same series of experiments for gas phase acidic halides, HF, HCl, and HBr, Figure 21. Generally, as the ions are separated the size increases to a point. However, in the case of a fully dissociated  $\text{H}^+$  and  $\text{X}^-$ , the proton no longer possesses electron density, resulting in a terminal decrease in size after approximately 3-4 Å separation. These experiments point to two key observations; i) that size depends on interatomic proximity, and ii) that the size of ionic systems deviates from rigid size metrics, simply because of charge (de)shielding.

The effect of interatomic proximity and charge (de)shielding on chemical system size is further highlighted by the comparison of electric field-derived and electron density-derived volumes of a series of geometrically equilibrated diatomic molecules (HF, HCl, HBr, LiF, LiCl, LiBr), Figure 22. Size dependency on increasing dipole moment is only exhibited by electric field-based size metrics. Across the gas phase acidic halides, the increase in dipole moment leads to an increased deviation between the electric field-derived and electron density-derived



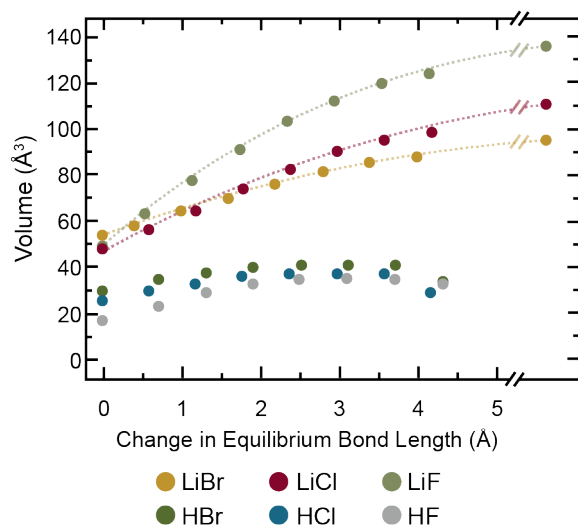
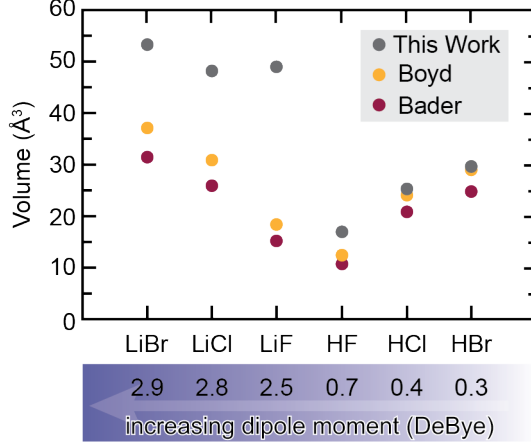


Figure 21. STREUSEL volumes (y-axis) for a series of six diatomic molecules were calculated for the optimized structures, and a series of models with expanded bond lengths (x-axis). Individual ion volumes (*i.e.*  $\text{Li}^+$ ,  $\text{F}^-$ ,  $\text{Cl}^-$ , and  $\text{Br}^-$ ) were calculated and summed to obtain the maximum volume for each ionic compound.

volumes; the studied gas phase acidic halides are more similar in size than conventional metrics purport.

While a similar relationship is exhibited in the Li-based diatomic molecules, there are additional factors at play. The higher valence-to-core charge of the  $\text{Li}^+$ -based diatomic molecules introduces competing effects, which results in a larger field-based size. The increased electronegativity of the  $\text{F}^-$  in this instance is exacerbated, leading to an amplified electric field-derived size – a phenomenon that is neglected in the electron density-based size calculations. This is further demonstrated by the relationship between electric field and electronegativity.

Since STREUSEL assigns size based on the electric field produced by the atoms, which is determined by the Coulombic charge of the atoms, the higher valence-to-core charge should yield a larger field. Indeed, we may derive the mathematical relationship between electric field ( $E$ ) and electronegativity ( $\bar{\chi}$ )



*Figure 22.* Comparison of molecular volumes for a series of geometrically equilibrated diatomic molecules with varying dipole moments. Divergence between electronic density-based size metrics and STREUSEL depends on the system polarity and atomic electronegativity.

defined by Rahm as the average energy of the electrons,<sup>(300)</sup>

$$\bar{\chi} = \frac{1}{n} \sum_{i=1}^n n_i \varepsilon_i \quad (3.1)$$

where  $n$  is the total number of electrons,  $\varepsilon_i$  is the energy of the electrons in the  $i^{\text{th}}$  level, and  $n_i$  is the occupancy of the  $i^{\text{th}}$  level. We can expand this equation to describe the electronegativity of a region in space,  $(\bar{\chi}(r))$ , where the total number of electrons becomes the number density of electrons within region  $\mathbf{r}$  ( $n(r)$ ) and the summation of energy is the energy density of that region ( $\mu_E(r)$ ). Thus,

$$\bar{\chi}(r) = \frac{\mu_E(r)}{n(r)} \quad (3.2)$$

from electromagnetics, the energy density in free space is occupied by an electric field ( $E$ ) is

$$\mu_E = \frac{1}{2} \varepsilon_0 E^2 \quad (3.3)$$

where  $\varepsilon_0$  is the permittivity of free space. Combining (3.2) and (3.3) and taking advantage of the relationship between charge density ( $\rho(r)$ ) and number density

$$(\rho(r) = qn(r))$$

$$E(r) = \sqrt{\frac{2\rho(r)\bar{\chi}(r)}{q\epsilon_0}} \quad (3.4)$$

thus,  $E \propto \sqrt{\bar{\chi}}$ ; as  $\bar{\chi}(r)$  increases, so does  $E$ .

This is further demonstrated by comparing the recovered electron density-based and electric field-based surfaces for this series of diatomic molecules, Figure 23. Owing to the polarity of these molecules, the recovered surfaces are noticeably aspherical. From an electronic structure perspective, polarity necessitates the use of basis sets composed of multiple functions. Moreover, while two molecules may take up a similar amount of space, the shape may be inherently different. The gas phase acidic halides specifically demonstrate that the cationic components of these molecules, which are protons and do not possess electron density, generate a field. We show that the majority of the space occupied by the gas phase acidic diatomic molecules is centered over the proton – in direct opposition o the electron density-based surface.

**Ionic Liquids.** As a more sophisticated example of the utility of STREUSEL, we can use our approach to assess sizes of molecules and their ions. Specifically with regard to molecular ions, for example those found in ionic liquids, molar volume is a critical parameter which is thought to govern a wealth of physical properties including density, viscosity, and so forth.<sup>(301)</sup> However, the density and molar volume should depend on the size of the ions, which itself depends on whether they are computed together or separately (see the relationship presented in Figure 21). This is inpart why the van der Waals approach seems to be widely employed for ion size estimates,<sup>(14)</sup> because the method implicitly accounts for intermolecular attractions. Yet, ions are thought to interact via their fields, which is neglected by van der Waals.

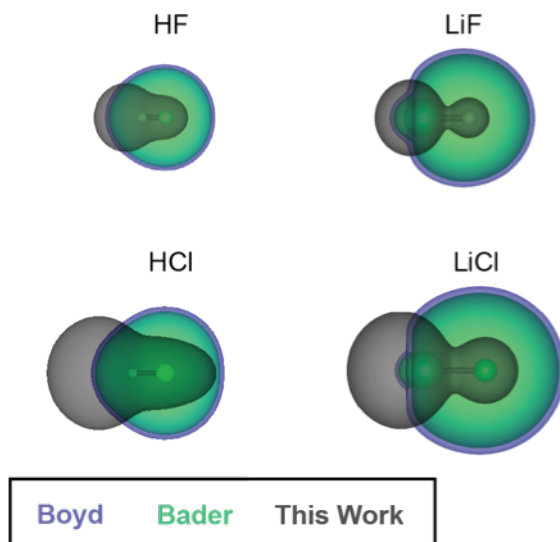


Figure 23. The Boyd (periwinkle), Bader (mint), and STREUSEL (charcoal) surfaces of a series of diatomic molecules. All surfaces are plotted using VESTA. The Boyd surface is depicted at an isosurface value of  $0.00015 \text{ e}\text{\AA}^{-3}$ . The Bader surface is depicted at an isosurface value of  $0.00030 \text{ e}\text{\AA}^{-3}$ . The STREUSEL surface is depicted at an isosurface value relative to the minimum value of the electric field surface mapped on the electrostatic potential map.

Table 5. Boyd, Bader, Batsanov and STREUSEL-derived molecular volume ( $\text{\AA}^3$ ) comparison for two ionic liquids possessing perhalometallate anions. The sum of single molecule volumes for the individual constituents ( $[BMIM]^+$ ,  $[VCl_4]^-$ ,  $[CoCl_4]^{2-}$ ) are presented, as well as the fully geometry-optimized ion pair. The percent difference (%) is presented for each ionic liquid model. BMIM = 1-butyl-3-methylimidazolium

|                             |                    | Batsanov | Boyd  | Bader | STREUSEL |
|-----------------------------|--------------------|----------|-------|-------|----------|
| $[BMIM]^+ + [VCl_4]^-$      | ( $\text{\AA}^3$ ) | 268.6    | 139.3 | 124.9 | 246.7    |
| $[BMIM][VCl_4]$             | ( $\text{\AA}^3$ ) | 217.6    | 114.8 | 105.1 | 247.1    |
| Percent Difference          | (%)                | 20.98    | 18.57 | 17.22 | 0.1620   |
| $2[BMIM]^+ + [CoCl_4]^{2-}$ | ( $\text{\AA}^3$ ) | 430.2    | 216.3 | 159.6 | 404.2    |
| $[BMIM]_2[CoCl_4]$          | ( $\text{\AA}^3$ ) | 293.6    | 173.1 | 195.2 | 390.1    |
| Percent Difference          | (%)                | 37.75    | 22.19 | 20.07 | 3.550    |

Consider recently reported ionic liquids featuring inorganic perhalometallate anionic constituents, Table 5.<sup>(302)</sup> The rigid sphere approximation returns larger volumes than the electron density and electric field-based methods. The Bondi presentation of the van der Waals radii excludes atoms possessing an atomic number  $> 10$ ;<sup>(28)</sup> thus, the revised van der Waals radii presented by Batsanov<sup>(30)</sup> were used for these volume calculations of the ionic liquid constituents. Intuitively, we would expect anions to be larger in field than their neutral counterparts (Figure 23), thus, it is slightly unexpected that the van der Waals volumes are the largest across all studied species. This is likely due to the derivation of Batsanov radii from experimental contact distances coupled with the spherical atom approximation.<sup>(28;30)</sup> Indeed, the electron density of the halides in these anionic compounds is likely drawn towards the transition metal, which would result in an effectively smaller volume, yet produces a larger field.

## Conclusions

From Figure 21, we are initially inclined to think that as molecules are pulled apart their volume should increase, Yet, this is not the case for polynuclear systems (*e.g.* systems containing more than one molecule) presented in Table 5. Within polynuclear systems there are two competing phenomena determining the size of the ions, i) anionic and cationic electric fields interacting, leading to a decrease in size, and ii) electric fields of the anionic and cationic components are stabilizing each other, ultimately changing each other's shape. To explore this nuance, we further examine two ionic liquid systems,  $[BMIM][VCl_4]$  and  $[BMIM]_2[CoCl_4]$ , and the corresponding geometries of the equilibrated anionic ( $[VCl_4]^-$ ,  $[CoCl_4]^{2-}$ ) and cationic ( $[BMIM]^+$ ) constituents, Table 5 (here BMIM denotes 1-butyl-3-methylimidazolium). We present the electron density-derived,

STREUSEL-derived, and Batsanov-derived volumes for the geometry-optimized polynuclear system, individual components, and the sum of the individual components.

As a result of the electron density stabilization, the optimized ionic liquid systems possess a *smaller* electron density-derived volume than the summed volumes of their individual counterparts. While it is not due to electron density-stabilization, the rigid sphere volumes exhibit a similar trend. In this case, it is because of the rigid sphere overlap between anionic and cationic constituents of the polynuclear system is accounted for in the fully optimized model. STREUSEL, on the other hand, returns the contact surface (*e.g.* the extent to which each component *affects* its surroundings) of the ionic components. This is evident from the significantly smaller percent differences between the sum of single molecule volumes and fully geometry-optimized ion pairs, Table 5. These results indicate that the STREUSEL size metric is a viable option for assessing size-dependent ionic liquid properties using free-ion molecular calculations.

These studies reinforce the notion that there is not an ideal size metric for all chemical systems; rather, compatibility between size metric and chemical system is paramount. This is exemplified by Figures 21 and 22, where it is evident that the electric field, and resultant volume, depends on the proximity of the atoms within the molecule. When the proximity is changed, bonding changes as well, increasing the complexity of calculating size and necessitating electronic structure-based methods. And in order to properly compute the size of molecules, from Figure 33, we observe an exchange-correlation functional dependence – revealing that *ab initio* methods, MP3 and MP4, with a minimum triple-zeta basis set return geometries closest to CCSD-full. However, the more efficient functionals, B1LYP,

B3LYP, BHandH, BHandHLYP, and CAM-B3LYP, return geometries of adequate volume with respect to CCSD-full. It is ultimately the duty of the theorist to select a suitable functional for their system.

## CHAPTER IV

### CHEMICAL SIZE OF PORES

#### **Abstract**

Thus far, we have discussed the role of size in terms of the *volume* of **occupied space**. As demonstrated in Chapter 3, this of particular interest to atomic and molecular studies. Yet, the interactions between molecules and materials is also dependent on size. Consider the binding sites in pharmacology, or the role of porous materials in gas separation and storage. Indeed, void space properties (*i.e.* pore volumes and surface areas) are pivotal to our fundamental understanding of these processes and, for example, our abilities to predict ideal host-guest pairs. Within this chapter we discuss the expansion of the STREUSEL size calculation methodology to that of void spaces within porous materials, namely MOFs. Here, we examine the disadvantages of the current computational porous characterization techniques, and verify the performance of STREUSEL within this arena.

#### **Introduction**

Since their conception,<sup>(303)</sup> metal-organic frameworks (MOFs) have attracted practitioners from organic, inorganic, and materials disciplines,<sup>(304;305;306)</sup> each with a shared interest in physical properties afforded by mixing multitopic organic linkers and metal ions or clusters (secondary building units, SBUs, or nodes).<sup>(307;308)</sup> The combination of SBUs with the multitude of linkers has enabled a seemingly infinite landscape of materials with modular properties,<sup>(309)</sup> all featuring one commonality: crystallographically ordered void spaces.<sup>(310;311)</sup> Porosity in conjunction with functional MOF components catalyzed interest in these materials as atomically precise pores enable a series of heterogeneous



gas storage<sup>(15;16;17)</sup> and separation technologies<sup>(18;312)</sup> as well as access to extremely high loadings of catalytically active centers.<sup>(20;21;22;23)</sup> In more recent embodiments, exotic electronic structures have been discovered,<sup>(120;209;313)</sup> providing a foundation for applications in high surface area electrodes in electrochemical devices<sup>(314;315;316;317;318;319;320;321)</sup> and as ordered arrays of qubits for MOF-mediated quantum computing.<sup>(322;323;324)</sup> Clearly, their diverse composition and structure enable a wealth of possible applications.

Many of these applications depend on the accessibility of the pores; pore topology is largely determined by the shape, size, and composition of the linkers.<sup>(325;326)</sup> Of course, the node composition and topology also play a determining role in the structure,<sup>(308;327;328)</sup> but there are far fewer synthetic handles available to modify and create novel inorganic clusters. Thus, the prediction of MOF properties is well-suited to computation,<sup>(329)</sup> as we can rapidly construct a large family of MOFs using only the geometry of the SBUs and a nearly endless selection of linkers.<sup>(330)</sup> Indeed, one of the most elegant aspects of MOF chemistry is the ability to transmetallate<sup>(331;332;333;334;335)</sup> and geometrically substitute one linker for another of similar geometry<sup>(336;337;338)</sup> enabling a broad gamut of structurally related materials.<sup>(339)</sup> Such isoreticularity<sup>(340;341;342)</sup> is a cornerstone of the field<sup>(343;344;345)</sup> and has been a key focus for several years with notable successes (e.g., efficient absorption of water,<sup>(173;346;347;348)</sup> and as site isolated catalysts<sup>(349;350;351)</sup>).

The chemical and physical properties of a MOF are derived from the identity of its two building blocks: the metal center and organic linkages.<sup>(216;313;352;353)</sup> These two components generate the pore, which is the feature that imparts the macroscale material properties and functionality.<sup>(354)</sup>

The pore is thought to provide additional physical influence on properties such as site adsorptivity,<sup>(355)</sup> enantioselectivity,<sup>(356)</sup> and size selectivity<sup>(357;358)</sup> as functions of the pore volume, aperture, and composition. In such cases, a complete description of the pore aperture and/or cage created within may be necessary to explain intrapore reactivity. Such was the case for a borylation catalyst incorporated as the linker of a UiO-67-analogue.<sup>(359)</sup> The heterogenized system exhibited >99% chemoselectivity toward a monoborylated product, far exceeding the selectivity of its homogeneous counterpart.<sup>(357)</sup> Ultimately, this study concluded that selectivity of their catalytic reaction resulted from pore confinement restricting access to the diborylated product rather than local sterics or electronic interactions.<sup>(359)</sup>

The best structural characteristics describing the pore are the pore volume and surface area, which can be determined experimentally and computationally.<sup>(353;360)</sup> However, the experimental and computational methods use inert gas molecules to probe pore structure, yielding only the accessible surface area and neglecting the true pore topology, Figure 24.<sup>(232;360)</sup> Experimentally, Brunauer-Emmett-Teller (BET) models are used to derive surface area from adsorption-desorption isotherms and relies on multilayer surface coverage.<sup>(232;352;360)</sup> This is problematic because pore filling and formation of the monolayer and multilayer occur simultaneously.<sup>(232;360)</sup> Computational methods mimic experimental methods using a Grand Canonical Monte Carlo (GCMC) approach,<sup>(352;353;361)</sup> which is computationally expensive and relies on a rigid sphere approximations to depict the void space<sup>(362;363;364;365)</sup> (which, from Chapter 3, we know are not suitable for highly ionic materials, such as MOFs). From both the computational and experimental approaches, it is apparent that pore features with a radius of curvature less than

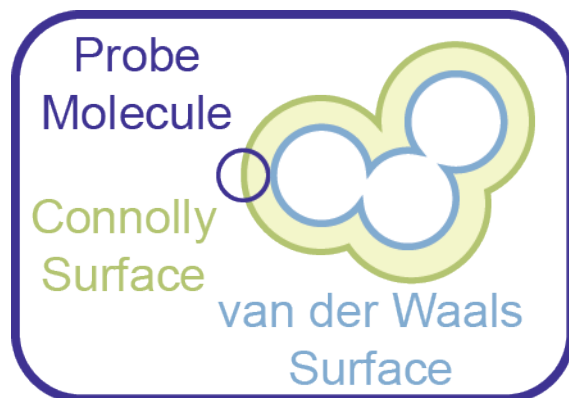


*Figure 24.* Connolly surface area lacks information. van der Waals surface area does not account for polarized bonds.

that of the gas molecule are neglected. Consequently, the resolution of the SA is limited by the radius of the chosen gas molecule.<sup>(360;366)</sup>

We can envision a method to calculate void space properties using STREUSEL, which would yield values that are independent of a probe gas molecule. We perform our solid-state DFT calculations using the popular software VASP; to accommodate this, STREUSEL has added functionalities that enable it to process VASP output files and calculate void space properties. Thus, we obtain a more precise image of the pore volume and surface area.

## Results and Discussion

**Pore Volumes and Surface Areas.** Since the logic of the STREUSEL size determination algorithm discussed in Chapter 3 relies only on the electrostatic potential obtained from DFT calculations, the presented electric field cutoff holds for solid-state calculations. To verify our approach we generate electrostatic potential maps from single-point calculations for the MOFs contained within the CoRE MOF database,<sup>(367)</sup> and calculate the STREUSEL pore volumes and surface areas.<sup>(70)</sup> In order to verify that the values we obtain from the electric field are realistic, we compare our calculated pore volumes with those obtained

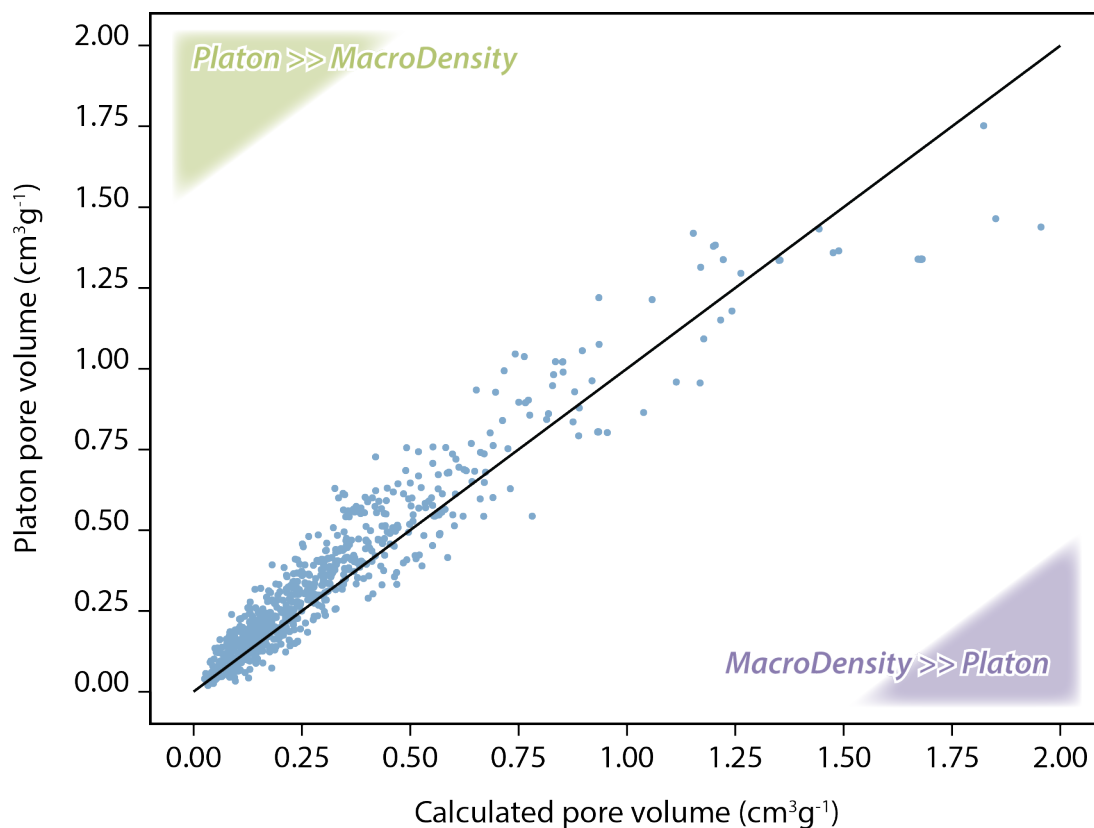


*Figure 25.* There is good agreement between the pore volumes obtained using Platon and STREUSEL. Both void space calculation metrics are performed using pristine structures. The solid black line represents the values where Platon = STREUSEL.

using the PLATON software, which is the industry standard for void space calculations,<sup>(362;363;364;365)</sup> Figure 25. Indeed, there is good agreement between the pore volumes obtained using Platon and those obtained using STREUSEL, suggesting that the STREUSEL methodology is a valid approach.

With the knowledge that STREUSEL yields realistic pore volumes, we compare these values with experimental measurements of pore volume and surface area for a dataset of 100 MOFs, Figures 26 and 27. Unsurprisingly, there is less agreement between experimental and STREUSEL pore volumes than seen with the Platon pore volumes, Figure 25; this is likely because the theoretical values

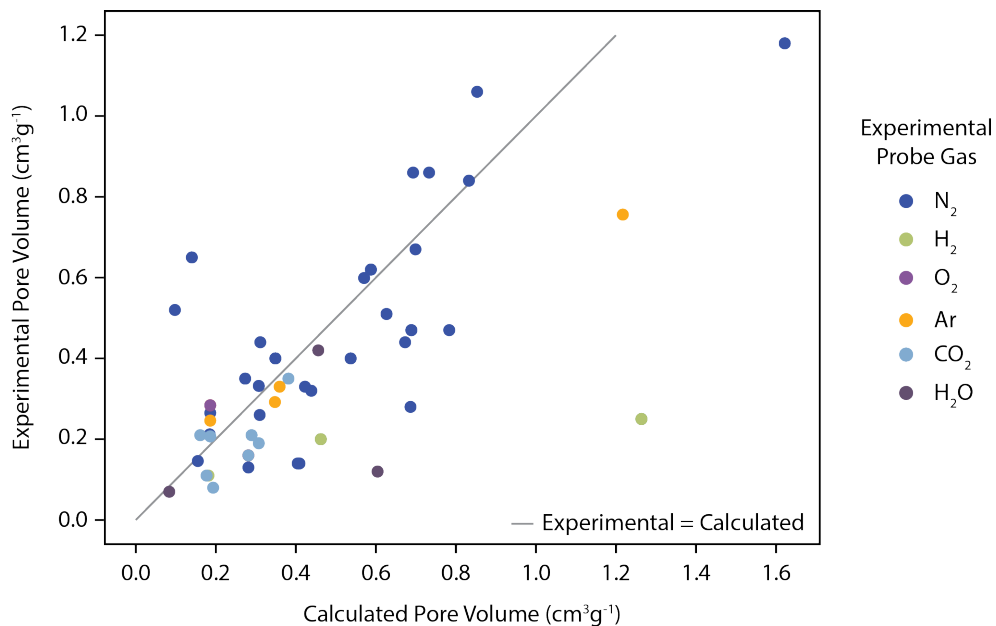


*Figure 26.* Comparison of experimental pore volumes and STREUSEL pore volumes for a series of MOFs. Data points are colored according to the probe gas molecules used in the experimental measurement. there appears to be no correlation with the experimental probe gas; this is likely due to unknown differences in sample preparation and measurement conditions. The full dataset with corresponding references is presented in Appendix B.

are obtained using pristine models, which is not representative of an experimental sample.<sup>(2)</sup> This is further reinforced by the overestimation of surface area by STREUSEL, Figure 27. Here, we observe that experimental samples are far less porous than their theoretical counterparts. A similar overestimation of pore volume is also observed. Indeed, this is expected; the STREUSEL methodology accesses topological features unobtainable by methods relying on gas probe molecules. Logically, additional topological features would increase calculated pore volumes and surface areas relative to experimental measurements.

In addition to the unavoidable presence of defects,<sup>(233)</sup> experimental preparation is known to have large impacts on measured void characteristics.<sup>(368)</sup> For example, Kaye *et al.* observed a  $1500 \text{ m}^2\text{g}^{-1}$  decrease in measured surface area

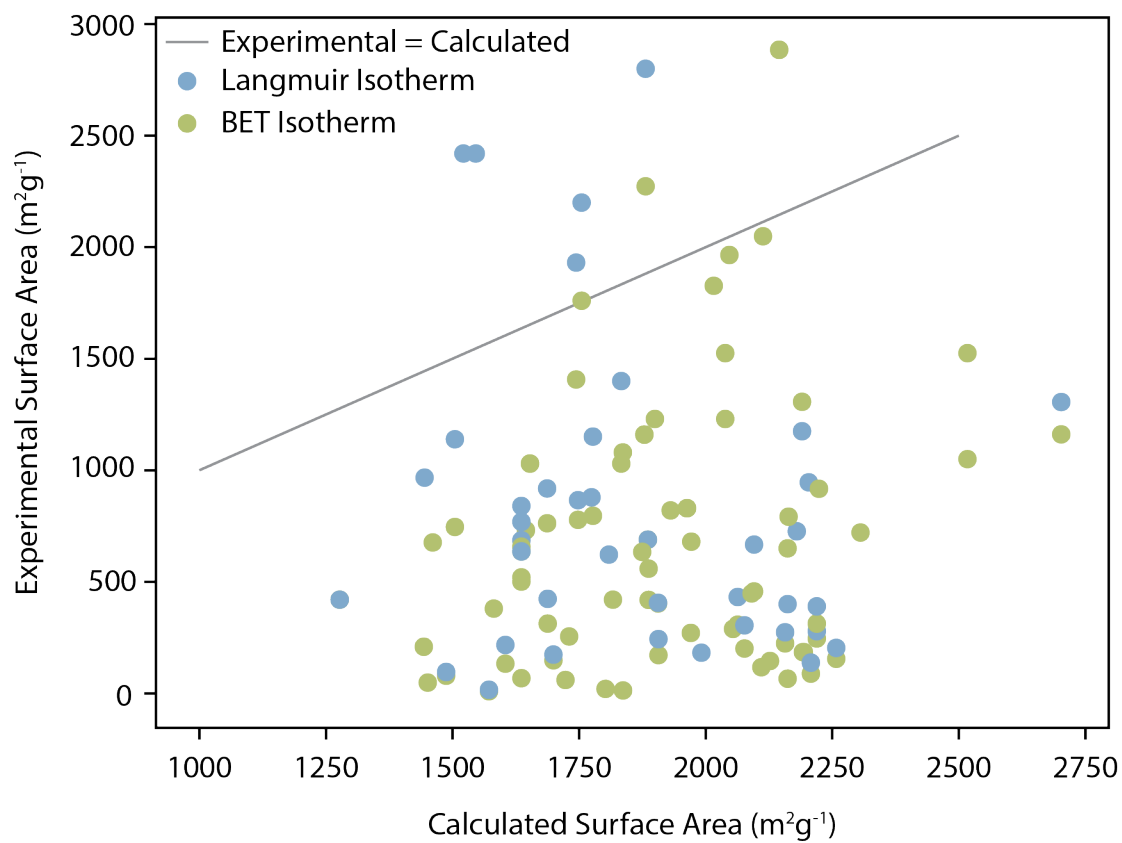


*Figure 27.* Comparison of experimental surface areas calculated via BET (green) and Langmuir (blue) isotherms and STREUSEL surface areas for a series of MOFs.

for MOF-5 prepared in air vs. air-free.<sup>(368)</sup> Consider eight published, experimental surface areas for MOF-5, Figure 28. While each value is valid, the large range in measured surface areas is likely due to three competing factors:<sup>(17;369)</sup>

1. Collapsed pores within the samples – This is likely due to the vacuous conditions that are required by pore volume and surface area measurements.
2. Occluded pores within samples – This is likely due to leftover reagent molecules that were not fully washed away after synthesis.
3. Linker and/or metal center vacancies – This is due to the entropic favorability of defect formation.

These factors have predictable effects on measured pore volumes – namely, the presence of occluded and collapsed pores will result in an artificial decrease in measured pore volume, while vacancies will result in an artificial increase. Effects on surface area are far more complex. While collapsed pores will understandably result in a decreased surface area, the effect of occluded pores notably depends on the pore aperture:pore surface area ratio. Abstractly, there may exist a topology whose pore aperture area is larger than the surface area of the chemical motif within the pore. In this instance, occluded pores would result in an artificially larger measured surface area. The effect of linker vacancies will be discussed in detail in the following section. Comfortingly, the STREUSEL surface area falls within the range of published surface areas for MOF-5.

**Imaging Linker Vacancies using the Electric Field.** Vacancies occur as either missing linkers or metal clusters, as well as single atom omissions from the inorganic clusters.<sup>(375)</sup> The elucidation of experimental vacancies is extremely challenging in MOFs and other solids, often requiring a potpourri of

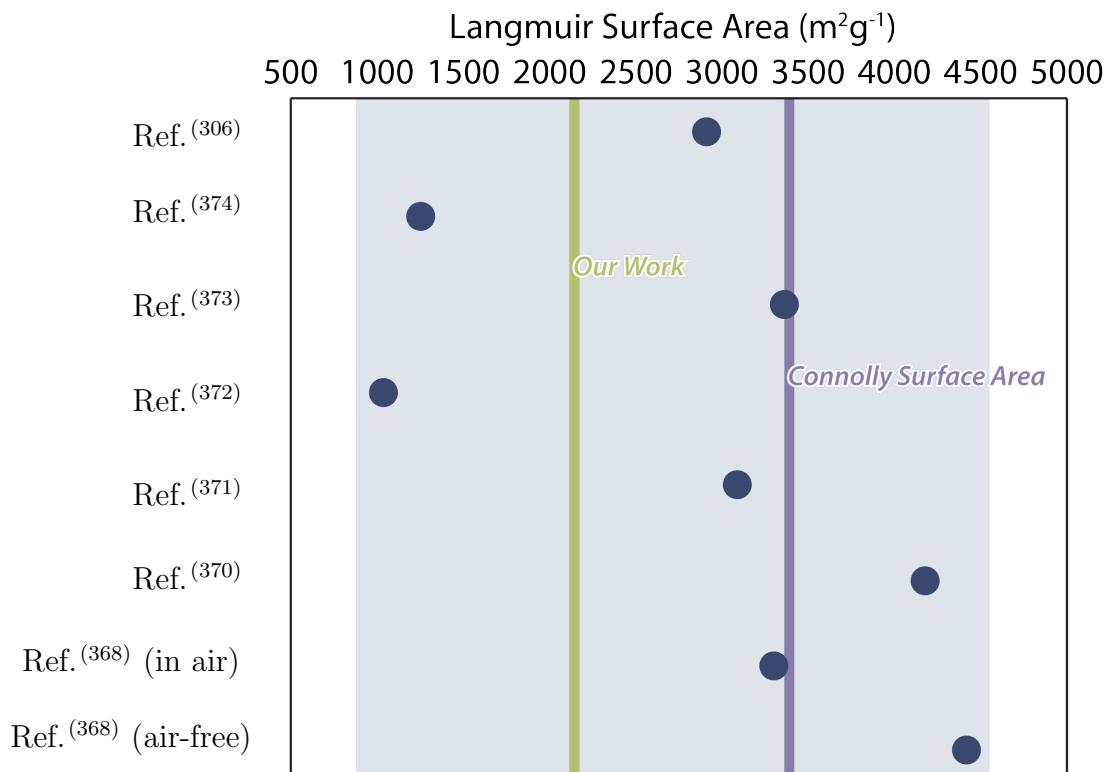


Figure 28. Comparison between published Langmuir surface areas for experimental samples of MOF-5, the Connolly surface area (purple), and the STREUSEL surface area (green).



experimental methods (PXRD, EXAFS, NMR, IR, etc.) to extract even an average defect concentration per node.<sup>(376;377;378)</sup> As a result, we are still learning about their formation in extremely well-studied materials and only have a rudimentary understanding of their formation.<sup>(379;380;381;382)</sup>

To completely characterize a defect in MOFs, a combined theory and experimental approach is often required. For example, the identity of anionic species coordinated to the node at a linker vacancy in UiO-66 and -67 was obtained by IR and NMR experiments; the catalytic mechanism occurring at active sites defined by these defects was then studied with an appropriate cluster model to assess reagent adsorption in the presence and absence of linkers.<sup>(383)</sup> More advanced experimental methods, such as diffuse scattering, electron microscopy, transmission electron microscopy, and electron crystallography, have also been paired with theory to refine structural motifs of defects.<sup>(384)(385)</sup>

Periodic models, however, still face challenges for defective systems because of the cost associated with forming a unit cell sufficiently large enough to mitigate artificial defect ordering.<sup>(386)</sup> Furthermore, vacancies are realistically either anionic or cationic and often compensated by an adventitious counterion, mandating some charge passivation routine.<sup>(387)</sup> In experiment, these ions originate from the salts or solvents used in the synthesis, and these salts can be used to inform model construction.<sup>(388)</sup>

Modulators can be used to deliberately install linker vacancies as they compete with the multitopic linker to bind to the metal node either during synthesis or postsynthetic modification.<sup>(240;377;389)</sup> Cluster vacancies may be targeted by achieving multiple linker vacancies; this causes either an absence of a linker for the cluster to bind to or the stability of an already bound cluster to

be compromised.<sup>(390)</sup> Linker vacancy concentration may be tuned using a variety of synthetic conditions ranging from modulator concentration and acidity<sup>(391)</sup> to solvent selection.<sup>(392;393)</sup> Selectively altering linker vacancy concentration not only enables cluster vacancy formation but also affords defect engineering, which can be used to intentionally alter macroscopic properties. For example, increased modulator concentration during synthesis correlated to increased gas uptake in defective UiO-66 due to additional missing linkers, as experimentally demonstrated by Wu et al. with N<sub>2</sub> uptake isotherms.<sup>(394)</sup>

Most computational defect studies have been performed on the UiO-series of materials, as they are known to feature high concentrations of defects. Here, we will use UiO-66 as a model to explore the effects of modulators on calculated pore volumes and surface areas, Figure 29.

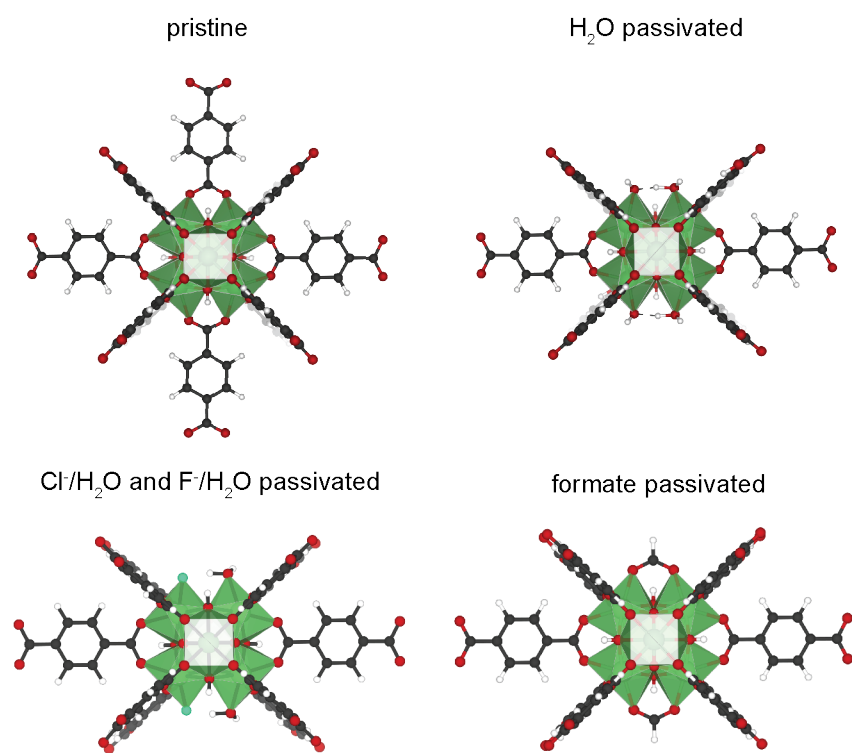


*Figure 29.* Three passivated models of UiO-66 are examined in this study; H<sub>2</sub>O, Cl<sup>-</sup>/H<sub>2</sub>O, F<sup>-</sup>/H<sub>2</sub>O, and formate.

CHAPTER V  
COVALENT BRIDGE INTERSTITIALS AS A ROUTE TOWARDS  
CONDUCTIVE FRAMEWORKS

**Abstract**

The high porosity, extended connectivity, and tunability of metal-organic frameworks (MOFs) makes them ideal candidates for the development of electrocatalysts, charge storage materials, and chemiresistive sensors. However, the highly ionic nature of the inorganic-organic interface inhibits the realization of high electrical conductivity thereby limiting their utility for these applications. In this project, we explore a retrofitting strategy to post-synthetically install redox-active interstitials that covalently interconnect MOF linkers as one avenue towards augmenting the electrical properties of these otherwise insulating frameworks. The formation of retrofitted organic linkages within a given scaffold is governed by a statistical distribution of the orientation of linkable units as demonstrated by an atomic level simulation examining the kinetics of wire formation and the resulting distribution within an extended unit cell of MOF-5. Periodic DFT calculations quantify the conductive capacity of the newly formed charge transport pathways. Examining other common scaffolds, we find that the macroscopic topology of post-synthetically installed wires (*i.e.* extended wires vs. conductive loops) formed through new covalent bonds, and their resultant capacity for electronic conduction, is dictated by the effect of MOF symmetry on the statistical distribution of linker orientations. By combining statistical models of wire formation with electronic structure theory applied to periodic models of the retrofitted MOFs we show that post-synthetic formation of pseudo-polymeric wires is a promising strategy to instill electrical conductivity in MOF scaffolds.

## Introduction

Tunable materials design is poised to solve a series of device performance challenges within the electrochemical device arena.<sup>(395;396)</sup> One of the material properties pinnacle to electrochemical device performance is surface area;<sup>(397)</sup> increased surface area is responsible for increased number of active sites in electrocatalysts,<sup>(398)</sup> increased capacitance in the case of supercapacitors,<sup>(399)</sup> increased rate of electrochromic switching,<sup>(400;401)</sup> and improved performance of resistivity-based chemical sensors<sup>(402)</sup> within the energy storage device realm,<sup>5</sup> among other benefits.<sup>(403;404;405)</sup> Currently, the leading class of materials for high surface area are metal-organic frameworks (MOFs).<sup>(15;406)</sup> The simple building block construction (metal nodes connected by organic linkers) further offers additional routes towards bulk property tuning via post-synthetic modification<sup>(407;408;409;410;411)</sup> and retrofitting.<sup>(412;413;414)</sup> Despite the compositional diversity of MOFs afforded by the simple construction, the majority of scaffolds within this class of nanoporous, crystalline materials are insulating.<sup>(217;415;416)</sup> This limits their application in the electrochemical industry, which would otherwise benefit from the large surface areas offered by MOFs.<sup>(217;313)</sup>

The insulating nature of MOFs can, in part, be attributed to their construction from redox-inactive organic linkers and closed shell metal centers.<sup>(415;416)</sup> Yet, due to the tunable nature of MOFs, redox chemistry may be promoted within these scaffolds by introducing redox-active components in several ways;<sup>(415;416)</sup> i) during synthesis,<sup>(417;418)</sup> ii) via post-synthetic modification,<sup>(419;420;421;422)</sup> or iii) as guest molecules within the pores.<sup>(404;423;424;425)</sup> Indeed redox-activity in MOFs has been shown to enhance gas uptake and

binding,<sup>(417)</sup> engender electrical conductivity,<sup>(402)</sup> as well as exhibit reversible electrochromism.<sup>(401)</sup>

Of the varying methods of inducing redox activity in MOFs,<sup>(416)</sup> this work focuses on installing redox-active covalent bridging motifs between aromatic linkers. This is similar to the host-guest interaction of HKUST-1 infiltrated with 7,7,8,8-tetracyanoquinodimethane (TCNQ) ( $0.07 \text{ S cm}^{-1}$ ), which yielded a million-fold increase in electrical conductivity over pristine HKUST-1 ( $10^{-8} \text{ S cm}^{-1}$ ).<sup>(423)</sup> TCNQ bridges Cu(II) paddlewheels, enabling improved electronic coupling between the these dimeric Cu subunits. In this way, Allendorf *et al.* not only render and otherwise insulating MOF conductive, but coordination between TCNQ and the Cu(II) paddlewheels results in a continuous charge transport path throughout the scaffold.

The TCNQ-Cu(II) paddlewheel coordination complexes within the scaffold are inherently composed of repeating subunits throughout the material. In this way, we can consider the TCNQ-Cu(II) subunit chain a monomer within the scaffold. This not unheard-of in the MOF community. Indeed, MOF-polymer hybrid materials have been synthesized and are advantageous for a range of applications,<sup>(426;427)</sup> including; improving the handling and implementation of the hybrid material over MOFs,<sup>(428)</sup> and improved gas storage a separation capabilities.<sup>(429)</sup> For instance, tetracyanoquinodimethane (TCNQ) is a tetratopic redox active molecule that fortuitously can bridge adjacent Cu-paddlewheels in  $\text{Cu}_3(\text{BTC})_2$ . The extent of bridging was shown to cause an increase in electrical conductivity (6 orders of magnitude, up to  $0.07 \text{ S cm}^{-1}$ ).<sup>(423)</sup> Comparing periodic models of the pristine framework and with the TCNQ interstitial showed strong binding ( $84 \text{ kJ mol}^{-1}$ ) and cluster models consisting of two benzoate-capped

paddlewheels saturated with water molecules and bridged by TCNQ, showed new conduction band states localized on the TCNQ molecule.<sup>(423;430)</sup> It was thus reasoned that thermally promoted charge transfer between the framework and guest molecule enhanced charge mobility. Later, scanning electron microscopy and porosimetry supported the bridging arrangement of TCNQ proposed by theory.<sup>(431)</sup>

Nonnative organic linkers bridging metal sites also impacted charge mobility in  $\text{Ni}_3(\text{HITP})_2$ .<sup>(412)</sup> Band structures, calculated using the B3LYP hybrid functional and the triple- $\zeta$  basis set, pob-TZVP, were constructed for different forms of  $\text{Ni}_3(\text{HITP})_2$  including a variant with layers separated by 4,4'-bipyridine bridging the nickel sites and pristine  $\text{Ni}_3(\text{HITP})_2$  with the same interlayer spacing as the bridged derivative. Bulk  $\text{Ni}_3(\text{HITP})_2$  is found to be metallic, but the band gap widens with increasing interlayer separation, and upon inclusion of the bipyridine interstitial band dispersion is seen to decrease, effective mass values increase, and the band gap widens;  $\text{Ni}_3(\text{HITP})_2$  is rendered a semiconductor. The authors note that square-planar Ni(II) bound to four nitrogen atoms results in filled  $d_{z^2}$  orbitals, which do not readily bond to additional out of plane organic linkers. Potential energy curves for pyridine coordination to this square planar motif showed the hypothetical semiconducting structure was unlikely to form, however  $\text{Cr}_3(\text{HITP})_2$  with bridging 4,4'-bipyridine may be an alternative, stable structure.

We present and validate a post-synthetic avenue towards electrically conductive MOFs by including redox active covalent bridging motifs between linkers, leading to bonded, redox non-innocent linkers that form a pseudo-polymer within the scaffold. Electronic properties of MOF-5-covalent-bridge pairs are assessed using periodic density functional theory (DFT) calculations. Wire formation pathways are examined using python-driven atomistic simulations.

Macroscopic wire conformations are investigated using an abstract statistical model.

## Results and Discussion

The tractability of this approach is established using MOF-5 ( $\text{Zn}_4\text{O}(\text{BDC})_3$  ( $\text{BDC} = 1,4\text{-benzenedicarboxylate}$ ))<sup>(17)</sup> for three main reasons: i) the simple 6-2 connected net, which results in cubic pores that are readily abstracted for the statistical model, ii) demonstrated propensity for redox reactivity,<sup>(420)</sup> and iii) prior evidence of linker crosslinking.<sup>(432;433)</sup>

Selection of the covalent bridging motif invited two design considerations; i) Fermi level shift, and ii) geometric constraints. Installation of the covalent bridging motif introduces additional states, resulting in a shift to the Fermi level; n-type interstitials shifts the bands up because additional electrons are introduced to the system, while p-type shifts bands down due to the inclusion of holes. Considering the mid-gap states, we focus our search on p-type interstitial bridging motifs, whose downward shift of the bands accommodate the additional states.

Taking into consideration the octahedral configuration of the inorganic MOF-5 node, we examine covalent bridging motifs that may fit within the 5.21 Å and 9.90 Å gaps, Figure 30. This leads us to a series monomers from redox-active electrically conductive organic polymers; polyphenylene sulfide (PPS),<sup>(434)</sup> polyaniline (PANI),<sup>(435;436)</sup> poly(p-phenylene vinylene) (PPV),<sup>(437)</sup> and two thienothiophene derivatives (TT1 and TT2).<sup>(438;439;440)</sup> For example, PANI-based electrode materials boast high specific capacitance ( $700 \text{ F g}^{-1}$ ),<sup>(436)</sup> as well as several accessible oxidation states.<sup>(441)</sup> The protonated form of polyaniline is electrically conductive,<sup>(435)</sup> featuring values on the order of  $2 - 10 \text{ S cm}^{-1}$  for pressed pellets.<sup>(442)</sup> Thus, we install the reduced form of PANI in MOF-5. In



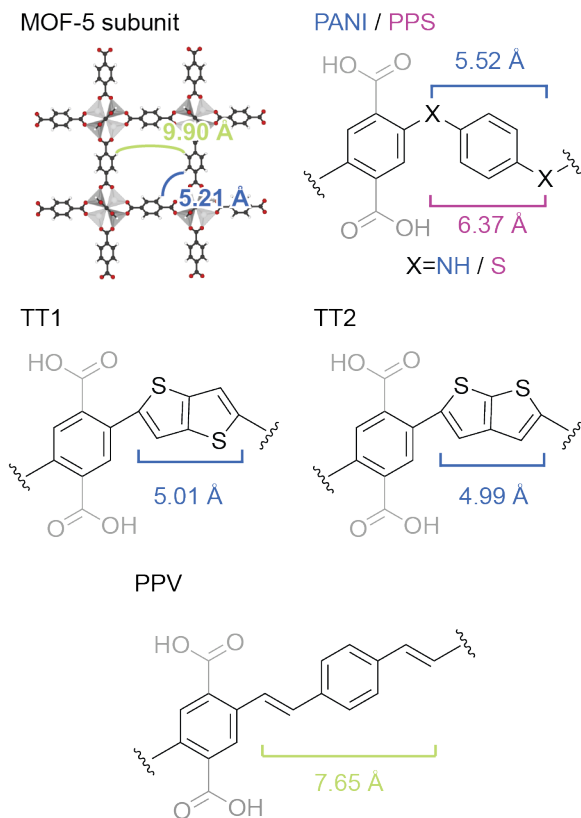


*Figure 30.* The two examined positions for the covalent bridging motifs are labelled within the MOF-5 subunit. Five covalent bridging motifs were examined – polyaniline (PANI), polyphenylene sulfide (PPS), two thienothiophene derivatives (TT1 and TT2), and poly(p-phenylene vinylene) (PPV). Covalent bridging motif lengths are displayed.

addition to, Thienothiophene derivative TT1 featuring aromatic caps offer charge mobilities on the order of  $0.1 \text{ cm}^2 (\text{V s})^{-1}$ .<sup>(443)</sup>

Three modeling approaches are used to assess the efficacy of each MOF-bridge pair; i) infinite wire models where we examine the bridging motif conformation that infinitely spans reciprocal space to obtain the ideal electronic properties, ii) atomistic simulations of bulk wire formation where we examine the subtle changes in scaffold geometry upon iterative inclusion of covalent bridges within a bulk model, and iii) statistical models where we assess the macroscopic wire topology yielded by each crystallographic configuration.

**Infinite wire models.** In order to identify the validity of electrical conductivity induced by covalently-bridged interstitials, we probe the electronic structure and properties of the ideal linear wire configuration within the MOF-5 scaffold for five bridging motifs: polyphenylene sulfide (MOF-5-PPS), poly(*p*-phenylene vinylene) (MOF-5-PPV), polyaniline (MOF-5-PANI), and two thienothiophene derivatives (MOF-5-TT1 and MOF-5-TT2). Calculation details provided in the following subsection. Results are summarized in Table 6.

**Calculation Details.** Density functional theory (DFT) was used to evaluate the structural and electronic properties of the pristine MOF-5 and MOF-5 scaffold with five bridging motifs: polyphenylene sulfide (MOF-5-PPS), poly(*p*-phenylene vinylene) (MOF-5-PPV), polyaniline (MOF-5-PANI), and two thienothiophene derivatives (MOF-5-TT1 and MOF-5-TT2).

Structural relaxation of pristine MOF-5 was performed using the PBESol functional,<sup>(141)</sup> as implemented in the Vienna ab initio Software Package (VASP).<sup>(73;74;75;76)</sup> The wavefunctions of the valence electrons were expanded with plane-waves with a cutoff of 500.00 eV; core electrons were treated with the projector augmented wave theory.<sup>(2)</sup> The total energy was converged within  $10^{-5}$  eV and forces to  $0.005 \text{ eV } \text{\AA}^{-1}$ ; the Brillouin-zone was integrated over a well converged and symmetrized  $2 \times 2 \times 2$   $k$ -point mesh.

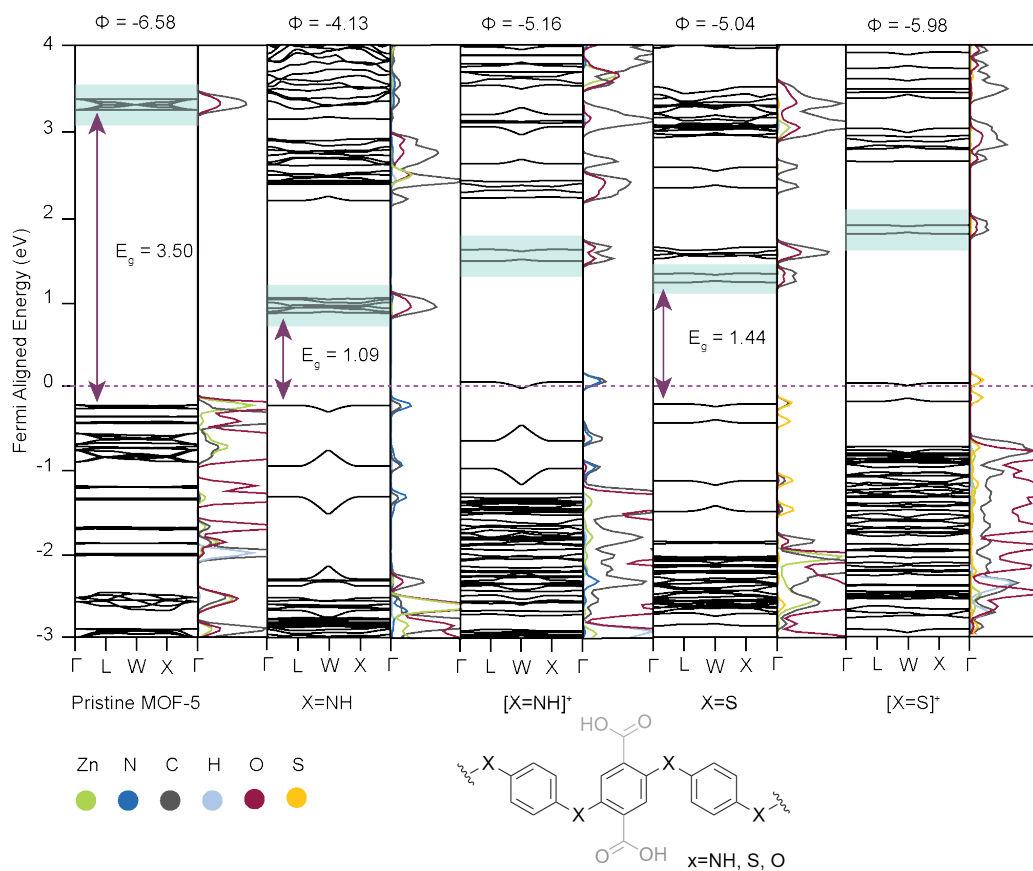
The MOF-5-X ( $X = \text{PPS, PANI, PPV, TT1, TT2}$ ) models were generated by manually inserting the covalent bridging motifs within the fully-optimized pristine MOF-5 structure such that they generate an infinite wire across the periodic boundary conditions. The resulting structures were optimized to the same criteria described above, and symmetry was not enforced.

Table 6. Comparison of electronic properties for the infinite wire models listed in order of decreasing band dispersion (meV).

| Model      | Band Gap (eV) | Dispersion (meV) | Work Function |
|------------|---------------|------------------|---------------|
| MOF-5-PPV  | 1.26          | 313.5            | -5.26         |
| MOF-5-PANI | 1.09          | 75.5             | -4.13         |
| MOF-5-TT1  | 2.07          | 69.0             | -5.28         |
| MOF-5-TT2  | 2.02          | 61.1             | -5.15         |
| MOF-5-PPS  | 1.44          | 29.6             | -5.98         |
| MOF-5      | 3.50          |                  | -6.58         |

Of the five models, MOF-5-PPV and MOF-5-PANI exhibited the smallest band gaps, 1.26 eV and 1.09 eV, respectively, and largest band dispersion, 313.5 meV and 75.5 meV, respectively Figure 2. Electronic band structures and density of states (DOS) for MOF-5-PPS, MOF-5-TT1, and MOF-5-TT2 are presented in the Supporting Information Figures 31 and 32. The pristine MOF-5 band structure is aligned to the background potential,<sup>(444)</sup> while the MOF-5-PPV and MOF-5-PANI band structures are aligned to the pristine MOF-5 conduction band (CB), highlighted in gray. Interestingly, the frontier bands of MOF-5-PPV are contributed by the PPV interstitial, while only the MOF-5-PANI valence band (VB) is located on the PANI interstitial. This is demonstrated by the atomic contributions to the VB in the DOS, Figure 33.

Introducing mid-gap states alters the atomic contribution to the band edges. For example, MOF-5 VB is localized on the inorganic and organic components of the scaffold, while the CB is localized solely on the organic linker (BDC). The band edges of MOF-5-PPV are localized on the PPV interstitial, suggesting charge transfer would occur within the covalent bridge upon photoexcitation.<sup>(189)</sup> The VB of the MOF-5-PANI model is localized on the PPS interstitial, while the CB is localized on the BDC of the MOF-5 scaffold. This suggests upon photexcitation charge-transfer would occur between the linker and covalent bridge.<sup>(189)</sup>



*Figure 31.* The Fermi-aligned band structure of pristine MOF-5 features flat bands with a large band gap (3.50 eV). MOF-5 models featuring polyaniline (MOF-5-PANI) and polyphenylene sulfide (MOF-5-PPS) interstitials reveal increased band dispersion and smaller band gaps than their pristine counterpart. Oxidized models of MOF-5-PANI and MOF-5-PPS are also presented and feature bands that cross the Fermi level.

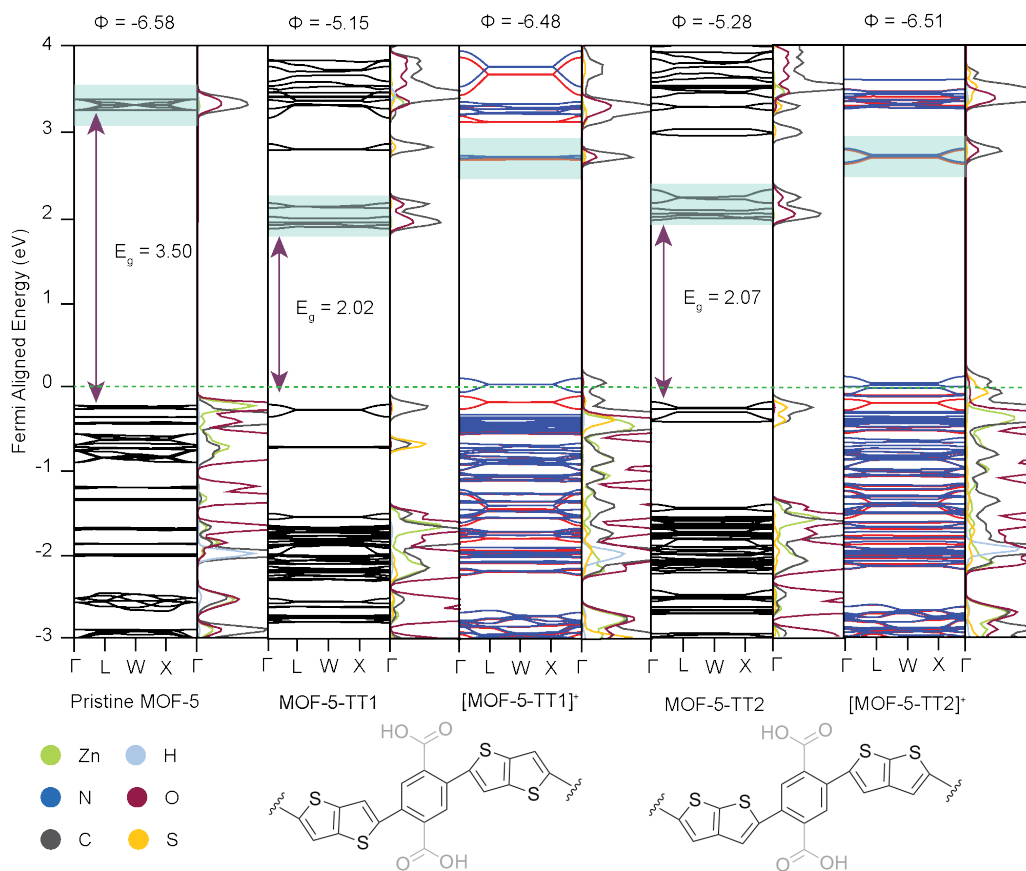


*Figure 32.* The Fermi-aligned band structure of pristine MOF-5 features flat bands with a large band gap (3.50 eV). MOF-5 models featuring two thienothiophene derivatives (MOF-5-TT1, and MOF-5-TT2) reveal increased band dispersion and smaller band gaps than their pristine counterpart. Spin-polarized electronic band structures of the oxidized models of MOF-5-TT1 and MOF-5-TT2 are also presented and feature bands that cross the Fermi level. Spins are separated by band color within the oxidized models.

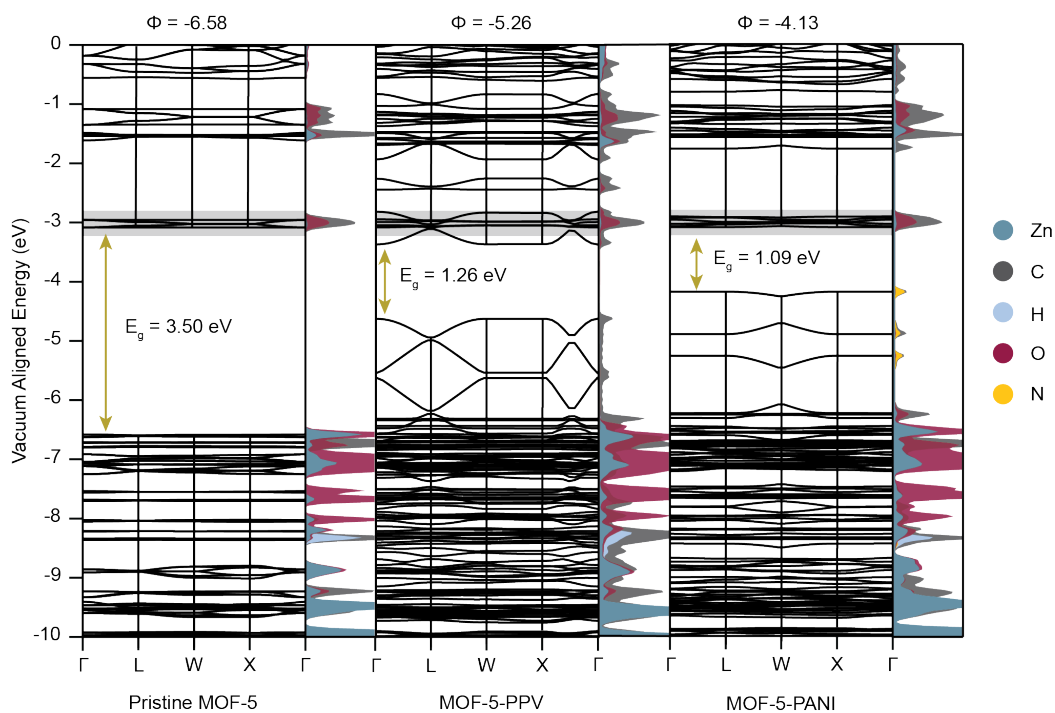


*Figure 33.* The vacuum-aligned band structure of pristine MOF-5 features flat bands with a large band gap (3.50 eV). MOF-5 models featuring polyaniline (MOF-5-PANI) and poly(p-phenylene vinylene) (MOF-5-PPV) interstitials reveal increased band dispersion and smaller band gaps than their pristine counterpart.

Upon inclusion of the interstitials, there is an increase in band dispersion (or band width), indicating more mobile charge carriers,<sup>(2)</sup> Table 6. Band dispersions are recovered using temperature-independent DFT calculations; band dispersions less than  $kT$  are considered flat because they are lost to thermal smearing. At standard-state conditions,  $kT = 25.7$  meV. Thus, the low band dispersion (29.6 meV) of the MOF-5-PPS model, may not be a factor in experimental observables at room temperature.

The band edges of each model are localized on different components of the scaffold. Notably, the wired models feature organic VB, while the VB of the pristine MOF-5 model is localized on the Zn node. Thus, inclusion of the p-type interstitials bypasses the insulating inorganic node of the MOF scaffold; this has been shown to be beneficial in photocatalytic systems.<sup>(189)</sup>

The infinite wire models reveal the ideal electronic properties. Thus, we use an atomistic simulation to examine the necessary, minute conformational changes upon covalent bridge insertion; in this way, we examine the effect of wire formation on the MOF-5 scaffold.

**Bulk wire formation simulations.** Inserting a series of kinetically-directed covalent bridges within a MOF scaffold breaks the symmetry of the crystalline framework.<sup>(445;446)</sup> Moreover, linkers may need to rotate to accommodate additional covalent bridges, which is difficult to capture within the infinite wire models – an inherently static picture. We assess the resulting spatial implications using an atomistic wire formation simulation; code is available on GitHub.<sup>(447)</sup> The employed model is comprised of a 3x3x3 supercell of MOF-5 consisting of dichloroterephthalic acid linkages in two configurations (2,5-dichloroterephthalic acid, and 3,6-dichloroterephthalic acid). The initial

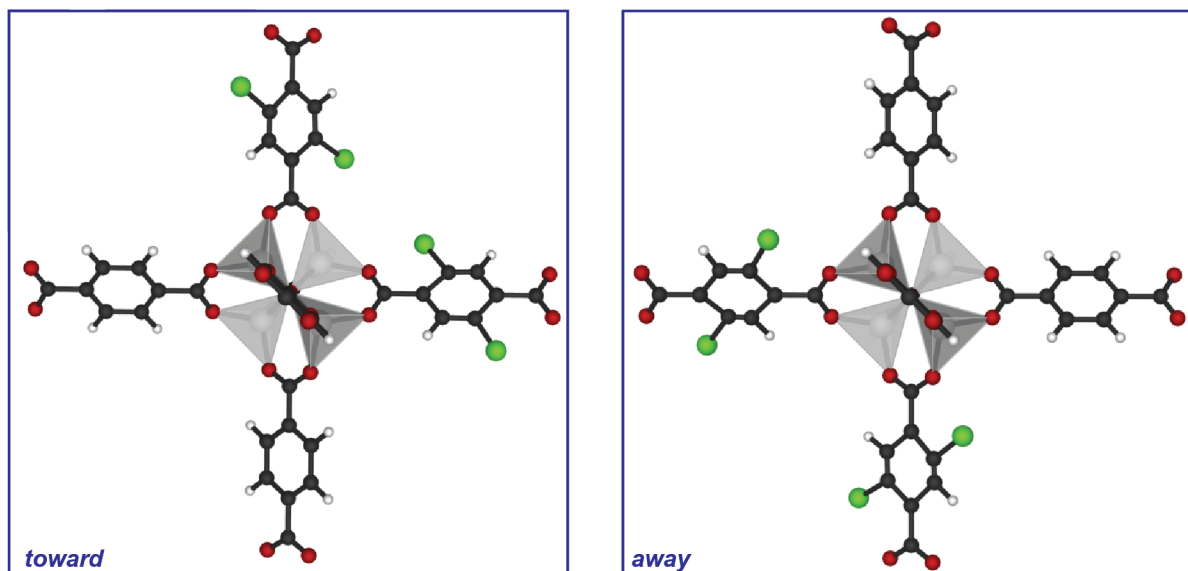


Figure 34. Two SH group orientations were sampled to determine the degree of linker rotational freedom; 1) toward, in which the SH groups of adjacent linkers point toward each other, and 2) away, in which the Cl groups of adjacent linkers point away from one another.

conformation of the dichloroterephthalic acid linkers is determined by sampling a Boltzmann distribution, described in the following subsection.

*Determining the degree of linker rotational freedom.* The orientational favorability of the BDC linkers within the pristine MOF-5 scaffold were determined using periodic DFT calculations. To assess the rotational restriction between adjacent 1,4-benzenedicarboxylate (BDC) linkers within the pristine MOF-5 primitive cell, the adjacent BDC linkers were thiolated, yielding 2,5-dithiol-1,4-benzenedicarboxylate linkers. Two models were constructed featuring the chloro groups pointed toward and away from each other, Figure 34, simulating the extrema of the rotational positions each linker samples.

Structural relaxation of the chlorinated MOF-5 models were performed using the PBESol functional,<sup>1</sup> as implemented in the Vienna ab initio Software Package (VASP).<sup>(73;74;75;76)</sup> The wavefunctions of the valence electrons were expanded



with plane-waves with a cutoff of 500.00 eV; core electrons were treated with the projector augmented wave theory.<sup>(2)</sup> The total energy was converged within  $10^{-5}$  eV and forces to  $0.005 \text{ eV } \text{\AA}^{-1}$ ; the Brillouin-zone was integrated over a well converged and symmetrized  $2 \times 2 \times 2$   $k$ -point mesh.

The absolute difference between the total energy for each optimized model ( $E_{diff}$ ) is calculated,

$$E_{diff} = |E_{away} - E_{toward}|^2 \quad (5.1)$$

and compared with  $kT$ , the Boltzmann distribution at the operating temperature (0.025 eV at standard state conditions), a viable assessment of the relevance for energy differences.<sup>(2)</sup>

In the case of the MOF-5 model, an energy difference of **INSERT** was obtained. Since this is less than 0.025 eV, we assume no favorability for linker orientation, and sample an unbiased random Boltzmann distribution of linker orientations for the atomistic simulation and general statistical model.

The atomistic wire formation simulation is composed of three iterative algorithmic steps; i) initialize each linker with a dichloroterephthalic acid configuration informed by sampling the Boltzmann distribution, ii) freeze the Cl atoms that are pointed toward each other within the model cell, and iii) reorient the free dichloroterephthalic acid linkers. These steps are repeated until no additional wires may be formed. Finally, the covalent bridging motifs are inserted between connected Cl atoms; the linkers of the MOF-5 scaffolds are rotated to accommodate the covalent bridging motifs.

Owing to the spatial separation and rotational freedom of the linkers in the octahedral, 6-2 connected net, we observe a preference for short ( $< 4$  subunits) linear wires across 100 wire formation simulations, Figure 35a. Only one of the 100

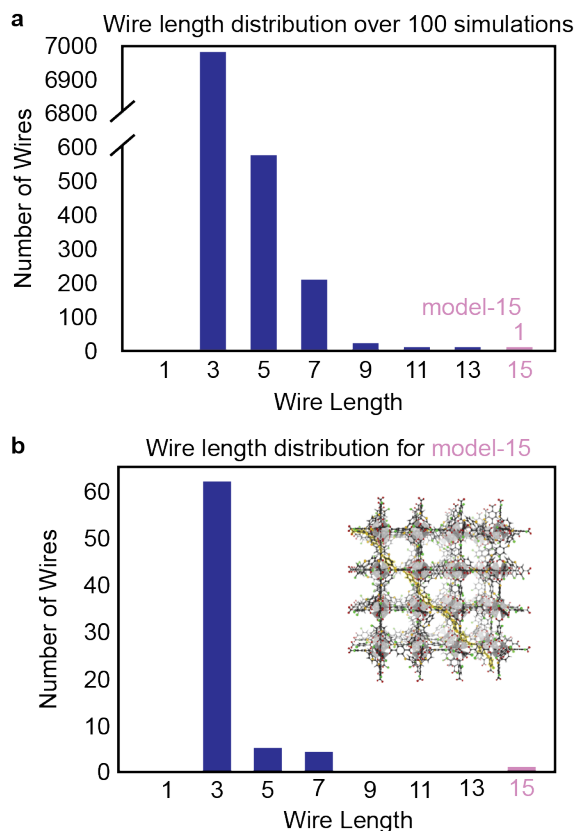


*Figure 35. a* The bulk wire length distribution totaled over 100 simulations. One run resulted in a wire length of 15 units, “model-15.” *b* The bulk wire length distribution for model-15. The MOF-5 depiction of model-15 with the longest wire highlighted in yellow.

wire formation simulations resulted in a wire that spans the width of the 3x3x3 supercell (“model-15”), Figure 35b. Unsurprisingly, the wire length distribution of model-15 mirrors that of the 100 simulations. Ultimately, the rotational freedom and spatial separation of the organic linkages afforded by the 6-2 net topology of MOF-5 results in only short, linear wires throughout the supercell.

While larger than the infinite wire models, the 3x3x3 model is not sufficient enough to examine the bulk wire conformation. Thus, we use a generalized statistical model and algorithm to probe bulk wire conformations within much larger (*e.g.* 50x50x50) cells.

**Generalized statistical model.** The macroscopic wire morphology is broadly directed by the rotational freedom of the linkers and the connectivity of the crystallographic net. To identify the exact implications of these contributing material features, we designed a statistical model to simulate wire growth and assess bulk wire conformation. Here, we describe the statistical model via the MOF-5 wired examples examined in this work; the code used to run the statistical model is available on GitHub.<sup>(447)</sup>

MOF-5 is described by a 6-2 connected net; the inorganic node is connected to six linkers, each of which only connect with two inorganic nodes. This net is decomposed into a tensor where each tensor element represents a different component of the MOF topology (i.e. metal, linker, pore), Figure 36a. The linker orientations are sampled from a weighted Boltzmann distribution. In this way, the linker orientation is directed by the degree of rotational freedom specific to the MOF described in the net. The degree of linker rotational freedom is obtained using the methodology described above.

There are two main algorithmic steps to the wire formation simulation, Figure 36b; i) sample Boltzmann distribution to determine linker orientations, ii) identify paths within the model. Importantly, once a linker is determined to be a part of a wire, it is no longer allowed to rotate – effectively simulating the presence of a covalent bridge. These two steps are repeated until no further linker orientation may result in a wire. We ensure that this is the case for a series of model sizes by plotting the number of unbridged linkers as a function of algorithmic step, Figure 37; we observe a plateau in unbridged linkers, indicating the model runs to termination.

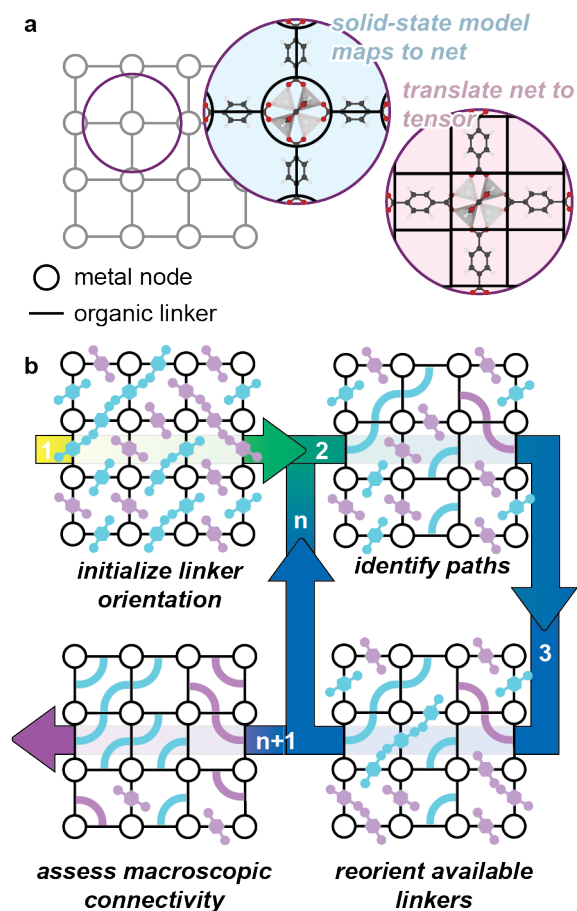


*Figure 36.* **a** Net theory is used to translate the crystalline structure of MOF-5 to a tensor. **b** The tensor elements may then be iterated to represent bulk wire formation in four distinct steps; 1) the initial tensor is initialized with linker orientations, 2) paths are then identified, 3) linkers that are not in a wire are reoriented, steps 1) – 3) are repeated until no linker reorientation will result in a new wire formation, at this point, 4) the macroscopic connectivity is assessed. For visual simplicity, we do not show the layers in the third dimension – although our statistical model does take these into account.

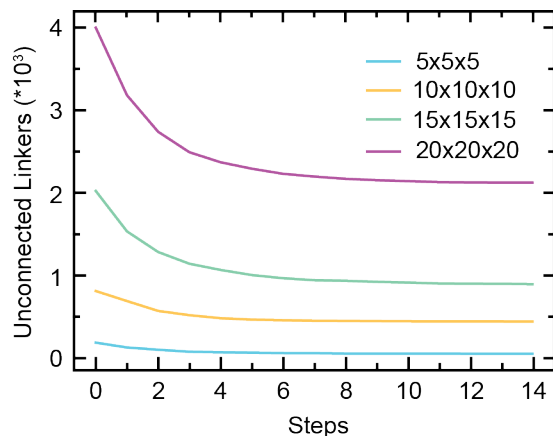
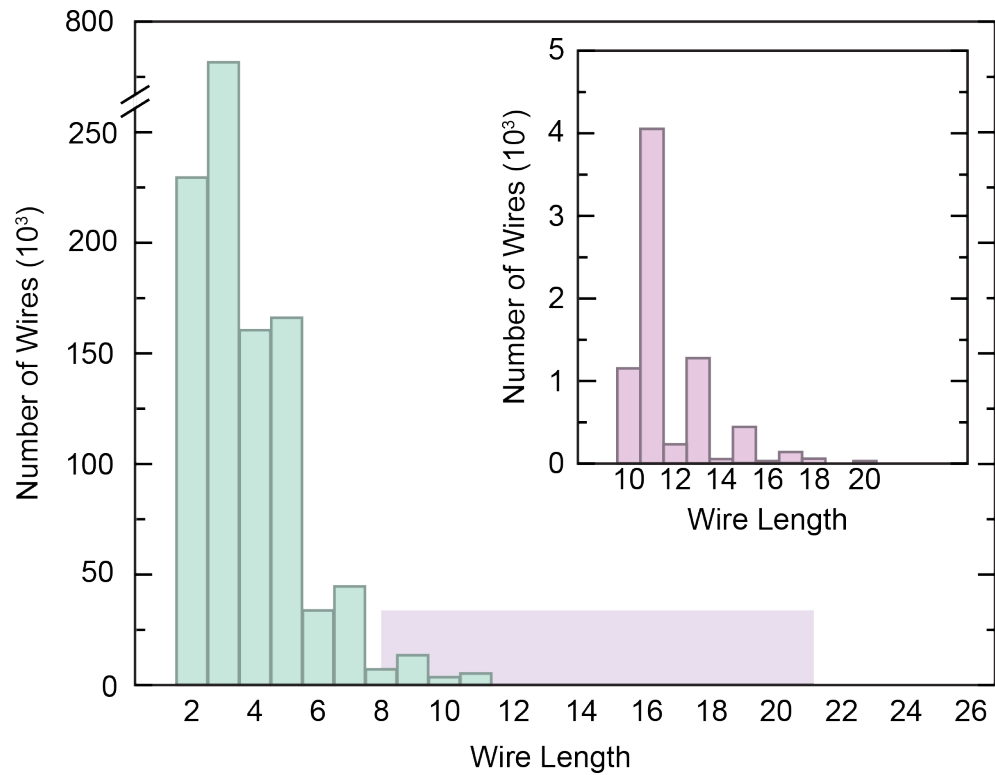


Figure 37. Unconnected linkers as a function of algorithmic step for a series of model sizes using the generalized statistical model.

Running a series of simulations on the same net topology reveals macroscopic wire formation patterns. Unsurprisingly, the 6-2 connected net in conjunction with no favorable linker orientation features a preference for short, linear, in-plane wires, Figure 38. Moreover, the wire length distribution of the general statistical model, Figure 38, is similar to that obtained using the atomistic wire formation simulation, Figure 35; this is expected considering these two models are describing the same MOF-5-polymer system. We modified the original algorithm to simulate PPV covalent bridges (linkers that were 180deg apart were allowed to bind), Figure 39. Unsurprisingly, the total number of wires decreases, yet the same distribution is achieved.

## Conclusions

The amalgamation of models employed within this study informs us of three major findings. First, incorporation of p-type, redox-active organic linkers within the otherwise insulating MOF-5 scaffold yield semi-conducting scaffolds that turn metallic upon oxidation. Indeed the MOF-5-PPV and MOF-5-PANI models outperform the other models explored in this study, suggesting they may



*Figure 38.* The bulk wire length distribution for a 6-2 net topology allowing connections between 90deg linkers, totaled over 100 iterations of the general statistical model.

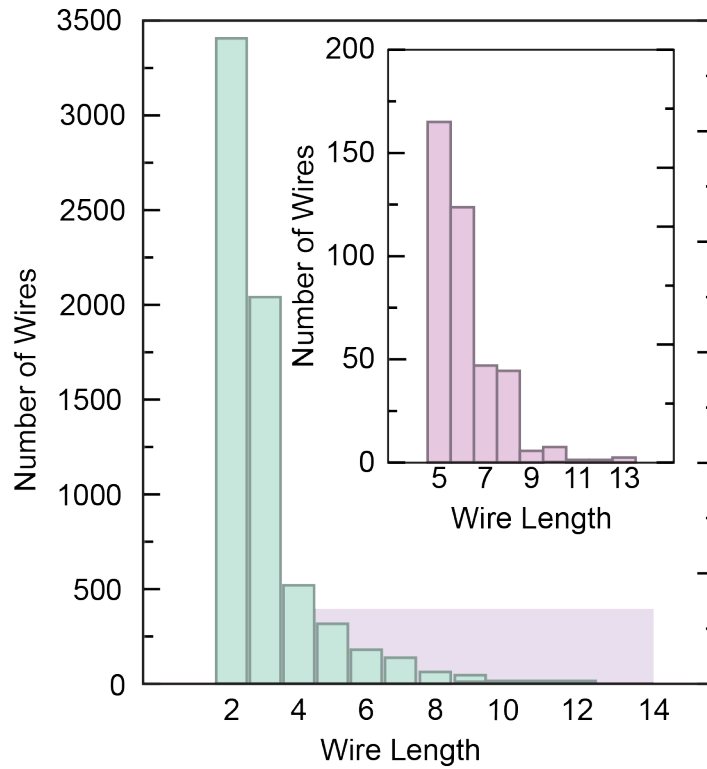


*Figure 39.* The bulk wire length distribution for a 6-2 net topology allowing connections between 180deg linkers, totaled over 100 iterations of the general statistical model.

be promising for experimental synthesis. Yet, the spin polarization observed in the thienothiophene derivatives is promising for chemical sensing applications.<sup>(448)</sup> Second, while the inclusion of covalent bridges breaks symmetry, it does not sufficiently distort the MOF-5 scaffold enough to prevent wire formation. Thus, the spatial separation and rotational freedom of the 6-2 net topology is, ultimately, beneficial to the overall integrity of the MOF scaffold. Third, agreement between the atomistic simulation and the general statistical model indicates that the statistical model is a promising route towards scanning diverse topological nets – enabling efficient identification of net topologies that may yield interesting (i.e. hoops, helices, etc.) wire conformations.



## REFERENCES CITED

1. Hendon, C. H.; Bonnefoy, J.; Quadrelli, E. A.; Canivet, J.; Chambers, M. B.; Rouse, G.; Walsh, A.; Fontecave, M.; Mellot-Draznieks, C. A Simple and Non-Destructive Method for Assessing the Incorporation of Bipyridine Dicarboxylates as Linkers within Metal–Organic Frameworks. *Chemistry – A European Journal* **2016**, *22*, 3713–3718.
2. Mancuso, J. L.; Mroz, A. M.; Le, K. N.; Hendon, C. H. Electronic Structure Modeling of Metal–Organic Frameworks. *Chem. Rev.* **2020**, *120*, 8641–8715.
3. Gemechis D. Degaga,; Pandey, R.; Gupta, C.; Bharadwaj, L. Tailoring of the Electronic Property of Zn-BTC Metal–Organic Framework via Ligand Functionalization: An Ab Initio Investigation. *RSC Advances* **2019**, 13959–14579.
4. Biswas, S.; Ahnfeldt, T.; Stock, N. New Functionalized Flexible Al-MIL-53-X (X = -Cl, -Br, -CH<sub>3</sub>, -NO<sub>2</sub>, -(OH)<sub>2</sub>) Solids: Syntheses, Characterization, Sorption, and Breathing Behavior. *Inorganic Chemistry* **2011**, *50*, 9518–9526.
5. Tulchinsky, Y.; Hendon, C. H.; Lomachenko, K. A.; Borfecchia, E.; Melot, B. C.; Hudson, M. R.; Tarver, J. D.; Korzyński, M. D.; Stubbs, A. W.; Kagan, J. J.; Lamberti, C.; Brown, C. M.; Dincă, M. Reversible Capture and Release of Cl<sub>2</sub> and Br<sub>2</sub> with a Redox-Active Metal–Organic Framework. *Journal of the American Chemical Society* **2017**, *139*, 5992–5997.
6. McDevitt, C. E.; Yglesias, M. V.; Mroz, A. M.; Sutton, E. C.; Yang, M. C.; Hendon, C. H.; DeRose, V. J. Monofunctional Platinum(II) Compounds and Nucleolar Stress: Is Phenanthriplatin Unique? *J. Biol. Inorg. Chem.* **2019**, *24*, 899–908.
7. Yue, X.; Taraban, M. B.; Hyland, L. L.; Yu, Y. B. Avoiding Steric Congestion in Dendrimer Growth through Proportionate Branching: A Twist on Da Vinci's Rule of Tree Branching. *J. Org. Chem.* **2012**, *77*, 8879–8887.
8. Luo, P.; Dinnocenzo, J. P.; Merkel, P. B.; Young, R. H.; Farid, S. Bimolecular Electron Transfers That Deviate from the Sandros–Boltzmann Dependence on Free Energy: Steric Effect. *J. Org. Chem.* **2012**, *77*, 1632–1639.
9. Durand, D. J.; Fey, N. Computational Ligand Descriptors for Catalyst Design. *Chem. Rev.* **2019**, *119*, 6561–6594.

10. Mohamed, R. K.; Peterson, P. W.; Alabugin, I. V. Concerted Reactions That Produce Diradicals and Zwitterions: Electronic, Steric, Conformational, and Kinetic Control of Cycloaromatization Processes. *Chem. Rev.* **2013**, *113*, 7089–7129.
11. Ravelli, D.; Fagnoni, M.; Fukuyama, T.; Nishikawa, T.; Ryu, I. Site-Selective C–H Functionalization by Decatungstate Anion Photocatalysis: Synergistic Control by Polar and Steric Effects Expands the Reaction Scope. *ACS Catal.* **2018**, *8*, 701–713.
12. Wagner, J. P.; Schreiner, P. R. London Dispersion in Molecular Chemistry – Reconsidering Steric Effects. *Angew. Chem. Int. Ed.* **2015**, *54*, 12274–12296.
13. Poli, G.; Martinelli, A.; Tuccinardi, T. Reliability Analysis and Optimization of the Consensus Docking Approach for the Development of Virtual Screening Studies. *Journal of Enzyme Inhibition and Medicinal Chemistry* **2016**, *31*, 167–173.
14. Ue, M.; Murakami, A.; Nakamura, S. A Convenient Method to Estimate Ion Size for Electrolyte Materials Design. *J. Electrochem. Soc.* **2002**, *149*, A1385–A1388.
15. Farha, O. K.; Özgür Yazaydın, A.; Eryazici, I.; Malliakas, C. D.; Hauser, B. G.; Kanatzidis, M. G.; Nguyen, S. T.; Snurr, R. Q.; Hupp, J. T. De Novo Synthesis of a Metal–Organic Framework Material Featuring Ultrahigh Surface Area and Gas Storage Capacities. *Nature Chemistry* **2010**, *2*, 944–948.
16. Mason, J. A.; Veenstra, M.; Long, J. R. Evaluating Metal–Organic Frameworks for Natural Gas Storage. *Chem. Sci.* **2014**, *5*, 32–51.
17. Rosi, N. L. Hydrogen Storage in Microporous Metal–Organic Frameworks. *Science* **2003**, *300*, 1127–1129.
18. Li, J.-R.; Kuppler, R. J.; Zhou, H.-C. Selective Gas Adsorption and Separation in Metal–Organic Frameworks. *Chem. Soc. Rev.* **2009**, *38*, 1477.
19. Li, Z.; Peters, A. W.; Bernales, V.; Ortuño, M. A.; Schweitzer, N. M.; DeStefano, M. R.; Gallington, L. C.; Platero-Prats, A. E.; Chapman, K. W.; Cramer, C. J.; Gagliardi, L.; Hupp, J. T.; Farha, O. K. Metal–Organic Framework Supported Cobalt Catalysts for the Oxidative Dehydrogenation of Propane at Low Temperature. *ACS Cent. Sci.* **2017**, *3*, 31–38.
20. Chughtai, A. H.; Ahmad, N.; Younus, H. A.; Laypkov, A.; Verpoort, F. Metal–Organic Frameworks: Versatile Heterogeneous Catalysts for Efficient Catalytic Organic Transformations. *Chemical Society Reviews* **2015**, *44*, 6804–6849.

21. Corma, A.; García, H.; Llabrés i Xamena, F. X. Engineering Metal Organic Frameworks for Heterogeneous Catalysis. *Chemical Reviews* **2010**, *110*, 4606–4655.
22. Farrusseng, D.; Aguado, S.; Pinel, C. Metal-Organic Frameworks: Opportunities for Catalysis. *Angewandte Chemie International Edition* **2009**, *48*, 7502–7513.
23. Gascon, J.; Corma, A.; Kapteijn, F.; Llabrés i Xamena, F. X. Metal Organic Framework Catalysis: *Quo Vadis ? ACS Catalysis* **2014**, *4*, 361–378.
24. Rahm, M.; Hoffmann, R.; Ashcroft, N. W. Atomic and Ionic Radii of Elements 1–96. *Chem. Eur. J.* **2016**, *22*, 14625–14632.
25. Meyer, L. Die Natur Der Chemischen Elemente Als Function Ihrer Atomgewichte. *Ann. Chem. Pharm.* **1870**, 354–364.
26. Bragg, W. L. The Arrangement of Atoms in Crystals. *Philos. Mag.* **1920**, *40*, 169–189.
27. Pauling, L. C. *An Introduction to Modern Structural Chemistry*, 3rd ed.; Cornell University Press: Ithaca, NY, 1960; p 644.
28. Bondi, A. Van Der Waals Volumes and Radii. *J. Phys. Chem.* **1964**, *68*, 441–451.
29. Bondi, A. Van Der Waals Volumes and Radii of Metals in Covalent Compounds. *J. Phys. Chem.* **1966**, *70*, 3006–2007.
30. Batsanov, S. Van Der Waals Radii of Elements. *Inorg. Mater.* **2001**, *37*, 1031–1046.
31. Alvarez, S. A Cartography of the van Der Waals Territories. *Dalton Trans.* **2013**, *42*, 8627–8636.
32. Cordero, B.; Gomez, V.; Platero-Prats, A. E.; Reves, M.; Echeverria, J.; Cremades, E.; Barragan, F.; Alvarez, S. Covalent Radii Revisited. *Dalton Trans.* **2008**, 2832–2838.
33. Ghosh, D. C.; Biswas, R. Theoretical Calculation of Absolute Radii of Atoms and Ions. Part. 1 The Atomic Radii. *Int. J. Mol. Sci.* **2002**, *3*, 87–113.
34. Delgado-Andrade, C.; Morales, F. J. Unraveling the Contribution of Melanoidins to the Antioxidant Activity of Coffee Brews. *Journal of Agricultural and Food Chemistry* **2005**, *53*, 1403–1407.

35. Vincze, J.; Valiskó, M.; Boda, D. The Nonmonotonic Concentration Dependence of the Mean Activity Coefficient of Electrolytes Is a Result of a Balance between Solvation and Ion-Ion Correlations. *The Journal of Chemical Physics* **2010**, *133*, 154507.
36. Fraenkel, D. Computing Excess Functions of Ionic Solutions: The Smaller-Ion Shell Model *versus* the Primitive Model. 1. Activity Coefficients. *J. Chem. Theory Comput.* **2015**, *11*, 178–192.
37. Schreiner, P. R.; Chernish, L. V.; Gunchenko, P. A.; Tikhonchuk, E. Y.; Hausmann, H.; Serafin, M.; Schlecht, S.; Dahl, J. E. P.; Carlson, R. M. K.; Fokin, A. A. Overcoming Lability of Extremely Long Alkane Carbon–Carbon Bonds through Dispersion Forces. *Nature* **2011**, *477*, 308–311.
38. Ishigaki, Y.; Shimajiri, T.; Takeda, T.; Katoono, R.; Suzuki, T. Longest C–C Single Bond among Neutral Hydrocarbons with a Bond Length beyond 1.8 Å. *Chem* **2018**, *4*, 795–806.
39. Li, J.; Pang, R.; Li, Z.; Lai, G.; Xiao, X.-Q.; Muller, T. Exceptionally Long C–C Single Bonds in Diamino-*o*-Carborane as Induced by Negative Hyperconjugation. *Angew. Chem. Int. Ed.* **2019**, *58*, 1397–1401.
40. Pyykko, P. Additive Covalent Radii for Single-, Double-, and Triple-Bonded Molecules and Tetrahedrally Bonded Crystals: A Summary. *J. Phys. Chem. A* **2015**, *119*, 2326–2337.
41. Bak, K. L.; Gauss, J.; Jørgensen, P.; Olsen, J.; Helgaker, T.; Stanton, J. F. The Accurate Determination of Molecular Equilibrium Structures. *The Journal of Chemical Physics* **2001**, *114*, 6548–6556.
42. Clementi, E.; Raimondi, D. L. Atomic Screening Constants from SCF Functions. *J. Chem. Phys.* **1963**, *38*, 2686.
43. Clementi, E.; Raimondi, D. L.; Reinhardt, W. P. Atomic Screening Constants from SCF Functions. II. Atoms with 37–86 Electrons. *J. Chem. Phys.* **1967**, *47*, 1300–1307.
44. Slater, J. C. Atomic Shielding Constants. *Phys. Rev.* **1930**, *36*, 57.
45. Zunger, A.; Cohen, M. L. First-Principles Nonlocal-Pseudopotential Approach in the Density-Functional Formalism: Development and Application to Atoms. *Physical Review B* **1978**, *18*, 5449–5472.
46. Zunger, A.; Cohen, M. L. First-Principles Nonlocal-Pseudopotential Approach in the Density-Functional Formalism. II. Application to Electronic and Structural Properties of Solids. *Physical Review B* **1979**, *20*, 4082–4108.

47. Zhang, S. B.; Cohen, M. L.; Phillips, J. C. Relativistic Screened Orbital Radii. *Physical Review B* **1987**, *36*, 5861–5867.
48. Nath, S.; Chattaqcharya, S.; Chattaraj, P. K. Density Functional Calculation of a Characteristic Atomic Radius. *THEOCHEM* **1995**, *331*, 267–279.
49. Putz, M. V.; Russo, N.; Sicilia, E. Atomic Radii Scale and Related Size Properties from Density Functional Electronegativity Formulation. *J. Phys. Chem. A* **2003**, *107*, 5461–5465.
50. Hollett, J. W.; Kelly, A.; Poirier, R. A. Quantum Mechanical Size and Steric Hindrance. *J. Phys. Chem. A* **2006**, *110*, 13884–13888.
51. Bader, R. F. W.; Henneker, W. H.; Cade, P. E. Molecular Charge Distributions and Chemical Binding. *J. Chem. Phys.* **1967**, *46*, 3341–3363.
52. Boyd, R. The Relative Sizes of Atoms. *J. Phys. B: Atom. Molec. Phys.* **1977**, *10*.
53. Lee, C.; Yang, W.; Parr, R. G. Development of the Colle-Salvetti Correlation-Energy Formula into a Functional of the Electron Density. *Physical Review B* **1988**, *37*, 785–789.
54. Perdew, J.; Burke, K.; Ernzerhof, M. Generalized Gradient Approximation Made Simple. *Phys. Rev. Lett.* **1996**, *77*, 3865–3868.
55. Perdew, J.; Burke, K.; Ernzerhof, M. Errata: Generalized Gradient Approximation Made Simple. *Phys. Rev. Lett.* **1997**, *78*, 1396.
56. Kohn, W.; Sham, L. J. Self-Consistent Equations Including Exchange and Correlation Effects. *Phys. Rev.* **1965**, *140*, A1133–A1138.
57. Kohn, W.; Becke, A. D.; Parr, R. G. Density Functional Theory of Electronic Structure. *J. Phys. Chem.* **1996**, *100*, 12974–12980.
58. Korth, M.; Grimme, S. “Mindless” DFT Benchmarking. *Journal of Chemical Theory and Computation* **2009**, *5*, 993–1003.
59. Bremond, E.; Savarese, M.; Su, N. Q.; Perez-Jimenez, A. J.; Xu, X.; Sancho-Garcia, J. C.; Adamo, C. Benchmarking Density Functionals on Structural Parameters of Small-/Medium-Sized Organic Molecules. *J. Chem. Theory Comput.* **2016**, *12*, 459–465.
60. Xu, X.; Zhang, W.; Tang, M.; Truhlar, D. G. Do Practical Standard Coupled Cluster Calculations Agree Better than Kohn–Sham Calculations with Currently Available Functionals When Compared to the Best Available Experimental Data for Dissociation Energies of Bonds to 3 *d* Transition Metals? *Journal of Chemical Theory and Computation* **2015**, *11*, 2036–2052.

61. Politzer, P.; Murray, J. S. The Fundamental Nature and Role of the Electrostatic Potential in Atoms and Molecules. *Theoretical Chemistry Accounts: Theory, Computation, and Modeling (Theoretica Chimica Acta)* **2002**, *108*, 134–142.
62. Shannon, R. D. Revised Effective Ionic Radii and Systematic Studies of Interatomic Distances in Halides and Chalcogenides. *Acta Crystallographica Section A* **1976**, *32*, 751–767.
63. Shannon, R. D.; Prewitt, C. T. Effective Ionic Radii in Oxides and Fluorides. *Acta Crystallographica Section B Structural Crystallography and Crystal Chemistry* **1969**, *25*, 925–946.
64. Ouyang, R. Exploiting Ionic Radii for Rational Design of Halide Perovskites. *Chemistry of Materials* **2020**, *32*, 595–604.
65. Agmon, N. Isoelectronic Theory for Cationic Radii. *Journal of the American Chemical Society* **2017**, *139*, 15068–15073.
66. Slater, J. C. Atomic Radii in Crystals. *The Journal of Chemical Physics* **1964**, *41*, 3199–3204.
67. Batsanov, S. S. Determination of Ionic Radii from Metal Compressibilities. *Journal of Structural Chemistry* **2004**, *45*, 896–899.
68. Gebbie, M. A.; Smith, A. M.; Dobbs, H. A.; Lee, A. A.; Warr, G. G.; Banquy, X.; Valtiner, M.; Rutland, M. W.; Israelachvili, J. N.; Perkin, S.; Atkin, R. Long Range Electrostatic Forces in Ionic Liquids. *Chem. Commun.* **2017**, *53*, 1214–1224.
69. Park, K. C.; Tsukahara, T. Quantitative Evaluation of Long-Range and Cooperative Ion Effect on Water in Polyamide Network. *J. Phys. Chem. B* **2019**, *123*, 2948–2955.
70. Mroz, A. STREUSEL.
71. May, L. In *ACS Symposium Series*; Giunta, C. J., Ed.; American Chemical Society: Washington, DC, 2010; Vol. 1044; pp 21–33.
72. Dalton, J. *A New System of Chemical Philosophy, Volume 1.*; Cambridge University Press: Cambridge, 1808.
73. Kresse, G.; Furthmüller, J. Efficient Iterative Schemes for Ab Initio Total-Energy Calculations Using a Plane-Wave Basis Set. *Phys. Rev. B* **1996**, *54*, 11169–11186.
74. Kresse, G.; Joubert, D. From Ultrasoft Pseudopotentials to the Projector Augmented-Wave Method. *Phys. Rev. B* **1999**, *59*, 1758–1775.

75. Kresse, G.; Hafner, J. Ab Initio Molecular Dynamics for Liquid Metals. *Phys. Rev. B* **1993**, *47*, 558–561.
76. Kresse, G.; Hafner, J. Ab Initio Molecular-Dynamics Simulation of the Liquid-Metal–Amorphous-Semiconductor Transition in Germanium. *Phys. Rev. B* **1994**, *49*, 14251–14269.
77. Gaussian 09, Revision A.02, M. J. Frisch, G. W. Trucks, H. B. Schlegel, G. E. Scuseria, M. A. Robb, J. R. Cheeseman, G. Scalmani, V. Barone, G. A. Petersson, H. Nakatsuji, X. Li, M. Caricato, A. Marenich, J. Bloino, B. G. Janesko, R. Gomperts, B. Mennucci, H. P. Hratchian, J. V. Ortiz, A. F. Izmaylov, J. L. Sonnenberg, D. Williams-Young, F. Ding, F. Lipparini, F. Egidi, J. Goings, B. Peng, A. Petrone, T. Henderson, D. Ranasinghe, V. G. Zakrzewski, J. Gao, N. Rega, G. Zheng, W. Liang, M. Hada, M. Ehara, K. Toyota, R. Fukuda, J. Hasegawa, M. Ishida, T. Nakajima, Y. Honda, O. Kitao, H. Nakai, T. Vreven, K. Throssell, J. A. Montgomery, Jr., J. E. Peralta, F. Ogliaro, M. Bearpark, J. J. Heyd, E. Brothers, K. N. Kudin, V. N. Staroverov, T. Keith, R. Kobayashi, J. Normand, K. Raghavachari, A. Rendell, J. C. Burant, S. S. Iyengar, J. Tomasi, M. Cossi, J. M. Millam, M. Klene, C. Adamo, R. Cammi, J. W. Ochterski, R. L. Martin, K. Morokuma, O. Farkas, J. B. Foresman, and D. J. Fox, Gaussian, Inc., Wallingford CT, 2016.
78. Planck, M. Ueber das Gesetz der Energieverteilung im Normalspectrum. *Ann. Phys.* **1901**, *309*, 553–563.
79. Einstein, A. Über einen die Erzeugung und Verwandlung des Lichtes betreffenden heuristischen Gesichtspunkt. *Ann. Phys.* **1905**, *322*, 132–148.
80. Bohr, N. I. *On the Constitution of Atoms and Molecules. The London, Edinburgh, and Dublin Philosophical Magazine and Journal of Science* **1913**, *26*, 1–25.
81. Gerlach, W.; Stern, O. Das magnetische Moment des Silberatoms. *Z. Physik* **1922**, *9*, 353–355.
82. De Broglie, L. Recherches Sur La Théorie Des Quanta. *Ann. Phys.* **1925**, *10*, 22–128.
83. Heisenberg, W. Über quantentheoretische Umdeutung kinematischer und mechanischer Beziehungen. *Z. Physik* **1925**, *33*, 879–893.
84. Born, M.; Heisenberg, W.; Jordan, P. Zur Quantenmechanik. II. *Z. Physik* **1926**, *35*, 557–615.
85. Born, M.; Jordan, P. Zur Quantenmechanik. *Z. Physik* **1925**, *34*, 858–888.

86. Schrödinger, E. Quantisierung als Eigenwertproblem. *Ann. Phys.* **1926**, *384*, 361–376.
87. Heisenberg, W. Über den anschaulichen Inhalt der quantentheoretischen Kinematik und Mechanik. *Z. Physik* **1927**, *43*, 172–198.
88. Dirac, P. A. M. *The Principles of Quantum Mechanics*, 4th ed.; The International Series of Monographs on Physics 27; Clarendon Press: Oxford, 2009.
89. McQuarrie, D. A. *Quantum Chemistry*; University Science Books: Mill Valley, Calif, 1983.
90. Szabo, A.; Ostlund, N. S. *Modern Quantum Chemistry: Introduction to Advanced Electronic Structure Theory*; Dover Publications: Mineola, N.Y, 1996.
91. Hohenberg, P.; Kohn, W. Inhomogeneous Electron Gas. *Phys. Rev.* **1964**, *136*, B864–B871.
92. Perdew, J. P.; Burke, K.; Wang, Y. Generalized Gradient Approximation for the Exchange-Correlation Hole of a Many-Electron System. *Phys. Rev. B* **1996**, *54*, 16533–16539.
93. Nazarian, D.; Ganesh, P.; Sholl, D. S. Benchmarking Density Functional Theory Predictions of Framework Structures and Properties in a Chemically Diverse Test Set of Metal–Organic Frameworks. *J. Mater. Chem. A* **2015**, *3*, 22432–22440.
94. Odoh, S. O.; Cramer, C. J.; Truhlar, D. G.; Gagliardi, L. Quantum-Chemical Characterization of the Properties and Reactivities of Metal–Organic Frameworks. *Chem. Rev.* **2015**, *115*, 6051–6111.
95. O’boyle, N. M.; Tenderholt, A. L.; Langner, K. M. Celib: A Library for Package-Independent Computational Chemistry Algorithms. *J. Comput. Chem.* **2008**, *29*, 839–845.
96. Lejaeghere, K.; Van Speybroeck, V.; Van Oost, G.; Cottenier, S. Error Estimates for Solid-State Density-Functional Theory Predictions: An Overview by Means of the Ground-State Elemental Crystals. *Critical Reviews in Solid State and Materials Sciences* **2014**, *39*, 1–24.
97. Hamad, S.; Hernandez, N. C.; Aziz, A.; Ruiz-Salvador, A. R.; Calero, S.; Grau-Crespo, R. Electronic Structure of Porphyrin-Based Metal–Organic Frameworks and Their Suitability for Solar Fuel Production Photocatalysis. *J. Mater. Chem. A* **2015**, *3*, 23458–23465.



98. Butler, K. T.; Hendon, C. H.; Walsh, A. Electronic Structure Modulation of Metal–Organic Frameworks for Hybrid Devices. *ACS Appl. Mater. Interfaces* **2014**, *6*, 22044–22050.
99. Tayfuroglu, O.; Kocak, A.; Zorlu, Y. In Silico Investigation into H<sub>2</sub> Uptake in MOFs: Combined Text/Data Mining and Structural Calculations. *Langmuir* **2020**, *36*, 119–129.
100. Park, S. S.; Hendon, C. H.; Fielding, A. J.; Walsh, A.; O’Keeffe, M.; Dincă, M. The Organic Secondary Building Unit: Strong Intermolecular  $\pi$  Interactions Define Topology in MIT-25, a Mesoporous MOF with Proton-Replete Channels. *Journal of the American Chemical Society* **2017**, *139*, 3619–3622.
101. Jackson, A. J.; Skelton, J. M.; Hendon, C. H.; Butler, K. T.; Walsh, A. Crystal Structure Optimisation Using an Auxiliary Equation of State. *The Journal of Chemical Physics* **2015**, *143*, 184101.
102. Hendrickx, K.; Vanpoucke, D. E. P.; Leus, K.; Lejaeghere, K.; Van Yperen-De Deyne, A.; Van Speybroeck, V.; Van Der Voort, P.; Hemelsoet, K. Understanding Intrinsic Light Absorption Properties of UiO-66 Frameworks: A Combined Theoretical and Experimental Study. *Inorg. Chem.* **2015**, *54*, 10701–10710.
103. Goodenough, J. B. Spin-Orbit-Coupling Effects in Transition-Metal Compounds. *Physical Review* **1968**, *171*, 466–479.
104. Davidson, E. R.; Feller, D. Basis Set Selection for Molecular Calculations. *Chemical Reviews* **1986**, *86*, 681–696.
105. Huzinaga, S. Basis Sets for Molecular Calculations. *Computer Physics Reports* **1985**, *2*, 281–339.
106. Schuchardt, K. L.; Didier, B. T.; Elsethagen, T.; Sun, L.; Gurumoorthi, V.; Chase, J.; Li, J.; Windus, T. L. Basis Set Exchange: A Community Database for Computational Sciences. *Journal of Chemical Information and Modeling* **2007**, *47*, 1045–1052.
107. Kenny, S.; Horsfield, A.; Fujitani, H. Transferable Atomic-Type Orbital Basis Sets for Solids. *Physical Review B* **2000**, *62*, 4899–4905.
108. Bultinck, P.; Ayers, P. W.; Fias, S.; Tiels, K.; Van Alsenoy, C. Uniqueness and Basis Set Dependence of Iterative Hirshfeld Charges. *Chemical Physics Letters* **2007**, *444*, 205–208.
109. Daga, L. E.; Civalleri, B.; Maschio, L. Gaussian Basis Sets for Crystalline Solids: All-Purpose Basis Set Libraries vs System-Specific Optimizations. *J. Chem. Theory Comput.* **2020**, *16*, 2192–2201.

110. Helgaker, T.; Klopper, W.; Tew, D. P. Quantitative Quantum Chemistry. *Molecular Physics* **2008**, *106*, 2107–2143.
111. Hill, J. G. Gaussian Basis Sets for Molecular Applications. *Int. J. Quantum Chem.* **2013**, *113*, 21–34.
112. Booth, G. H.; Tsatsoulis, T.; Chan, G. K.-L.; Grüneis, A. From Plane Waves to Local Gaussians for the Simulation of Correlated Periodic Systems. *J. Chem. Phys.* **2016**, *145*, 084111.
113. Frisch, M. J.; Pople, J. A.; Binkley, J. S. Self-consistent Molecular Orbital Methods 25. Supplementary Functions for Gaussian Basis Sets. *The Journal of Chemical Physics* **1984**, *80*, 3265–3269.
114. Ehrenreich, H.; Cohen, M. H. Self-Consistent Field Approach to the Many-Electron Problem. *Physical Review* **1959**, *115*, 786–790.
115. Medvedev, M. G.; Bushmarinov, I. S.; Sun, J.; Perdew, J. P.; Lyssenko, K. A. Density Functional Theory Is Straying from the Path toward the Exact Functional. *Science* **2017**, *355*, 49–52.
116. Jäger, M.; Freitag, L.; González, L. Using Computational Chemistry to Design Ru Photosensitizers with Directional Charge Transfer. *Coordination Chemistry Reviews* **2015**, *304-305*, 146–165.
117. Mattsson, A. E. DENSITY FUNCTIONAL THEORY: In Pursuit of The. *Science* **2002**, *298*, 759–760.
118. Vosko, S. H.; Wilk, L.; Nusair, M. Accurate Spin-Dependent Electron Liquid Correlation Energies for Local Spin Density Calculations: A Critical Analysis. *Can. J. Phys.* **1980**, *58*, 1200–1211.
119. Perdew, J. P.; Zunger, A. Self-Interaction Correction to Density-Functional Approximations for Many-Electron Systems. *Phys. Rev. B* **1981**, *23*, 5048–5079.
120. Chen, S.; Dai, J.; Zeng, X. C. Metal–Organic Kagome Lattices M<sub>3</sub>(2,3,6,7,10,11-Hexamino-triphenylene)<sub>2</sub> (M = Ni and Cu): From Semiconducting to Metallic by Metal Substitution. *Phys. Chem. Chem. Phys.* **2015**, *17*, 5954–5958.
121. Dou, J.-H.; Sun, L.; Ge, Y.; Li, W.; Hendon, C. H.; Li, J.; Gul, S.; Yano, J.; Stach, E. A.; Dincă, M. Signature of Metallic Behavior in the Metal–Organic Frameworks M<sub>3</sub>(Hexaiminobenzene)<sub>2</sub> (M = Ni, Cu). *J. Am. Chem. Soc.* **2017**, *139*, 13608–13611.

122. Clough, A. J.; Skelton, J. M.; Downes, C. A.; de la Rosa, A. A.; Yoo, J. W.; Walsh, A.; Melot, B. C.; Marinescu, S. C. Metallic Conductivity in a Two-Dimensional Cobalt Dithiolene Metal–Organic Framework. *Journal of the American Chemical Society* **2017**, *139*, 10863–10867.
123. Clough, A. J.; Orchanian, N. M.; Skelton, J. M.; Neer, A. J.; Howard, S. A.; Downes, C. A.; Piper, L. F. J.; Walsh, A.; Melot, B. C.; Marinescu, S. C. Room Temperature Metallic Conductivity in a Metal–Organic Framework Induced by Oxidation. *J. Am. Chem. Soc.* **2019**, *141*, 16323–16330.
124. Hmadeh, M. et al. New Porous Crystals of Extended Metal-Catecholates. *Chemistry of Materials* **2012**, *24*, 3511–3513.
125. Sheberla, D.; Sun, L.; Blood-Forsythe, M. A.; Er, S.; Wade, C. R.; Brozek, C. K.; Aspuru-Guzik, A.; Dincă, M. High Electrical Conductivity in  $\text{Ni}_3(2,3,6,7,10,11\text{-Hexaiminotriphenylene})_2$ , a Semiconducting Metal–Organic Graphene Analogue. *J. Am. Chem. Soc.* **2014**, *136*, 8859–8862.
126. Langreth, D. C.; Mehl, M. J. Beyond the Local-Density Approximation in Calculations of Ground-State Electronic Properties. *Physical Review B* **1983**, *28*, 1809–1834.
127. Perdew, J. P.; Chevary, J. A.; Vosko, S. H.; Jackson, K. A.; Pederson, M. R.; Singh, D. J.; Fiolhais, C. Atoms, Molecules, Solids, and Surfaces: Applications of the Generalized Gradient Approximation for Exchange and Correlation. *Phys. Rev. B* **1992**, *46*, 6671–6687.
128. Wang, J.; Zhou, Y. Dependence of Elastic Stiffness on Electronic Band Structure of Nanolaminate  $\text{M}_2\text{AlC}$  (  $\text{M} = \text{Ti}, \text{V}, \text{Nb}$ , and  $\text{Cr}$  ) Ceramics. *Physical Review B* **2004**, *69*.
129. Riley, J. M. et al. Direct Observation of Spin-Polarized Bulk Bands in an Inversion-Symmetric Semiconductor. *Nature Physics* **2014**, *10*, 835–839.
130. Ciofini, I.; Adamo, C.; Chermette, H. Self-Interaction Error in Density Functional Theory: A Mean-Field Correction for Molecules and Large Systems. *Chemical Physics* **2005**, *309*, 67–76.
131. Zhao, Y.; Truhlar, D. G. A New Local Density Functional for Main-Group Thermochemistry, Transition Metal Bonding, Thermochemical Kinetics, and Noncovalent Interactions. *The Journal of Chemical Physics* **2006**, *125*, 194101.

132. Tao, J.; Perdew, J. P.; Staroverov, V. N.; Scuseria, G. E. Climbing the Density Functional Ladder: Nonempirical Meta-Generalized Gradient Approximation Designed for Molecules and Solids. *Phys. Rev. Lett.* **2003**, *91*, 146401.
133. Adamo, C.; Barone, V. Toward Reliable Density Functional Methods without Adjustable Parameters: The PBE0 Model. *The Journal of Chemical Physics* **1999**, *110*, 6158–6170.
134. Heyd, J.; Scuseria, G. E.; Ernzerhof, M. Erratum: “Hybrid Functionals Based on a Screened Coulomb Potential” [J. Chem. Phys. 118, 8207 (2003)]. *The Journal of Chemical Physics* **2006**, *124*, 219906.
135. Yanai, T.; Tew, D. P.; Handy, N. C. A New Hybrid Exchange–Correlation Functional Using the Coulomb-Attenuating Method (CAM-B3LYP). *Chemical Physics Letters* **2004**, *393*, 51–57.
136. Becke, A. D. Density-Functional Exchange-Energy Approximation with Correct Asymptotic Behavior. *Phys. Rev. A* **1988**, *38*, 3098–3100.
137. Janthon, P.; Luo, S. A.; Kozlov, S. M.; Viñes, F.; Limtrakul, J.; Truhlar, D. G.; Illas, F. Bulk Properties of Transition Metals: A Challenge for the Design of Universal Density Functionals. *J. Chem. Theory Comput.* **2014**, *10*, 3832–3839.
138. Zhao, Y.; Truhlar, D. G. The M06 Suite of Density Functionals for Main Group Thermochemistry, Thermochemical Kinetics, Noncovalent Interactions, Excited States, and Transition Elements: Two New Functionals and Systematic Testing of Four M06-Class Functionals and 12 Other Functionals. *Theor Chem Account* **2008**, *120*, 215–241.
139. Heyd, J.; Scuseria, G. E.; Ernzerhof, M. Hybrid Functionals Based on a Screened Coulomb Potential. *The Journal of Chemical Physics* **2003**, *118*, 8207–8215.
140. Musho, T.; Li, J.; Wu, N. Thermodynamics of the Oxygen Evolution Electrocatalysis in a Functionalized UiO-66 Metal-Organic Frameworks. *Int. J. Quantum Chem.* **2016**, *116*, 1153–1159.
141. Perdew, J. P.; Ruzsinszky, A.; Csonka, G. I.; Vydrov, O. A.; Scuseria, G. E.; Constantin, L. A.; Zhou, X.; Burke, K. Restoring the Density-Gradient Expansion for Exchange in Solids and Surfaces. *Phys. Rev. Lett.* **2008**, *100*, 136406.
142. Vruble, I. I.; Senkevich, N. Y.; Khramenkova, E. V.; Polozkov, R. G.; Shelykh, I. A. Electronic Structure and Optical Response of Zn-Based Metal–Organic Frameworks. *Advanced Theory and Simulations* **2018**, *1*.

143. Zhang, F.-M.; Sheng, J.-L.; Yang, Z.-D.; Sun, X.-J.; Tang, H.-L.; Lu, M.; Dong, H.; Shen, F.-C.; Liu, J.; Lan, Y.-Q. Rational Design of MOF/COF Hybrid Materials for Photocatalytic H<sub>2</sub> Evolution in the Presence of Sacrificial Electron Donors. *Angewandte Chemie International Edition* **2018**, *57*, 12106–12110.
144. Dong, H. C.; Nguyen, H. L.; Le, H. M.; Thoai, N.; Kawazoe, Y.; Nguyen-Manh, D. Monitoring Mechanical, Electronic, and Catalytic Trends in a Titanium Metal Organic Framework Under the Influence of Guest-Molecule Encapsulation Using Density Functional Theory. *Sci Rep* **2018**, *8*, 16651.
145. Bennett, T. D.; Cheetham, A. K.; Fuchs, A. H.; Coudert, F.-X. Interplay between Defects, Disorder and Flexibility in Metal-Organic Frameworks. *Nat. Chem.* **2017**, *9*, 11–16.
146. Bennett, T. D.; Cheetham, A. K. Amorphous Metal–Organic Frameworks. *Accounts of Chemical Research* **2014**, *47*, 1555–1562.
147. Bennett, T. D.; Horike, S. Liquid, Glass and Amorphous Solid States of Coordination Polymers and Metal–Organic Frameworks. *Nature Reviews Materials* **2018**, *3*, 431–440.
148. Bennett, T. D.; Yue, Y.; Li, P.; Qiao, A.; Tao, H.; Greaves, N. G.; Richards, T.; Lampronti, G. I.; Redfern, S. A. T.; Blanc, F.; Farha, O. K.; Hupp, J. T.; Cheetham, A. K.; Keen, D. A. Melt-Quenched Glasses of Metal–Organic Frameworks. *Journal of the American Chemical Society* **2016**, *138*, 3484–3492.
149. Gaillac, R.; Pullumbi, P.; Beyer, K. A.; Chapman, K. W.; Keen, D. A.; Bennett, T. D.; Coudert, F.-X. Liquid Metal–Organic Frameworks. *Nature Materials* **2017**, *16*, 1149–1154.
150. Umeyama, D.; Horike, S.; Inukai, M.; Itakura, T.; Kitagawa, S. Reversible Solid-to-Liquid Phase Transition of Coordination Polymer Crystals. *Journal of the American Chemical Society* **2015**, *137*, 864–870.
151. Bennett, T. D.; Goodwin, A. L.; Dove, M. T.; Keen, D. A.; Tucker, M. G.; Barney, E. R.; Soper, A. K.; Bithell, E. G.; Tan, J.-C.; Cheetham, A. K. Structure and Properties of an Amorphous Metal-Organic Framework. *Physical Review Letters* **2010**, *104*.
152. Bloch, F. Über die Quantenmechanik der Elektronen in Kristallgittern. *Z. Physik* **1929**, *52*, 555–600.

153. Ashcroft, N. W.; Mermin, N. D. *Solid State Physics*; Holt, Rinehart and Winston: New York, 1976.
154. Zhang, X.-G.; Varga, K.; Pantelides, S. T. Generalized Bloch Theorem for Complex Periodic Potentials: A Powerful Application to Quantum Transport Calculations. *Phys. Rev. B* **2007**, *76*, 035108.
155. Kratzer, P.; Neugebauer, J. The Basics of Electronic Structure Theory for Periodic Systems. *Front. Chem.* **2019**, *7*, 106.
156. Baldereschi, A. Mean-Value Point in the Brillouin Zone. *Phys. Rev. B* **1973**, *7*, 5212–5215.
157. Aroyo, M. I.; Orobengoa, D.; de la Flor, G.; Tasci, E. S.; Perez-Mato, J. M.; Wondratschek, H. Brillouin-Zone Database on the *Bilbao Crystallographic Server*. *Acta Crystallogr A Found Adv* **2014**, *70*, 126–137.
158. Chadi, D. J. Special Points for Brillouin-Zone Integrations. *Phys. Rev. B* **1977**, *16*, 1746–1747.
159. Monkhorst, H. J.; Pack, J. D. Special Points for Brillouin-Zone Integrations. *Phys. Rev. B* **1976**, *13*, 5188–5192.
160. Genova, A.; Pavanello, M. Exploiting the Locality of Periodic Subsystem Density-Functional Theory: Efficient Sampling of the Brillouin Zone. *J. Phys.: Condens. Matter* **2015**, *27*, 495501.
161. Takahashi, K.; Yoshikawa, A.; Sandhu, A. *Wide Bandgap Semiconductors: Fundamental Properties and Modern Photonic and Electronic Devices*; Springer: Berlin, 2007.
162. Spoerke, E. D.; Small, L. J.; Foster, M. E.; Wheeler, J.; Ullman, A. M.; Stavila, V.; Rodriguez, M.; Allendorf, M. D. MOF-Sensitized Solar Cells Enabled by a Pillared Porphyrin Framework. *J. Phys. Chem. C* **2017**, *121*, 4816–4824.
163. Foster, M. E.; Azoulay, J. D.; Wong, B. M.; Allendorf, M. D. Novel Metal–Organic Framework Linkers for Light Harvesting Applications. *Chem. Sci.* **2014**, *5*, 2081–2090.
164. Stavila, V.; Talin, A. A.; Allendorf, M. D. MOF-Based Electronic and Opto-Electronic Devices. *Chem. Soc. Rev.* **2014**, *43*, 5994–6010.
165. Butler, K. T.; Hendon, C. H.; Walsh, A. Designing Porous Electronic Thin-Film Devices: Band Offsets and Heteroepitaxy. *Faraday Discussions* **2017**, *201*, 207–219.

166. Bredas, J.-L. Mind the Gap! *Mater. Horiz.* **2014**, *1*, 17–19.
167. Mori-Sánchez, P.; Cohen, A. J. The Derivative Discontinuity of the Exchange–Correlation Functional. *Phys. Chem. Chem. Phys.* **2014**, *16*, 14378–14387.
168. Mori-Sánchez, P.; Cohen, A. J.; Yang, W. Localization and Delocalization Errors in Density Functional Theory and Implications for Band-Gap Prediction. *Phys. Rev. Lett.* **2008**, *100*, 146401.
169. Yamada, K. *Electron Correlation in Metals*; Cambridge University Press: Leiden, 2004.
170. Matsuda, Y.; Tahir-Kheli, J.; Goddard, W. A. Definitive Band Gaps for Single-Wall Carbon Nanotubes. *J. Phys. Chem. Lett.* **2010**, *1*, 2946–2950.
171. Godby, R. W.; Schlüter, M.; Sham, L. J. Accurate Exchange-Correlation Potential for Silicon and Its Discontinuity on Addition of an Electron. *Phys. Rev. Lett.* **1986**, *56*, 2415–2418.
172. Fritsch, D.; Morgan, B. J.; Walsh, A. Self-Consistent Hybrid Functional Calculations: Implications for Structural, Electronic, and Optical Properties of Oxide Semiconductors. *Nanoscale Res Lett* **2017**, *12*, 19.
173. Rieth, A. J.; Wright, A. M.; Skorupskii, G.; Mancuso, J. L.; Hendon, C. H.; Dincă, M. Record-Setting Sorbents for Reversible Water Uptake by Systematic Anion Exchanges in Metal–Organic Frameworks. *J. Am. Chem. Soc.* **2019**, *141*, 13858–13866.
174. Monserrat, B.; Dreyer, C. E.; Rabe, K. M. Phonon-Assisted Optical Absorption in BaSnO<sub>3</sub> from First Principles. *Phys. Rev. B* **2018**, *97*, 104310.
175. Morris, A. J.; Monserrat, B. Optical Absorption Driven by Dynamical Symmetry Breaking in Indium Oxide. *Phys. Rev. B* **2018**, *98*, 161203.
176. Pathak, A. et al. Integration of a (–Cu–S–)<sub>n</sub> Plane in a Metal–Organic Framework Affords High Electrical Conductivity. *Nat Commun* **2019**, *10*, 1721.
177. Haldar, R.; Batra, K.; Marschner, S. M.; Kuc, A. B.; Zahn, S.; Fischer, R. A.; Bräse, S.; Heine, T.; Wöll, C. Bridging the Green Gap: Metal–Organic Framework Heteromultilayers Assembled from Porphyrinic Linkers Identified by Using Computational Screening. *Chem. Eur. J.* **2019**, *25*, 7847–7851.
178. Li, Y.; Xu, H.; Ouyang, S.; Ye, J. Metal–Organic Frameworks for Photocatalysis. *Phys. Chem. Chem. Phys.* **2016**, *18*, 7563–7572.

179. Dhakshinamoorthy, A.; Li, Z.; Garcia, H. Catalysis and Photocatalysis by Metal Organic Frameworks. *Chem. Soc. Rev.* **2018**, *47*, 8134–8172.
180. Wang, H.; Zhu, Q.-L.; Zou, R.; Xu, Q. Metal-Organic Frameworks for Energy Applications. *Chem* **2017**, *2*, 52–80.
181. Liu, W.; Yin, X.-B. Metal–Organic Frameworks for Electrochemical Applications. *TrAC Trends in Analytical Chemistry* **2016**, *75*, 86–96.
182. Zeng, L.; Guo, X.; He, C.; Duan, C. Metal–Organic Frameworks: Versatile Materials for Heterogeneous Photocatalysis. *ACS Catal.* **2016**, *6*, 7935–7947.
183. Usman, M.; Mendiratta, S.; Lu, K.-L. Semiconductor Metal-Organic Frameworks: Future Low-Bandgap Materials. *Adv. Mater.* **2017**, *29*, 1605071.
184. Madelung, O. *Introduction to Solid-State Theory*; Solid-State Sciences; Springer, 1978; Vol. 2.
185. Rosenberg, H. M. *The Solid State*, 3rd ed.; Oxford Physics; Oxford Science, 1988; Vol. 9.
186. Aziz, A.; Ruiz-Salvador, A. R.; Hernández, N. C.; Calero, S.; Hamad, S.; Grau-Crespo, R. Porphyrin-Based Metal-Organic Frameworks for Solar Fuel Synthesis Photocatalysis: Band Gap Tuning via Iron Substitutions. *J. Mater. Chem. A* **2017**, *5*, 11894–11904.
187. Syzgantseva, M. A.; Ireland, C. P.; Ebrahim, F. M.; Smit, B.; Syzgantseva, O. A. Metal Substitution as the Method of Modifying Electronic Structure of Metal–Organic Frameworks. *J. Am. Chem. Soc.* **2019**, *141*, 6271–6278.
188. Yang, L.-M.; Ravindran, P.; Vajeeston, P.; Tilset, M. Properties of IRMOF-14 and Its Analogues M-IRMOF-14 (M = Cd, Alkaline Earth Metals): Electronic Structure, Structural Stability, Chemical Bonding, and Optical Properties. *Phys. Chem. Chem. Phys.* **2012**, *14*, 4713.
189. Mancuso, J. L.; Hendon, C. H. Titanium(IV) Inclusion as a Versatile Route to Photoactivity in Metal–Organic Frameworks. *Adv. Theory Simul.* **2019**, 1900126.
190. Chong, S.; Kim, J. Rational Modifications of PCN-700 to Induce Electrical Conductivity: A Computational Study. *Dalton Transactions* **2020**, *49*, 102–113.



191. Choi, J. H.; Choi, Y. J.; Lee, J. W.; Shin, W. H.; Kang, J. K. Tunability of Electronic Band Gaps from Semiconducting to Metallic States via Tailoring Zn Ions in MOFs with Co Ions. *Phys. Chem. Chem. Phys.* **2009**, *11*, 628–631.
192. Li, J.; Musho, T.; Bright, J.; Wu, N. Functionalization of a Metal–Organic Framework Semiconductor for Tuned Band Structure and Catalytic Activity. *Journal of The Electrochemical Society* **2019**, *166*, H3029–H3034.
193. Hendon, C. H.; Tiana, D.; Fontecave, M.; Sanchez, C.; D’arras, L.; Sassoie, C.; Rozes, L.; Mellot-Draznieks, C.; Walsh, A. Engineering the Optical Response of the Titanium-MIL-125 Metal–Organic Framework through Ligand Functionalization. *J. Am. Chem. Soc.* **2013**, *135*, 10942–10945.
194. Li, Y.; Fu, Y.; Ni, B.; Ding, K.; Chen, W.; Wu, K.; Huang, X.; Zhang, Y. Effects of Ligand Functionalization on the Photocatalytic Properties of Titanium-Based MOF: A Density Functional Theory Study. *AIP Advances* **2018**, *8*, 035012.
195. Mu, X.; Jiang, J.; Chao, F.; Lou, Y.; Chen, J. Ligand Modification of UiO-66 with an Unusual Visible Light Photocatalytic Behavior for RhB Degradation. *Dalton Transactions* **2018**, *47*, 1895–1902.
196. Musho, T.; Li, J.; Wu, N. Band Gap Modulation of Functionalized Metal–Organic Frameworks. *Phys. Chem. Chem. Phys.* **2014**, *16*, 23646–23653.
197. Taddei, M.; Schukraft, G. M.; Warwick, M. E. A.; Tiana, D.; McPherson, M. J.; Jones, D. R.; Petit, C. Band Gap Modulation in Zirconium-Based Metal–Organic Frameworks by Defect Engineering. *Journal of Materials Chemistry A* **2019**, *7*, 23781–23786.
198. Zhang, G.; Chan, J. M. W. Reversibly Thermochromic Bismuth–Organic Materials with Tunable Optical Gaps. *Journal of Materials Chemistry C* **2017**, *5*, 10007–10015.
199. Grau-Crespo, R.; Aziz, A.; Collins, A. W.; Crespo-Otero, R.; Hernández, N. C.; Rodriguez-Albelo, L. M.; Ruiz-Salvador, A. R.; Calero, S.; Hamad, S. Modelling a Linker Mix-and-Match Approach for Controlling the Optical Excitation Gaps and Band Alignment of Zeolitic Imidazolate Frameworks. *Angew. Chem. Int. Ed.* **2016**, *55*, 16012–16016.

200. Taddei, M.; Tiana, D.; Casati, N.; van Bokhoven, J. A.; Smit, B.; Ranocchiari, M. Mixed-Linker UiO-66: Structure–Property Relationships Revealed by a Combination of High-Resolution Powder X-Ray Diffraction and Density Functional Theory Calculations. *Phys. Chem. Chem. Phys.* **2017**, *19*, 1551–1559.
201. Fuentes-Cabrera, M.; Nicholson, D. M.; Sumpter, B. G.; Widom, M. Electronic Structure and Properties of Isorecticular Metal–Organic Frameworks: The Case of M-IRMOF1 (M=Zn, Cd, Be, Mg, and Ca). *The Journal of Chemical Physics* **2005**, *123*, 124713.
202. Choi, J. H.; Jeon, H. J.; Choi, K. M.; Kang, J. K. Metal–Organic Frameworks for Visible Light Absorption via Anion Substitution. *J. Mater. Chem.* **2012**, *22*, 10144.
203. Botas, J. A.; Calleja, G.; Sánchez-Sánchez, M.; Orcajo, M. G. Cobalt Doping of the MOF-5 Framework and Its Effect on Gas-Adsorption Properties. *Langmuir* **2010**, *26*, 5300–5303.
204. Venkataramanan, N. S.; Sahara, R.; Mizuseki, H.; Kawazoe, Y. Probing the Structure, Stability and Hydrogen Adsorption of Lithium Functionalized Isorecticular MOF-5 (Fe, Cu, Co, Ni and Zn) by Density Functional Theory. *IJMS* **2009**, *10*, 1601–1608.
205. Pham, H. Q.; Mai, T.; Pham-Tran, N.-N.; Kawazoe, Y.; Mizuseki, H.; Nguyen-Manh, D. Engineering of Band Gap in Metal–Organic Frameworks by Functionalizing Organic Linker: A Systematic Density Functional Theory Investigation. *J. Phys. Chem. C* **2014**, *118*, 4567–4577.
206. Gascon, J.; Hernández-Alonso, M. D.; Almeida, A. R.; van Klink, G. P. M.; Kapteijn, F.; Mul, G. Isorecticular MOFs as Efficient Photocatalysts with Tunable Band Gap: An Operando FTIR Study of the Photoinduced Oxidation of Propylene. *ChemSusChem* **2008**, *1*, 981–983.
207. Salih, Z. I.; Guo, Y.-J.; Zheng, J.-J.; Zhao, X. Effect of Modified Linkers of MOF-5 on Enhancing Interaction Energies: A Theoretical Study. *Computational and Theoretical Chemistry* **2015**, *1058*, 28–33.
208. Yang, L.-M.; Ravindran, P.; Vajeeston, P.; Tilset, M. Ab Initio Investigations on the Crystal Structure, Formation Enthalpy, Electronic Structure, Chemical Bonding, and Optical Properties of Experimentally Synthesized Isorecticular Metal–Organic Framework-10 and Its Analogues: M-IRMOF-10 (M = Zn, Cd, Be, Mg, Ca, Sr and Ba). *RSC Adv.* **2012**, *2*, 1618–1631.

209. Hendon, C. H.; Rieth, A. J.; Korzyński, M. D.; Dincă, M. Grand Challenges and Future Opportunities for Metal–Organic Frameworks. *ACS Central Science* **2017**, *3*, 554–563.
210. Yilmaz, G.; Peh, S. B.; Zhao, D.; Ho, G. W. Atomic- and Molecular-Level Design of Functional Metal–Organic Frameworks (MOFs) and Derivatives for Energy and Environmental Applications. *Advanced Science* **2019**, *6*, 1901129.
211. Santaclara, J. G.; Kapteijn, F.; Gascon, J.; van der Veen, M. A. Understanding Metal–Organic Frameworks for Photocatalytic Solar Fuel Production. *CrystEngComm* **2017**, *19*, 4118–4125.
212. Evarestov, R. A.; Smirnov, V. P. Special points of the brillouin zone and their use in the solid state theory. *phys. stat. sol. (b)* **1983**, *119*, 9–40.
213. Chadi, D. J.; Cohen, M. L. Special Points in the Brillouin Zone. *Phys. Rev. B* **1973**, *8*, 5747–5753.
214. Hoffmann, R. How Chemistry and Physics Meet in the Solid State. *Angewandte Chemie International Edition in English* **1987**, *26*, 846–878.
215. Hoffmann, R. Interaction of Orbitals through Space and through Bonds. *Acc. Chem. Res.* **1971**, *4*, 1–9.
216. Sun, L.; Campbell, M. G.; Dincă, M. Electrically Conductive Porous Metal–Organic Frameworks. *Angew. Chem. Int. Ed.* **2016**, *55*, 3566–3579.
217. Skorupskii, G.; Trump, B. A.; Kasel, T. W.; Brown, C. M.; Hendon, C. H.; Dincă, M. Efficient and Tunable One-Dimensional Charge Transport in Layered Lanthanide Metal–Organic Frameworks. *Nature Chemistry* **2020**, *12*, 131–136.
218. Ivanov, M. V.; Wadumethrige, S. H.; Wang, D.; Rathore, R. Through-Space or Through-Bond? The Important Role of Cofaciality in Orbital Reordering and Its Implications for Hole (De)Stabilization in Polychromophoric Assemblies. *The Journal of Physical Chemistry C* **2017**, *121*, 15639–15643.
219. Scholes, G. D.; Ghiggino, K. P.; Oliver, A. M.; Paddon-Row, M. N. Through-Space and through-Bond Effects on Exciton Interactions in Rigidly Linked Dinaphthyl Molecules. *Journal of the American Chemical Society* **1993**, *115*, 4345–4349.
220. Liu, Z.; Liu, F.; Wu, Y.-S. Exotic Electronic States in the World of Flat Bands: From Theory to Material. *Chinese Phys. B* **2014**, *23*, 077308.

221. Pedersen, F. B. Simple Derivation of the Effective-Mass Equation Using a Multiple-Scale Technique. *Eur. J. Phys.* **1997**, *18*, 43–45.
222. Liu, J. et al. Photoinduced Charge-Carrier Generation in Epitaxial MOF Thin Films: High Efficiency as a Result of an Indirect Electronic Band Gap? *Angew. Chem. Int. Ed.* **2015**, *54*, 7441–7445.
223. Yu, S.; Li, S.; Meng, X.; Wan, C.; Ju, X. Tuning the Hydrogen Adsorption Properties of Zn-Based Metal–Organic Frameworks: Combined DFT and GCMC Simulations. *Journal of Solid State Chemistry* **2018**, *266*, 31–36.
224. Erkartal, M.; Durandurdu, M. Pressure-Induced Amorphization of MOF-5: A First Principles Study. *Chemistry Select* **2018**, *3*, 8056–8063.
225. Xie, L. S.; Sun, L.; Wan, R.; Park, S. S.; DeGayner, J. A.; Hendon, C. H.; Dincă, M. Tunable Mixed-Valence Doping toward Record Electrical Conductivity in a Three-Dimensional Metal–Organic Framework. *Journal of the American Chemical Society* **2018**, *140*, 7411–7414.
226. Žutić, I.; Fabian, J.; Das Sarma, S. Spintronics: Fundamentals and Applications. *Reviews of Modern Physics* **2004**, *76*, 323–410.
227. Zhang, Y.; Riduan, S. N.; Wang, J. Redox Active Metal- and Covalent Organic Frameworks for Energy Storage: Balancing Porosity and Electrical Conductivity. *Chem. Eur. J.* **2017**, *23*, 16419–16431.
228. Wentz, H. C.; Skorupskii, G.; Bonfim, A. B.; Mancuso, J. L.; Hendon, C. H.; Oriel, E. H.; Sazama, G. T.; Campbell, M. G. Switchable Electrical Conductivity in a Three-Dimensional Metal–Organic Framework *via* Reversible Ligand n-Doping. *Chem. Sci.* **2020**, *11*, 1342–1346.
229. Darago, L. E.; Aubrey, M. L.; Yu, C. J.; Gonzalez, M. I.; Long, J. R. Electronic Conductivity, Ferrimagnetic Ordering, and Reductive Insertion Mediated by Organic Mixed-Valence in a Ferric Semiquinoid Metal–Organic Framework. *J. Am. Chem. Soc.* **2015**, *137*, 15703–15711.
230. Usov, P. M.; Huffman, B.; Epley, C. C.; Kessinger, M. C.; Zhu, J.; Maza, W. A.; Morris, A. J. Study of Electrocatalytic Properties of Metal–Organic Framework PCN-223 for the Oxygen Reduction Reaction. *ACS Appl. Mater. Interfaces* **2017**, *9*, 33539–33543.
231. Lin, S.; Usov, P. M.; Morris, A. J. The Role of Redox Hopping in Metal–Organic Framework Electrocatalysis. *Chem. Commun.* **2018**, *54*, 6965–6974.

232. Walton, K. S.; Snurr, R. Q. Applicability of the BET Method for Determining Surface Areas of Microporous Metal-Organic Frameworks. *J. Am. Chem. Soc.* **2007**, *129*, 8552–8556.
233. Marshall, C. R.; Staudhammer, S. A.; Brozek, C. K. Size Control over Metal-Organic Framework Porous Nanocrystals. *Chem. Sci.* **2019**,
234. McCluskey, M. D.; Haller, E. E. *Dopants and Defects in Semiconductors*, 2nd ed.; CRC Press.
235. Müller, K.; Fink, K.; Schöttner, L.; Koenig, M.; Heinke, L.; Wöll, C. Defects as Color Centers: The Apparent Color of Metal–Organic Frameworks Containing Cu<sup>2+</sup>-Based Paddle-Wheel Units. *ACS Applied Materials & Interfaces* **2017**, *9*, 37463–37467.
236. Sholl, D. S.; Lively, R. P. Defects in Metal–Organic Frameworks: Challenge or Opportunity? *J. Phys. Chem. Lett.* **2015**, *6*, 3437–3444.
237. Fang, Z.; Bueken, B.; De Vos, D. E.; Fischer, R. A. Defect-Engineered Metal-Organic Frameworks. *Angew. Chem. Int. Ed.* **2015**, *54*, 7234–7254.
238. Smyth, D. M. *The Defect Chemistry of Metal Oxides*, 1st ed.; Monographs on the Physics and Chemistry of Materials; Oxford University Press, 2000.
239. Canivet, J.; Vandichel, M.; Farrusseng, D. Origin of Highly Active Metal–Organic Framework Catalysts: Defects? Defects! *Dalton Trans.* **2016**, *45*, 4090–4099.
240. Shearer, G. C.; Chavan, S.; Ethiraj, J.; Vitillo, J. G.; Svelle, S.; Olsbye, U.; Lamberti, C.; Bordiga, S.; Lillerud, K. P. Tuned to Perfection: Ironing Out the Defects in Metal–Organic Framework UiO-66. *Chem. Mater.* **2014**, *26*, 4068–4071.
241. Jiang, Z.-R.; Wang, H.; Hu, Y.; Lu, J.; Jiang, H.-L. Polar Group and Defect Engineering in a Metal-Organic Framework: Synergistic Promotion of Carbon Dioxide Sorption and Conversion. *ChemSusChem* **2015**, *8*, 878–885.
242. Studt, F.; Abild-Pedersen, F.; Bligaard, T.; Sorensen, R. Z.; Christensen, C. H.; Norskov, J. K. Identification of Non-Precious Metal Alloy Catalysts for Selective Hydrogenation of Acetylene. *Science* **2008**, *320*, 1320–1322.
243. Norskov, J. K.; Abild-Pedersen, F.; Studt, F.; Bligaard, T. Density Functional Theory in Surface Chemistry and Catalysis. *Proceedings of the National Academy of Sciences* **2011**, *108*, 937–943.

244. Nilsson, A.; Pettersson, L. G. M.; Hammer, B.; Bligaard, T.; Christensen, C. H.; Nørskov, J. K. The Electronic Structure Effect in Heterogeneous Catalysis. *Catal Lett* **2005**, *100*, 111–114.
245. Gajdo, M.; Eichler, A.; Hafner, J. CO Adsorption on Close-Packed Transition and Noble Metal Surfaces: Trends from *Ab Initio* Calculations. *J. Phys.: Condens. Matter* **2004**, *16*, 1141–1164.
246. Nanba, Y.; Koyama, M. NO Adsorption on 4d and 5d Transition-Metal (Rh, Pd, Ag, Ir, and Pt) Nanoparticles: Density Functional Theory Study and Supervised Learning. *J. Phys. Chem. C* **2019**, *123*, 28114–28122.
247. Queisser, H. J. Defects in Semiconductors: Some Fatal, Some Vital. *Science* **1998**, *281*, 945–950.
248. Nasalevich, M. A.; Hendon, C. H.; Santaclara, J. G.; Svane, K.; van der Linden, B.; Veber, S. L.; Fedin, M. V.; Houtepen, A. J.; van der Veen, M. A.; Kapteijn, F.; Walsh, A.; Gascon, J. Electronic Origins of Photocatalytic Activity in D0 Metal Organic Frameworks. *Sci Rep* **2016**, *6*, 23676.
249. Lee, S. J.; Doussot, C.; Baux, A.; Liu, L.; Jameson, G. B.; Richardson, C.; Pak, J. J.; Trouselet, F.; Coudert, F.-X.; Telfer, S. G. Multicomponent Metal–Organic Frameworks as Defect-Tolerant Materials. *Chem. Mater.* **2016**, *28*, 368–375.
250. Kannemann, F. O.; Becke, A. D. Van Der Waals Interactions in Density-Functional Theory: Intermolecular Complexes. *J. Chem. Theory Comput.* **2010**, *6*, 1081–1088.
251. *Compendium of Biophysics*; John Wiley & Sons, Inc.: Hoboken, NJ, USA, 2017; pp 109–116.
252. McAnanama-Brereton, S.; Waller, M. P. Rational Density Functional Selection Using Game Theory. *Journal of Chemical Information and Modeling* **2018**, *58*, 61–67.
253. Dunning, T. H. Gaussian Basis Sets for Use in Correlated Molecular Calculations. I. The Atoms Boron through Neon and Hydrogen. *The Journal of Chemical Physics* **1989**, *90*, 1007–1023.
254. Scuseria, G. E.; Janssen, C. L.; Schaefer, H. F. An Efficient Reformulation of the Closed-shell Coupled Cluster Single and Double Excitation (CCSD) Equations. *The Journal of Chemical Physics* **1988**, *89*, 7382–7387.

255. Scuseria, G. E.; Schaefer, H. F. Is Coupled Cluster Singles and Doubles (CCSD) More Computationally Intensive than Quadratic Configuration Interaction (QCISD)? *The Journal of Chemical Physics* **1989**, *90*, 3700–3703.
256. Purvis, G. D.; Bartlett, R. J. A Full Coupled-cluster Singles and Doubles Model: The Inclusion of Disconnected Triples. *The Journal of Chemical Physics* **1982**, *76*, 1910–1918.
257. LeFebvre, R., Moser, C., Eds. *Advances in Chemical Physics: LeFebvre/Advances*; Advances in Chemical Physics; John Wiley & Sons, Inc.: Hoboken, NJ, USA, 1969.
258. Becke, A. D. Density-functional Thermochemistry. IV. A New Dynamical Correlation Functional and Implications for Exact-exchange Mixing. *The Journal of Chemical Physics* **1996**, *104*, 1040–1046.
259. Slater, J. C. *Quantum Theory of Molecules and Solids*; International Series in Pure and Applied Physics; McGraw-Hill: New York, 1963.
260. Pople, J. A.; Seeger, R.; Krishnan, R. Variational Configuration Interaction Methods and Comparison with Perturbation Theory. *Int. J. Quantum Chem.* **2009**, *12*, 149–163.
261. Pople, J. A.; Binkley, J. S.; Seeger, R. Theoretical Models Incorporating Electron Correlation. *Int. J. Quantum Chem.* **2009**, *10*, 1–19.
262. Gill, P. M. W. A New Gradient-Corrected Exchange Functional. *Molecular Physics* **1996**, *89*, 433–445.
263. Krishnan, R.; Frisch, M. J.; Pople, J. A. Contribution of Triple Substitutions to the Electron Correlation Energy in Fourth Order Perturbation Theory. *The Journal of Chemical Physics* **1980**, *72*, 4244–4245.
264. Krishnan, R.; Pople, J. A. Approximate Fourth-Order Perturbation Theory of the Electron Correlation Energy. *Int. J. Quantum Chem.* **1978**, *14*, 91–100.
265. Handy, N. C.; Cohen, A. J. Left-Right Correlation Energy. *Molecular Physics* **2001**, *99*, 403–412.
266. Hoe, W.-M.; Cohen, A. J.; Handy, N. C. Assessment of a New Local Exchange Functional OPTX. *Chemical Physics Letters* **2001**, *341*, 319–328.
267. Chai, J.-D.; Head-Gordon, M. Long-Range Corrected Hybrid Density Functionals with Damped Atom–Atom Dispersion Corrections. *Phys. Chem. Chem. Phys.* **2008**, *10*, 6615.

268. Perdew, J. P.; Burke, K.; Ernzerhof, M. Generalized Gradient Approximation Made Simple [Phys. Rev. Lett. 77, 3865 (1996)]. *Physical Review Letters* **1997**, *78*, 1396–1396.
269. Austin, A.; Petersson, G. A.; Frisch, M. J.; Dobek, F. J.; Scalmani, G.; Throssell, K. A Density Functional with Spherical Atom Dispersion Terms. *J. Chem. Theory Comput.* **2012**, *8*, 4989–5007.
270. Yanai, T.; Tew, D.; Handy, N. A New Hybrid Exchange-Correlation Functional Using the Coulomb-Attenuating Method. *Chem. Phys. Lett.* **2004**, *393*, 51–57.
271. Grimme, S. Semiempirical GGA-Type Density Functional Constructed with a Long-Range Dispersion Correction. *J. Comput. Chem.* **2006**, *27*, 1787–1799.
272. Miehlich, B.; Savin, A.; Stoll, H.; Preuss, H. Results Obtained with the Correlation-Energy Density Functionals of Becke and Lee, Yang and Par. *Chem. Phys. Lett.* **1989**, *157*, 200–206.
273. Becke, A. D. A New Mixing of Hartree–Fock and Local Density-functional Theories. *The Journal of Chemical Physics* **1993**, *98*, 1372–1377.
274. Boese, A. D.; Handy, N. C. A New Parametrization of Exchange–Correlation Generalized Gradient Approximation Functionals. *The Journal of Chemical Physics* **2001**, *114*, 5497–5503.
275. Boese, A. D.; Doltsinis, N. L.; Handy, N. C.; Sprik, M. New Generalized Gradient Approximation Functionals. *The Journal of Chemical Physics* **2000**, *112*, 1670–1678.
276. Hamprecht, F. A.; Cohen, A. J.; Tozer, D. J.; Handy, N. C. Development and Assessment of New Exchange-Correlation Functionals. *The Journal of Chemical Physics* **1998**, *109*, 6264–6271.
277. Vydrov, O. A.; Scuseria, G. E.; Perdew, J. P. Tests of Functionals for Systems with Fractional Electron Number. *The Journal of Chemical Physics* **2007**, *126*, 154109.
278. Vydrov, O. A.; Scuseria, G. E. Assessment of a Long-Range Corrected Hybrid Functional. *The Journal of Chemical Physics* **2006**, *125*, 234109.
279. Vreven, T.; Frisch, M. J.; Kudin, K. N.; Schlegel, H. B.; Morokuma, K. Geometry Optimization with QM/MM Methods II: Explicit Quadratic Coupling. *Molecular Physics* **2006**, *104*, 701–714.



280. Peverati, R.; Truhlar, D. G. Improving the Accuracy of Hybrid Meta-GGA Density Functionals by Range Separation. *J. Phys. Chem. Lett.* **2011**, *2*, 2810–2817.
281. Perdew, J. P.; Chevary, J. A.; Vosko, S. H.; Jackson, K. A.; Pederson, M. R.; Singh, D. J.; Fiolhais, C. Erratum: Atoms, Molecules, Solids, and Surfaces: Applications of the Generalized Gradient Approximation for Exchange and Correlation. *Phys. Rev. B* **1993**, *48*, 4978–4978.
282. Dobson, J. F., Vignale, G., Das, M. P., Eds. *Electronic Density Functional Theory: Recent Progress and New Directions*; Plenum Press: New York, 1998.
283. Ernzerhof, M.; Scuseria, G. E. Assessment of the Perdew–Burke–Ernzerhof Exchange–Correlation Functional. *The Journal of Chemical Physics* **1999**, *110*, 5029–5036.
284. Peverati, R.; Zhao, Y.; Truhlar, D. G. Generalized Gradient Approximation That Recovers the Second-Order Density-Gradient Expansion with Optimized Across-the-Board Performance. *J. Phys. Chem. Lett.* **2011**, *2*, 1991–1997.
285. Xu, X.; Goddard, W. A. From The Cover: The X3LYP Extended Density Functional for Accurate Descriptions of Nonbond Interactions, Spin States, and Thermochemical Properties. *Proceedings of the National Academy of Sciences* **2004**, *101*, 2673–2677.
286. Adamo, C.; Barone, V. Exchange Functionals with Improved Long-Range Behavior and Adiabatic Connection Methods without Adjustable Parameters: The mPW and mPW1PW Models. *The Journal of Chemical Physics* **1998**, *108*, 664–675.
287. Boese, A. D.; Martin, J. M. L. Development of Density Functionals for Thermochemical Kinetics. *The Journal of Chemical Physics* **2004**, *121*, 3405–3416.
288. Peverati, R.; Truhlar, D. G. M11-L: A Local Density Functional That Provides Improved Accuracy for Electronic Structure Calculations in Chemistry and Physics. *J. Phys. Chem. Lett.* **2012**, *3*, 117–124.
289. Staroverov, V. N.; Scuseria, G. E.; Tao, J.; Perdew, J. P. Comparative Assessment of a New Nonempirical Density Functional: Molecules and Hydrogen-Bonded Complexes. *The Journal of Chemical Physics* **2003**, *119*, 12129–12137.

290. Staroverov, V. N.; Scuseria, G. E.; Tao, J.; Perdew, J. P. Erratum: “Comparative Assessment of a New Nonempirical Density Functional: Molecules and Hydrogen-Bonded Complexes” [J. Chem. Phys. 119, 12129 (2003)]. *J. Chem. Phys.* **2004**, *121*, 11507.
291. Van Voorhis, T.; Scuseria, G. E. A Novel Form for the Exchange-Correlation Energy Functional. *The Journal of Chemical Physics* **1998**, *109*, 400–410.
292. Boese, A. D.; Handy, N. C. New Exchange-Correlation Density Functionals: The Role of the Kinetic-Energy Density. *The Journal of Chemical Physics* **2002**, *116*, 9559–9569.
293. Kafader, J. O.; Ray, M.; Jarrold, C. C. Low-Lying Electronic Structure of EuH, EuOH, and EuO Neutrals and Anions Determined by Anion Photoelectron Spectroscopy and DFT Calculations. *The Journal of Chemical Physics* **2015**, *143*, 034305.
294. Breck, D. W. Zeolite Molecular Sieves: Structure, Chemistry, and Use. *Journal of Chromatographic Science* **1975**, *13*, 18A–18A.
295. Yampol'skii, Y. P., Pinnau, I., Freeman, B. D., Eds. *Materials Science of Membranes for Gas and Vapor Separation*; Wiley: Chichester, England ; Hoboken, NJ, 2006.
296. Adil, K.; Belmabkhout, Y.; Pillai, R. S.; Cadiau, A.; Bhatt, P. M.; Assen, A. H.; Maurin, G.; Eddaoudi, M. Gas/Vapour Separation Using Ultra-Microporous Metal–Organic Frameworks: Insights into the Structure/Separation Relationship. *Chemical Society Reviews* **2017**, *46*, 3402–3430.
297. Correia, D. M.; Barbosa, J. C.; Costa, C. M.; Reis, P. M.; Esperança, J. M. S. S.; de Zea Bermudez, V.; Lanceros-Méndez, S. Ionic Liquid Cation Size-Dependent Electromechanical Response of Ionic Liquid/Poly(Vinylidene Fluoride)-Based Soft Actuators. *The Journal of Physical Chemistry C* **2019**, *123*, 12744–12752.
298. Spohr, H. V.; Patey, G. N. Structural and Dynamical Properties of Ionic Liquids: The Influence of Ion Size Disparity. *The Journal of Chemical Physics* **2008**, *129*, 064517.
299. Scanlon, D. O.; Watson, G. W. Understanding the P-Type Defect Chemistry of CuCrO<sub>2</sub>. *J. Mater. Chem.* **2011**, *21*, 3655.
300. Rahm, M.; Zeng, T.; Hoffmann, R. Electronegativity Seen as the Ground-State Average Valence Electron Binding Energy. *J. Am. Chem. Soc.* **2019**, *141*, 342–351.

301. Chaban, V. V.; Andreeva, N. A.; Fileti, E. E. Graphene/Ionic Liquid Ultracapacitors: Does Ionic Size Correlate with Energy Storage Performance? *New Journal of Chemistry* **2018**, *42*, 18409–18417.
302. LeRoy, M. A.; Mroz, A. M.; Mancuso, J. L.; Miller, A.; Van Cleve, A.; Check, C.; Heinz, H.; Hendon, C. H.; Brozek, C. K. Post-Synthetic Modification of Ionic Liquids Using Ligand-Exchange and Redox Coordination Chemistry. *J. Mater. Chem. A* **2020**, *8*, 22674–22685.
303. Yaghi, O. M.; Li, G.; Li, H. Selective Binding and Removal of Guests in a Microporous Metal–Organic Framework. *Nature* **1995**, *378*, 703–706.
304. Furukawa, H.; Cordova, K. E.; O’Keeffe, M.; Yaghi, O. M. The Chemistry and Applications of Metal–Organic Frameworks. *Science* **2013**, *341*, 1230444–1230444.
305. Kitagawa, S.; Kitaura, R.; Noro, S.-i. Functional Porous Coordination Polymers. *Angewandte Chemie International Edition* **2004**, *43*, 2334–2375.
306. Li, H.; Eddaoudi, M.; O’Keeffe, M.; Yaghi, O. M. Design and Synthesis of an Exceptionally Stable and Highly Porous Metal–Organic Framework. *Nature* **1999**, *402*, 276–279.
307. Eddaoudi, M.; Moler, D. B.; Li, H.; Chen, B.; Reineke, T. M.; O’Keeffe, M.; Yaghi, O. M. Modular Chemistry: Secondary Building Units as a Basis for the Design of Highly Porous and Robust Metal–Organic Carboxylate Frameworks. *Accounts of Chemical Research* **2001**, *34*, 319–330.
308. Tranchemontagne, D. J.; Mendoza-Cortés, J. L.; O’Keeffe, M.; Yaghi, O. M. Secondary Building Units, Nets and Bonding in the Chemistry of Metal–Organic Frameworks. *Chem. Soc. Rev.* **2009**, *38*, 1257.
309. Kawano, M.; Kawamichi, T.; Haneda, T.; Kojima, T.; Fujita, M. The Modular Synthesis of Functional Porous Coordination Networks. *Journal of the American Chemical Society* **2007**, *129*, 15418–15419.
310. Furukawa, H.; Ko, N.; Go, Y. B.; Aratani, N.; Choi, S. B.; Choi, E.; Yazaydin, A. O.; Snurr, R. Q.; O’Keeffe, M.; Kim, J.; Yaghi, O. M. Ultrahigh Porosity in Metal–Organic Frameworks. *Science* **2010**, *329*, 424–428.
311. Eddaoudi, M.; Li, H.; Yaghi, O. M. Highly Porous and Stable Metal–Organic Frameworks: Structure Design and Sorption Properties. *Journal of the American Chemical Society* **2000**, *122*, 1391–1397.
312. Li, J.-R.; Sculley, J.; Zhou, H.-C. Metal–Organic Frameworks for Separations. *Chemical Reviews* **2012**, *112*, 869–932.

313. Stassen, I.; Burtch, N.; Talin, A.; Falcaro, P.; Allendorf, M.; Ameloot, R. An Updated Roadmap for the Integration of Metal–Organic Frameworks with Electronic Devices and Chemical Sensors. *Chem. Soc. Rev.* **2017**, *46*, 3185–3241.
314. Liu, L.; Zhou, Y.; Liu, S.; Xu, M. The Applications of Metal–Organic Frameworks in Electrochemical Sensors. *ChemElectroChem* **2018**, *5*, 6–19.
315. Choi, K. M.; Jeong, H. M.; Park, J. H.; Zhang, Y.-B.; Kang, J. K.; Yaghi, O. M. Supercapacitors of Nanocrystalline Metal–Organic Frameworks. *ACS Nano* **2014**, *8*, 7451–7457.
316. Morozan, A.; Jaouen, F. Metal Organic Frameworks for Electrochemical Applications. *Energy & Environmental Science* **2012**, *5*, 9269.
317. Sheberla, D.; Bachman, J. C.; Elias, J. S.; Sun, C.-J.; Shao-Horn, Y.; Dincă, M. Conductive MOF Electrodes for Stable Supercapacitors with High Areal Capacitance. *Nature Materials* **2017**, *16*, 220–224.
318. Wang, L.; Han, Y.; Feng, X.; Zhou, J.; Qi, P.; Wang, B. Metal–Organic Frameworks for Energy Storage: Batteries and Supercapacitors. *Coordination Chemistry Reviews* **2016**, *307*, 361–381.
319. Xia, W.; Mahmood, A.; Zou, R.; Xu, Q. Metal–Organic Frameworks and Their Derived Nanostructures for Electrochemical Energy Storage and Conversion. *Energy & Environmental Science* **2015**, *8*, 1837–1866.
320. Xu, Y.; Li, Q.; Xue, H.; Pang, H. Metal–Organic Frameworks for Direct Electrochemical Applications. *Coordination Chemistry Reviews* **2018**, *376*, 292–318.
321. Zheng, S.; Li, X.; Yan, B.; Hu, Q.; Xu, Y.; Xiao, X.; Xue, H.; Pang, H. Transition-Metal (Fe, Co, Ni) Based Metal–Organic Frameworks for Electrochemical Energy Storage. *Advanced Energy Materials* **2017**, *7*, 1602733.
322. Yamabayashi, T.; Atzori, M.; Tesi, L.; Cosquer, G.; Santanni, F.; Boulon, M.-E.; Morra, E.; Benci, S.; Torre, R.; Chiesa, M.; Sorace, L.; Sessoli, R.; Yamashita, M. Scaling Up Electronic Spin Qubits into a Three-Dimensional Metal–Organic Framework. *Journal of the American Chemical Society* **2018**, *140*, 12090–12101.
323. Zadrozny, J. M.; Gallagher, A. T.; Harris, T. D.; Freedman, D. E. A Porous Array of Clock Qubits. *J. Am. Chem. Soc.* **2017**, *139*, 7089–7094.

324. Mezenov, Y. A.; Krasilin, A. A.; Dzyuba, V. P.; Nominé, A.; Milichko, V. A. Metal–Organic Frameworks in Modern Physics: Highlights and Perspectives. *Advanced Science* **2019**, *6*, 1900506.
325. Lu, W.; Wei, Z.; Gu, Z.-Y.; Liu, T.-F.; Park, J.; Park, J.; Tian, J.; Zhang, M.; Zhang, Q.; Gentle III, T.; Bosch, M.; Zhou, H.-C. Tuning the Structure and Function of Metal–Organic Frameworks via Linker Design. *Chem. Soc. Rev.* **2014**, *43*, 5561–5593.
326. Burnett, B. J.; Barron, P. M.; Hu, C.; Choe, W. Stepwise Synthesis of Metal–Organic Frameworks: Replacement of Structural Organic Linkers. *Journal of the American Chemical Society* **2011**, *133*, 9984–9987.
327. Schoedel, A.; Li, M.; Li, D.; O’Keeffe, M.; Yaghi, O. M. Structures of Metal–Organic Frameworks with Rod Secondary Building Units. *Chemical Reviews* **2016**, *116*, 12466–12535.
328. Vodak, D. T.; Braun, M. E.; Kim, J.; Eddaoudi, M.; Yaghi, O. M. Metal-Organic Frameworks Constructed from Pentagonal Antiprismatic and Cuboctahedral Secondary Building Units. *Chem. Commun.* **2001**, 2534–2535.
329. Colón, Y. J.; Snurr, R. Q. High-Throughput Computational Screening of Metal–Organic Frameworks. *Chem. Soc. Rev.* **2014**, *43*, 5735–5749.
330. Wilmer, C. E.; Leaf, M.; Lee, C. Y.; Farha, O. K.; Hauser, B. G.; Hupp, J. T.; Snurr, R. Q. Large-Scale Screening of Hypothetical Metal-Organic Frameworks. *Nat. Chem.* **2012**, *4*, 83–89.
331. Lalonde, M.; Bury, W.; Karagiari, O.; Brown, Z.; Hupp, J. T.; Farha, O. K. Transmetalation: Routes to Metal Exchange within Metal–Organic Frameworks. *Journal of Materials Chemistry A* **2013**, *1*, 5453.
332. Grancha, T.; Ferrando-Soria, J.; Zhou, H.-C.; Gascon, J.; Seoane, B.; Pasán, J.; Fabelo, O.; Julve, M.; Pardo, E. Postsynthetic Improvement of the Physical Properties in a Metal-Organic Framework through a Single Crystal to Single Crystal Transmetalation. *Angewandte Chemie International Edition* **2015**, *54*, 6521–6525.
333. Asha, K. S.; Bhattacharjee, R.; Mandal, S. Complete Transmetalation in a Metal-Organic Framework by Metal Ion Metathesis in a Single Crystal for Selective Sensing of Phosphate Ions in Aqueous Media. *Angewandte Chemie International Edition* **2016**, *55*, 11528–11532.

334. Das, S.; Kim, H.; Kim, K. Metathesis in Single Crystal: Complete and Reversible Exchange of Metal Ions Constituting the Frameworks of Metal–Organic Frameworks. *Journal of the American Chemical Society* **2009**, *131*, 3814–3815.
335. Song, X.; Kim, T. K.; Kim, H.; Kim, D.; Jeong, S.; Moon, H. R.; Lah, M. S. Post-Synthetic Modifications of Framework Metal Ions in Isostructural Metal–Organic Frameworks: Core–Shell Heterostructures via Selective Transmetalations. *Chemistry of Materials* **2012**, *24*, 3065–3073.
336. Islamoglu, T.; Goswami, S.; Li, Z.; Howarth, A. J.; Farha, O. K.; Hupp, J. T. Postsynthetic Tuning of Metal–Organic Frameworks for Targeted Applications. *Accounts of Chemical Research* **2017**, *50*, 805–813.
337. Kim, M.; Cahill, J. F.; Su, Y.; Prather, K. A.; Cohen, S. M. Postsynthetic Ligand Exchange as a Route to Functionalization of ‘Inert’ Metal–Organic Frameworks. *Chem. Sci.* **2012**, *3*, 126–130.
338. Kim, M.; Cahill, J. F.; Fei, H.; Prather, K. A.; Cohen, S. M. Postsynthetic Ligand and Cation Exchange in Robust Metal–Organic Frameworks. *Journal of the American Chemical Society* **2012**, *134*, 18082–18088.
339. Doonan, C. J.; Morris, W.; Furukawa, H.; Yaghi, O. M. Isoreticular Metalation of Metal–Organic Frameworks. *Journal of the American Chemical Society* **2009**, *131*, 9492–9493.
340. Ma, L.; Falkowski, J. M.; Abney, C.; Lin, W. A Series of Isoreticular Chiral Metal–Organic Frameworks as a Tunable Platform for Asymmetric Catalysis. *Nature Chemistry* **2010**, *2*, 838–846.
341. Bellarosa, L.; Castillo, J. M.; Vlught, T.; Calero, S.; López, N. On the Mechanism Behind the Instability of Isoreticular Metal–Organic Frameworks (IRMOFs) in Humid Environments. *Chemistry - A European Journal* **2012**, *18*, 12260–12266.
342. Colombo, V.; Montoro, C.; Maspero, A.; Palmisano, G.; Masciocchi, N.; Galli, S.; Barea, E.; Navarro, J. A. R. Tuning the Adsorption Properties of Isoreticular Pyrazolate-Based Metal–Organic Frameworks through Ligand Modification. *Journal of the American Chemical Society* **2012**, *134*, 12830–12843.
343. Eddaoudi, M. Systematic Design of Pore Size and Functionality in Isoreticular MOFs and Their Application in Methane Storage. *Science* **2002**, *295*, 469–472.

344. Garibay, S. J.; Cohen, S. M. Isoreticular Synthesis and Modification of Frameworks with the UiO-66 Topology. *Chemical Communications* **2010**, *46*, 7700.
345. Sagara, T.; Klassen, J.; Ortony, J.; Ganz, E. Binding Energies of Hydrogen Molecules to Isoreticular Metal–Organic Framework Materials. *The Journal of Chemical Physics* **2005**, *123*, 014701.
346. Burtch, N. C.; Jasuja, H.; Walton, K. S. Water Stability and Adsorption in Metal–Organic Frameworks. *Chemical Reviews* **2014**, *114*, 10575–10612.
347. Furukawa, H.; Gándara, F.; Zhang, Y.-B.; Jiang, J.; Queen, W. L.; Hudson, M. R.; Yaghi, O. M. Water Adsorption in Porous Metal–Organic Frameworks and Related Materials. *Journal of the American Chemical Society* **2014**, *136*, 4369–4381.
348. Hanikel, N.; Prévot, M. S.; Fathieh, F.; Kapustin, E. A.; Lyu, H.; Wang, H.; Diercks, N. J.; Glover, T. G.; Yaghi, O. M. Rapid Cycling and Exceptional Yield in a Metal–Organic Framework Water Harvester. *ACS Central Science* **2019**, *5*, 1699–1706.
349. Ma, L.; Abney, C.; Lin, W. Enantioselective Catalysis with Homochiral Metal–Organic Frameworks. *Chemical Society Reviews* **2009**, *38*, 1248.
350. Zhang, T.; Lin, W. Metal–Organic Frameworks for Artificial Photosynthesis and Photocatalysis. *Chem. Soc. Rev.* **2014**, *43*, 5982–5993.
351. Zhu, L.; Liu, X.-Q.; Jiang, H.-L.; Sun, L.-B. Metal–Organic Frameworks for Heterogeneous Basic Catalysis. *Chemical Reviews* **2017**, *117*, 8129–8176.
352. Ramprasad, R.; Batra, R.; Pilania, G.; Mannodi-Kanakkithodi, A.; Kim, C. Machine Learning in Materials Informatics: Recent Applications and Prospects. *npj Computational Materials* **2017**, *3*.
353. Coudert, F.-X.; Fuchs, A. H. Computational Characterization and Prediction of Metal–Organic Framework Properties. *Coordination Chemistry Reviews* **2016**, *307*, 211–236.
354. Coudert, F.-X. Responsive Metal–Organic Frameworks and Framework Materials: Under Pressure, Taking the Heat, in the Spotlight, with Friends. *Chemistry of Materials* **2015**, *27*, 1905–1916.
355. Dybtsev, D. N.; Nuzhdin, A. L.; Chun, H.; Bryliakov, K. P.; Talsi, E. P.; Fedin, V. P.; Kim, K. A Homochiral Metal–Organic Material with Permanent Porosity, Enantioselective Sorption Properties, and Catalytic Activity. *Angew. Chem.* **2006**, *118*, 930–934.

356. Seo, J. S.; Whang, D.; Lee, H.; Jun, S. I.; Oh, J.; Jeon, Y. J.; Kim, K. A Homochiral Metal–Organic Porous Material for Enantioselective Separation and Catalysis. *Nature* **2000**, *404*, 982–986.
357. Zhang, X.; Huang, Z.; Ferrandon, M.; Yang, D.; Robison, L.; Li, P.; Wang, T. C.; Delferro, M.; Farha, O. K. Catalytic Chemoselective Functionalization of Methane in a Metal-organic Framework. *Nat Catal* **2018**, *1*, 356–362.
358. Horike, S.; Dincă, M.; Tamaki, K.; Long, J. R. Size-Selective Lewis Acid Catalysis in a Microporous Metal-Organic Framework with Exposed Mn<sup>2+</sup> Coordination Sites. *J. Am. Chem. Soc.* **2008**, *130*, 5854–5855.
359. Yang, B.; Wu, X.-P.; Gagliardi, L.; Truhlar, D. G. Methane Functionalization by an Ir(III) Catalyst Supported on a Metal–Organic Framework: An Alternative Explanation of Steric Confinement Effects. *Theor Chem Acc* **2019**, *138*, 107.
360. de Lange, M. F.; Lin, L.-C.; Gascon, J.; Vlugt, T. J. H.; Kapteijn, F. Assessing the Surface Area of Porous Solids: Limitations, Probe Molecules, and Methods. *Langmuir* **2016**, *32*, 12664–12675.
361. Willems, T. F.; Rycroft, C. H.; Kazi, M.; Meza, J. C.; Haranczyk, M. Algorithms and Tools for High-Throughput Geometry-Based Analysis of Crystalline Porous Materials. *Microporous and Mesoporous Materials* **2012**, *149*, 134–141.
362. Spek, A. L. Single-Crystal Structure Validation with the Program *PLATON*. *J Appl Crystallogr* **2003**, *36*, 7–13.
363. Spek, A. L. Structure Validation in Chemical Crystallography. *Acta Crystallogr D Biol Crystallogr* **2009**, *65*, 148–155.
364. Spek, A. L. What Makes a Crystal Structure Report Valid? *Inorganica Chimica Acta* **2018**, *470*, 232–237.
365. Spek, A. L. *checkCIF* Validation ALERTS: What They Mean and How to Respond. *Acta Crystallogr E Cryst Commun* **2020**, *76*, 1–11.
366. Ongari, D.; Boyd, P. G.; Barthel, S.; Witman, M.; Haranczyk, M.; Smit, B. Accurate Characterization of the Pore Volume in Microporous Crystalline Materials. *Langmuir* **2017**, *33*, 14529–14538.



367. Chung, Y. G.; Camp, J.; Haranczyk, M.; Sikora, B. J.; Bury, W.; Krungleviciute, V.; Yildirim, T.; Farha, O. K.; Sholl, D. S.; Snurr, R. Q. Computation-Ready, Experimental Metal–Organic Frameworks: A Tool To Enable High-Throughput Screening of Nanoporous Crystals. *Chemistry of Materials* **2014**, *26*, 6185–6192.
368. Kaye, S. S.; Dailly, A.; Yaghi, O. M.; Long, J. R. Impact of Preparation and Handling on the Hydrogen Storage Properties of Zn<sub>4</sub>O(1,4-Benzenedicarboxylate)<sub>3</sub> (MOF-5). *Journal of the American Chemical Society* **2007**, *129*, 14176–14177.
369. Düren, T.; Millange, F.; Férey, G.; Walton, K. S.; Snurr, R. Q. Calculating Geometric Surface Areas as a Characterization Tool for Metal–Organic Frameworks. *J. Phys. Chem. C* **2007**, *111*, 15350–15356.
370. Wong-Foy, A. G.; Matzger, A. J.; Yaghi, O. M. Exceptional H<sub>2</sub> Saturation Uptake in Microporous Metal–Organic Frameworks. *Journal of the American Chemical Society* **2006**, *128*, 3494–3495.
371. Dailly, A.; Vajo, J. J.; Ahn, C. C. Saturation of Hydrogen Sorption in Zn Benzenedicarboxylate and Zn Naphthalenedicarboxylate. *The Journal of Physical Chemistry B* **2006**, *110*, 1099–1101.
372. Millward, A. R.; Yaghi, O. M. Metal–Organic Frameworks with Exceptionally High Capacity for Storage of Carbon Dioxide at Room Temperature. *J. Am. Chem. Soc.* **2005**, *127*, 17998–17999.
373. Rowsell, J. L. C.; Millward, A. R.; Park, K. S.; Yaghi, O. M. Hydrogen Sorption in Functionalized Metal–Organic Frameworks. *Journal of the American Chemical Society* **2004**, *126*, 5666–5667.
374. Huang, L. Synthesis, Morphology Control, and Properties of Porous Metal–Organic Coordination Polymers. *Microporous and Mesoporous Materials* **2003**, *58*, 105–114.
375. Walsh, A.; Catlow, C. R. A. Photostimulated Reduction Processes in a Titania Hybrid Metal–Organic Framework. *Chem. Eur. J. of Chem. Phys.* **2010**, *11*, 2341–2344.
376. Vermoortele, F.; Bueken, B.; Le Bars, G.; Van de Voorde, B.; Vandichel, M.; Houthoofd, K.; Vimont, A.; Daturi, M.; Waroquier, M.; Van Speybroeck, V.; Kirschhock, C.; De Vos, D. E. Synthesis Modulation as a Tool To Increase the Catalytic Activity of Metal–Organic Frameworks: The Unique Case of UiO-66(Zr). *J. Am. Chem. Soc.* **2013**, *135*, 11465–11468.

377. Dissegna, S.; Epp, K.; Heinz, W. R.; Kieslich, G.; Fischer, R. A. Defective Metal-Organic Frameworks. *Adv. Mater.* **2018**, *30*, 1704501.
378. Kozachuk, O.; Luz, I.; Llabrés i Xamena, F. X.; Noei, H.; Kauer, M.; Albada, H. B.; Bloch, E. D.; Marler, B.; Wang, Y.; Muhler, M.; Fischer, R. A. Multifunctional, Defect-Engineered Metal-Organic Frameworks with Ruthenium Centers: Sorption and Catalytic Properties. *Angew. Chem. Int. Ed.* **2014**, *53*, 7058–7062.
379. Wu, X.; Luo, Y.; Sun, M.; Qian, J.; Cao, Y.; Ai, X.; Yang, H. Low-Defect Prussian Blue Nanocubes as High Capacity and Long Life Cathodes for Aqueous Na-Ion Batteries. *Nano Energy* **2015**, *13*, 117–123.
380. Goodwin, A. L. Opportunities and Challenges in Understanding Complex Functional Materials. *Nature Communications* **2019**, *10*.
381. Ruankaew, N.; Yoshida, N.; Phongphanphanee, S. Solvated Lithium Ions in Defective Prussian Blue. *IOP Conference Series: Materials Science and Engineering* **2019**, *526*, 012032.
382. Kumar, A.; Yusuf, S. M.; Yakhmi, J. V.; Aswal, D. K.; Debnath, A. K. Study Of Nature Of Structural Defects In A Prussian Blue Type  $\text{Cu}[\text{Sub } 0.73]\text{Mn}[\text{Sub } 0.77][\text{Fe}(\text{CN})[\text{Sub } 6]]\cdot z\text{H}[\text{Sub } 2]\text{O}$  Molecular Magnet. Mumbai, (India), 2010; pp 218–220.
383. Yang, D.; Ortuno, M. A.; Bernales, V.; Cramer, C. J.; Gagliardi, L.; Gates, B. C. Structure and Dynamics of  $\text{Zr}_6\text{O}_8$  Metal-Organic Framework Node Surfaces Probed with Ethanol Dehydration as a Catalytic Test Reaction. *J. Am. Chem. Soc.* **2018**, *140*, 3751–3759.
384. Cliffe, M. J.; Wan, W.; Zou, X.; Chater, P. A.; Kleppe, A. K.; Tucker, M. G.; Wilhelm, H.; Funnell, N. P.; Coudert, F.-X.; Goodwin, A. L. Correlated Defect Nanoregions in a Metal–Organic Framework. *Nat Commun* **2014**, *5*, 1–8.
385. Liu, L.; Chen, Z.; Wang, J.; Zhang, D.; Zhu, Y.; Ling, S.; Huang, K.-W.; Belmabkhout, Y.; Adil, K.; Zhang, Y.; Slater, B.; Eddaoudi, M.; Han, Y. Imaging Defects and Their Evolution in a Metal–Organic Framework at Sub-Unit-Cell Resolution. *Nat. Chem.* **2019**, *11*, 622–628.
386. Zhang, C.; Han, C.; Sholl, D. S.; Schmidt, J. R. Computational Characterization of Defects in Metal–Organic Frameworks: Spontaneous and Water-Induced Point Defects in ZIF-8. *J. Phys. Chem. Lett.* **2016**, *7*, 459–464.

387. He, H.; Hashemi, L.; Hu, M.-L.; Morsali, A. The Role of the Counter-Ion in Metal-Organic Frameworks' Chemistry and Applications. *Coord. Chem. Rev.* **2018**, *376*, 319–347.
388. Svane, K. L.; Bristow, J. K.; Gale, J. D.; Walsh, A. Vacancy Defect Configurations in the Metal–Organic Framework UiO-66: Energetics and Electronic Structure. *J. Mater. Chem. A* **2018**, *6*, 8507–8513.
389. Gutov, O. V.; Hevia, M. G.; Escudero-Adán, E. C.; Shafir, A. Metal–Organic Framework (MOF) Defects under Control: Insights into the Missing Linker Sites and Their Implication in the Reactivity of Zirconium-Based Frameworks. *Inorg. Chem.* **2015**, *54*, 8396–8400.
390. Shearer, G. C.; Chavan, S.; Bordiga, S.; Svelle, S.; Olsbye, U.; Lillerud, K. P. Defect Engineering: Tuning the Porosity and Composition of the Metal–Organic Framework UiO-66 via Modulated Synthesis. *Chem. Mater.* **2016**, *28*, 3749–3761.
391. Bristow, J. K.; Svane, K. L.; Tiana, D.; Skelton, J. M.; Gale, J. D.; Walsh, A. Free Energy of Ligand Removal in the Metal–Organic Framework UiO-66. *The Journal of Physical Chemistry C* **2016**, *120*, 9276–9281.
392. Cai, G.; Jiang, H.-L. A Modulator-Induced Defect-Formation Strategy to Hierarchically Porous Metal-Organic Frameworks with High Stability. *Angew. Chem. Int. Ed.* **2017**, *56*, 563–567.
393. Marreiros, J.; Caratelli, C.; Hajek, J.; Krajnc, A.; Fleury, G.; Bueken, B.; De Vos, D. E.; Mali, G.; Roeffaers, M. B. J.; Van Speybroeck, V.; Ameloot, R. Active Role of Methanol in Post-Synthetic Linker Exchange in the Metal–Organic Framework UiO-66. *Chem. Mater.* **2019**, *31*, 1359–1369.
394. Wu, H.; Chua, Y. S.; Krungleviciute, V.; Tyagi, M.; Chen, P.; Yildirim, T.; Zhou, W. Unusual and Highly Tunable Missing-Linker Defects in Zirconium Metal–Organic Framework UiO-66 and Their Important Effects on Gas Adsorption. *J. Am. Chem. Soc.* **2013**, *135*, 10525–10532.
395. Chen, K.; Xue, D. Materials Chemistry toward Electrochemical Energy Storage. *J. Mater. Chem. A* **2016**, *4*, 7522–7537.
396. Chang, P.; Mei, H.; Zhou, S.; Dassios, K. G.; Cheng, L. 3D Printed Electrochemical Energy Storage Devices. *J. Mater. Chem. A* **2019**, *7*, 4230–4258.
397. Li, H.-Y.; Zhao, S.-N.; Zang, S.-Q.; Li, J. Functional Metal–Organic Frameworks as Effective Sensors of Gases and Volatile Compounds. *Chem. Soc. Rev.* **2020**, *49*, 6364–6401.

398. Wang, H.-F.; Chen, L.; Pang, H.; Kaskel, S.; Xu, Q. MOF-Derived Electrocatalysts for Oxygen Reduction, Oxygen Evolution and Hydrogen Evolution Reactions. *Chem. Soc. Rev.* **2020**, *49*, 1414–1448.
399. Xu, G.; Nie, P.; Dou, H.; Ding, B.; Li, L.; Zhang, X. Exploring Metal Organic Frameworks for Energy Storage in Batteries and Supercapacitors. *Materials Today* **2017**, *20*, 191–209.
400. AlKaabi, K.; Wade, C. R.; Dincă, M. Transparent-to-Dark Electrochromic Behavior in Naphthalene-Diimide-Based Mesoporous MOF-74 Analogs. *Chem* **2016**, *1*, 264–272.
401. Kung, C.-W.; Wang, T. C.; Mondloch, J. E.; Fairen-Jimenez, D.; Gardner, D. M.; Bury, W.; Klingsporn, J. M.; Barnes, J. C.; Van Duyne, R.; Stoddart, J. F.; Wasielewski, M. R.; Farha, O. K.; Hupp, J. T. Metal–Organic Framework Thin Films Composed of Free-Standing Acicular Nanorods Exhibiting Reversible Electrochromism. *Chem. Mater.* **2013**, *25*, 5012–5017.
402. Kung, C.-W.; Platero-Prats, A. E.; Drout, R. J.; Kang, J.; Wang, T. C.; Audu, C. O.; Hersam, M. C.; Chapman, K. W.; Farha, O. K.; Hupp, J. T. Inorganic “Conductive Glass” Approach to Rendering Mesoporous Metal–Organic Frameworks Electronically Conductive and Chemically Responsive. *ACS Appl. Mater. Interfaces* **2018**, *10*, 30532–30540.
403. Ifraemov, R.; Shimoni, R.; He, W.; Peng, G.; Hod, I. A Metal–Organic Framework Film with a Switchable Anodic and Cathodic Behaviour in a Photo-Electrochemical Cell. *J. Mater. Chem. A* **2019**, *7*, 3046–3053.
404. Hod, I.; Bury, W.; Gardner, D. M.; Deria, P.; Roznyatovskiy, V.; Wasielewski, M. R.; Farha, O. K.; Hupp, J. T. Bias-Switchable Permselectivity and Redox Catalytic Activity of a Ferrocene-Functionalized, Thin-Film Metal–Organic Framework Compound. *J. Phys. Chem. Lett.* **2015**, *6*, 586–591.
405. Goswami, S.; Ma, L.; Martinson, A. B. F.; Wasielewski, M. R.; Farha, O. K.; Hupp, J. T. Toward Metal–Organic Framework-Based Solar Cells: Enhancing Directional Exciton Transport by Collapsing Three-Dimensional Film Structures. *ACS Appl. Mater. Interfaces* **2016**, *8*, 30863–30870.
406. Farha, O. K.; Eryazici, I.; Jeong, N. C.; Hauser, B. G.; Wilmer, C. E.; Sarjeant, A. A.; Snurr, R. Q.; Nguyen, S. T.; Yazaydin, A. Ö.; Hupp, J. T. Metal–Organic Framework Materials with Ultrahigh Surface Areas: Is the Sky the Limit? *J. Am. Chem. Soc.* **2012**, *134*, 15016–15021.

407. Howarth, A. J.; Liu, Y.; Li, P.; Li, Z.; Wang, T. C.; Hupp, J. T.; Farha, O. K. Chemical, Thermal and Mechanical Stabilities of Metal–Organic Frameworks. *Nature Reviews Materials* **2016**, *1*.
408. Manna, K.; Zhang, T.; Greene, F. X.; Lin, W. Bipyridine- and Phenanthroline-Based Metal–Organic Frameworks for Highly Efficient and Tandem Catalytic Organic Transformations via Directed C–H Activation. *Journal of the American Chemical Society* **2015**, *137*, 2665–2673.
409. Feng, D.; Chung, W.-C.; Wei, Z.; Gu, Z.-Y.; Jiang, H.-L.; Chen, Y.-P.; Darensbourg, D. J.; Zhou, H.-C. Construction of Ultrastable Porphyrin Zr Metal–Organic Frameworks through Linker Elimination. *Journal of the American Chemical Society* **2013**, *135*, 17105–17110.
410. Klet, R. C.; Wang, T. C.; Fernandez, L. E.; Truhlar, D. G.; Hupp, J. T.; Farha, O. K. Synthetic Access to Atomically Dispersed Metals in Metal–Organic Frameworks via a Combined Atomic-Layer-Deposition-in-MOF and Metal-Exchange Approach. *Chemistry of Materials* **2016**, *28*, 1213–1219.
411. Mondloch, J. E.; Bury, W.; Fairen-Jimenez, D.; Kwon, S.; DeMarco, E. J.; Weston, M. H.; Sarjeant, A. A.; Nguyen, S. T.; Stair, P. C.; Snurr, R. Q.; Farha, O. K.; Hupp, J. T. Vapor-Phase Metalation by Atomic Layer Deposition in a Metal–Organic Framework. *J. Am. Chem. Soc.* **2013**, *135*, 10294–10297.
412. Foster, M. E.; Sohlberg, K.; Spataru, C. D.; Allendorf, M. D. Proposed Modification of the Graphene Analogue Ni<sub>3</sub> (HITP)<sub>2</sub> To Yield a Semiconducting Material. *J. Phys. Chem. C* **2016**, *120*, 15001–15008.
413. Kapustin, E. A.; Lee, S.; Alshammari, A. S.; Yaghi, O. M. Molecular Retrofitting Adapts a Metal–Organic Framework to Extreme Pressure. *ACS Cent. Sci.* **2017**, *3*, 662–667.
414. Schneider, C.; Bodesheim, D.; Ehrenreich, M. G.; Crocellà, V.; Mink, J.; Fischer, R. A.; Butler, K. T.; Kieslich, G. Tuning the Negative Thermal Expansion Behavior of the Metal–Organic Framework Cu<sub>3</sub> BTC<sub>2</sub> by Retrofitting. *Journal of the American Chemical Society* **2019**, *141*, 10504–10509.
415. D’Alessandro, D. M. Exploiting Redox Activity in Metal–Organic Frameworks: Concepts, Trends and Perspectives. *Chem. Commun.* **2016**, *52*, 8957–8971.
416. Calbo, J.; Golomb, M. J.; Walsh, A. Redox-Active Metal–Organic Frameworks for Energy Conversion and Storage. *J. Mater. Chem. A* **2019**, *7*, 16571–16597.

417. Mulfort, K. L.; Hupp, J. T. Chemical Reduction of Metal-Organic Framework Materials as a Method to Enhance Gas Uptake and Binding. *J. Am. Chem. Soc.* **2007**, *129*, 9604–9605.
418. Dan-Hardi, M.; Serre, C.; Frot, T.; Rozes, L.; Maurin, G.; Sanchez, C.; Férey, G. A New Photoactive Crystalline Highly Porous Titanium(IV) Dicarboxylate. *J. Am. Chem. Soc.* **2009**, *131*, 10857–10859.
419. Usov, P. M.; McDonnell-Worth, C.; Zhou, F.; MacFarlane, D. R.; D'Alessandro, D. M. The Electrochemical Transformation of the Zeolitic Imidazolate Framework ZIF-67 in Aqueous Electrolytes. *Electrochimica Acta* **2015**, *153*, 433–438.
420. Brozek, C. K.; Dincă, M. Ti<sup>3+</sup> -, V<sup>2+/3+</sup> -, Cr<sup>2+/3+</sup> -, Mn<sup>2+</sup> -, and Fe<sup>2+</sup> -Substituted MOF-5 and Redox Reactivity in Cr- and Fe-MOF-5. *J. Am. Chem. Soc.* **2013**, *135*, 12886–12891.
421. Brozek, C. K.; Miller, J. T.; Stoian, S. A.; Dincă, M. NO Disproportionation at a Mononuclear Site-Isolated Fe<sup>2+</sup> Center in Fe<sup>2+</sup>-MOF-5. *J. Am. Chem. Soc.* **2015**, *137*, 7495–7501.
422. Halls, J. E.; Hernán-Gómez, A.; Burrows, A. D.; Marken, F. Metal–Organic Frameworks Post-Synthetically Modified with Ferrocenyl Groups: Framework Effects on Redox Processes and Surface Conduction. *Dalton Trans.* **2012**, *41*, 1475–1480.
423. Talin, A. A.; Centrone, A.; Ford, A. C.; Foster, M. E.; Stavila, V.; Haney, P.; Kinney, R. A.; Szalai, V.; El Gabaly, F.; Yoon, H. P.; Léonard, F.; Allendorf, M. D. Tunable Electrical Conductivity in Metal-Organic Framework Thin-Film Devices. *Science* **2014**, *343*, 66–69.
424. Meilikhov, M.; Yussenko, K.; Fischer, R. A. Incorporation of Metallocenes into the Channel Structured Metal–Organic Frameworks MIL-53(Al) and MIL-47(V). *Dalton Trans.* **2010**, *39*, 10990.
425. Halls, J. E.; Ahn, S. D.; Jiang, D.; Keenan, L. L.; Burrows, A. D.; Marken, F. Proton Uptake vs. Redox Driven Release from Metal–Organic-Frameworks: Alizarin Red S Reactivity in UCMCM-1. *Journal of Electroanalytical Chemistry* **2013**, *689*, 168–175.
426. Kalaj, M.; Bentz, K. C.; Ayala, S.; Palomba, J. M.; Barcus, K. S.; Katayama, Y.; Cohen, S. M. MOF-Polymer Hybrid Materials: From Simple Composites to Tailored Architectures. *Chem. Rev.* **2020**, *120*, 8267–8302.
427. Kitao, T.; Zhang, Y.; Kitagawa, S.; Wang, B.; Uemura, T. Hybridization of MOFs and Polymers. *Chem. Soc. Rev.* **2017**, *46*, 3108–3133.

428. Kalaj, M.; Denny, M. S.; Bentz, K. C.; Palomba, J. M.; Cohen, S. M. Nylon–MOF Composites through Postsynthetic Polymerization. *Angew. Chem. Int. Ed.* **2019**, *58*, 2336–2340.
429. Li, X.; Liu, Y.; Wang, J.; Gascon, J.; Li, J.; Van der Bruggen, B. Metal–Organic Frameworks Based Membranes for Liquid Separation. *Chem. Soc. Rev.* **2017**, *46*, 7124–7144.
430. Hendon, C. H.; Walsh, A. Chemical Principles Underpinning the Performance of the Metal–Organic Framework HKUST-1. *Chem. Sci.* **2015**, *6*, 3674–3683.
431. Schneider, C.; Ukaj, D.; Koerver, R.; Talin, A. A.; Kieslich, G.; Pujari, S. P.; Zuilhof, H.; Janek, J.; Allendorf, M. D.; Fischer, R. A. High Electrical Conductivity and High Porosity in a Guest@MOF Material: Evidence of TCNQ Ordering within Cu<sub>3</sub> BTC<sub>2</sub> Micropores. *Chem. Sci.* **2018**, *9*, 7405–7412.
432. Allen, C. A.; Boissonnault, J. A.; Cirera, J.; Gulland, R.; Paesani, F.; Cohen, S. M. Chemically Crosslinked Isorecticular Metal–Organic Frameworks. *Chem. Commun.* **2013**, *49*, 3200.
433. Allen, C. A.; Cohen, S. M. Exploration of Chemically Cross-Linked Metal–Organic Frameworks. *Inorg. Chem.* **2014**, *53*, 7014–7019.
434. Ando, S.; Nishida, J.-i.; Fujiwara, E.; Tada, H.; Inoue, Y.; Tokito, S.; Yamashita, Y. Novel P- and n-Type Organic Semiconductors with an Anthracene Unit. *Chem. Mater.* **2005**, *17*, 1261–1264.
435. Song, E.; Choi, J.-W. Conducting Polyaniline Nanowire and Its Applications in Chemiresistive Sensing. *Nanomaterials* **2013**, *3*, 498–523.
436. Cao, Y.; Mallouk, T. E. Morphology of Template-Grown Polyaniline Nanowires and Its Effect on the Electrochemical Capacitance of Nanowire Arrays. *Chem. Mater.* **2008**, *20*, 5260–5265.
437. Wang, C.; Dong, H.; Hu, W.; Liu, Y.; Zhu, D. Semiconducting  $\pi$ -Conjugated Systems in Field-Effect Transistors: A Material Odyssey of Organic Electronics. *Chem. Rev.* **2012**, *112*, 2208–2267.
438. McCulloch, I. et al. Semiconducting Thienothiophene Copolymers: Design, Synthesis, Morphology, and Performance in Thin-Film Organic Transistors. *Adv. Mater.* **2009**, *21*, 1091–1109.
439. McCullough, R. The Chemistry of Conducting Polythiophenes. *Adv. Mater.* **1998**, *10*, 93–116.

440. Pipertzis, A.; Mühlinghaus, M.; Mezger, M.; Scherf, U.; Floudas, G. Polymerized Ionic Liquids with Polythiophene Backbones: Self-Assembly, Thermal Properties, and Ion Conduction. *Macromolecules* **2018**, *51*, 6440–6450.
441. Nyholm, L.; Nyström, G.; Mihranyan, A.; Strømme, M. Toward Flexible Polymer and Paper-Based Energy Storage Devices. *Adv. Mater.* **2011**, n/a–n/a.
442. Zhang, X.; Goux, W. J.; Manohar, S. K. Synthesis of Polyaniline Nanofibers by “Nanofiber Seeding”. *J. Am. Chem. Soc.* **2004**, *126*, 4502–4503.
443. Liu, Y.; Wang, Y.; Wu, W.; Liu, Y.; Xi, H.; Wang, L.; Qiu, W.; Lu, K.; Du, C.; Yu, G. Synthesis, Characterization, and Field-Effect Transistor Performance of Thieno[3,2-b]Thieno[2',3':4,5]Thieno[2,3-d]Thiophene Derivatives. *Adv. Funct. Mater.* **2009**, *19*, 772–778.
444. Logsdail, A. J.; Scanlon, D. O.; Catlow, C. R. A.; Sokol, A. A. Bulk Ionization Potentials and Band Alignments from Three-Dimensional Periodic Calculations as Demonstrated on Rocksalt Oxides. *Phys. Rev. B* **2014**, *90*, 155106.
445. Cheetham, A. K.; Bennett, T. D.; Coudert, F.-X.; Goodwin, A. L. Defects and Disorder in Metal Organic Frameworks. *Dalton Trans.* **2016**, *45*, 4113–4126.
446. Burdett, J. K.; Mitchell, J. F. Nonstoichiometry in Early Transition Metal Compounds with the Rocksalt Structure. *Progress in Solid State Chemistry* **1995**, *23*, 131–170.
447. Mroz, A. M. Wires.
448. Bartual-Murgui, C.; Akou, A.; Thibault, C.; Molnár, G.; Vieu, C.; Salmon, L.; Bousseksou, A. Spin-Crossover Metal–Organic Frameworks: Promising Materials for Designing Gas Sensors. *J. Mater. Chem. C* **2015**, *3*, 1277–1285.